Ultrasound characterization of tumor angiogenesis, stiffness and microstructure under conventional and innovative therapies

Alexandre Dizeux

THESE DE DOCTORAT DE
L'UNIVERSITE PIERRE ET MARIE CURIE

Spécialité
Informatique biomédicale

Ecole doctorale Pierre Louis de santé publique à Paris : épidémiologie et sciences de l'information biomédicale

Présentée par

M. DIZEUX Alexandre

Pour obtenir le grade de

DOCTEUR de l'UNIVERSITÉ PIERRE ET MARIE CURIE

Sujet de la thèse :

Caractérisation ultrasonore de l'angiogenèse, de l'élasticité et de la microstructure tumorale sous l'effet de thérapies conventionnelles et innovantes.

Directrice de thèse : Mme S. Lori Bridal

Soutenue le 26 juin 2015

Devant le jury composé de :

Mme. S. Lori Bridal	Directeur de thèse
Mme. Bich-Thuy Doan	Rapporteur
M. Frédéric Padilla	Rapporteur
Mme. Delphine Le Guillou	Examinateur
M. Erwan Jouannot	Examinateur
Mme. Emilie Franceschini	Examinateur
M. Michael Oelze	Examinateur
M. Jean-Luc Gennisson	Examinateur

Acknowledgments

I will start the acknowledgments in English and finish in French. I would like to thanks Michael and Rita for their warm welcome in Urbana Champaign. We had a lot of work with sonosensitization experiments but we formed an efficient trio. Before coming to UIUC, I knew what was a “tail vein” but thanks to Michael I discovered what was a “tail gate”. The football game was a bit historic because it was stopped for almost 2 hours because of lightning storm. Finally, spending 3 weeks in UIUC was very pleasant and Michael and Rita have contributed a lot to this feeling.

Je voudrais remercier Lori d’avoir cru en moi et de m’avoir accueilli dans son équipe au sein du laboratoire d’imagerie biomédicale (anciennement paramétrique). Merci de m’avoir laissé des libertés pour explorer différents aspects de mon sujet initial et de m’avoir suivi sur des thématiques annexes comme l’imagerie optique de la vascularisation ou bien les mesures de pression interstitielle. Tout ne marche pas aussi bien qu’on l’aurai souhaité mais j’ai appris pendant ces presque 4 années que c’était aussi ça la recherche, avoir une idée, la tester, échouer, essayer de comprendre ce qui n’a pas fonctionner et recommencer, il faut avoir beaucoup d’énergie pour aller jusqu’au bout d’une idée. Merci pour tous tes conseils avisés et pour toute l’énergie et la rigueur apportées dans la correction de mon manuscrit. Je voudrais remercier également Delphine, LA biologiste de notre équipe avec qui j’ai découvert comment on cultivait des cellules et j’ai beaucoup apprécié le fait de me sentir à l’interface entre biologie et physique.

Merci à Thomas, ancien « pilier de l’équipe », avec qui j’ai découvert l’imagerie ultrasonore et appris le geste technique de la piqure dans la veine caudale de la souris. On a passé un nombre d’heure incalculable dans « notre » salle d’imagerie *in vivo*, on a formé une super équipe ! J’ai une grosse pensée pour Guillaume, on a commencé notre thèse le même jour et partagé nos bureaux pendant trois ans, le goûté de 17h était sacré et il a évolué au cours de ces trois années, tablettes de chocolat, kinder country, fruit, compote de pomme, galette gerblé… tout ça pour dire qu’en tant que partenaire de bureau j’ai préféré certaines périodes à d’autres (oui je préfère les carrés de chocolat aux galettes de blé). C’est avec nostalgie que je repense à cette période, dans quelques jours je vais fermer la marche du trio mais je suis content de voir que la relève est déjà présente avec Bassem, Maxime et on l’espère très bientôt Jérôme. Voici peut être un nouveau trio prêt à jongler entre Matlab et les souris.

En parlant de souris je voudrais remercier tous les gens travaillant au CEF qui s’occupe des souris, des rats et de toute la logistique. J’ai une pensée particulière pour Valérie qui a du gérer plus d’une fois des demandes urgentes d’hébergement et à Georges qui m’a appris beaucoup de gestes techniques, je le remercie sincèrement pour sa disponibilité et sa pédagogie.

Enfin je voudrais remercier toutes les personnes du labo avec qui j’ai pris un grand plaisir à échanger que ce soit au labo ou à l’extérieur. Je souhaite plein de courage pour la fin de thèse à Andresito, Quentinito, Chaoito, Xiranito, Bassemito et Maximito et vous souhaite plein de bonne chose pour la suite.

TABLE OF CONTENTS

I. Introduction

Each year in France, 355 000 new cases of cancer are diagnosed (based on data from 2012, report: INCa 2015). As summarized in Figure 1, the most frequent cancers in France for men and women are, respectively, prostate (56 800 cases each year, 28%) and breast cancer (48 800 cases each year, 31%). Each year, 85 000 men and 63 000 women die because of cancer (based on data from 2012, report: INCa 2015). The most deadly cancers for men and women are, respectively, lung and breast. Moreover, the relative 5 and 10-year survival rates for lung cancer in men is significantly lower (13% and 9%, respectively) than those for breast cancer (86% and 76%, respectively) (Grosclaude et al. 2013).

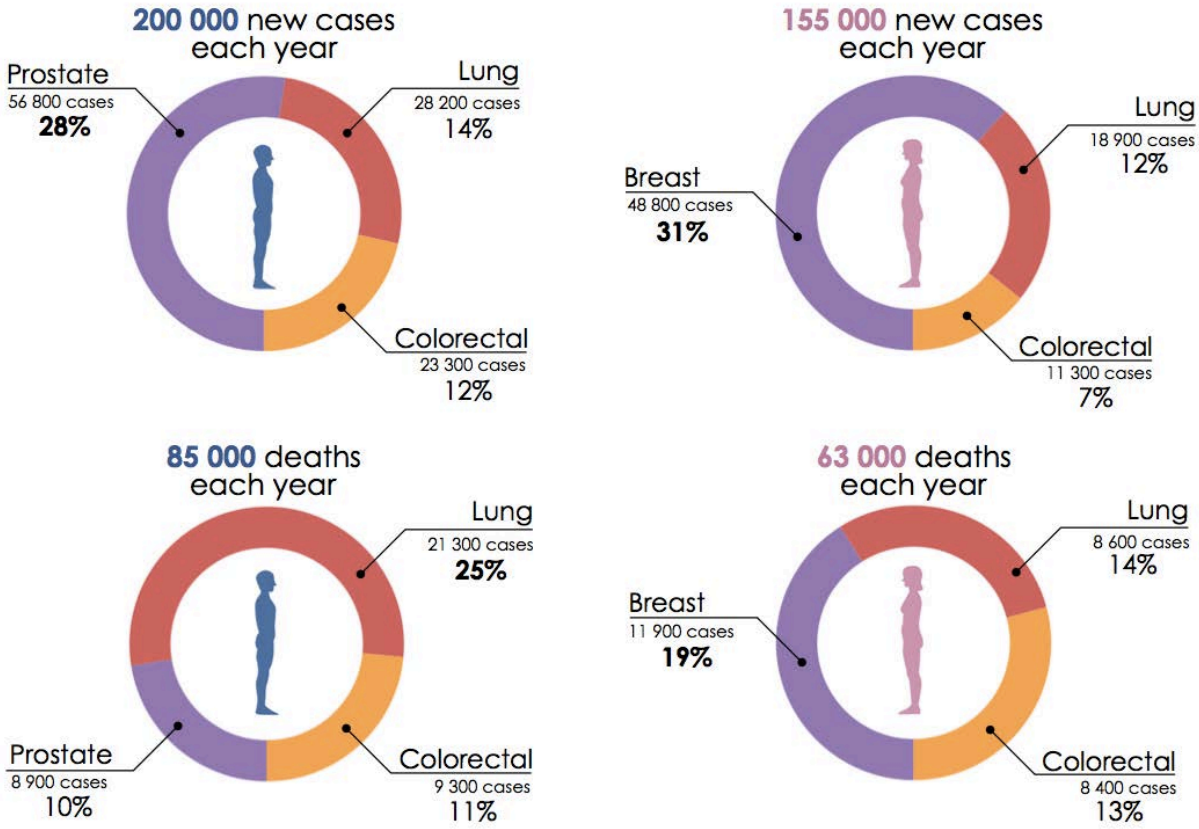

Figure 1: **Number of cancers diagnosed and number of deaths due to cancer each year in France**. Prostate and breast cancers represent the most diagnosed cancer in men and women, respectively The most deadly cancers for men and women are, respectively, lung and breast cancers. These statistics refer to data through 2012 (INCa 2015)

As summarized in Figure 2, important geographic inequalities exist in France in terms of cancer mortality with fewer deaths per capita in the south than in the north. Geographic repartition of mortality for men is much more strongly contrasted than for women. Epidemiological studies such as the ones summarized in Figures 1 and 2 underline that both cancer incidence and mortality are influenced by the gender-distribution and the geographical location of populations in France. Such inequalities in the cancer incidence can hold clues regarding the factors contributing to cancer development. Demographic differences in survival may also underline inequalities concerning access to the diagnostic and therapeutic approaches that are most effective in the fight against cancer.

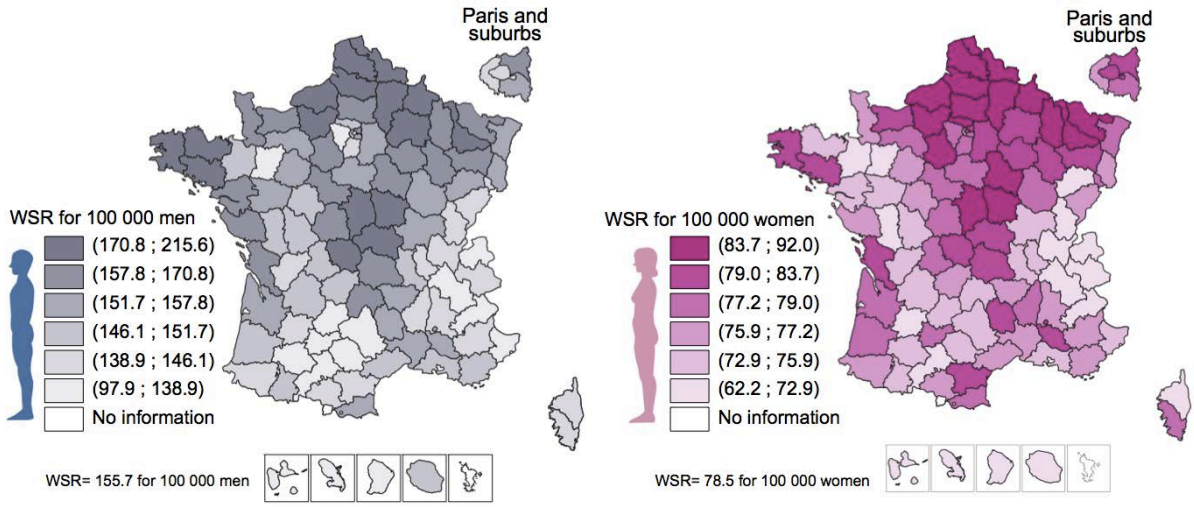

Figure 2: **Geographic repartition of mortality due to cancer in France**. The World Standardized Rate (WSR) enables the comparison with other countrys. *Adapted from* (INCa 2015).

Factors contributing to cancer development

It can be very difficult to precisely determine the underlying mechanisms contributing to the development of cancer in response to carcinogenic agents. Even though descriptions of the biological processes are often not available, correlation and meta-analysis can be used to identify potential carcinogens. Based on the precautionary principle, governments can then better regulate carcinogens in the environment to protect their citizens. For example, the French government has actively regulated tobacco and alcohol in an attempt to reduce cancers related to their consumption.

Environmental factors have been graded by the International Agency for Research on Cancer (IARC) into three different categories depending on their level of risk[1]: proven (group 1), potential (group 2A) or possible (group 2B) carcinogen. For example, physical agents (e.g. ultraviolet radiation, Group 1 (IARC 2007); electromagnetic fields, Group 2B (Inserm, 2008, p889)); chemicals (e.g. radon, Group 1 (Catelinois et al. 2007); atmospheric pollution, Group 1 (Loomis et al. 2013); pesticides, Group depending on chemical molecule (INCa 2014)); biological agents (endocrine disruptors: benzo(a)pyrene, 2,3,7,8-tetrachlorodibenzo-*p*-dioxin, Polychlorinated biphenyl… Group 1 (Cavalieri et al. 1988; De et al. 2004; Fenichel et al. 2013; Inserm 2011; Kociba et al. 1978); viruses) have been shown to be associated with increased cancer incidence.

Diagnosis and therapy

The cancer plan launched in 2014 in France defines three main lines of battle: cure more people, preserve continuity and quality of life of people suffering from cancer and, finally, invest in prevention and in cancer research. The earlier a cancer is diagnosed, the better the chances are for patient survival. The clinical armetarium for cancer diagnosis includes colonoscopy, biopsy, blood sample analysis, ultrasonic imaging, computed tomography (CT), magnetic resonance imaging (MRI) and positron emission tomography (PET). Improving the capacity of these techniques for earlier

[1] Additional description of groups and classifications of chemical substances can be found at the following link: http://monographs.iarc.fr/ENG/Classification/index.php.

diagnosis requires state-of-the-art devices and analysis procedures, use of validated and standardized protocols and insuring wide-spread availability of the best practices. Numerous recent advancements in preclinical and clinical research have contributed to provide a more precise and complete characterization of tumors. As new aspects concerning the tumor are revealed, cancers can potentially be detected earlier and followed more reliably throughout therapy.

As shown in Figure 3 the most common treatments used in the clinic are chemotherapy (use of chemical substances), radiotherapy (ionizing radiation) and surgery. By designing techniques for well-localized delivery of chemotherapy and radiotherapy, considerable progress has been made to increase therapeutic efficiency while reducing toxicity to healthy tissues.

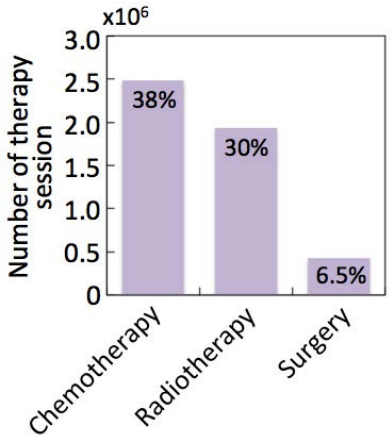

Figure 3: **Nature and number of therapy sessions in France in 2013.** The data concerning radiotherapy do not include radiotherapy done in the private sector (Source: database PMSI MCO 2013 provided by INCa).

This thesis evaluates the capacity of emerging ultrasound imaging techniques to better characterize tumors and explores the ability to apply theses imaging techniques to monitor changes occurring during chemotherapy, anti-angiogenic therapy and novel therapies based on local, physical-interactions. Chapter II reviews cancer biology from the initial development on the cellular scale to the ensuing physiologic modifications. Chapter III provides a summary of available state-of-the art imaging techniques and describes how they can be used to probe specific aspects of the tumor and its surrounding microenvironment. In Chapter IV, the thesis focuses on experimental developments in our laboratory that were implemented to reduce the variability of ultrasonic measurements. Using the techniques thus developed to improve the reproducibility of tumor characterization, a multiparametric study is presented in Chapter V that uses three different ultrasound modalities (quantitative ultrasound, elastography and contrast-enhanced ultrasound) to differentiate modifications in the tumor under antiangiogenic and cytotoxic therapies. In Chapter VI, ultrasonic elastography and contrast-enhanced ultrasound are applied to monitor tumors receiving a new type of ultrasound based-activation, sonosensitization, to enhance the effect of a conventional chemotherapy. Finally, in the Chapter VII the results presented in the thesis are discussed and positioned with respect to other current advancements in diagnosis and the treatment of cancer. Preliminary results concerning multi-parametric ultrasound monitoring of tumors exposed to an innovative therapy referred to as cold plasma are also presented in this final summary chapter.

Bibliography

Catelinois O, Rogel A, Laurier D, Billon S, Hémon D, Verger P, Tirmarche M. Assessment of the health impact related to indoor exposure to radon in France. BEH 2007;18-19:155–157.

Cavalieri E, Rogan E, Cremonesi P, Higginbotham S, Salmasi S. Torigenicity of 6-halogenated derivatives of benzo(a)pyrene in mouse skin and rat mammary gland. J Cancer Res Clin Oncol 1988;114:10–15.

De S, Pramanik SK, Williams AL, Dutta SK. Toxicity of Polychlorobiphenyls and its Bioremediation. Int J Hum Genet 2004;4:281–290.

Fenichel P, Chevalier N, Brucker-Davis F. Bisphenol A: an endocrine and metabolic disruptor. Ann Endocrinol (Paris) 2013;74:211–20.

Grosclaude P, Remontet L, Belot A, Danzon A, Rasamimanana Cerf N, Bossard N. Survie des personnes atteintes de cancer en France 1989-2007. 2013.

INCa. Pesticides et risques de cancers. 2014. Available from: http://www.e-cancer.fr/component/docman/doc_download/12497-pesticides-et-risques-de-cancers

INCa. Les cancers en France. 2015. Available from: http://www.e-cancer.fr/component/docman/doc_download/13267-les-cancers-en-france-en-2014-lessentiel-des-faits-et-chiffres

Inserm. Cancer et environnement. 2008. Available from: http://www.inserm.fr/content/download/946/9496/file/ec_cancers_environnement_der.pdf

Inserm. Reproduction et environnement. 2011. Available from: http://www.inserm.fr/content/download/34821/220855/file/Synthese_Reproduction_environnement.pdf

Kociba RJ, Keyes DG, Beyer JE, Carreon RM, Wade CE, Dittenber DA, Kalnins RP, Frauson LE, Park CN, Barnard SD, Hummel RA, Humiston CG. Results of a two-year chronic toxicity and oncogenicity study of 2,3,7,8-tetrachlorodibenzo-p-dioxin in rats. Toxicol Appl Pharmacol 1978;46:279–303.

Loomis D, Grosse Y, Lauby-Secretan B, Ghissassi F El, Bouvard V, Benbrahim-Tallaa L, Guha N, Baan R, Mattock H, Straif K. The carcinogenicity of outdoor air pollution. Lancet Oncol Elsevier, 2013;14:1262–1263.

II. THE TUMOR MICROENVIRONMENT (TME): A KEY IN TUMOR DEVELOPMENT

Before undertaking research towards better characterization of tumors with novel imaging methods, the tumor's biological components, physiological structures and their interactions need to be considered. The following sections present a summary of key elements of tumor development and explores how therapy can be used to modify these elements. This review will provide a basis for the interpretation of modifications observed using imaging that will be reported in subsequent chapters.

II. The Tumor Microenvironment (TME): a key in tumor development

The development of a tumor cell is the consequence of specific genetic alterations of the cells' DNA. Tumor growth from the initial cell, involves a cascade of chemical messengers exchanged between the cell and its microenvironment. Several physiopathological changes such as an increase of acidity in the TME or an increase of interstitial fluid pressure (IFP) arise from these molecular modifications and impact tumor development (invasiveness) and drug delivery. To reduce tumor invasiveness and drug resistance, several therapeutic strategies have been developed that will be presented at the end of this chapter.

II.1. A cell goes wrong

II.1.1. Deoxyribonucleic acid

Genetic information is stored in the deoxyribonucleic acid (DNA) molecule located in each cell's nucleus. Although the DNA molecule remains inside the cell's nuclei, on a larger scale, it influences the development and the function of the entire organism using intermediary proteins. These polypeptide chains are synthetized in the cell's cytoplasm thanks to messenger ribonucleic acid (mRNA) which brings information from a gene (DNA fragment) to the cytoplasm. The entire set of proteins expressed by a genome is called the proteome.

The Universal Protein Resource (UniProt) gathers research on the proteome, in an accessible database. The last update of the database in August 2014, revealed 64 336 proteins for *Homo sapiens* (proteome ID: UP000005640) and 43 186 proteins for the mouse, *Mus musculus* (proteome ID: UP000000589). Because proteins are built using information stored in genes, their synthesis can be altered by modifications in the DNA sequences. The mutation of certain genes can lead to the development of tumor cells.

II.1.2. Balance between cell death and cell division

To develop and live normally, an organism needs a balance between the proto-oncogenes involved in the stimulation of cell growth and proliferation and suppressor genes that prevent cell division and control the apoptotic process.

A number of proto-oncogenes code for cell surface receptors that span the plasma membrane to communicate between the extracellular environment and the inside of the cell. As shown in Figure 1, these transmembrane receptors have three parts: (1) an extracellular region that is exposed to the outside of the cell and acts like an antenna to collect outside signals; (2) a transmembrane region that spans the plasma membrane; (3) and an intracellular region that initiates the signal transduction leading to a physiological cellular response. These receptors play a crucial role in cell life as they

control delivery of messages concerning, for example, cell division, cell death and secretion of growth factors. Proto-oncogenes may also code for intracellular proteins that normally act downstream from the cell surface receptor pathways to stimulate cell growth and division. If proto-oncogene or suppressor genes undergo mutations that imply overexpression or neutralized expression, respectively, then uncontrolled cell proliferation and cancer can result.

A mutation of the proto-oncogene Ras is present in numerous human cancers (Thomas et al. 2007). As this gene codes for a protein involved in the initial activation of the cascade reaction (phosphorylation) occurring in the intracellular domain, a dysfunction of the Ras gene may lead to an intracellular reaction even when the corresponding extracellular receptor has not been activated.

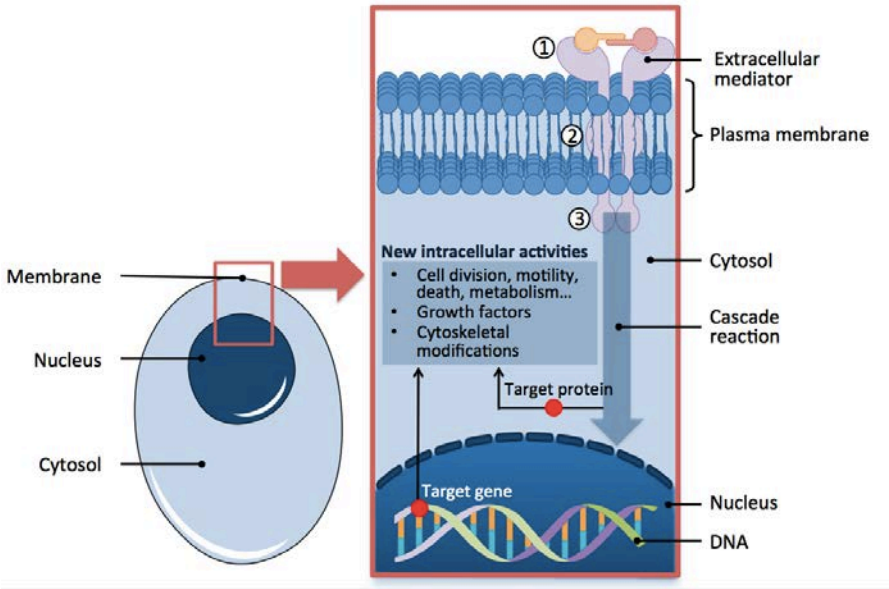

Figure 1: **Signal transduction trough a tyrosine kinase receptor (TKR)**. After the activation of the extracellular receptor, a cascade of reactions is induced that modifies either the activity of proteins located in the cytosol or DNA located in the nucleus. These modifications have a significant effect on cell functions.

Another well-known mutation effecting the p53 suppressor has been observed in at least 50% of human cancers (Levine 1997). This p53 gene is directly involved in stopping the cell cycle or in the initiation of apoptosis when DNA molecules are damaged. Thus, when mutations occur on the p53 gene, continuous division and proliferation of cells with impaired DNA becomes possible. This may lead to the development of cells with a tumor phenotype. In summary, the appearance of tumor cells is directly related to the activation of proliferative pathways and/or suppression of inhibition pathways.

II.1.3. The tumor cell

Due to the alteration of specific genes, tumor cells develop a different phenotype compared to normal cells. Tumor cells:

- develop in a way that is not appropriately controlled by growth factors in the environment.
- have lost sensitivity to anti-proliferative pathways.
- resist apoptosis.
- can present unlimited proliferation (telomeres[2] are preserved after division)

[2] Telomere is region that protects the end of the chromosomes from deterioration or from fusion with neighboring chromosomes. After each chromosome replication, the telomere is shortened until senescence

Morphological abnormalities affect the nucleus' shape, the size of tumor cells, the cytoplasm and membrane cytoplasm (modification of cell adhesion). Unlike normal cells, tumor cells can divide and proliferate without any control. A solid tumor can emerge. To keep growing, tumor cells then need to interact with the surrounding microenvironment.

II.2. The stroma and parenchyma

The stroma designates the loose connective tissue, blood vessels and nerves. The loose connective tissue contains the extracellular matrix (ECM), fibroblasts and free immune system cells (white blood cells or leukocytes). In the following paragraphs each part of the stroma is described.

II.2.1. Extra cellular matrix (ECM)

The ECM designates the extracellular macromolecules making up the connective tissue. The main macromolecules of the ECM are polysaccharides (glycosaminoglycan and proteoglycan) and two types of fibrotic proteins (glycoproteins): structural (collagen, elastin) and adherence (fibronectin, laminin). The fibrotic proteins play a crucial role in cell-cell and cell-ECM interactions.

Proteoglycans are formed from a protein core linked to glycosaminoglycans (GAGs). These proteoglycans aggregate on hyaluronic acid and form large molecules. The high negative charge of GAGs allow them to retain large volumes of water. Proteoglycans have the ability to attach certain cytokines[3] or growth factors and can thus modulate their bioavailability.

Fibrotic proteins form a tridimensional meshwork. Collagen fibers are synthesized in the extracellular space by the assembly of glycoproteins that are synthesized and excreted by fibroblasts. There exist a large family of collagens. The most widely distributed is collagen I. Collagen microfibers have variable lengths. They gather in fibers which themselves are assembled in bundles with different orientations to provide a mechanical support for connective tissue. Collagen I is easily detectable by optical microscopy using red Sirius staining. The fibers which provide elastic properties to connective tissue are mainly composed of elastin, an amorphous substance (no order on a microscopic scale) and a microfibrillar network composed of different types of glycoproteins such as fibrillin.

Cell adhesion in the ECM is principally due to fibronectin secreted by fibroblasts and some endothelial cells. Fibronectin presents numerous connection sites for proteins in the ECM: collagen, membrane receptors (integrin), proteins from circulating blood (fibrin) and GAGs (heparin). In addition to its role in the adhesion between cells and connective tissue, fibronectin intervenes in cell communication. The membrane connection fibronectin-integrin can activate signaling pathways and thus modify the cell's behavior as described in Figure 1. Finally, the basement membrane, composed mainly by laminin and collagen IV, is present at the interface between epithelial cells and ECM.

II.2.2. Fibroblasts

Fibroblasts are fusiform, or star-shaped, cells with long cytoplasmic prolongations: their characteristic size is 20-30 µm in length and 5-10 µm in width. The fibroblast phenotype is adjustable

---

and apoptosis are induced. During cancer development, tumor cells prevent telomere shortening by using the telomerase enzyme.

[3] Cytokines are small soluble proteins synthesized by many different cells and are involved in the communication between cells.

with respect to their level of activation. Fibroblasts can be activated under different conditions such as wound healing or tumor development. Activated fibroblasts are associated with an increased proliferative activity and enhanced secretion of ECM proteins such as type I collagen and also fibronectin.

II.2.3. Immune system cells: whites blood cells (WBCs)

Free, immune-system cells, known as WBCs or leukocytes, are contained in the stroma or can invade the stroma if an inflammation occurs (Figure 2). The myeloid cells have a non-specific action in that they are not steered to a specific target. For example, macrophages and monocytes can phagocytose any unrecognized, solid particles. Granulocytes of different types exist: phagocytic activity of neutrophils can decrease the inflammatory reaction, basophils attract WBCs and activate inflammatory response and eosinophils destroy parasites by liberating enzymes.

Lymphoid cells produce a specific immune response. Lymphocytes (T and B cells) are activated to recognize specific "non-self" antigens and induce the response necessary for the elimination of these antigens. Natural killer cells do not require previous activation to eliminate antigens.

Dendritic cells act at the frontier between myeloid and lymphoid cells. They recognized "non-self" antigens and present them to T-cells (Shevach 2009).

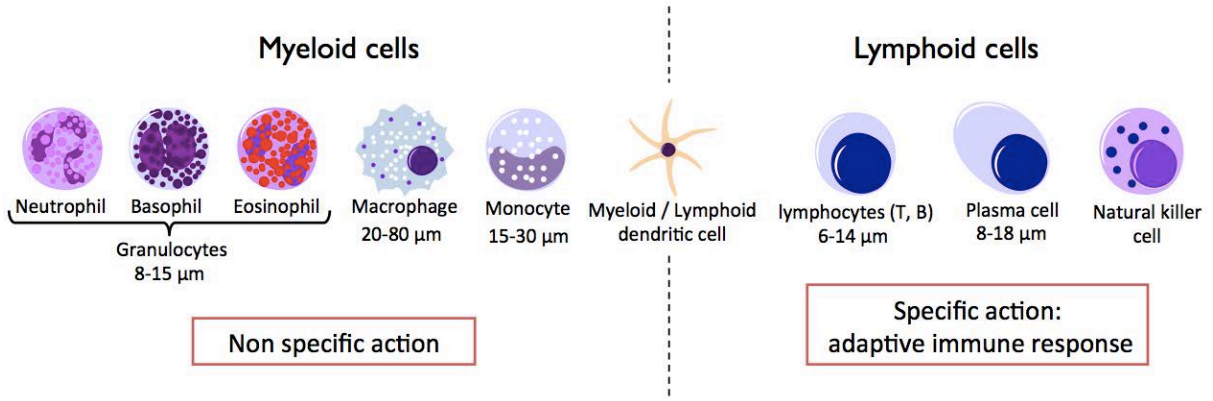

Figure 2: Presentation of the different types of white blood cells present in the stroma and the surrounding organs.

II.2.4. Blood vessels – capillaries

The organ surrounded by the stroma is sustained physiologically by a supply of oxygen and nutrients delivered via the smallest blood vessels, the capillaries (Figure 3).

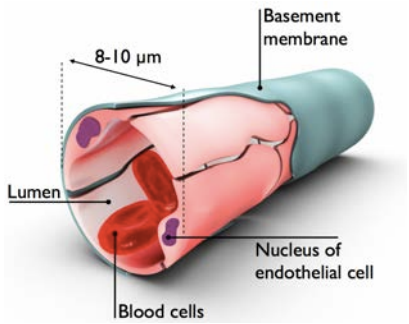

Figure 3: **Diagram of a capillary, the smallest blood vessel in the organism**. It is characterized by a mean diameter between 8 and 10 µm, and fenestration at the junctions between endothelial cells (the size of the gaps varies as a function of the vascularized organ). The formation of a basement membrane and coverage by pericytes (not shown) occurs to develop mature blood vessels.

By a specific assembly, endothelial cells form a capillary which is surrounded by a basement membrane. Once an organ has metabolized oxygen and nutrients, it evacuates waste products via the lymphatic network. Lymphatic vessels consist of endothelial cells surrounded by a thin layer of smooth muscle cells and adventitia. Lymphatic capillaries drain interstitial fluid which is, ultimately, transported to the subclavian vein. Because it provides mechanical support via the ECM (fibrotic and elastic proteins), immune protection with WBCs and an energy supply with capillaries, the stroma is essential for organ function. Under normal conditions, all the components of the stroma are in balance, but the appearance of a cell with a tumoral phenotype can break this equilibrium.

II.3. Tumor cell-stroma interaction

A tumor cell is theoretically immortal and will live as long as it receives oxygen and nutrients. During the initial phase of tumor development, as cells multiply, hypoxic regions develop. Via the secretion of soluble proteins, a tumor cell calls upon its surrounding environment, the stroma, to recruit and modify "normal" cells like fibroblasts, myeloid cells or endothelial cells (Liotta and Kohn 2001). Pro-angiogenic factors to create a new microvascular network able to supply the tumor cells with oxygen and nutrients.

II.3.1. Hypoxia Inducible Factor (HIF)

When tumor cells proliferate and form an aggregate with a volume greater than 1 mm^3, hypoxic regions develop because oxygen cannot diffuse over distances superior to 100 µm (Carmeliet and Jain 2000). Hypoxic stress is mediated by HIF-1. It has a heterodimeric structure consisting of two subunits HIF-1α and β. Due to its sensitivity to oxygen, HIF-1 has a half life of 4 to 6 min (Moroz et al. 2009). Under hypoxic conditions, HIF-1α is protected from degradation. It migrates into the nucleus where it heterodimerizes with the HIF-1β subunit and induces the expression of targeted genes coding for vascular endothelial growth factor (VEGF), platelet derived growth factor (PDGF), fibroblast growth factor (FGF), transforming growth factor (TGF-β), angiopoietins, stromal cell-derived factor 1 (SDF1α) and certainenzymes from glycolysis (Du et al. 2008; Pugh and Ratcliffe 2003). As presented in the following section, these proteins contribute at different levels to the development of the tumor neo-vasculature.

II.3.2. ECM remodeling

The activation of fibroblasts, proteases and integrins disturb normal tissue homeostasis and induce stromal reactions like angiogenesis (Bergers and Benjamin 2003) and inflammatory response (Coussens and Werb 2002).

II.3.3. Cancer-associated fibroblasts (CAFs) and proteases

Fibroblast activation stimulates growth of fibrous and connective tissue. Cancer-associated fibroblasts (CAFs) secrete proteases such as matrix metalloproteinase (Boire et al. 2005; Kessenbrock et al. 2010) that can, for example, increase the migratory behavior of cancer cells by modifying cell-cell adhesion properties (epithelial to mesenchymal transition) (Lochter et al. 1997; Thierry 2002).

CAFs, within the TME, secrete SDF-1 chemokines[4] that enable the adhesion of tumor cells to stromal cells which contributes to their survival, growth and drug resistance (Burger and Peled 2009).

II.3.4. Integrins

Integrins[5] bind to distinct ECM proteins, thereby inducing survival signals and mechanical traction that enables endothelial cells penetrate the interstitial space (Desgrosellier and Cheresh 2010). Abundant collagen deposition through integrin signaling is associated with the stimulation of tumor cell proliferation and survival, chemoresistance and possibly contributes to the establishment and progression of metastatic lesions (Cardones et al. 2003; Conti et al. 2008).

Finally, the ECM degradation and the resulting modifications of tumor cells and endothelial cell adhesion enable the development of a neovascular network from the preexisting one and may lead to the dissemination of metastasis.

II.3.5. Tumor angiogenesis

Vascular Endothelial Growth Factor (VEGF) has an essential role in the remodeling of the vasculature in the stroma. This protein can be secreted by tumor cells but the main source of VEGF comes from fibroblasts and inflammatory cells (Fukumura et al. 1998). VEGF expression is upregulated by numerous other growth factors such as epidermal growth factor (EGF), TGF-α, TGF-β, insulin-like growth factor-1 (IGF), fibroblast growth factor (FGF) and PDGF (Neufeld et al. 1999). The VEGF family includes a large range of interactive factors. By activating integrins and proteases they solicit the creation of new vessels.

The primary integrins in the angiogenic process are the cell-matrix adhesion molecules that control signals between the ECM and endothelial cells. They initiate intracellular signaling pathways promoting migration, invasion, survival and proliferation that are needed for vessel sprouting (Desgrosellier and Cheresh 2010). Interestingly, by degrading proteoglycan complex, some proteases (MMP-9) liberate sequestered VEGF and thus modulate its bioavailability for the receptor VEGFR-2 (Bergers et al. 2000).

II.3.6. Inflammatory response & immune escape

Because of strong proangiogenic stimuli induced by tumor cells, the myeloid cells conveyed into hypoxic areas undergo differentiation into tumor-associated macrophages (TAM), neutrophils, dendritic or endothelial cells and release their own supplies of cytokines and proangiogenic growth factors (Biswas and Mantovani 2010; Carmeliet and Jain 2000; Lin et al. 2006). Normally, immune system cells should reject the tumor, which is recognized as a foreign entity, but the TME is immunosuppressive (Elgert et al. 1998; Ohm and Carbone 2001). One of the mechanisms for immune escape relies on dendritic cells (DCs). When antigens are detected by DCs in an inflammatory environment, it triggers their maturation and leads to a phenotype that enables a strong immune response. However, antigens captured by DCs in non-inflammatory regions fail to induce a productive T-cell response, leading instead to the development of T cell tolerance (Steinman et al. 2003).

[4] Chemokines are cytokines that mediates chemoattraction between cells (chemotaxis: movement of a cell in response to a chemical stimulant).

[5] Integrin is a transmembrane heterodimer receptor involved in cell-cell and cell-ECM adhesion.

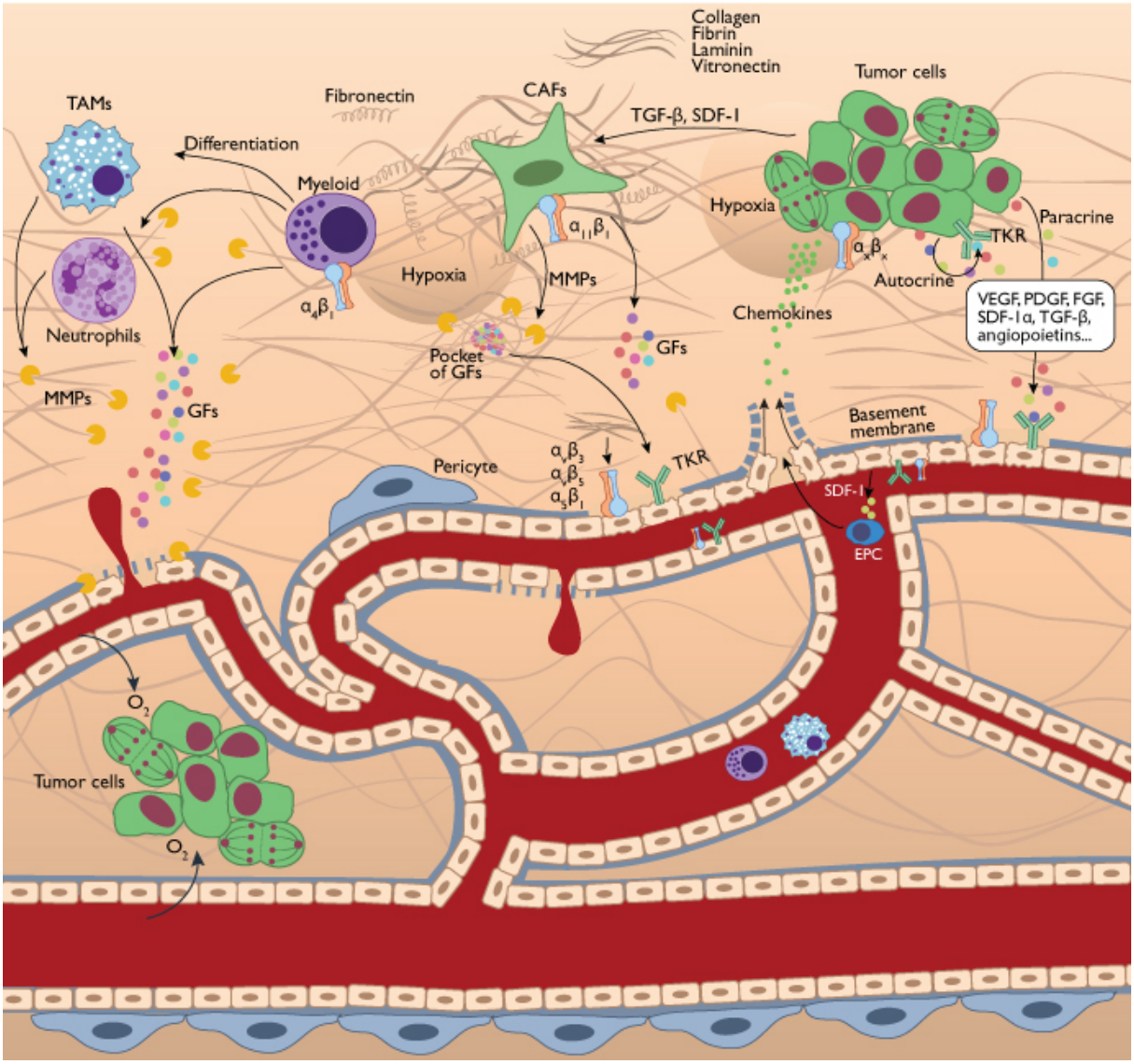

Figure 4: **Tumor development.** The appearance of hypoxic areas triggers the release of a range of proteins that initiate recruitment and modification of stroma cells. The activation and recruitment of fibroblasts due to factors such as TGF-β, chemokines and ECM-degrading proteases leads to an activated phenotype promoting the deposition of ECM proteins (Collagen, Fibrin, Laminin) that foster the remodeling required for tumor expansion. These cancer-associated fibroblasts (CAFs) also release a range of proteases (MMPs) that can degrade components of the quiescent basement membrane of the endothelium, exposing binding sites or forming fragments that affect the function of integrins on neighboring cells. Various growth factors are released by tumor cells to initiate vessel sprouting. VEGF-A activates the VEGFR2 present at the surface of endothelial quiescent cells and induces a modification of their phenotype to increase motility, survival and rate of cell division. Thus, new blood vessels can emerge from pre-existing ones and sprout along a direction following a gradient of chemokines released by tumor cells. Endothelial progenitor cells (EPCs), attracted via SDF-1, also participate in the constitution of new blood vessels. This angiogenic process is promoted by other cells like those of the immune system such as TAMs, neutrophils or dendritic cells which release their own supplies of cytokines and proangiogenic factors. The release of proteases tunes the bioavailability of proangiogenic growth factors (GFs) that would normally remain sequestered in fibrous ECM. Finally, the new tumor microvascular network is not as efficient as the network that feeds healthy organs. It remains in a state of constant evolution that is facilitated by the continuous stimulation of pericytes (blood vessel coverage).

In summary, the creation of the tumor microvascular network is a very complex process involving interactions between many cellular types with exchanges of various messengers (growth factors, cytokines, chemokines…). The main goal of all the processes is to provide enough oxygen and

nutrients to sustain the tumor development (Figure 4). Because of leaks, tortuosity and a heterogeneous distribution, the new microvascular network is not as efficient as normal capillaries that feed healthy organs and this lead to physiopathologies on a macroscopic scale.

II.4. The physiological tumor microenvironment

II.4.1. Genetic and phenotypic variations

The genetic and phenotypic variations that exist within tumors can significantly influence tumor growth and thus the related physiologic modifications. As described in Figure 6, during their development, genetic alterations in tumors can accumulate. This leads to the aggregation of tumor cells with various phenotypes. These phenotypic variations can significantly impact how a tumor will interact with its surrounding microenvironment and so will affect the tumor's physiopathology and therapeutic response.

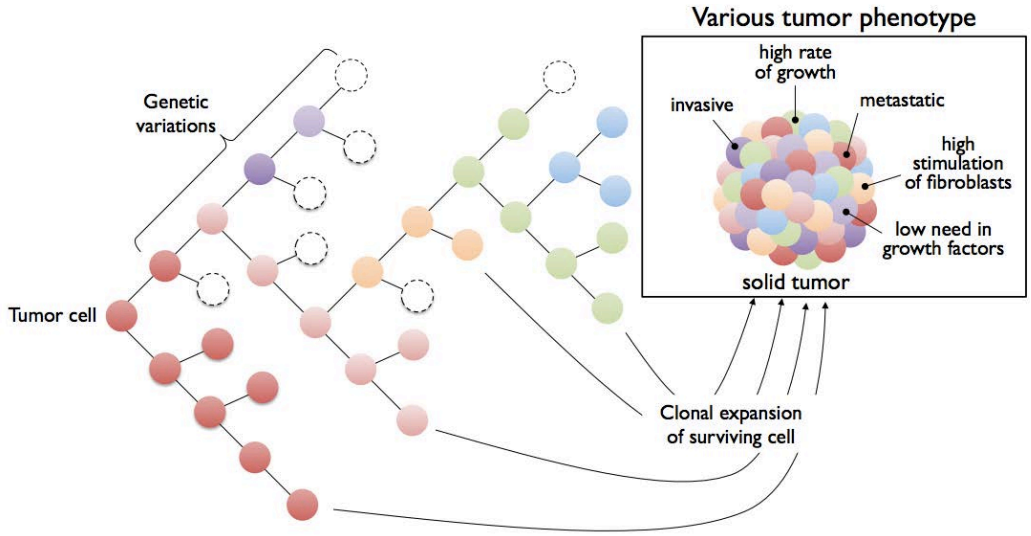

Figure 6: Diagram presenting a schematic view of the evolution of cancer cells during tumor growth. The initial cells (in dark rose) proliferate and mutate. Various genetic alterations accumulate leading to a solid tumor with a heterogeneous phenotype.

II.4.2. Interstitial Fluid Pressure

Interstitial fluid has an ionic composition close to that of the blood plasma[6]. It is found in the space between blood capillaries and cells, and it facilitates the exchange of nutrients, oxygen and waste between these two compartments. In capillaries from normal tissues, the osmotic[7] pressure tends to keep fluid inside vessels whereas hydrostatic[8] pressure tends to move fluid out from the capillaries. This results in a net outward filtration (Figure 5-A). Conversely, in most solid tumors, hydrostatic pressure exerts a pressure from the interstitial space to the blood vessel due, in part, to the leakiness of the defective vascular network, lymph-vessel abnormalities, interstitial fibrosis and a contraction of the interstitial matrix mediated by stromal fibroblasts. The consequence is a net

[6] Blood plasma is constituted about 91% water including a wide range of ionic compounds such as Na^+, Cl^-, K^+, PO_4^{3-}, Ca^{2+}, Mg^{2+}, SO_4^{2-}.

[7] The concentration gradient of solute between compartments (capillaries/cells) separated by a semipermeable membrane (basement membrane) leads to fluid flow from the lowest to the highest concentration. The pressure needed to overcome this movement corresponds to the osmotic pressure.

[8] Hydrostatic pressure is related to the pressure exerted by a fluid in a confined space.

inward filtration because of the overall elevation of interstitial fluid pressure in tumor tissue. (Heldin et al. 2004) (Figure 5-B). This high IFP creates a physiological barrier that can prevent drugs from reaching the tumor core. Understanding mechanisms underlying the elevation of IFP in tumors is crucial to address the problem of drug delivery in solid tumors.

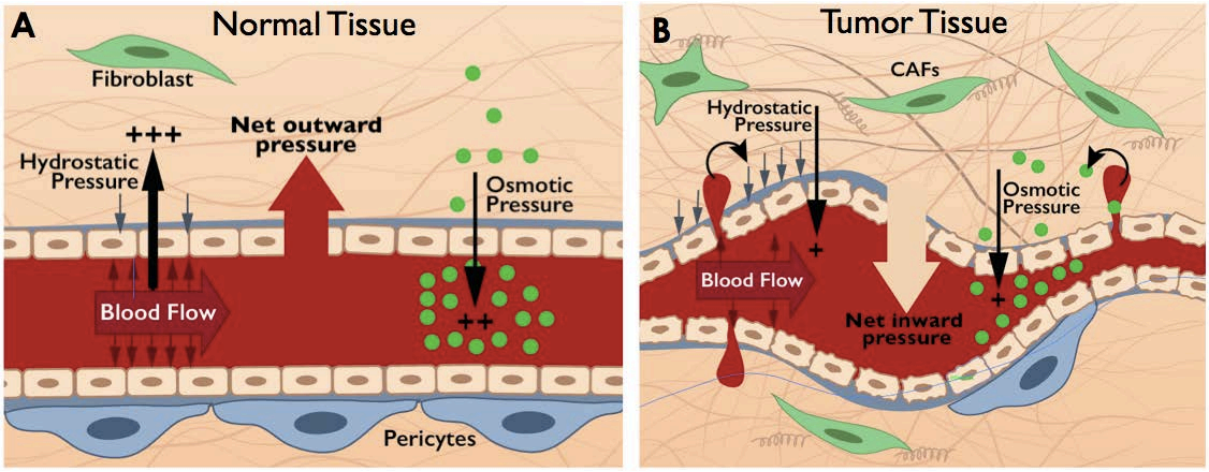

Figure 5: **Transcapillary exchanges and resulting pressures in normal and tumor tissues.** The figure shows the gradient of hydrostatic and osmotic pressures in a normal capillary (**A**) and in a tumor blood vessel (**B**). In normal tissue a net outward pressure (vessel to interstitial space) is present because hydrostatic pressure is higher than osmotic pressure. Conversely, in tumors tissues, the hydrostatic pressure is inverted and is associated with osmotic pressure to induce a net inward pressure on capillaries.

- Fibroblasts and ECM's microfibrillar network

Reed et al. (2001) proposed a model describing how IFP is mediated by the loose connective tissues. Fibroblasts exert tension on the collagen microfibrillar network of the ECM through collagen-binding integrins. It was shown *in vitro* that PDGF (Clark et al., 1989; Gullberg et al., 1990) and TGF-β (Montesano and Orci 1988) significantly enhance the contractile activity of fibroblasts but, when the link between fibroblasts and collagen is broken due to inhibition of specific integrins (Gullberg et al. 1990), their contractile activity is suppressed. These *in vitro* findings are consistent with *in vivo* experiments in which a specific blockage of β1-integrins in rat skin significantly reduced the IFP by releasing the tension in the network of matrix molecules (Reed et al. 1992). Like TGF-β, the inhibition of PDGF in tumor leads to a decrease of IFP (Pietras et al. 2001). Therefore, the effects of PDGF antagonists on the tumor IFP seem to be mediated primarily through PDGF's effect on the stromal fibroblasts rather than its effect on the tumor vessels (Pietras et al., 2002).

- Defective tumor microvascular network

The architecture and functionality of the tumor microvascular network modulated by diverse growth factors, with VEGF being the most significant, also play an important role in the increase of IFP in tumors. The poor efficiency of tumor vessels is the consequence of many factors. By initiating vessel sprouting, VEGF modulates the permeability of capillaries and thus enables leakage into the interstitial space. This leads to increased IFP (Dvorak et al., 1995; Tong et al., 2004). Persistent activation of PDGF in tumors prevents blood vessels from reaching a mature state which also contributes to a defective tumor vasculature (Hellberg et al. 2010). The high level of ramification coupled with the heterogeneous distribution of vessel size may also contribute to the elevation of the IFP within tumors. Moreover, the high rate of tumor cell growth may lead to mechanical compression of blood vessels and so reduce blood flow (Jain 2004).

Significantly decreased tumor IFP was observed in 6 patients suffering from rectal carcinoma that received Anti-VEGF therapy (bevacizumab) (Willett et al. 2004). This reduction of IFP was accompanied with a decrease in the number of tumor endothelial cells, tumor perfusion, vascular volume, and microvascular density associated with the pruning of abnormal vessels. The decrease of IFP initiated by the tumor vasculature renormalization might also be due, in part, to the reduction of vessel permeability. For example, in islet-cell tumor (pancreatic tumor) in transgenic mice, VEGF antagonist induced a reduction of endothelial-cell fenestration (Inai et al. 2004).

II.4.3. Acidity modifications

The absence or non-functional nature of the lymphatic network will also affect the acidity within tumor tissue and will thus impact its development (Alitalo and Carmeliet 2002). Lymphatic vessels in the periphery of tumors are enlarged and perfused, but those deeper within the tumor are compressed and nonfunctional (Jain and Fenton 2002). In normal cells, aerobic glycolysis converts glucose into acetyl-coenzyme A (acetyl-CoA) via pyruvate and these acetyl-CoA molecules undergo a complete oxidation with the creation of CO_2 and H_2O leading to the formation of carbonic acid (H_2CO_3). This process generates 38 ATP molecules per molecule of glucose, whereas, in tumor cells, only 2 ATP molecules per molecule of glucose are created (Kroemer and Pouyssegur 2008). Because tumors are not well oxygenated, the complete oxidation of pyruvate cannot occur and waste products such as lactic acid are generated. The subsequent decreased clearance of acidic products resulting from glucose metabolism leads to a significant decrease of the interstitial pH to levels between 6.5 – 6.9 (Estrella et al., 2013; Helminger et al., 1997; Tannock & Rotin, 1989).

The pH in the TME can significantly impact the cytotoxic effect of anticancer drugs. The passive diffusion of molecules through a cell membrane is most efficient when molecules are uncharged. Because of the pH gradient between intra ($pH \geq 7.4$) and extracellular ($pH < 7.4$) tumor, weakly basic drugs with an acid dissociation constant (7.5 – 9.5) such as doxorubicin, mitoxantrone and vincristine are protonated (a conjugate acid is created by addition of proton H^+) and cellular uptake is significantly decreased (Gerweck et al., 2006; Tannock & Rotin, 1989).

In summary, high IFP and low pH in a solid tumor have a strong impact on tumor development and therapeutic response. They have been established as a marker of poor prognosis in many types of cancers (Curti et al. 1993; Estrella et al. 2013; Milosevic et al. 2001). Different strategies have been developed to modify these physiopathologic parameters in order to bring tumors and their microenvironment back to “normal” conditions for better delivery of therapy.

II.5. Therapeutic strategies that consider the specific tumor physiopathology

II.5.1. Molecular profiling

Le Tourneau et al. (2014) performed a multicentric, randomized proof-of-concept phase II trial comparing molecularly targeted therapy based on tumor molecular profiling vs. conventional therapy in patients with any type of refractory cancer. By mapping the molecular profile of tumors including gene mutations, therapy was selected based on the tumor molecular profile instead of by considering tumor localization. Molecular abnormalities were detected in 40% of the tumors from patients enrolled in the study for which a molecularly targeted agent was available. As the clinical

trial is recent, results presented in the study are limited to showing the feasibility of introducing such protocol in clinical routine.

II.5.2. Reducing IFP

A strategy to enhance the cytotoxicity of conventional therapy is to return physiopathologic parameters to conditions comparable to those observed in healthy organs so that the drug can better treat the whole tumor. Tong et al. (2004) inhibited the VEGF expression in MCaIV-tumor-bearing mice and observed a significant reduction of IFP due to a transient renormalization of the vascular network by the pruning of immature vessels. They also showed that VEGF inhibition induced a hydrostatic gradient across the vascular wall which led to a deeper penetration of therapeutic molecules into tumors. Matsuo et al. (2014) observed a similar renormalization of tumor vasculature in SCCVII tumor-bearing mouse using a multi-tyrosine kinase inhibitor (sunitinib). Vascular renormalization was coupled with an increase of the oxygen level which significantly enhanced the efficiency of radiotherapy.

II.5.3. Modification of pH

Modulation of the pH in tumors can also participate in enhancing drug uptake. To enable drug dissociation in and around tumor cells, an acid-base reaction is needed. A weakly basic drug (pH>7.4) needs an acid environment (pH<7.4) to increase its uptake, whereas, a drug that is weakly acid needs a basic environment to increase its uptake and effectiveness. Tumor pH can be transiently decreased by bolus administration of glucose (with or without a specific mitochondrial inhibitor). Glucose decreases pH through an increase in the production of lactate (Kalliomäki and Hill 2004). It was shown that a transient drop in pH (alkalinization) allowed enhancement of the antitumor effect of chlorambucil and melphalan (weakly basic drugs) in a murine tumor model (Kozin et al. 2001; Kuin et al. 1999). Conversely, an increase in pH can be induced by bolus administration of sodium bicarbonate. It was shown that pretreating animals with bicarbonate before administering mitoxantrone or doxorubicin (weakly acid drugs) significantly increased the response in CH3 or MCF7 breast cancer models, respectively (Raghunand et al., 1999; Raghunand et al., 2001).

II.5.4. Restoring immune capability

Another way to influence tumor growth consists in restoring the immune capability of WBCs present in the surrounding tumor stroma (Figure 7). Two different approaches exist. The conventional one relies on supplementing the immune system by providing fundamental immune elements such as tumor-associated antigens (TAAs), antigen-presenting cells (APCs), effector T cells and cytokines. This approach aims to boost TAA-specific immunity. Novel tumor immunotherapy directly targets to destroy T_{reg} cells or immune suppressive molecules. This approach can enable the restoration of immune capability of, for example, NK cells (Gorelik and Flavell 2001; Grivennikov et al. 2010; Mellman et al. 2011; Palucka and Banchereau 2012; Zou 2006).

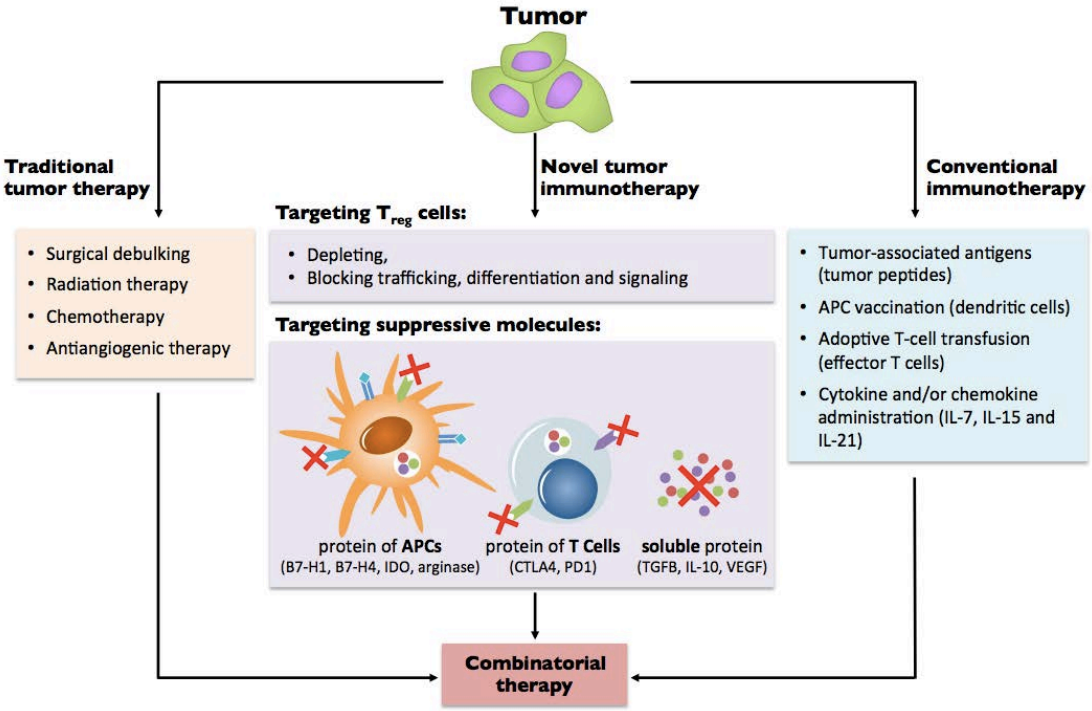

Figure 7 **Therapeutic targeting of suppressive mechanisms including regulatory T cells**. **Traditional tumor therapy** targets the tumor itself and remains the 'gold standard' therapy. **Conventional immunotherapy** supplements the immune system and provides essential immune elements, including tumor-associated antigens (TAAs), antigen-presenting cells (APCs), effector T cells, cytokines and/or chemokines with the aim of boosting TAA-specific immunity. **Novel immunotherapeutic strategies** target the immunosuppressive network of tumors, including regulatory T cells (T_{reg}), suppressive molecules and dysfunctional antigen-presenting cells (APCs), with the aim of recovering TAA-specific immunity. Abbreviations: COX2, cyclooxygenase 2; CTLA4, cytotoxic T-lymphocyte-associated antigen 4; FOXP3, forkhead box P3; IDO, indoleamine 2,3-dioxygenase; IL, interleukin; PD1, programmed cell death 1; TGF β , transforming growth factor- β ; VEGF, vascular endothelial growth factor. *Figure adapted from* (Zou 2006)

II.5.5. Targeting the defective tumor cell metabolism

Targeting cancer cell metabolism also represents a promising new strategy to fight cancer. Metformin, a widely used anti-diabetic agent, drastically effects cancer cell metabolism. Several clinical pilot studies, showed a strong benefit for the use of metformin alone or in combination with conventional therapy. For example, Niraula et al. (2012) conducted a neo-adjuvant pilot study in 39 women with breast cancer. There was a significant increase in tumor cell apoptosis (TUNEL staining) and a significant decrease of the cell division rate (Ki 67 staining) after metformin administration. Hirsch and colleagues (2009) have administrated a combination of metformin and doxorubicin (Dox) in prostate tumor xenografts, and they showed a significant decrease in tumor volume compared to control and Dox-alone groups. Moreover, mice that had undergone combinatorial therapy remained tumor-free for at least 2 months after the end of therapy, whereas, tumor volume of the Dox-alone group reached 1000 mm^3 after 1 month. Evaluation of the clinical relevance of the use of metformin in adequately powered clinical trials using clinical endpoints such as survival is in progress.

II.5.6. Summary of recently developed therapies

Numerous therapies have been developed to target angiogenesis, ECM and the immune aspects of the TME in order to modify tumor development. Table 1 summarizes a range of therapeutic molecules that target tumor stroma and immunity in the TME.

Molecule	Target	Molecule type	Company	Status (reference)
ECM/fibroblasts				
Marimastat	MMP — broad spectrum	Small molecule	British Biotech	✗ Phase III negative for NSCLC, SCLC and breast cancer (NCT00002911, NCT00003010, NCT00003011)
Prinomastat	MMP 2, 3, 9, 13 and 14	Small molecule	Agouron/Pfizer	✗ Phase III negative for NSCLC and prostate cancer (NCT00004199, NCT00003343)
Tanomastat	MMP 2, 3 and 9	Small molecule	Bayer	Phase III terminated (NCIC-CTG trial OV12)
Neovastat	VEGFR2, MMP 2, 9, 12	Small molecule	AEterna Laboratories	✗ Phase III negative for NSCLC (NCT00005838)
Rebimastat	MMP 1, 2, 8, 9 and 14	Small molecule	Bristol-Myers Squibb	✗ Phase III negative for NSCLC (NCT00006229)
Vismodegib	SMO	Small molecule	Genentech/Roche	✗ Phase II negative for CRC and ovarian cancer and phase II for PDAC (NCT00636610, NCT00739661, NCT01064622)
Saridegib	SMO	Small molecule	Infinity Pharmaceuticals	Phase II terminated for PDAC (NCT01130142, NCT01310816)
Sonidegib	SMO	Small molecule	Novartis	Phase III (NCT01708174)
Vasculature				
Bevacizumab	VEGFA	Antibody	Genentech/Roche	FDA-approved ((BLA) 125085)
Vandetanib	VEGFRs, PDGFRs, EGFR	Small molecule	AstraZeneca	FDA-approved ((NDA) 022405)
Sunitinib	VEGFRs, PDGFRs, FLT3, CSF1R	Small molecule	Pfizer	FDA-approved ((NDA) 021938)
Axitinib	VEGFRs, PDGFRs, KIT	Small molecule	Pfizer	FDA-approved ((NDA) 202324)
Sorafenib	VEGFRs, RAF, PDGFRs, KIT	Small molecule	Bayer	FDA-approved ((NDA) 021923)
Pazopanib	VEGFRs, PDGFRs, KIT	Small molecule	GlaxoSmithKline	FDA-approved ((NDA) 022465)
Cabozantinib	VEGFR2, RET, MET	Small molecule	Exelixis	FDA-approved ((NDA) 203756)
Ziv-aflibercept	VEGFA, VEGFB, PlGF	Receptor–Fc fusion	Regeneron	FDA-approved ((BLA) 125418)
Cilengitide	Integrins $\alpha_v\beta_3$, $\alpha_v\beta_5$ and $\alpha_5\beta_1$	Small molecule	Merck Serono	✗ Phase III negative for GBM (NCT00689221)
AMG386	ANG2	RP–Fc fusion protein	Amgen	Phase III (NCT01281254)
Parsatuzumab	EGFL-7	Antibody	Genentech/Roche	Phase II (NCT01399684, NCT01366131)
Enoticumab	DLL4	Antibody	Regeneron	Phase I (NCT00871559)
Demcizumab	DLL4	Antibody	OncoMed	Phase I (NCT00744562, NCT01189968, NCT01189942, NCT01189929)
Nesvacumab	ANG2	Antibody	Regeneron	Phase I (NCT01688960, NCT01271972)
Immune				
Ipilimumab	CTLA-4	Antibody	Bristol-Myers Squibb	FDA-approved ((BLA) 125377)
Sipuleucel-T	PAP	DC vaccine	Dendreon	FDA-approved ((BLA) 125197)
Aldesleukin	IL-2	RP	Prometheus	FDA-approved ((BLA) 103293)
IFN α-2b	IFN-α receptor	RP	Merck	FDA-approved ((BLA) 103132)
MK-3475	PD1	Antibody	Merck	Phase III (NCT01866319)
Nivolumab	PD1	Antibody	Bristol-Myers Squibb	Phase III (NCT01668784, NCT01673867, NCT01642004, NCT01721772, NCT01721746, NCT01844505)
Nivolumab	OX40	Antibody	Bristol-Myers Squibb and PPMC	Phase III (NCT01668784, NCT01642004, NCT01673867, NCT01721772, NCT01721746, NCT01844505)
MPDL3280A	PDL1	Antibody	Genentech/Roche	Phase II (NCT01846416)
PLX3397	KIT, CSF1R, FLT3	Small molecule	Plexxikon	Phase II (NCT01349036)
BMS-663513	CD137 (4-1BB)	Antibody	Bristol-Myers Squibb	Phase II (NCT00612664)
Blinatumomab	CD3 and CD19	Bi-specific scFv	Amgen	Phase II (NCT01741792, NCT01466179, NCT01207388, NCT01471782, NCT00560794, NCT01209286)
AMG 820	CSF1R	Antibody	Amgen	Phase I (NCT01444404)
AMP-224	PD1	Antibody	GlaxoSmithKline	Phase I (NCT01352884)
TRX-518	GITR	Antibody	GITR, Inc.	Phase I (NCT01239134)
IMC-CS4	CSF1R	Antibody	ImClone/Eli Lilly	Phase I (NCT01346358)
CP-870,893	CD40	Antibody	Pfizer	Phase I (NCT00711191, NCT01008527, NCT00607048, NCT01456585, NCT01103635)

Table 1: **Examples of therapies that target the tumor stroma listed by compartment**; red crosses indicate drugs that failed during clinical trial (Junttila and de Sauvage 2013).

Clinical trial results were sufficiently positive to acquire Food and Drug Administration (FDA) approval for several antiangiogenic and immuno-therapies. These drugs can now be used in clinical routine. However, despite promising results obtained in preclinical studies, many other molecules that target ECM and fibroblasts failed during Phase III clinical trials (Table 1).

Longitudinal, *in vivo* monitoring of tumor modifications induced by innovative targeted therapies will provide a better understanding of the tumor response and the specific modifications occurring in the TMD. By developing a better understanding of the therapeutic changes that occur it

may be possible to better predict which molecules will provide useful therapeutic response in human studies. Furthermore, *in vivo* monitoring in clinical trials can potentially provide earlier study end-points or could be used to gauge and adapt individual therapeutic response.

In preclinical studies, a range of imaging modalities is available to investigate tumor modifications and thus provide essential information about their functional and dynamic therapeutic response. In the following chapter, a review of the different imaging tools available and under development for preclinical research will be presented.

II.6. Bibliography

Alitalo K, Carmeliet P. Molecular mechanisms of lymphangiogenesis in health and disease. Cancer Cell 2002;1:219–227.

Bergers G, Benjamin LE. TUMORIGENESIS AND THE ANGIOGENIC SWITCH. Nat Rev Cancer 2003;3:401–410.

Bergers G, Brekken R, Mcmahon G, Vu TH, Itoh T, Tamaki K, Tanzawa K, Thorpe P, Itohara S, Hanahan D. Matrix metalloproteinase-9 triggers the angiogenic switch during carcinogenesis. Nat Cell Biol 2000;2:737–744.

Biswas SK, Mantovani A. Macrophage plasticity and interaction with lymphocyte subsets: cancer as a paradigm. Nat Immunol Nature Publishing Group, 2010;11:889–96.

Boire A, Covic L, Agarwal A, Jacques S, Sherifi S, Kuliopulos A. PAR1 is a matrix metalloprotease-1 receptor that promotes invasion and tumorigenesis of breast cancer cells. Cell 2005;120:303–13.

Burger J a, Peled a. CXCR4 antagonists: targeting the microenvironment in leukemia and other cancers. Leuk Off J Leuk Soc Am Leuk Res Fund, UK 2009;23:43–52.

Cardones AR, Murakami T, Hwang ST. CXCR4 enhances adhesion of B16 tumor cells to endothelial cells in vitro and in vivo via beta(1) integrin. Cancer Res 2003;63:6751–6757.

Carmeliet P, Jain RK. Angiogenesis in cancer and other diseases. Nature 2000;407:249–257.

Clark RAF, Folkvord JM, Heart CE, Murray MJ, McPherson JM. Platelet Isoforms of Platelet-derived Growth Factor Stimulate Fibroblasts To Contract Collagen Matrices. J Clin Invest 1989;84:1036–1040.

Conti J a., Kendall TJ, Bateman A, Armstrong T a., Papa-Adams A, Xu Q, Packham G, Primrose JN, Benyon RC, Iredale JP. The desmoplastic reaction surrounding hepatic colorectal adenocarcinoma metastases aids tumor growth and survival via αv integrin ligation. Clin Cancer Res 2008;14:6405–6413.

Coussens LM, Werb Z. Inflammation and cancer. Nature 2002;420:860–867.

Curti BD, Urba WJ, Alvord WG, Janik JE, Ii JWS, Madara K, Longo DL. Interstitial Pressure of Subcutaneous Nodules in Melanoma and Lymphoma Patients : Changes during Treatment. Cancer Res 1993;53:2204–2207.

Desgrosellier JS, Cheresh D a. Integrins in cancer: biological implications and therapeutic opportunities. Nat Rev Cancer Nature Publishing Group, 2010;10:9–22.

Du R, Lu K V, Petritsch C, Liu P, Ganss R, Passegué E, Song H, Vandenberg S, Johnson RS, Werb Z, Bergers G. HIF1alpha induces the recruitment of bone marrow-derived vascular modulatory cells to regulate tumor angiogenesis and invasion. Cancer Cell 2008;13:206–20.

Dvorak HF, Brown LF, Detmar M, Dvorak AM. Vascular Permeability FactorNascular Endothelial Growth Factor, Microvascular Hyperpermeability, and Angiogenesis. Am J Pathol 1995;146:1029–1039.

Elgert KD, Alleva DG, Mullins DW. Tumor-induced immune dysfunction : the macrophage connection. J Leukoc Biol 1998;64:275–290.

Estrella V, Chen T, Lloyd M, Wojtkowiak J, Cornnell HH, Ibrahim-Hashim A, Bailey K, Balagurunathan Y, Rothberg JM, Sloane BF, Johnson J, Gatenby R a, Gillies RJ. Acidity generated by the tumor microenvironment drives local invasion. Cancer Res 2013;73:1524–35.

Fukumura D, Xavier R, Sugiura T, Chen Y, Park E, Lu N, Selig M, Nielsen G, Taksir T, Jain RK, Seed B, Melvin B, Nessel BK. Tumor Induction of VEGF Promoter Activity in Stromal Cells. Cell 1998;94:715–725.

Gerweck LE, Vijayappa S, Kozin S. Tumor pH controls the in vivo efficacy of weak acid and base chemotherapeutics. Mol Cancer Ther 2006;5:1275–9. Available from:

Gorelik L, Flavell RA. Immune-mediated eradication of tumors through the blockade of transforming growth factor- β signaling in T cells. Nat Med 2001;7:1118–1122.

Grivennikov SI, Greten FR, Karin M. Immunity, inflammation, and cancer. Cell Elsevier Inc., 2010 ;140:883–99. Available from:

Gullberg D, Tingström A, Thuresson A-C, Olsson L, Terracio L, Borg TK, Rubin K. beta1 Integrin-Mediated Collagen Gel Contraction Is Stimulated by PDGF. Exp Cell Res 1990;186:264–272.

Heldin C-H, Rubin K, Pietras K, Ostman A. High interstitial fluid pressure - an obstacle in cancer therapy. Nat Rev Cancer 2004;4:806–13. Available from:

Hellberg C, Östman A, Heldin CH. PDGF and Vessel Maturation. Springer, ed. 2010.

Helminger G, Yuan F, Dellian M, Jain RK. Interstitial pH and PO2 gradients in solid tumors in vivo: High-resolution measurments reveal a lack of correlation. Nature 1997;3:177–182.

Hirsch H a., Iliopoulos D, Tsichlis PN, Struhl K. Metformin selectively targets cancer stem cells, and acts together with chemotherapy to block tumor growth and prolong remission. Cancer Res 2009;69:7507–7511.

Inai T, Mancuso M, Hashizume H, Baffert F, Haskell A, Baluk P, Hu-Lowe DD, Shalinsky DR, Thurston G, Yancopoulos GD, McDonald DM. Inhibition of vascular endothelial growth factor (VEGF) signaling in cancer causes loss of endothelial fenestrations, regression of tumor vessels, and appearance of basement membrane ghosts. Am J Pathol 2004;165:35–52.

Jain RK. Cancer cells compress intratumour vessels. Nature 2004;427:695.

Jain RK, Fenton BT. Intratumoral Lymphatic Vessels : A Case of Mistaken. J Natl Cancer Inst 2002;94:417–421.

Junttila MR, de Sauvage FJ. Influence of tumour micro-environment heterogeneity on therapeutic response. Nature 2013;501:346–54. Available from:

Kalliomäki T, Hill RP. Effects of tumour acidification with glucose+MIBG on the spontaneous metastatic potential of two murine cell lines. Br J Cancer 2004;90:1842–9.

Kessenbrock K, Plaks V, Werb Z. Matrix metalloproteinases: regulators of the tumor microenvironment. Cell 2010;141:52–67. Available from:

Kozin S V, Shkarin P, Gerweck LE. The Cell Transmembrane pH Gradient in Tumors Enhances Cytotoxicity of Specific Weak Acid Chemotherapeutics. Cancer Res 2001;61:4740–4743.

Kroemer G, Pouyssegur J. Tumor cell metabolism: cancer's Achilles' heel. Cancer Cell 2008;13:472–82.

Kuin a, Aalders M, Lamfers M, van Zuidam DJ, Essers M, Beijnen JH, Smets L a. Potentiation of anti-cancer drug activity at low intratumoral pH induced by the mitochondrial inhibitor m-iodobenzylguanidine (MIBG) and its analogue benzylguanidine (BG). Br J Cancer 1999;79:793–801.

Le Tourneau C, Paoletti X, Servant N, Bièche I, Gentien D, Rio Frio T, Vincent-Salomon a, Servois V, Romejon J, Mariani O, Bernard V, Huppe P, Pierron G, Mulot F, Callens C, Wong J, Mauborgne C, Rouleau E, Reyes C, Henry E, Leroy Q, Gestraud P, La Rosa P, Escalup L, Mitry E, Trédan O, Delord J-P, Campone M, Goncalves a, Isambert N, Gavoille C, Kamal M. Randomised proof-of-concept phase II trial comparing targeted therapy based on tumour molecular profiling vs conventional therapy in patients with refractory cancer: results of the feasibility part of the SHIVA trial. Br J Cancer 2014;111:17–24.

Levine AJ. p53, the Cellular Gatekeeper for Growth and Division. Cell 1997;88:323–331.

Lin EY, Li J-F, Gnatovskiy L, Deng Y, Zhu L, Grzesik D a, Qian H, Xue X, Pollard JW. Macrophages regulate the angiogenic switch in a mouse model of breast cancer. Cancer Res 2006;66:11238–46.

Liotta LA, Kohn EC. The microenvironment of the tumour–host interface. Nature 2001;411:375–379.

Lochter A, Galosy S, Muschler J, Freedman N, Werb Z, Bissell MJ. Matrix Metalloproteinase Stromelysin-1 Triggers a Cascade of Molecular Alterations That Leads to Stable Epithelial-to-Mesenchymal Conversion and a Premalignant Phenotype in Mammary Epithelial Cells. J Cell Biol 1997;139:1861–1872.

Matsuo M, Matsumoto S, Mitchell JB, Krishna MC, Camphausen K. Magnetic resonance imaging of the tumor microenvironment in radiotherapy: perfusion, hypoxia, and metabolism. Semin Radiat Oncol Elsevier, 2014;24:210–7.

Mellman I, Coukos G, Dranoff G. Cancer immunotherapy comes of age. Nature Nature Publishing Group, 2011;480:480–9.

Milosevic M, Fyles A, Hedley D, Pintilie M, Levin W, Manchul L, Hill R. Interstitial Fluid Pressure Predicts Survival in Patients with Cervix Cancer Independent of Clinical Prognostic Factors and Tumor Oxygen Measurements. Cancer Res 2001;61:6400–6405.

Montesano R, Orci L. Transforming growth factor beta stimulates collagen-matrix contraction by fibroblasts: implications for wound healing. Proc Natl Acad Sci U S A 1988;85:4894–7.

Moroz E, Carlin S, Dyomina K, Burke S, Thaler HT, Blasberg R, Serganova I. Real-time imaging of HIF-1alpha stabilization and degradation. PLoS One 2009;4:e5077.

Neufeld G, Cohen T, Gengrinovitch S, Poltorak Z. Vascular endothelial growth factor (VEGF) and its receptors. FASEB J 1999;13:9–22.

Niraula S, Dowling RJO, Ennis M, Chang MC, Done SJ, Hood N, Escallon J, Leong WL, McCready DR, Reedijk M, Stambolic V, Goodwin PJ. Metformin in early breast cancer: A prospective window of opportunity neoadjuvant study. Breast Cancer Res Treat 2012;135:821–830.

Ohm JE, Carbone DP. VEGF as a mediator of tumor-associated immunodeficiency. Immunol Res 2001;23:263–272.

Palucka K, Banchereau J. Cancer immunotherapy via dendritic cells. Nat Rev Cancer 2012;12:265–277.

Pietras K, Östman A, Sjöquist M, Sjo M, Arne O, Buchdunger E, Reed RK, Heldin C, Rubin K. Inhibition of Platelet-derived Growth Factor Receptors Reduces Interstitial Hypertension and Increases Transcapillary Transport in Tumors Inhibition of Platelet-derived Growth Factor Receptors Reduces Interstitial Hypertension and Increases Transcapillary. Cancer Res 2001;61:2929–2934.

Pietras K, Rubin K, Sjo T, Buchdunger E, Sjo M, Heldin C, Arne O, Uppsala S-, Biochemistry M, Microbiology KR. Inhibition of PDGF Receptor Signaling in Tumor Stroma Enhances Antitumor Effect of Chemotherapy. Cancer Res 2002a;62:5476–5484.

Pietras K, Rubin K, Sjöblom T, Buchdunger E, Sjöquist M, Heldin C-H, Arne Ö. Inhibition of PDGF Receptor Signaling in Tumor Stroma Enhances Antitumor Effect of Chemotherapy. Cancer Res 2002b;62:5476–5484.

Pugh CW, Ratcliffe PJ. Regulation of angiogenesis by hypoxia: role of the HIF system. Nat Med 2003;9:677–84.

Raghunand N, He X, Sluis R Van, Mahoney B, Baggett B, Taylor CW, Roe D, Bhujwalla ZM, Gilles R. Enhancement of chemotherapy by manipulation of tumour pH. Br J Cancer 1999;80:1005–1011.

Raghunand N, Mahoney B, van Sluis R, Baggett B, Gillies RJ. Acute Metabolic Alkalosis Enhances Response of C3H Mouse Mammary Tumors to the Weak Base Mitoxantrone. Neoplasia 2001;3:227–235.

Reed RK, Berg A, Gjerde E-AB, Rubin K. Control of Interstitial Fluid Pressure: Role of β1-Integrins. Semin Nephrol 2001;21:222–230.

Reed RK, Rubin K, Wiig H, Rodt SA. Blockade of beta1-Integrins in Skin Causes Edema Through Lowering of Interstitial Fluid Pressure. Circ Res 1992;71:978–983.

Shevach EM. Mechanisms of Foxp3+ T Regulatory Cell-Mediated Suppression. Immunity Elsevier Inc., 2009;30:636–645.

Steinman RM, Hawiger D, Nussenzweig MC. Tolerogenic Dendritic Cells. Annu Rev Immunol 2003;21:685–711.

Tannock IF, Rotin D. Acid pH in Tumors and Its Potential for Therapeutic Exploitation. Cancer Res 1989;49:4373–4384.

Thierry JP. Epithelial-mesenchymal transitions in tumor progression. Nat Rev Cancer 2002;2:442–454.

Thomas RK, Baker AC, Debiasi RM, Winckler W, Laframboise T, Lin WM, Wang M, Feng W, Zander T, MacConaill L, Macconnaill LE, Lee JC, Nicoletti R, Hatton C, Goyette M, Girard L, Majmudar K, Ziaugra L, Wong K-K, Gabriel S, Beroukhim R, Peyton M, Barretina J, Dutt A, Emery C, Greulich H, Shah K, Sasaki H, Gazdar A, Minna J, Armstrong S a, Mellinghoff IK, Hodi FS, Dranoff G, Mischel PS, Cloughesy TF, Nelson SF, Liau LM, Mertz K, Rubin M a, Moch H, Loda M, Catalona W, Fletcher J, Signoretti S, Kaye F, Anderson KC, Demetri GD, Dummer R, Wagner S, Herlyn M, Sellers WR, Meyerson M, Garraway L a. High-throughput oncogene mutation profiling in human cancer. Nat Genet 2007;39:347–51.

Tong RT, Boucher Y, Kozin S V, Winkler F, Hicklin DJ, Jain RK. Vascular Normalization by Vascular Endothelial Growth Factor Receptor 2 Blockade Induces a Pressure Gradient Across the Vasculature and Improves Drug Penetration in Tumors. Cancer Res 2004;64:3731–3736.

Willett CG, Boucher Y, di Tomaso E, Duda DG, Munn LL, Tong RT, Chung DC, Sahani D V, Kalva SP, Kozin S V, Mino M, Cohen KS, Scadden DT, Hartford AC, Fischman AJ, Clark JW, Ryan DP, Zhu AX, Blaszkowsky LS, Chen HX, Shellito PC, Lauwers GY, Jain RK. Direct evidence that the VEGF-specific antibody bevacizumab has antivascular effects in human rectal cancer. Nat Med 2004;10:145–7.

Zou W. Regulatory T cells, tumour immunity and immunotherapy. Nat Rev Immunol 2006;6:295–307.

III. *In-vivo* characterization of tumors and their microenvironment

In recent years, technological advancements have widened the capacities of all the existing biomedical imaging modalities. In parallel, a great body of scientific research has been developed using these different modalities to explore new facets of the tumor microenvironment or to improve the evaluation of existing biomarkers. It is thus of central interest to review the current state-of-the-art for the *in vivo* characterization of tumors and their microenvironment by imaging. Four types of imaging will be considered in turn: imaging using ionizing radiation, magnetic nuclear resonance, optical imaging and ultrasound.

III.1 Imaging using ionizing radiation

Several imaging modalities rely on the use of ionizing radiation carrying enough energy to liberate electrons from atoms or molecules. If the energy of radiation is too high it can have a strong toxic impact on a patient and thus the number of exams that a patient can receive is limited.

III.1.1. Micro computed tomography (µCT)

Micro CT imaging provides anatomical information based on the difference of x-ray tissue absorption. X-rays easily penetrate soft tissue which mostly consists of light elements like carbon, oxygen, and nitrogen. Conversely, dense mater absorbs x-rays strongly and enables, for example, the characterization of bone tissue. The resolution of µCT scans can reach 5 to 10 µm with isotropic voxels. It provides a convenient means to investigate tumor modifications in murine models. Radiopaque (high atomic number) non-targeted and targeted contrast agents can be used to provide structural information on the tumor microvascular network or the level of expression of receptors involved in tumor development.

Savai et al. (2009) used µCT to quantify the vascular structure and volume in an orthotopic Lewis lung carcinoma (LLC) under bevacizumab therapy (anti-VEGF drug). They revealed significantly reduced lung tumor volume and lung tumor angiogenesis compared with untreated mice (Figure 1). Vessels were characterized in terms of extent and ramifications. Results revealed that Bevacizumab principally reduced vascularization of the smaller vessels (area ranging from 0.0005-0.02 mm^2).

Reuveni et al. (2011) demonstrated the *in vivo* feasibility of cancer diagnosis based on molecular markers detected using clinical computed tomography. Anti-epidermal growth factor receptor (anti-EGFR) conjugated gold nanoparticles (GNPs, 30 nm) were injected intravenously into nude mice with subcutaneous implantation of human squamous cell carcinoma head and neck cancer. During the early phase of contrast uptake (0 to3 h), no difference was observed between the accumulation of targeted and nontargeted GNPs. But during the late phase of contrast uptake (3 to6 h) signal intensity was significantly higher in tumors which received targeted GNPs. Moreover, the targeted contrast agent remained in the tumor, whereas, the nontargeted GNPs were found in others tissues (red arrows, Figure 2). Since CT scans are in widespread clinical use, development of such targeted molecular probes could ultimately be useful to assess the level of expression of various tumor-development receptors in patients.

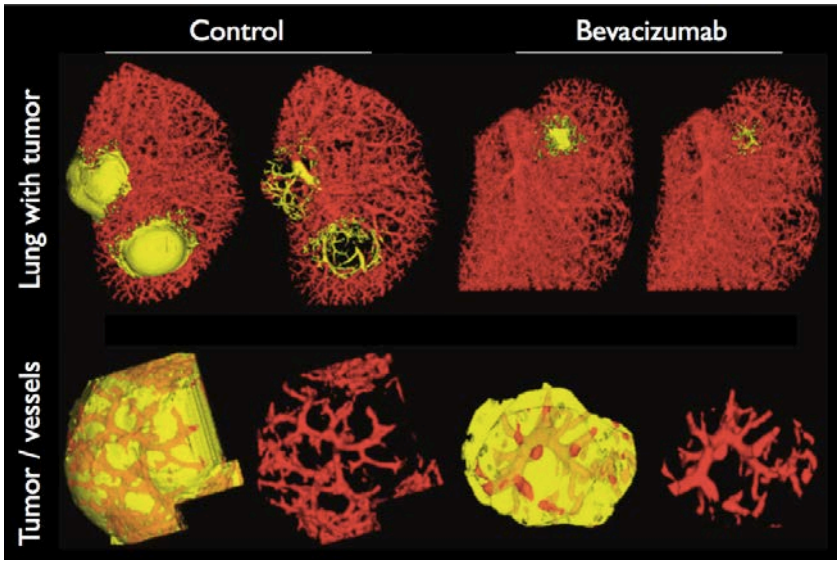

Figure 1: **µCT imaging of tumor vasculature**. Three-dimensional surface rendering images of lung tumors from untreated and bevacizumab-treated mice. Tumors and tumor microvascularization are shown (yellow represents tumor tissue extent; red represents tumor vessels). *Figure adapted from* (Savai et al. 2009).

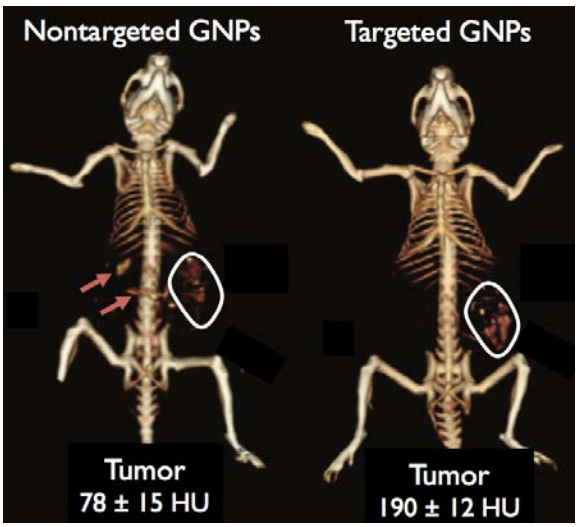

Figure 2: **Molecular imaging in µCT**. *In vivo* X-ray computed tomography (CT) volume-rendered images of, on the left, a mouse 6 hours postinjection of nonspecific immunoglobulin G-coated GNPs as a passive targeting experiment, and, on the right, a mouse 6 hours postinjection of anti-EGFR-coated GNPs that specifically targeted the squamous cell carcinoma head and neck tumor. The anti-EGFR-targeted GNPs show clear contrast enhancement of the tumor (white outline around the ROI). The contrast enhancement, estimated from the full tumor volume, was quantitatively determined according to the differential contrast in CT numbers (in Hounsfield units [HU]), compared to that of the same mouse before injection. *Figure adapted from (Reuveni et al. 2011).*

III.1.2. Positron Emission Tomography (PET)

PET imaging is based on the coincident detection of two photons (511 keV) that are simultaneously emitted after the annihilation of a positron with an electron. The creation of the positron is due to the disintegration of an unstable isotope of atoms like ^{18}F, ^{15}O, ^{13}N or ^{11}C. The resolution of this imaging modality is limited by the distance that the positron travels before annihilation which is of the order of 1 mm (Figure 3). To overcome this limitation in spatial

resolution, a CT scan can be acquired and co registered with the PET scan to anatomically locate PET signal. Within the tumor, this imaging modality can assess physiological processes and the molecular expression of various types of receptors.

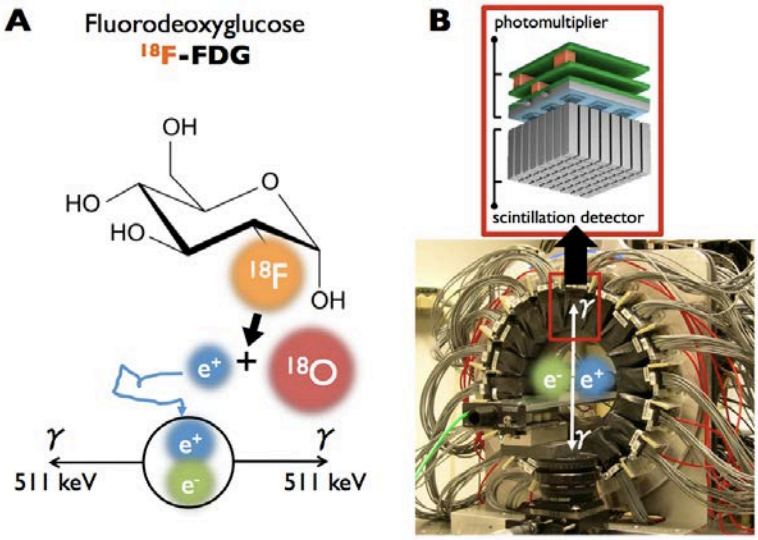

Figure 3: **TEP imaging. A)** Fluorodeoxyglucose (^{18}F-FDG) is one of the radiotracers that is the most commonly used in clinical routine because it enables the detection of tumors based on their high glucose metabolism. The ^{18}F atom (half-life = 110 min) disintegrates into ^{18}O (stable) and a positron which annihilates with an electron after a free travel of ≈1 mm. **B)** The annihilation creates two coincident photons with an energy of 511 keV which are detected with a scintillation detector from which the signals are amplified with photomultiplier.

The development of alveolar type rhabdomyosarcoma (ARMS) is principally driven by the expression of tyrosine kinase receptors such as insulin-like growth factor (IGF1R), PDGFR, c-Met and c-Kit. By inhibiting IGF1R in ARMS with a picropodophyllin drug, Soundararajan et al. (2012) demonstrated a significant decrease in the uptake of ^{18}F-FDG in treated vs. control mice. Tumor volume was not significantly different between the two groups. Since ^{18}F-FDG is a marker of cell metabolism, these results indicate that the inhibition of IGF1R in this tumor model reduces tumor metabolism.

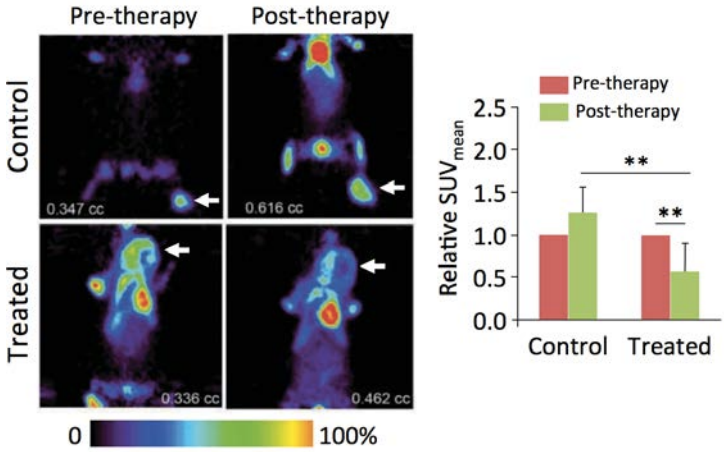

Figure 4: **Molecular imaging with PET**. White arrows designate the tumor position. The presented data are reported in terms of the mean standard uptake value (SUV_{mean}=[Activity in tumor/Tumor weight]/[Injected activity/Body weight]). N=6 in the treated group and N=3 in the control group (drug vehicle), ** p<0.01 ANOVA test. *Figure adapted from* (Soundararajan et al. 2012).

^{18}F-FDG is not suitable for the study of brain tumors because of the high rate of glucose metabolism in normal brain tissue. Conversely, radiolabeled amino acids have a relatively low uptake in normal brain tissue and usually accumulate intensely in tumor cells. The high tumor-to-brain (T/B) ratio makes radiolabeled amino acids particularly applicable in the study of brain tumor (Hutterer et al. 2011). As shown in Figure 6, in an orthotopic xenograft model of human glioblastome multiform (GBM), Nedergaard et al. (2014) detected early response to an antitumor therapy using ^{18}F-FET, a radiolabeled amino acid.

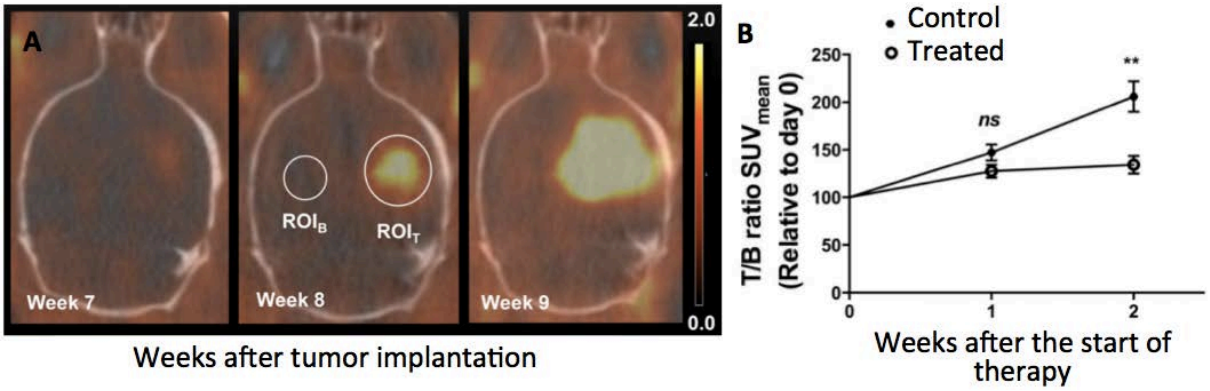

Figure 5: **Detection of cerebral tumor with ^{18}F-FET imaging. A)** Fused ^{18}F-FET µPET/CT images showing tumor progression 7–9 weeks after tumor cell injection. Transverse views through the brain of the same mouse. The ROI_T was drawn around the region with maximum tracer uptake and a 4 mm^3 ROI_B was drawn in the contralateral hemisphere. Scale bar: 0.0–2.0 SUV_{max}. **B)** The relative T/B ratio of SUV_{mean} versus time after tumor engraftment. Values are expressed as mean ± SEM in the treated group (n = 5 to 7) and in the control group (n = 4 to7), **p<0.01, unpaired Student's t-test.

Hypoxia, which is one of the physiologic patterns that trigger the recruitment of cells surrounding a tumor, can be traced using fluoroazomycin arabinoside (FAZA) in murine tumor models (Busk et al. 2013; Tran et al. 2012) or in clinical routine (Bollineni et al. 2013). Moreover, by grafting specific antibodies to a radionuclide, it is possible to assess the molecular expression of specific receptors. Battle et al. (2011) used the ability of ^{18}F-Fluciclatide to bind $\alpha_v\beta_3$ and $\alpha_v\beta_5$, two integrins that are highly expressed on a range of tumor cells and neovasculature, to assess the efficacy of an antiangiogenic drug (sunitinib) in human glioblastoma xenografts (U87-MG). Findings revealed that this drug induced a reduction in the tumor uptake of ^{18}F-fluciclatide compared with that in vehicle-treated controls over the 2-week dosing regimen while no significant difference was observed in term of tumor volume. These results suggest that the antiangiogenic drug induced a significant decrease in the expression of $\alpha_v\beta_3$ and $\alpha_v\beta_5$ integrins. Another team assessed the molecular expression of the epidermal growth factor receptor (EGFR) in a human head and neck squamous carcinoma model in nude mice using a [^{18}F]FBEM-cEGF probe consisting in a Cys-tagged EGF (cEGF) labeled with ^{18}F thanks to a coupling between Cys-tag and N-[2-(4-^{18}F]fluorobenzamido)ethyl]maleimide ([^{18}F]FBEM) (Li et al. 2012). The CXCR4 receptor is another interesting molecular imaging target for which the level of molecular expression can be assessed *in vivo* using the targeted radionuclide, 4-^{18}F-T140, designed by Jacobson et al (2010). This receptor is involved at different levels in tumor development and several studies have shown a correlation between high levels of CXCR4 expression in cancers and tumor aggressiveness, poor prognosis and resistance to chemotherapy (Azab et al. 2011; Kurtova et al. 2009; Nie et al. 2010; Oda et al. 2009; Zeng et al. 2006).

TEP imaging not only provides information about the level of expression of growth factor receptors (GFr) but may also assess the activity of proteases involved in ECM remodeling. Selivanova et al. (2013) have developed a selective gelatinase inhibitor for *in vivo* TEP imaging of active MMP-2 and MMP-9. To prepare the way toward application of this PET in TME imaging, they used this targeted radionuclide for the detection and characterization of atherosclerosis (Müller et al. 2014). The association of PET radiotracers with antibodies allows assessment of the physiologic status of tumors by mapping viable (perfused), hypoxic and necrotic tissues. Huang et al. (2012) performed experiments with mouse models of human non–small cell lung cancer in which they evaluated the intratumoral accumulation of 3 different PET tracers to determine tumor heterogeneity. By coinjecting ^{18}F-FDG, ^{18}F-fluorothymidine (^{18}F-FLT), and ^{18}F-fluoromisonidazole (^{18}F-FMISO) with fluorescent anti-bodies marker of cell proliferation (bromodeoxyuridine), tumor perfusion (Hoechst 33342) and hypoxia (pimonidazole), they mapped and correlated regions of proliferation, hypoxia, perfusion, stroma, and necrosis with digital autoradiography of PET tracers and fluorescent histology. They also showed the possibility to perform an *in vivo* follow-up of the level of apoptosis in a human head and neck squamous cell cancer tumor xenograft model under doxorubicin therapy using ^{18}F-annexin[9] V (Hu et al. 2012)

A similar study has been performed *in vivo* by Cho et al. (2009) by coupling dynamic contrast enhanced MRI (DCE-MRI, intravascular contrast agent: Gd-DTPA) with PET ^{18}F-Fmiso (hypoxia marker) for the characterization of a rat prostatic carcinoma (R3327-AT). The *in vivo* imaging results were validated by *ex vivo* staining with hematoxylin/eosin (H&E, tumor necrosis) and pimonidazole (PIMO, tumor hypoxia) on tumor tissue sections accurately registered to the corresponding *in vivo* slices (Figure 6). Finally, by demonstrating the relationships between DCE-MRI and hematoxylin/eosin slices and between ^{18}F-Fmiso PET and pimonidazole slices they confirmed the validity of MRI/PET measurements to image the tumor microenvironment and to identify regions of tumor necrosis, hypoxia, and well-perfused tissue. The *in vivo* mapping of such biomarkers (necrosis, hypoxia and well-perfused tissue) could be very useful to predict the future evolution of a tumor.

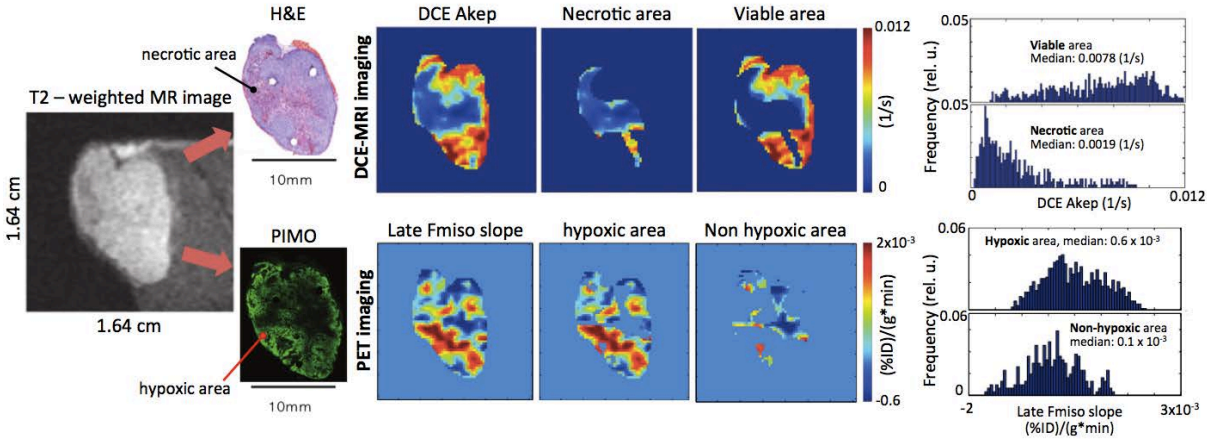

Figure 6: **Characterization of TME using multimodal MRI/PET imaging.** The T2-weighted MR image of the tumor slice and the corresponding H&E and pimonidazole (PIMO) slices are presented. Hypoxic and necrotic areas were extracted form histology slices and masks were positioned on DCE-MRI and PET images to highlight these specific areas. Based on *in vivo* imaging, a precise characterization of necrotic, viable, hypoxic and non-hypoxic areas was made using histograms for each type of area and each imaging modality. Akep: rate constant of movement of Gd-DTPA between the interstitial space and plasma; %ID = percentage of injected dose. *Figure adapted from (Cho et al. 2009)*

[9] The annexins protein family is involved in physiological processes such as inflammation and apoptosis. Annexin-V is used for early detection of apoptosis.

III.1.3. Single-photon emission computed tomography (SPECT)

Another imaging modality using the emission of high-energy photons is single-photon emission computed tomography (SPECT). SPECT also enables the assessment of physiologic processes that occur within tumors. This imaging modality is principally used to highlight molecular expression in tumors.

Due to the fact that only one photon is emitted from the atom disintegration or electronic transition this imaging device has a different architecture compared to PET scans. As described in Figure 7, a metal grid is placed in front of the sensor (gamma camera). Its architecture will directly impact the sensitivity of photon detection and the image resolution. For preclinical studies the use of pinhole devices is essential to image small regions. Of note, different SPECT radionuclides emit positrons at different energy levels, which can be distinguished by the gamma cameras. This method can be used to label two different cell populations with different SPECT isotopes and track them simultaneously in the same subject.

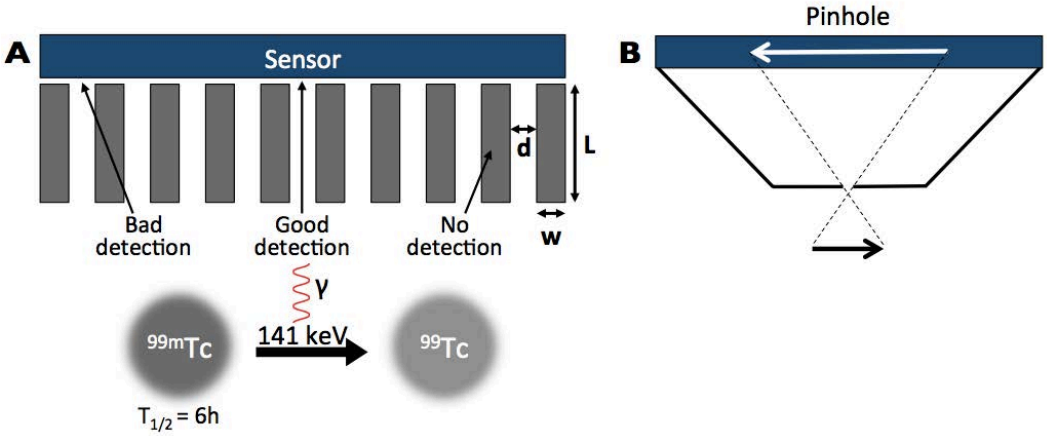

Figure 7: **Basic description of a SPECT scan detector**. **A)** The width (w), length (L) and the spacing (d) are the main characteristics of the metal-mesh grid positioned in front of the gamma camera (sensor). Its characteristics have a direct impact on the sensitivity and resolution of images acquired. Metastable technetium is widely used because it emits a 141 keV photon when it returns to its stable state. **B)** To image small objects for preclinical studies, single pinhole, or pinhole arrays are necessary (µSPECT).

Using µSPECT, McLarty et al. (2009) assessed the level of expression of the TKR HER2 (human epidermal growth factor receptor 2) which is a TKR overexpressed in around 20-30% of breast cancers and is associated with aggressive disease, higher recurrence rate, and increased mortality (Mitri et al. 2012). To target HER2, McLarty and colleagues grafted pertuzumab molecules on ^{111}In-diethylenetriaminepenta-aceticacid (^{111}In-DTPA-pertuzumab). To assess the sensitivity of this targeting, they downregulated HER2 expression by administering trastuzumab in a subcutaneous xenograft of human breast carcinoma (MDA-MB-361). Results revealed that after 3 days of trastuzumab treatment, *in vivo* tumor uptake of ^{111}In-DTPA-pertuzumab decreased 2-fold compared to the placebo group (*P = 0.05) (Figure 8-A). The ability of this radiotracer to target HER2 thereby established HER2 downregulation under trastuzumab therapy.

Another team described tumor uptake and biodistribution of two anti-epidermal growth factor receptor nanobodies (^{99m}Tc-7C12 and ^{99m}Tc-7D12) in a human skin carcinoma (A431) model expressing EGFR and in a rhabdomyosarcoma (R1M) model that did not express EGFR (Gainkam Tchouate et al. 2008). It was shown that, for these two radiotracers, there is a significantly higher

uptake in A431 tumor compared to R1M tumor. These results demonstrate that molecular expression of this receptor can be assessed using SPECT detection of anti-epidermal growth factor receptor nanobodies (Figure 8-B).

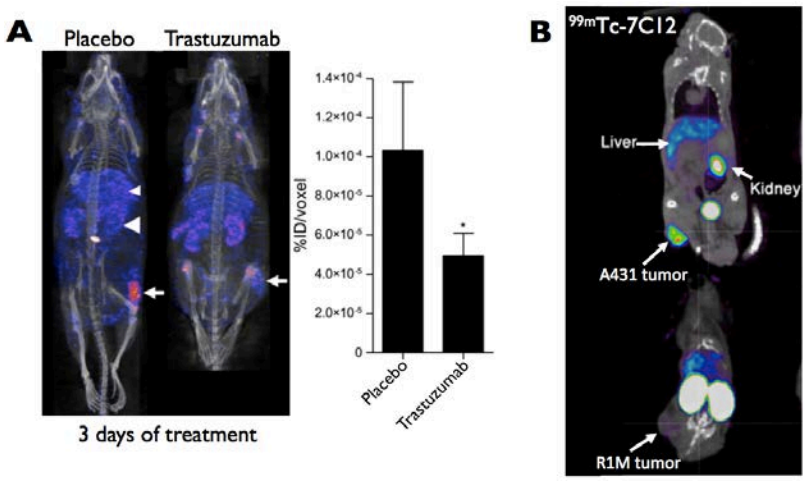

Figure 8: **Molecular imaging of the epidermal growth factor receptor using SPECT imaging**. **A)** After 3 days of trastuzumab treatment, a significant decrease was observed in the percentage of the injected dose per voxel (%ID/voxel) in the MDA-MB-361 breast tumor model. This indicates a significant reduction of the HER2 expression level in the treated tumor. *Figure adapted from (McLarty et al. 2009)*. **B)** The ^{99m}Tc-7C12 and ^{99m}Tc-7D12 (not shown) radiotracers target EGFR and can be used to quantify the molecular expression of EGF-receptor in tumors. Images in panel B show that the targeting is EGFR specific. *Figure adapted from (Gainkam Tchouate et al. 2008).*

In summary, µCT, µPET and µSPECT represent powerful tools to monitor the level of molecular expression of specific receptors involved in tumor development *in vivo*. Moreover, thanks to the availability of numerous radiotracers, it is possible to target and map specific biomarkers such as hypoxia, perfusion and necrotic area in tumor using these modalities.

III.2. Magnetic resonance imaging (MRI)

Among the non-ionizing imaging modalities available for assessment of the TME, MRI is one of the most powerful and versatile. The magnet of an MRI device produces a constant magnetic field (B_0) that aligns a small but sufficient proportion of the magnetic moments of ^{1}H atoms present in the body. During an MRI acquisition, the aligned magnetic moments are acted on by a perpendicular oscillating magnetic field ($B_1 \perp B_0$) chosen to precisely match the resonant frequency (Larmor frequency) of the studied atoms. When the magnetic field B_1 is switched off, the magnetic moments of the atoms return to their equilibrium positions, aligning with B_0. Two characteristic times emerge from this relaxation that are related, respectively, to the time taken by the transverse and longitudinal component of the nuclear magnetic moment to reach equilibrium (Figure 9). As these relaxation times are different in biologic tissues, it is then possible to image the same tissues but with different contrasts and information.

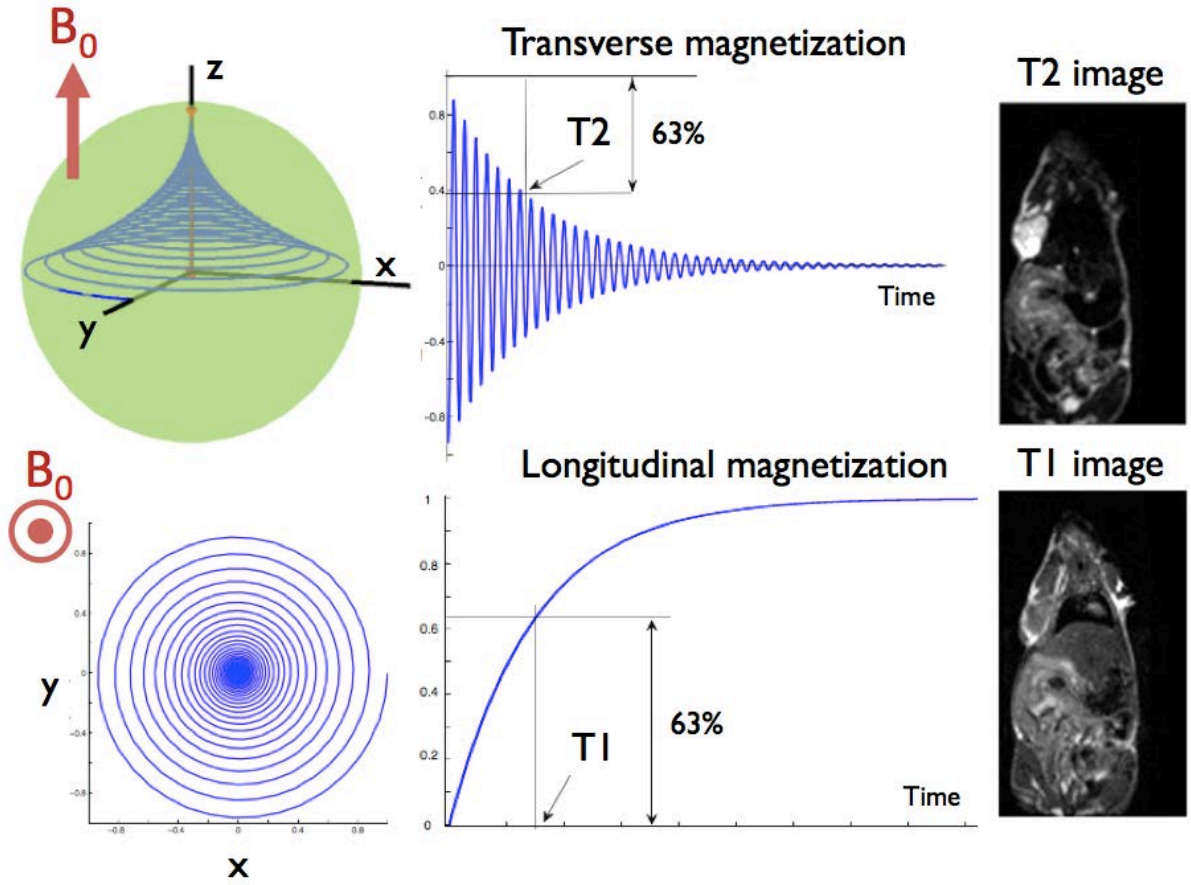

Figure 9: **T2 and T1 images in MRI**. The relaxation time of transverse (T2) and longitudinal (T1) components of the magnetic moment to reach their equilibrium positions, aligned to B_0, are measured to produce T1 and T2 images. The images on the right display a coronal plane of a mouse (from Wang et al. 2015).

MRI provides precise images of anatomic structures without using any ionizing radiation. Contrast agent can be used in the context of tumor characterization to monitor tumor microvascularization or the level of molecular expression of specific receptors. The spatial resolution of MRI is directly related to the intensity of the magnetic field and the acquisition time.

III.2.1. Dynamic contrast enhanced MRI (DCE-MRI)

III.2.1.1 Natural contrast agents

As already underlined, hypoxic regions in tumors can trigger angiogenic processes and subsequent tumor development. Quantifying the level of hypoxia can help in the prediction of tumor development and treatment outcome (Bussink et al. 2003; Vaupel and Mayer 2007). When blood is oxygenated (oxyhemoglobin), it presents a weak magnetic susceptibility and conversely a strong magnetic susceptibility when it is deoxygenated (deoxyhemoglobin). Specific sequences can be used in MRI for blood-oxygen-level dependent (BOLD) contrast imaging to reflect the ratio of non-paramagnetic oxygenated hemoglobin to paramagnetic deoxygenated hemoglobin. This imaging modality has historically been used in the study of neural activity but it may also provide information about the level of oxygenation in tumors (Baudelet and Gallez 2002; Hallac et al. 2014; Padhani et al. 2007; Peller et al. 1998; Zhao et al. 2009). Despite its capacity to interpret blood oxygenation based on magnetic susceptibility, BOLD signal can also be influenced by other parameters such blood flow,

blood volume and vascular architecture. Furthermore, several studies have shown a correlation between tissue oxygen partial pressure (pO_2) and BOLD signal (Al-Hallaq et al. 1998; Elas et al. 2003). In a study performed by Zaho et al. (2009), the relaxation of hexafluorobenzene ($H^{19}FB$) was monitored after intratumoral injection (Zhao et al. 2004) to assess the level of oxygenation in a rodent mammary carcinoma (13762NF). They showed a strong correlation between BOLD signal and reference oximetry measurements made with ^{19}F NMR in the same tumor model. Experiments consisted in changing the percentage of oxygen breathed by the rats and quantifying the associated variation of oxygen in tumor tissues (Figure 9). Measurements were performed in 9 rats receiving no therapy revealing a large intra- and inter- tumor heterogeneity in terms of oxygenation for this tumor model. A similar study more recently demonstrated the correlation between BOLD signal and ^{19}F oxygen partial pressure (pO_2) measurements (Hallac et al. 2014).

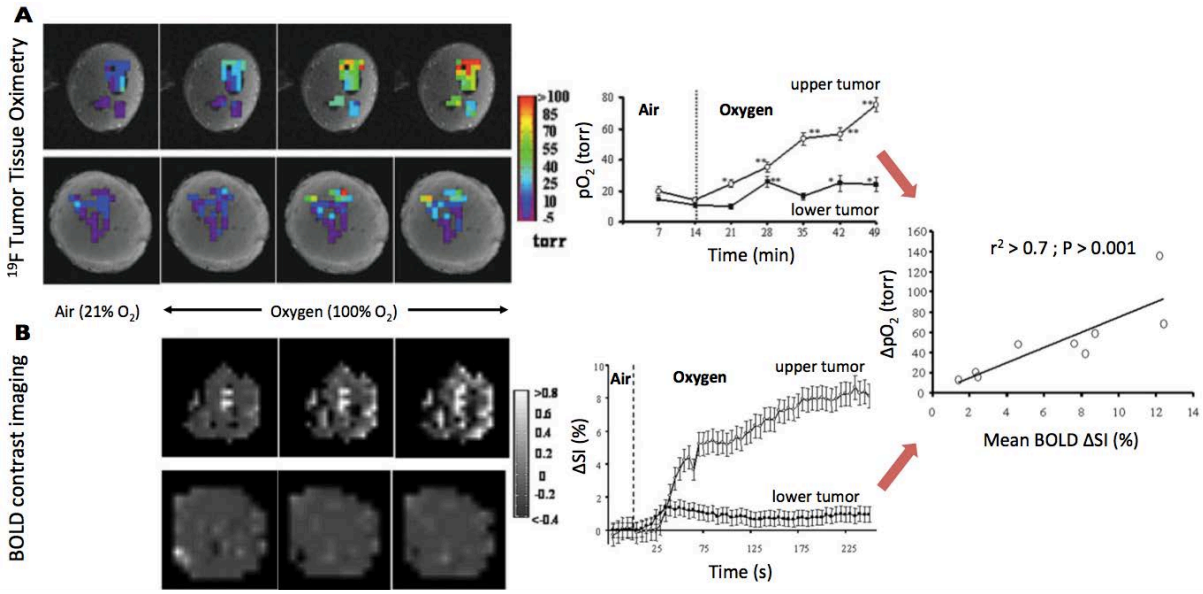

Figure 9: **Variation of pO_2 and BOLD contrast with oxygen challenge**. **A)** pO_2 maps obtained at successive times overlaid on T1-weighted images of two tumors. In response to breathing oxygen, all the individual locations (34 voxels) in the upper tumor (upper row) responded significantly and became well oxygenated. By contrast, some of the initially hypoxic regions in the other tumor (lower row) remained hypoxic, while others became well oxygenated. These temporal variations are reported in the associated graph (mean pO_2 vs time). **B)** Data were acquired under the same conditions using BOLD contrast imaging. When air was replaced by oxygen, the two tumors showed heterogeneous signal enhancement. Regions of decreased signal intensity (SI) were also observed (dark regions). The variation of normalized SI with time for the tumors with respect to the oxygen challenge are presented on the associated graph. Measurements of these two imaging modalities correlate significantly and suggest that BOLD signal is suitable for assessing oxygen level in biologic tissues. *Figure adapted from (Zhao et al. 2009)*

A pilot study has been led in seven patients to predict breast cancer response to chemotherapy using BOLD contrast imaging (Jiang et al. 2013). The results exhibit a significantly enhanced BOLD signal in tumor tissues (high level of oxygenation) for patients who presented a complete response to therapy. These findings suggest that BOLD MRI may help to predict treatment response in human breast cancer.

To provide more specific information about physiologic modifications (acidity, IFP and immunity response) that occur within tumors and their associated microenvironment, contrast agents must be used to enhance specific targets and to quantitatively evaluate tumor modifications during growth or therapy.

III.2.2.1 Contrast MRI

DCE-MRI contrast agents have an effect on the ^{1}H relaxation time. The most common T1 contrast agent is $Gd3^{+}$ which consists of chelates of paramagnetic metal ions and exhibits a high magnetic moment due to its seven unpaired electrons. Normal sized (≈ 150 nm) or ultrasmall (≈ 30 nm) superparamagnetic iron oxide nanoparticles (SPIO/USPIO) composed of a core of iron oxide coated with either dextran, polymer or citrate (Kircher and Willmann 2012a) are commonly used to enhance T2 weighted images.

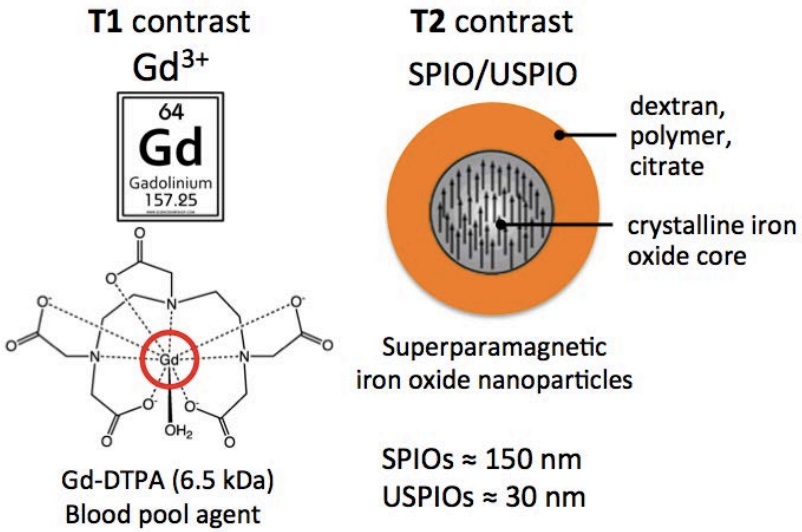

Figure 10: **Contrast agents in MRI**. The most common contrast agents used in MRI modify the relaxation time of water protons. Gd-DTPA is a blood pool agent used to trace the microvascular network and thus to provide information on its structure and functionality. SPIO and USPIO can be functionalized and thus targeted toward specific receptors or molecules of interest by conjugating ligands to their shell such as antibodies, peptides or small molecules.

By an ingenious use of the common Gd-DTPA MRI contrast agent, Hompland et al. (2012) demonstrated the feasibility of the assessment of the interstitial fluid pressure (IFP) in xenografts of human cervical carcinoma (TS-415) and human melanoma (U-25). After the injection of the blood pool agent, a high-signal intensity rim appears in the tumor periphery and moves outward with time. A simple model for peritumoral interstitial fluid flow was then used to calculate the fluid flow velocity (V_0 in mm/s) at the tumor surface based on the rim's movement. They showed that the speed of displacement of the high-intensity rim was highly correlated with IFP. The higher the IFP the faster the outward advancement of the high-intensity rim. Using this tool, they investigated the value of IFP in tumor models and the associated level of metastasis. Findings demonstrate significantly higher IFP in metastatic nodules as compared to primary tumor tissue. The results suggest that Gd-DTPA-based DCE-MRI can noninvasively visualize tumor IFP, and reveal the potential interest of the assessment of fluid flow velocity by this method to provide a novel, general biomarker of tumor aggressiveness.

Some elaborated MRI contrast agents can be used to monitor tumor pH. For example, Nwe et al. (2013) have developed a pH-responsive glycol chitosan Gd-labeled MR contrast agent (GC-**NH_2**-GdDOTA) that was designed to allow rapid imaging (within several hours) and to generate positive T1 contrast. GC-**NH_2**-GdDOTA exhibits near-neutral surface charges at physiologic pH because of

deprotonation of the amines (NH_2) on the glycol chitosan. The presence of a neutral surface charge minimizes nanoparticle association with blood components and normal tissue. In acidic microenvironments, the amino groups of GC-**NH_2**-GdDOTA yield a positive charge (NH_3^+), leading to electrostatic interactions with negatively charged cell membranes and extracellular matrix components. These interactions result in enhanced retention of the agent in acidic areas. Results exhibit a significant contrast enhancement in T1- weighted images in acidic zones for as long as 4 h following the injection of GC-**NH_2**-GdDOTA, with the greatest contrast observed at 2 h postinjection.

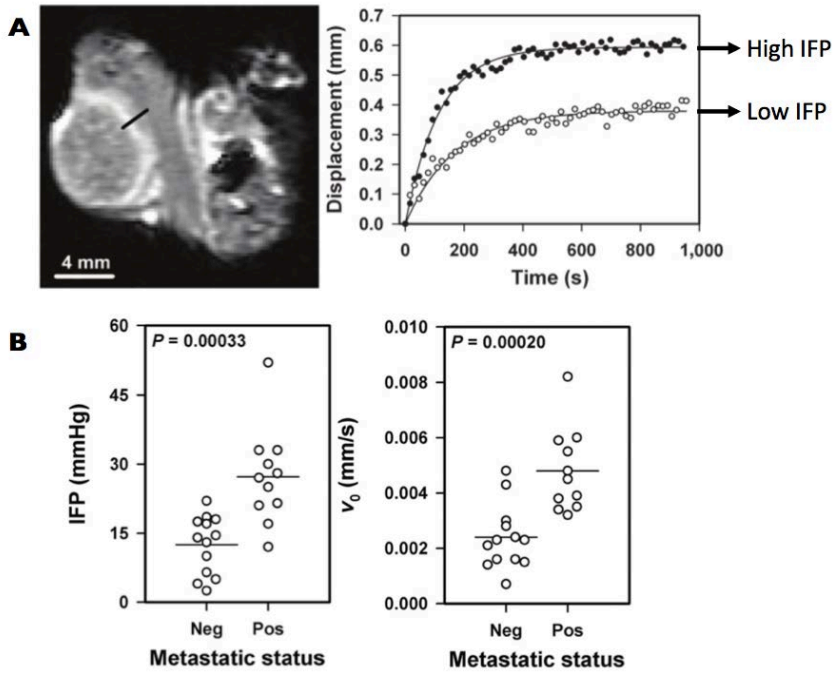

Figure 11: **IFP measurements using a Gd-DTPA blood pool agent**. **A)** The black line on the image indicates where the velocity (V_0) of the rim movement was measured. As shown on the graph, high IFP is associated with higher velocity of the rim movement than lower IFP. **B)** Both, IFP and V_0 enable the distinction between primary tumor and metastasis. *Figure adapted from (Hompland et al. 2012).*

Tumor vasculature can be characterized with MR imaging using contrast agents. Ullrich et al. (2011) used the SPIO Endorem® (Guerbet) contrast agent associated with 7T, high spatial resolution (voxel size: 0.25×0.25×0.3 mm^3) MRI to simultaneously quantify tumor microvessel density and vessel size. The small size (120 to 180 nm) and hydrophilic coating of Endorem provides longer circulation in the intravascular space and prevents rapid accumulation of particles in the reticuloendothelial[10] system. They performed a longitudinal follow-up of non–small cell lung cancer xenograft treated with vatalanib, a TKR inhibitor with a strong affinity for PDGFR and VEGFR. The strongest variations between the placebo and treated groups were identified based on the microvascular density index which displayed lowest values for the antiangiogenic group (Figure 12). Moreover, a strong reduction in the apparent diffusion coefficient (ADC), a measurement related to the confinement of the contrast agent, was observed for the antiangiogenic group. Because it was previously shown that inhibition of VEGFR2 expression reduces vascular permeability (Jain 2005), Wang et al interpreted the lower values in ADC maps in the treated group as a decline in vessel permeability that reduced interstitial edema and, thus, intra-tumor diffusion. Finally in this study,

[10] Reticuloendothelial system: mononuclear phagocyte system which is a part of the immune system consisting of phagocytic cells such as monocytes and macrophages.

Ullrich and colleagues demonstrated the sensitivity of DCE-MRI to modifications of the tumor vasculature under antiangiogenic therapy.

Specific MRI contrast agents can be used to follow immunotherapy response by targeting immune cells. For example, in the context of the infusion of genetically modified NK cells that recognize tumor-associated surface antigens, Meier et al. (2011) demonstrated the ability of MR imaging to assess SPIO-labeled NK-cell accumulation in a xenograft prostate cancer model (DU145) in rats. The *in vivo* accumulation of NK cells in tumor was confirmed *ex vivo* by anti-CD57 immunohistochemistry stains directed against the antigen CD57 on the surface of NK cells. Similar results were reported by Sheu et al. (2013) in a hepatocellular carcinoma model. They performed intra-arterial infusion of SPIO-labeled NK cells and observed a significant reduction of tumor volume 8 days after NK cell accumulation. The ability of SPIO to label lymphocytes was shown up to 72 h after their injection. This should enable monitoring of NK-cell trafficking in the tumor, and the associated microenvironment (Smirnov et al. 2006).

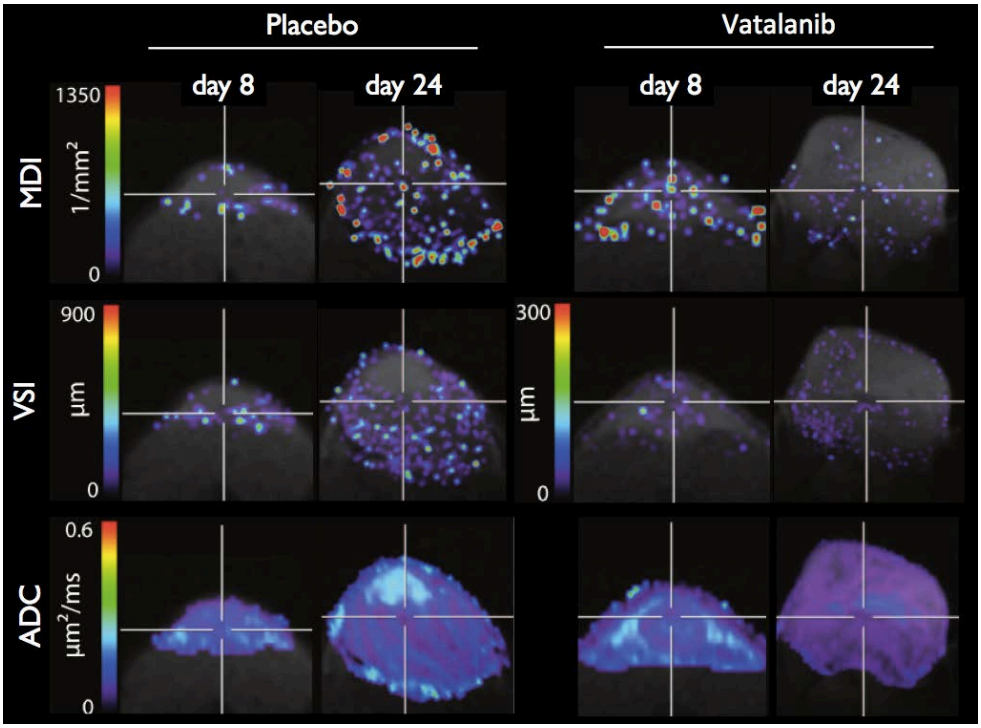

Figure 12: **Multiparameter-imaging in MRI**. Longitudinal investigations of vascular dynamics during tumor growth and antiangiogenic therapy. The effect of treatment with vatalanib on the tumor microvessel density index (MDI), tumor vessel size (VSI) and apparent diffusion coefficient (ADC) during tumor growth and treatment was investigated. *Figure adapted from (Ullrich et al. 2011)*.

III.2.2. Magnetic resonance spectroscopy (MRS)

Magnetic resonance also offers the possibility to image the metabolism of living cells using magnetic resonance spectroscopy (MRS). The MRS technique consists in imaging not only the ^{1}H atoms but also other atoms that have a non-null spin and are present in the body (Figure 13-A). The atoms that are most often studied with MRS are the proton ^{1}H, carbon ^{13}C, fluorine ^{19}F, sodium ^{23}Na and phosphorus ^{31}P. To image certain isotopes with a low natural abundance and low nuclear spin polarization like the ^{13}C isotope (1.1%), it is necessary to inject a hyperpolarized, enriched compound. As opposed to standard MRI contrast agents which act on the relaxation rate of water protons,

hyperpolarized molecules are themselves sources of NMR signal. They thus increase signal intensity and SNR in a manner that is linearly dependent on their concentration and polarization level.

By using ^{13}C MRS and assuming that pK_a[11] is known Gallaher et al. (2008) applied the chemical equation $pH = pK_a + \log_{10}([HCO_3^-]/[CO_2])$ to determine pH levels *in vivo*. To measure the relative concentrations of $H^{13}CO3^-$ and $^{13}CO_2$ Gallaher and colleagues increased the sensitivity of their detection by injecting hyperpolarized ^{13}C-labeled bicarbonate. Using this approach, they mapped the intratumoral pH (Figure 12-B). Ha et al. (2013) demonstrated the ability to quantify the intra-cellular pH in brain tumors by measuring the chemical shift of specific metabolites of ^{31}P MRS.

A

Isotope	bio availability (%)	natural abundance (%)	Spin	Frequency at 7T (MHz)
^{1}H	**10**	**99.984**	**1/2**	**300.1**
^{2}H		0.016	1	46.1
^{12}C	23	98.9	0	0
^{13}C		**1.1**	**1/2**	**75.5**
^{14}N	2.6	99.64	1	21.7
^{15}N		0.37	1/2	30.4
^{16}O	61	99.76	0	0
^{17}O		0.0317	5/2	40.7
^{19}F	traces	100	1/2	282.4
^{31}P	1.1	100	1/2	121.4

B

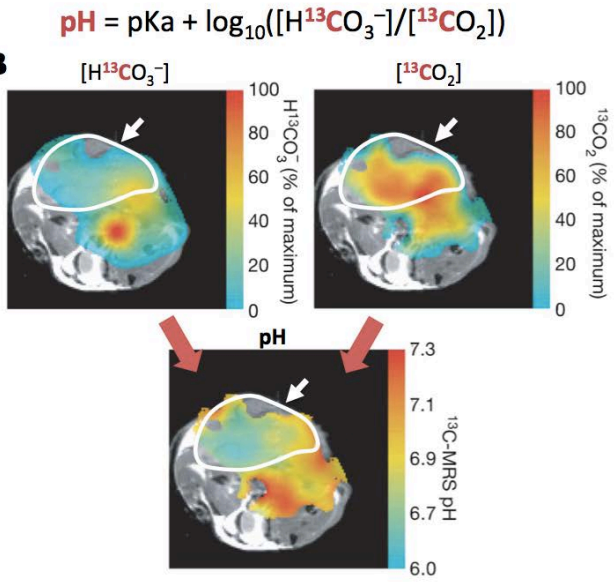

Figure 13: **pH assessment by MRS imaging**. **A)** Table indicates the atomic composition of the human body (Conseil National de Recherches Canada, CNRC: http://goo.gl/V6HCpx) in terms of the natural abundance of each isotope and the associated resonance frequency under a magnetic field of 7T (MIT department of chemistry, http://goo.gl/id109S). **B)** pH maps in a mouse calculated from the ratio of the $H^{13}CO_3^-$ and $^{13}CO_2$ voxel intensities in ^{13}C chemical shift images acquired ≈10 s after intravenous injection of ≈100mM hyperpolarized $H^{13}CO_3^-$ and assuming a pKa of 6.17. The tumor is designated by a white outline and white arrow. *Figure B was adapted from (Gallagher et al. 2008)*

Other studies have shown that hyperpolarized ^{13}C can be used with MRS to evaluate the glycolytic status of living cells. Thus, the presence of tumor cells can be highlighted by mapping levels of pyruvate, lactate, and alanine (Golman et al. 2006). Cell metabolism assessment using simultaneous ^{31}P and ^{1}H MRS under a magnetic field of 7T was demonstrated in human breast cancer (Klomp et al. 2011).

III.2.3. Multiparametric imaging in MRI

MR imaging provides a very versatile tool to quantitatively evaluate many parameters *in vivo*. One of the direct benefits for the study of tumors is the possibility to image several physiologic parameters for the same subject to, thus, obtain a more complete description of its status.

[11] In the case of weak acid solutions, the equilibrium constant of acid dissociation of the following chemical equation, $AH + H_2O \rightleftharpoons A^- + H_3O^+$ is designated Ka and is equal to $[A^-][H^+]/[AH]$. pKa is defined from Ka by the relation pKa = -log Ka.

Matsumoto et al. (2011) used DCE-MRI to assess blood volume and electron paramagnetic resonance (EPR) imaging to map tissue pO_2 (imaging modality sensitive to the spin of unpaired electrons) in a murine squamous cell carcinoma model treated with an anti-angiogenic therapy (sunitinib). As shown in Figure 14, the group of mice treated with sunitinib presented a significant increase of the level of O_2 simultaneous to a reduction of blood volume compared to the placebo group. They interpreted these findings as a normalization of tumor vasculature leading to improvement of the functionality and efficiency of blood vessels (Tong et al. 2004). The immunostaining findings for hypoxia (pimonidazole) and oxygen gradient (CD31-pimonidazole) corroborated results presented in Figure 14. Together, the results of this study demonstrate the capacity to noninvasively assess transient vascular normalization and the resultant improvement of tumor oxygenation after antiangiogenic treatment. Moreover, Matsumoto and colleagues showed that transient renormalization of tumor microvascular network and the associated increase of O_2 can significantly enhance the efficiency of radiotherapy.

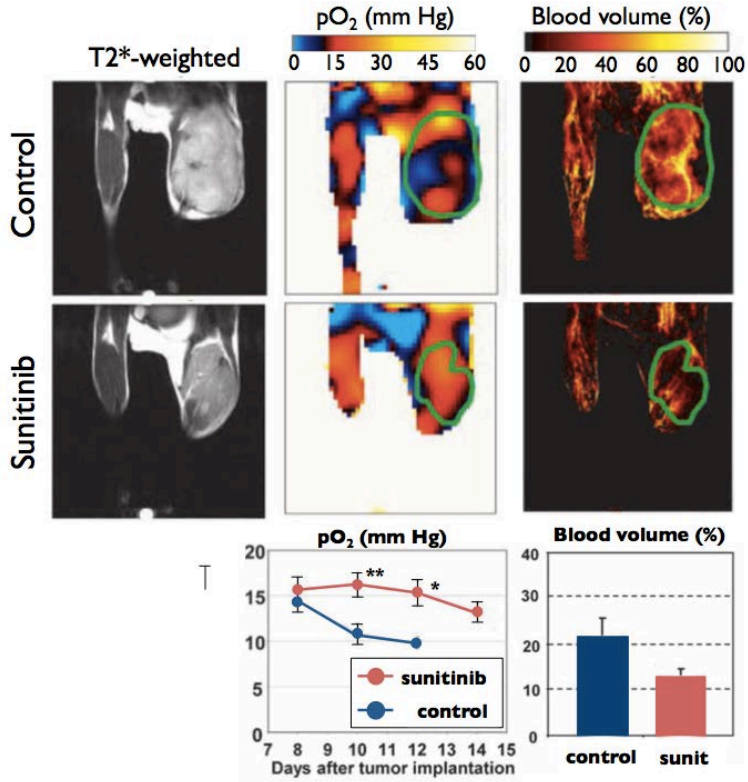

Figure 14: **MRI comparison between the level of oxygen pO_2 and blood volume**. Response of a murine squamous cell carcinoma to antiangiogenic therapy was investigated using DCE-MRI and EPR imaging. Sunitinib (an antiangiogenic drug) simultaneously induced an increase of pO2 and a decrease of blood volume. *Figure adapted from (Matsumoto et al. 2011).*

Jugé et al. (2012) conducted a study characterizing the response of ectopic and orthotopic murine colorectal carcinoma (CT26) to an antivascular drug (combretastatin A4 phosphate, CA4P) by characterizing the tumors' mechanical properties with MR elastography and their vasculature with diffusion-weighted MR imaging (measurement of ADC). In the ectopic tumor model, the stiffness decreased and the ADC increased simultaneously and significantly. Histologic results indicated high levels of necrosis (43 ± 3 % vs7 ± 2 %) and low microvessel density (MVD) in the treated group as compared to the placebo group. Jugé and colleagues interpreted the reduction in stiffness in the group treated with the antivascular therapy as an indication of decreased MVD.

In summary, MRI represents a very powerful and versatile tool that can provide many types of information about the anatomy, physiology or molecular expression of tissues with a strong level of precision. The use of MRI is widespread in the clinical setting so conclusive results in preclinical research can be tested rapidly for clinical translation. This potential is moderated by the high cost of MRI and the duration of exams that can easily exceed one hour per subject.

III.3. Optical imaging

Optical imaging, mainly used in preclinical research, represents another very interesting modality that provides a range of techniques enabling *in vivo* characterization of different aspects of the TME as reviewed in the following paragraphs.

The use of visible light to study biologic tissues began four centuries ago with the invention of the microscope. Light is an electromagnetic wave (photons) that can be characterized by its frequency, amplitude, phase and polarization. Photons can diffuse through biological tissues but are absorbed over a very short distance (≈ 100 µm). It was shown that near infrared (NIR) photons (700–900 nm) penetrate deeper (≈ 1mm) into biological tissues (Chance et al. 1998) and, thus, this range of wavelengths are most adapted to the *in vivo* study of biologic processes. In some cases, components of tissues can be revealed using natural optical contrast but an injection of fluorescent molecules is generally needed in order to highlight specific anatomical structures or physiological processes. There is a plethora of fluorescent molecules, each with a specific wavelength of absorption and emission, such that multi-targeted imaging can be achieved by using more than one fluorescent marker. A brief description of fluorescent probes will be presented in Section III.3.2.
The optical device most adapted to image a fluorochrome is determined based on the resolution, depth of observation and duration of physiologic processes necessary for the observation (Figure 16). Most commonly, to record fluorescence from deeper tissues, a plane wave light source is used to illuminate the tissue. Fluorescent signals emitted toward a camera are then collected. These methods are generally referred to as planar methods and can be applied in epi-illumination (reflectance) or transillumination modes. Fluorescence molecular tomography (FMT) provides a 3D reconstruction of the internal distribution of fluorochromes in tissues based on light measurements collected at the tissue boundary. This technique, coupled with advanced instrumentation, can overcome many of the limitations of planar imaging and yields a robust and quantitative modality for fluorescent reporters *in vivo*. Finally, intravital microscopy enables the use of optical imaging modalities that have been previously developed for *ex vivo* characterization. Very high spatial resolution on the order of that obtained with confocal microscopy can be obtained. Innovative methods such as optical coherence tomography (OCT) or optical frequency domain imaging (OFDI) can be applied intravitaly.

III.3.1. Natural contrast

The optical frequency domain imaging **(**OFDI) technique developed by Vakoc et al. (2009; 2012) is based on OCT imaging. It measures how light propagates in tissue and how it scatters from tissue structures. As described in Figure 17-A, at a given depth, the amplitude and phase of the reflected signal as a function of time are used to derive the optical scattering properties and, thereby, the tissue structure and function. Vakoc and colleagues used this new imaging tool coupled with an intravital window to quantify how the tumor vascular network was modified by an anti-VEGF drug (DC101) (Figure 17-B). A significant deference was identified in the mean vessel diameters

which was lower (≈ 35 µm) for mice treated with anti-VEGF drug (n = 6) as compared to control mice (≈ 55 µm, n = 5). Using the correlation between scattering properties and the microvasculature, they mapped viable tissue by quantifying the expansion of regions identified as necrotic or apoptotic based on light scattering. During tumor progression, they revealed an increase in these areas within the tumor associated with a decrease in the number of vessels and a decrease of the portion of viable tissues. Another interesting capacity provided by OFDI is the ability to characterize the lymphatic network surrounding the tumor (Figure 17-B, blue).

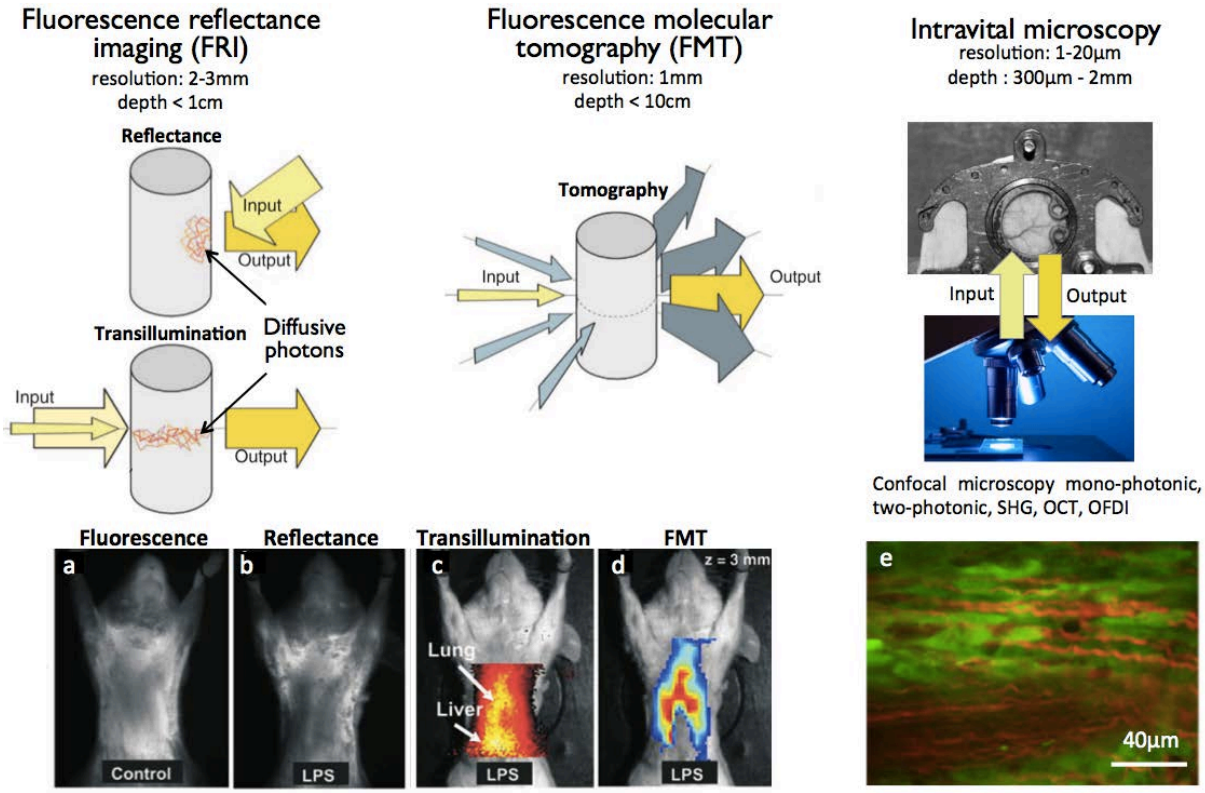

Figure 16: ***In vivo* fluorescence imaging**. (a–e) Imaging of proteolytic activity in pulmonary inflammation induced by intratracheal lipopolysaccharides (LPS). (a,b). Fluorescence transillumination images of control and LPS-challenged mice, respectively (d). Fluorescence Molecular Tomography slice at z = 3mm (e) (images from Ntziachristos et al. 2005). Intravital microscopy enables the visualization of single cells. Cancer cells expressing GFP fluoresce green and collagen fibrils, visualized by second harmonic generation imaging (SHG), are red (f). SHG of collagen and GFP were excited simultaneously at a wavelength of 790 nm (f: Uchugonova et al. 2013).

York et al. (2014) have developed a sensor that is bioinspired to mimic the structure of shrimp mantis eyes. The purpose of all eyes is to convert light for neural signaling interpreted by the brain. Depending on eye structure and composition, the photosensitive cells within eyes can be sensitive to the wavelength (color) and/or polarization of light. As described in Figure 18, the particularity of mantis eyes resides in their ability to filter photons through a pigment cell (color sensitivity) and a series of photosensitive retinular cells (R-cells for sensitivity to polarization status). York and colleagues have developed a sensor that mimics these structures of mantis eyes and they have used the sensor in multiple applications including tumor characterization. This sensor has the capability to simultaneously quantify several properties of polarized light such as the degree of linear or circular polarization (DoLP and DoCP) and the angle of polarization (AoP) which gives the orientation of the polarization wavefront. Using their Complementary Metal Oxide Semiconductor (CMOS) sensor coupled with endoscopy, they assessed the presence of tumor cells based on the

higher density of light-scattering agents in the cells. Higher scattering leads to a greater level of depolarization as compared with neighboring, healthy tissue (Charanya et al. 2014; York et al. 2014).

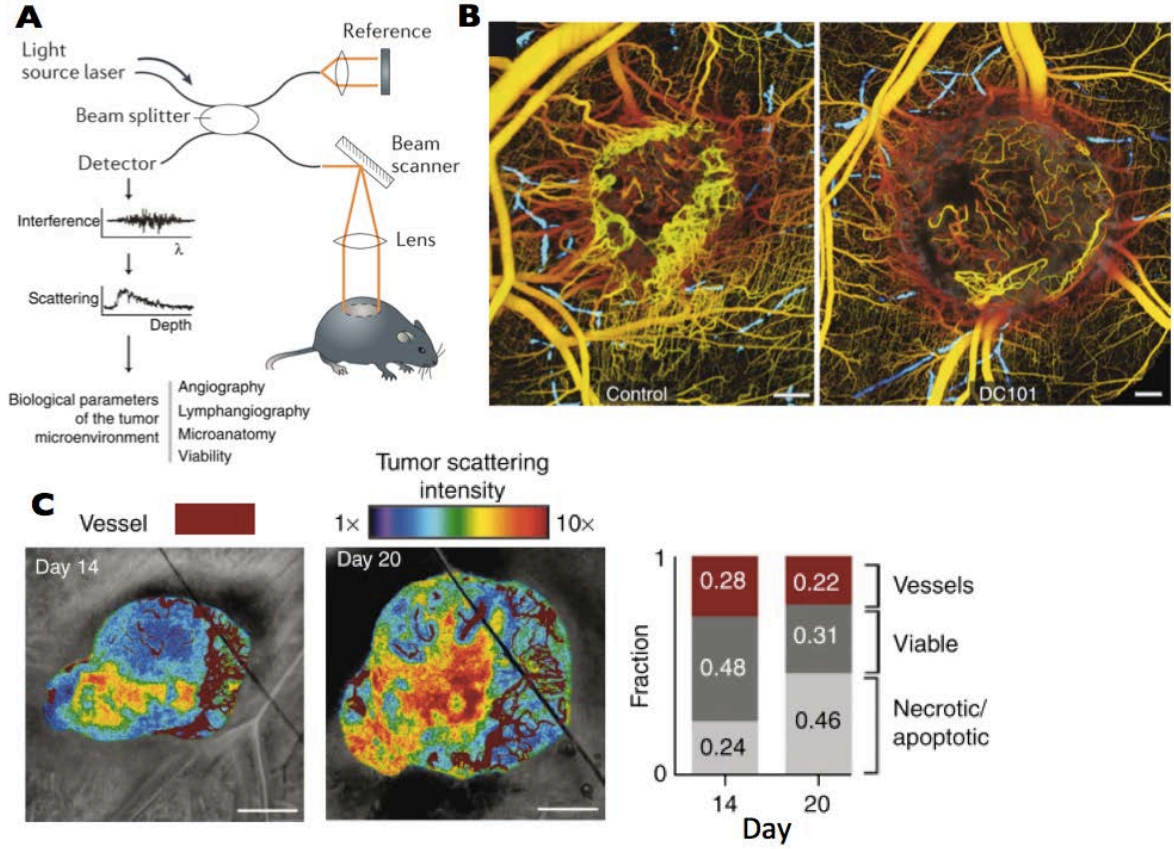

Figure 17: The **optical frequency domain imaging (OFDI) technique and its use in TME characterization**. **A)** The OFDI modality relies on the interference of near infrared light between a reference path and the tissues of interest. By measuring how light propagates and scatters in tissue, the OFDI technique enables *in vivo* characterization of tissue structures. **B)** OFDI images of representative control and treated tumors, 5 days after initiation of antiangiogenic (VEGFR-2) therapy. The lymphatic network is also presented (blue) for both tumors. Scale bar 500 µm. **C)** OFDI reveals the association of tissue necrosis with high scattering regions. Scattering properties were correlated with the microvasculature during tumor progression, illustrating the expansion of necrotic or apoptotic regions in areas with minimal vascular supply. Scale bar 1 mm. *Figure adapted from (Vakoc et al. 2009; Vakoc et al. 2012).*

III.3.2. Fluorescence imaging

Whatever imaging technique is used, most *in vivo* optical imaging requires the use of fluorescent molecules to highlight the presence of specific cells, to monitor their circulation and to evaluate the associated physiological processes.

As described in Figure 19, fluorescent probes can be divided into three different categories: active, activatable and indirect probes (Ntziachristos 2006). Active probes are essentially fluorochromes that are attached to an affinity ligand specific for a certain target. This paradigm is similar to probe design practices seen in nuclear imaging, except that a fluorochrome is used instead of the isotope. Activatable probes are molecules that carry quenched fluorochromes. The fluorochromes are usually arranged in close proximity to each other so that they self-quench, or they are placed next to a quencher using enzyme-specific peptide sequences. These peptide sequences can be cleaved in the presence of a specific enzyme, thus freeing the fluorochromes that can then emit light upon excitation. Finally, for the indirect probes, several strategies exist but the most

common relies on the introduction of a transgene (called a reporter gene) into the cell. The transgene encodes for a fluorescent protein (FP), which acts as an intrinsically produced reporter probe. The modified protein maintains the functionality of the original protein, but because it is fluorescent, it can be visualized *in vivo*. Several different fluorescent protein approaches have been developed to allow interrogation of protein-protein interactions through the utilization of fluorescence energy transfer (FRET).

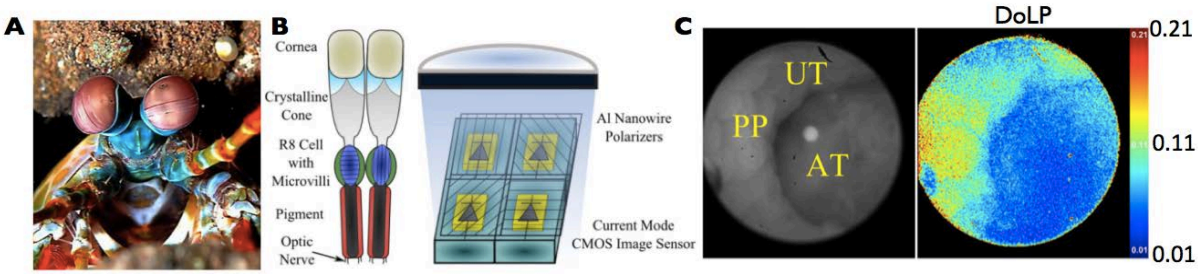

Figure 18: **Bioinspired sensor enables tumor cell detection**. **A)** The mantis shrimp in its natural environment. **B)** (Left) the compound eye of the mantis shrimp. Ommatidia[12] combine polarization-filtering microvilli[13] with light-sensitive receptors. (Right) A bioinspired Complementary Metal Oxide Semiconductor (CMOS) imager constructed with polarization sensitivity, where aluminum nanowires placed directly on top of photodiodes act as linear polarization filters. **C)** Image from *in vivo* endoscopy of the mouse colon. AT: adenomatous tumor; PP: Peyer's patch (drives immune response in the intestine); UT: uninvolved tissue. The degree of linear polarization (DoLP) measures how linearly polarized the light is, with 0 being no linear polarization and 1 being completely linearly polarized. *Figure adapted from (York et al. 2014).*

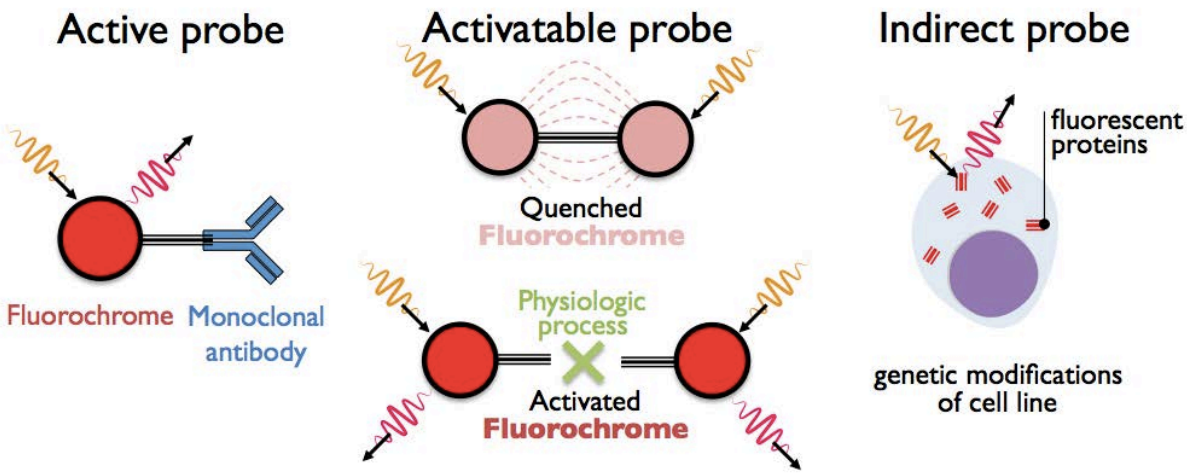

Figure 19: **Fluorescent imaging strategies.** Active probes consist of a fluorochrome attached to an antibody that targets a specific receptor. Activatable probes are composed of quenched fluorochromes that are able to emit photons after physiological degradation of their binding molecule. Indirect probes include those that induce fluorescent proteins by genetic modifications of cell lines or within the genome of the mouse.

[12] The compound eyes of arthropods like insects, crustaceans and millipedes are composed of units called Omnatidia.

[13] Microvilli are microscopic cellular membrane protrusions that increase the surface area of cells and minimize any increase in volume, and are involved in a wide variety of functions including absorption, secretion, cellular adhesion and mechanotransduction.

III.3.2.1 Active probes

The association of active probes with epi-fluorescence enables the assessment of the molecular expression of specific receptors within tumor. For example, the ability to target the EGF receptor, overexpressed in tumor cells, was shown in a breast adenocarcinoma xenograft (MDA-MB-468/435) using a cyanine 5.5 dye (excitation = 675 nm, emission = 694 nm) fluorochrome bound to EGF protein (Ke et al. 2003). Using the same imaging modality and the same fluorochrome, Chen and colleagues (2004) demonstrated the ability to image *in vivo* the cell adhesion molecule $\alpha_v\beta_3$ integrin in a subcutaneous brain tumor xenograft (U87MG).

Using FMT imaging coupled with two blood pool fluorescent agents (Angiosense 680 and 750), Montet et al. (2007) quantified the vascular volume fraction (VVF) in murine colorectal carcinoma (CT26) in order to assess the efficiency of bevacizumab therapy (anti-VEGF). They showed a significant reduction of VVF in tumors treated with anti-VEGF therapy compared to those in the control group indicating the expected effect of the anti-angiogenic drug on tumor vasculature.

Active probes not only allow the detection of the molecular expression of GFRs or the characterization of tumor vasculature but they can provide information about the level of apoptosis in tumors. By using annexin V–Cy5.5 probe coupled with FMT modality, Ntziachristos et al. (2004) characterized the apoptotic response of two different Lewis lung carcinomas (LLC), a drug-sensitive one and one that was resistant to cyclophosphamide (cytotoxic drug). As described in Figure 20, for both FMT and immunofluorescence, LLC sensitive to the cytotoxic drug exhibited a higher level of apoptosis compared to the resistant one. Ntziachristos and colleagues have demonstrated the ability of the annexin V – Cy5.5 probe to monitor the level of apoptosis *in vivo*.

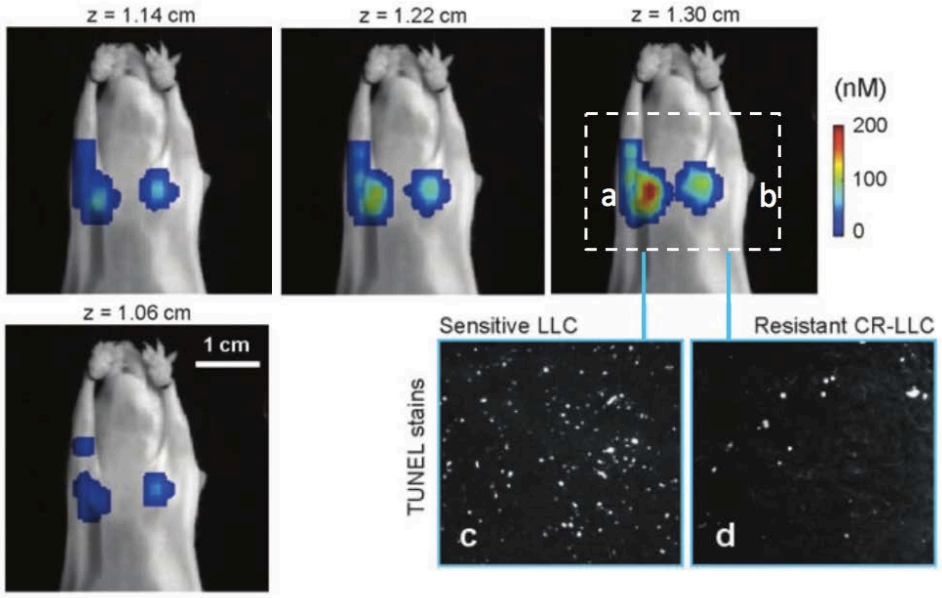

Figure 20: **In vivo imaging of apoptotic response**. Mice implanted with a Lewis lung carcinoma (LLC) tumor sensitive to chemotherapy (a) and a LLC tumor resistant to chemotherapy (b) were imaged for detection of annexin V-Cy5.5 marking apoptosis after two administrations of cyclophosphamide, 24 h apart. followed by the injection of annexin V–Cy5.5 probe. (b) Four consecutive FMT slices (in color) were superimposed on the planar image of the mouse. (c, d) TUNEL stained histological slices from the sensitive and resistant tumors, respectively. *Figure adapted from (Ntziachristos et al. 2004).*

The visualization of drug-induced cell death can be achieved *in vivo* with single-cell resolution using the Angiosense 680/750 and Annexin-Vivo 750 fluorescent probes coupled with multi-photon confocal microscopy (Earley et al. 2012). These strategies using high resolution microscopy also

enable the *in vivo* assessment of immunotherapy mechanisms by imaging the dynamic interplay of T cells, cancer cells, cancer antigen loss variants, and stromal cells (Schietinger et al. 2013).

III.3.2.2 Activatable probes

Activatable probes can monitor specific physiopathologies in tumors such as its acidic environment and enzymatic degradation of the ECM component. For example, Lee et al. (2011) designed a pH-sensitive fluorescent NIR probe targeting $\alpha_v\beta_3$ integrin. This fluorescent probe is silent in the NIR window at pH > 5 but becomes highly fluorescent in an acidic environment (pH < 5). Lee and colleagues demonstrated the efficacy of the probe design in a 4T1 mammary tumor model. Concerning proteases monitoring, Bremer et al. (2001) developed similar strategies to assess the concentration of MMP-2 proteases in the TME of a human fibrosarcoma tumor model (HT1080). The fluorochrome becomes active when the peptide substrate is degraded by the MMP-2 protease and thus becomes detectable by conventional fluorescence imaging (Figure 21-B). They treated tumors with prinomastat (AG3340), a potent MMP inhibitor, to reveal that the effect of this drug can be successfully imaged within hours after initiation of treatment using this specific, activatable fluorochrome.

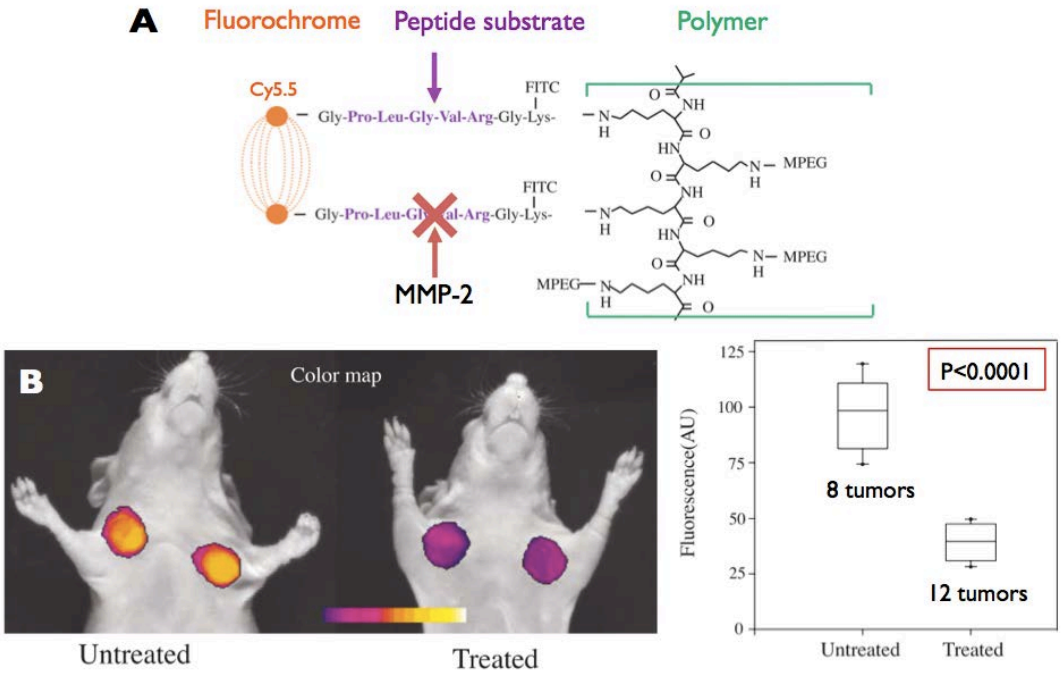

Figure 21: **In vivo imaging of MMP-2 protease. A)** The MMP-2-sensitive imaging probe consists of 3 structural elements: The quenched NIR fluorochrome, a MMP-2 peptide substrate and a copolymer graft. **B)** *In vivo* NIR imaging of HT1080 tumor-bearing animals. Color-coded tumor maps of MMP-2 activity superimposed onto white-light images (untreated (left), treated with 150 mg/kg prinomastat, twice a day, i.p. for 2 days (right)). Quantitative image analysis was performed over 20 tumors. Tumor NIR signals are summarized in the box plot (bars indicate 10th and 90th percentile). *Adapted from (Bremer et al. 2001)*.

III.3.2.3 Indirect probes

Tumor cells can be genetically modified to express FP. Kedrin and colleagues (2008) used photoactivatable fluorescent proteins (PAFPs) that were first reported by Gurskaya et al. (2006) that can be switched from green to red fluorescence with high stability. By using this photoswitchable

fluorescent protein, they tracked selected tumor cell subpopulations in different breast tumor microenvironments and revealed that, within the same orthotopic mammary tumor model, the invasion and intravasation of tumor cells can be very different depending on the TME (Figure 22). Similar studies investigated metastatic tumor cell extravasation using tumor cells labeled with quantum dot nanocrystals that enabled their *in vivo* tracking with fluorescent microscopy (Voura et al. 2004).

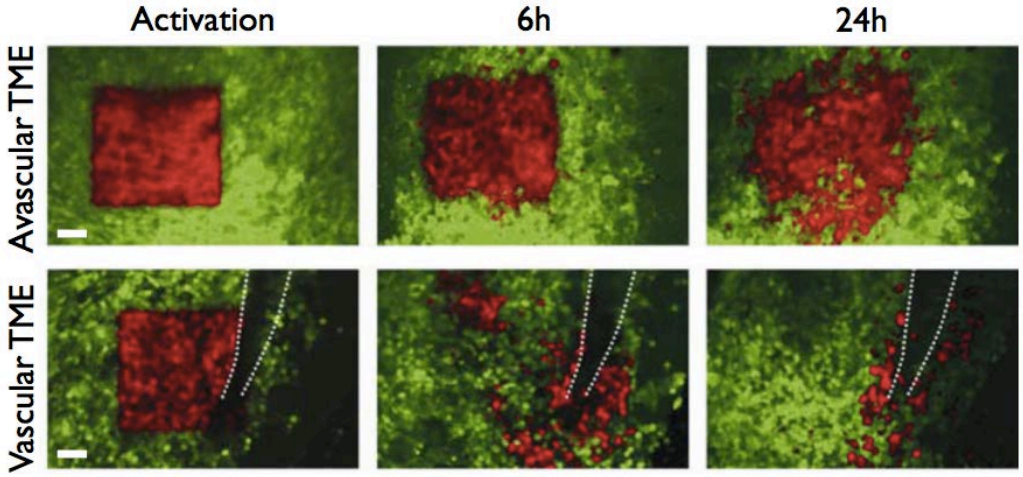

Figure 22: **Photoswitching through the mammary imaging window (MIW), a tool for studying orthotopic tumor microenvironments**. Non-photoswitched cells (green) and photoswitched cells (red) are shown at 0, 6 and 24 h after the photoswitch in avascular and vascular microenvironments (visible vessel indicated by white dotted lines). Scale bar 60 µm. *Figure adapted from (Kedrin et al. 2008)*

Ke et al. (2013) investigated the role of mesenchymal stromal cells (MSCs), multipotent[14] adult stem cells, in tumor progression. They examined the effects of MSCs on the tumorigenic capacity of 4T1 murine mammary cancer cells. They monitored the interaction between GFP-expressing[15] MSCs and RFP-expressing[16] 4T1 cells *in vivo* and revealed that, after being recruited in the TME, MSCs create a vascularized environment which enhances the ability of 4T1 cells to colonize and proliferate (GFP and RFP are respectively green and red fluorescent proteins).

Intravital microscopy coupled with fluorescent probes can provide very precise information, at single-cell resolution, about changes in the behavior or activity of tumor cells after administration of therapy. In a pancreatic ductal adenocarcinoma (PDAC) model, Nobis et al. (2013) investigated the *in vivo* activity of the Src nonreceptor tyrosine kinase[17] which has been shown to contribute to various types of invasive tumor cell behavior (evasion of apoptosis, enhanced proliferation, deregulation of cell–cell and cell–matrix adhesions). They transfected PDAC cells with the ECFP-YPet/**Src**-FRET biosensor (described in Figure 23-A). When the substrate was unphosphorylated the biosensor adopted a compact conformation in which the fluorochromes are in close proximity, resulting in high FRET efficiency. Upon Src-induced phosphorylation, the substrate peptide bound to the SH2 domain and separated YPet from ECFP, thereby decreasing FRET. They used fluorescence

[14] Multipotent cells have the ability to proliferate and differentiate in many cell types depending on their location and received cues.
[15] GFP = green fluorescent protein.
[16] RFP = red fluorescent protein.
[17] Non-receptor tyrosine kinases are cytoplasmic enzymes that are responsible for catalyzing the transfer of a phosphate group from a triphosphate donor, such as ATP, to a tyrosine residue in proteins.

lifetime imaging microscopy (FLIM) to measure the duration of the FRET interaction which enabled them to analyze and quantify Src activity at a single/subcellular level *in vivo*. They, thus, demonstrated the potential of this imaging modality to monitor drug response at single cell resolution in a model treated with a small-molecule Src kinase inhibitor, dasatinib. After the daily administration of dasatinib for 3 days, they imaged Src activity in tumors 1-2 h, 4-6 h and 24 h after the last administration of dasatinib. During drug treatment, Src was inactive (lifetime of FRET <2.35ns) but 1 h after receiving the last dose of dasatinib some tumor cells recovered their Src activity and after 24 h, most of the tumor cells recovered Src activity. The same imaging modality has been used to assess the *in vivo* activity of the RohA GTPase protein that is involved in cell motility (Timpson et al. 2011).

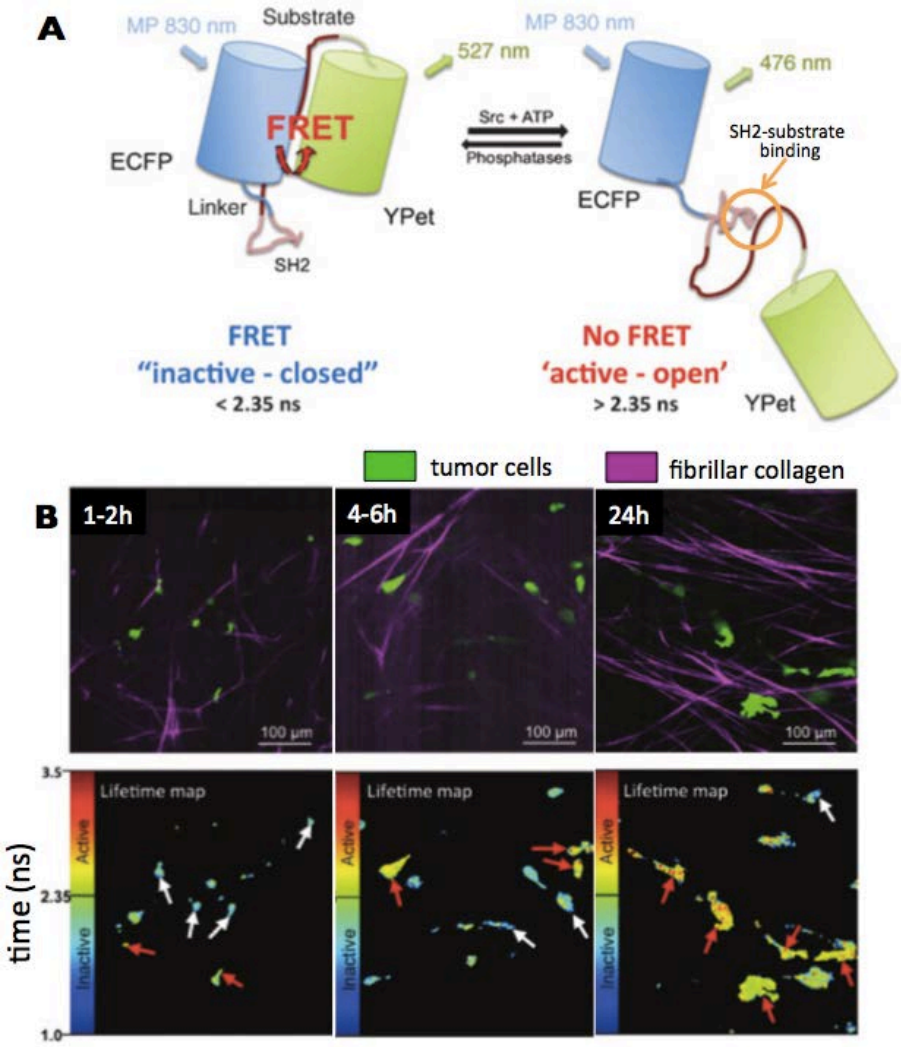

Figure 23: **FLIM-FRET imaging at single cell resolution**. **A)** When the substrate is unphosphorylated the biosensor adopts a compact conformation in which the fluorophores are in close proximity, resulting in high FRET efficiency. Upon Src-induced phosphorylation, the substrate peptide binds to the SH2 domain and separates YPet from ECFP, thereby decreasing FRET. **B)** Representative *in vivo* fluorescence images of PDACs expressing the Src-reporter (green) with SHG signal from host ECM components (purple) at 1 to 2 hours (left), 4 to 6 hours (middle), and 24 hours (right), post-oral administration of dasatinib. Corresponding *in vivo* lifetime maps (bottom) showing the capacity to monitor single cell fluctuations in the fraction of active/inactive cells over the time course of dasatinib treatment in live tumor tissue. In the lifetime color maps, low basal Src activity is represented as blue, whereas high Src activity is represented as warm red/yellow colors. Red arrows, active tumor subpopulation; white arrows, inactive cells. *Figure adapted from (Nobis et al. 2013).*

In summary, optical imaging represents a unique tool for the investigation of tumor development and drug response with single-cell resolution. Due to the low penetration of visible light and NIR photons in biologic tissues, optical imaging modalities are mainly used in preclinical research but some clinical applications are being developed such as volumetric microscopy of epithelial, mucosal and endothelial tissues in living human patients using endoscopy coupled with OFDI (Yun et al. 2006) or the characterization of breast tumor using NIR diffusive imaging (Leff et al. 2008).

III.4. Ultrasound

Ultrasound imaging provides significantly deeper penetration for tissue exploration than optical techniques enabling its use in both the preclinical and clinical environment. The ultrasonic techniques used to characterize different aspects of the TME such as the microvasculature, level of oxygenation, mechanical properties and tissue microstructure will be reviewed in the following sections.

Piezoelectric elements have the ability to create electric charges in response to applied mechanical stress. Reciprocally, application of an electric field to a piezoelectric solid will induce a variation of its volume. Such piezoelectric elements, which constitute ultrasonic probes, enable the generation and observation of mechanical waves propagating in biological tissues. Part of the mechanical waves propagating in a medium are reflected or scattered to produce echoes when they encounter structures with different acoustic impedances. Bmode images are formed from such echoes and provide anatomical information about biological tissue. The ultrasound wave frequency is directly related to image resolution and to the attenuation of the wave by the medium. The higher the frequency, the better the resolution but the more limited the imaged depth (higher attenuation). In soft tissues, attenuation is logarithmically dependent of frequency. For emitted frequencies of 10 MHz and 30 MHz, the attenuation in soft tissue will be on the order of 10 dB/cm and 30 dB/cm, respectively, which means that the intensity of the initial signal will be divided by 10 and 1000, respectively, after propagating across a distance of 1 cm.

In the context of tumor characterization, information provided by B-mode images can be used to detect tumors or to assess their volume. Many other ultrasound-based techniques have been developed that enable investigation of the tumor vasculature, its mechanical properties and also its microstructure.

III.4.1. Contrast-enhanced ultrasound (CEUS)

As for the other imaging modalities that were presented previously, use of contrast agents can highlight specific structures and/or functionalities of the TME. Ultrasound contrast agents (UCA) are injected intravenously to characterize the tumor microvasculature. There are many ultrasound contrast agents (UCAs). The most used in preclinical research and in clinical routine are microbubbles (MBs) (Figure 24-A). One class of MBs is composed of a phospholipid shell encapsulating a gas. Due to their size (µm) they do not extravasate and remain inside the vasculature. Their detection enables the characterization of the spatial distribution and the functionality of the vascularization. It is also

possible to functionalize MBs by grafting (chemical link) antibodies or other ligands onto the shell. Detection of such targeted-MBs can be used to assess the molecular expression of specific receptors expressed on the vascular endothelium (paragraph III-4.2.2). The acoustic detection of MBs relies upon the specific detection of their harmonic response. MBs present a harmonic response to an acoustic pressure field and biologic tissues have a linear response. It is thus possible to selectively detect and display only the signal of MBs and thus evaluate the tumor microvasculature (Figure 24-B). Other types of agents have been conceived for use with ultrasound. For example, nanobubbles (NBs) are under development that can preferentially accumulate in tumors due to the enhanced permeability and retention (EPR) effect of leaky tumor vessels. Once drug-laden NBs have extravasated from the tumor vasculature they accumulate in the interstitial space in contact with tumor cells and the release of drugs can be trigged by the application of high acoustic pressures or by a local acidic environment (Acharya and Sahoo 2011; Kobayashi et al. 2014; Zhou et al. 2014). Ultrasonic imaging of the accumulation of such nanobubbles has also been investigated (Theek et al. 2014; Yin et al. 2012). Such techniques combining therapy and imaging are referred to as theranostic (Kelkar and Reineke 2011).

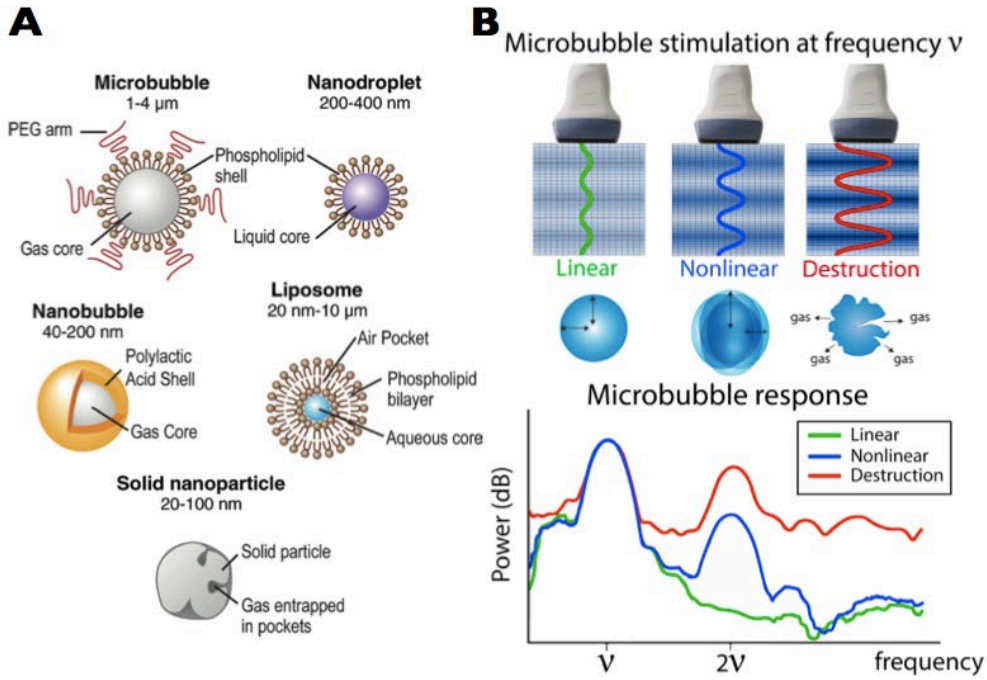

Figure 24: **Ultrasound contrast agents and harmonic imaging. A) Different types of ultrasound contrast agents. In current practice,** microbubbles are generally used, such as the one diagramed with a polyethylene glycol (PEG) polymer on their surface to prevent aggregation. Perfluorocarbon emulsion nanodroplets in liquid-liquid emulsions are being developed to provide vaporizable acoustic activation of echogenic gas bubbles. Liposomes, such as the one diagramed consisting of phospholipid bilayers, can enclose air pockets to render them detectable by US imaging. Nanobubbles have also been conceived that are gas-liquid emulsions that can fuse into echogenic microbubbles at the targeted site. Finally, solid nanoparticles can be made from solid amorphous substances with gas entrapped in their pores or fissures to increase their echogenicity (Kircher and Willmann 2012b). **B)** Depending on the amplitude of the cyclic acoustic pressure applied during imaging, microbubbles (MB) can present different acoustic responses: linear, nonlinear and destruction bursts. Nonlinear and burst responses can be detected at harmonic frequencies (2ν, for excitation at ν in the diagrammed example).

III.4.1.1 Tumor vasculature

As presented in Figure 25, the bolus injection of a blood pool UCA enables the assessment of the very slow blood flow that is characteristic of tumor microvascular perfusion. The arrival of MBs in the tissue of interest (tumor) induces an increase of the echo-power signal with a specific wash-in rate (WIR). After reaching a maximum of intensity (PE, peak-enhancement) at a specific time (TTP, time to peak) the MBs are eliminated with a specific washout rate (WOR) and the echo-power signal decreases progressively. These CEUS parameters can be extracted from a lognormal fit (Barrois et al. 2013; Rognin et al. 2010) performed on the time-dependent signal recorded in a region of interest (ROI). Two others important functional parameters extracted form the fit curve are the mean transit time (MTT) and the area under the curve (AUC). These perfusion parameters can be divided into two different categories, those related to the blood volume are PE and AUC, and those related to the dynamics of the perfusion are WIR, TTP, MTT and WOR.

CEUS imaging represents an interesting tool to investigate modifications occurring in the tumor vasculature following the administration of antiangiogenic therapy (Lamuraglia et al. 2010). In a study characterizing the effect of an anti-VEGF therapy (bevacizumab) in an orthotopic renal carcinoma model (SK-NEP-1), Guibal et al. (2010) demonstrated the ability of CEUS imaging to make the distinction between a continuous and discontinued antiangiogenic treatment. Williams et al. (2011) conducted a study in 17 patients with renal cell carcinoma and assessed the efficiency of antiangiogenic therapy using CEUS imaging. Findings exhibited a significant decrease of 73% of the fractional blood volume in treated patients.

Anti-angiogenic drugs do not only affect the fractional blood volume of the tumor but can also modify the dynamics of persisting blood flow. For example, a significant increase of the TTP parameter compared to placebo group was observed in the perfused area of tumors in ectopic LLC tumors treated with sunitinib (Dizeux et al. 2013). These results suggest that due to the changes that occur in tumor vasculature, UCA takes more time to penetrate vessels in the anti-angiogenic treated group as compared to the placebo group. A more complete study using CEUS to monitor the effect of antiangiogenic and cytotoxic therapy will be presented in Chapter V.

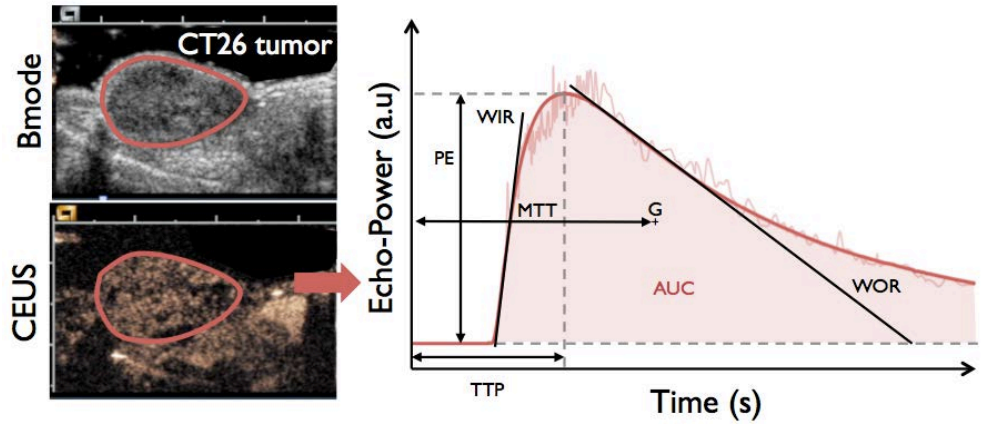

Figure 25: **CEUS imaging.** The contrast passage is quantified in a ROI by fitting echo-power data to a lognormal model. Functional parameters are extracted from the fit curve. Peak-enhancement (PE) corresponds to the maximum echo-power value of the curve; time to peak is the time to reach PE; wash-in and washout rate (WIR and WOR) are related to the maximum slope at the initial and late phase of contrast uptake, respectively; the mean transit time (MTT) is the mean value of the lognormal distribution of transit times in the imaging plane; and the AUC parameter is the area under the curve.

III.4.1.2 Molecular imaging

The assessment of the level of molecular expression of specific endothelial receptors requires intravenous injection of targeted MBs. Part of the targeted MBs will attach to specific receptors within the tumor and the other part will keep circulating freely. After a significant decrease of the concentration of free MBs, all the MBs present in the imaging plane are burst using a brief increase of acoustic pressure. A few seconds later, the tumor is perfused anew by freely circulating MBs. The relative amount of agent attached to targets is assessed by subtracting the mean echo-power value measured before the burst to the one after (Leong-Poi et al. 2005). This parameter, sometimes called differential targeted enhancement (dTE), reflects the specific marker's presence and density (Willmann et al. 2008) (Figure 26). Several studies have investigated the molecular expression of VEGFR-2 and $\alpha_v\beta_3$ integrins in different tumor models during tumor growth and under anti-VEGF therapies (Deshpande et al. 2011; Fischer et al. 2010; Payen et al. 2015; Pysz et al. 2010; Tardy et al. 2010; Willmann et al. 2008; Willmann et al. 2010).

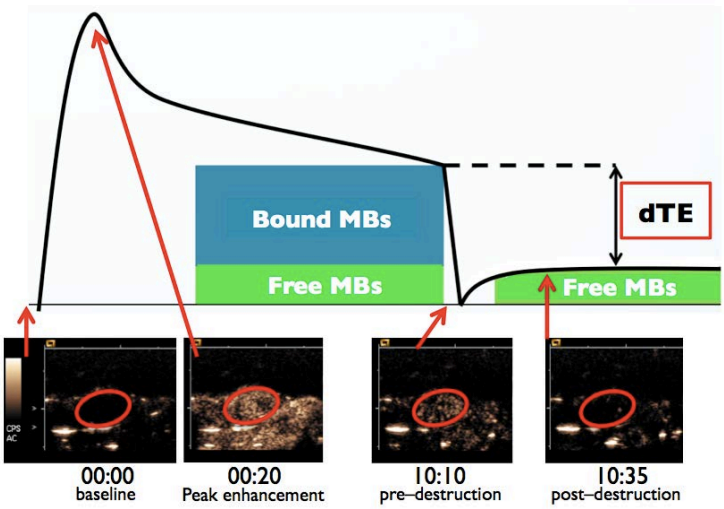

Figure 26: **CEUS targeted imaging.** After the significant decrease in the concentration of freely-circulating microbubbles (MBs), the echo-power is measured in the region of interest. Then all the MBs in the imaging plane are burst and after few seconds the echo-power of renewed, freely circulating microbubbles is assessed in the region of interest. The level of molecular expression (differential target enhanced: dTE) can be assessed by subtracting the echo-power signal from images of pre- and post- MB destruction.

III.4.2. Acoustic Angiography

Most nonlinear imaging techniques are most efficient near the resonant frequencies of UCAs. This resonant frequency is typically less than 10 MHz which is highly suitable for clinical ultrasound imaging applications. However, high frequency ultrasound systems used for high resolution, small animal imaging typically utilize frequencies in the 20 to 60 MHz range. This range is substantially above the resonant frequencies of most UCA microbubbles. To overcome this limitation in preclinical research and to improve the spatial resolution of vascular images, Gessner and colleagues (2013) developed a prototype transducer. The designed probe has two different elements: a low frequency element (4 MHz) to excite the UCA MBs near their resonant frequency and a high frequency element (30 MHz) that is able to receive the high frequency acoustic response (super-harmonic) from the excited MBs. Figure 27 presents a three-dimensional rendering of the tumor vasculature assessed

with acoustic angiography, the axial and lateral resolutions are approximately 150 and 200 µm, respectively. The current limitation of this technic remains its penetration depth which is on the order of several centimeters. Furthermore, it requires a specialized transducer with well-separated frequencies for transmission and reception.

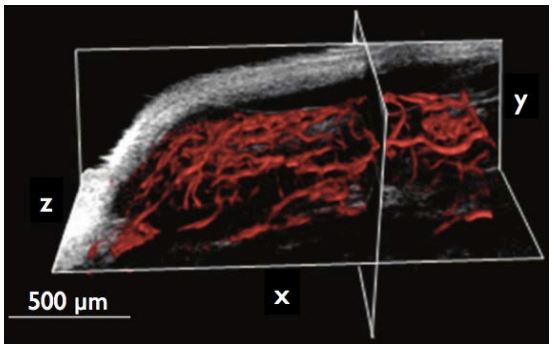

Figure 27: **Acoustic angiography**. An overlay of the microvasculature within a tumor provided by acoustic angiography (red) onto a tissue-only image provided by high frequency B-mode (grayscale) (Gessner et al. 2013).

III.4.3. Ultrafast Doppler Tomography (UFD-T)

Doppler imaging is a technique that enables the *in vivo* measurement of blood flow based on the measurement of shifts in the frequency of echoes from red blood cells due to their relative movement with respect to the ultrasonic probe. Conventional Doppler ultrasound using a 10 MHz central frequency does not have the sensitivity necessary to image slow tumor microvascular blood flow (limited to detection of approximately 2 cm/s flow in vessels with sizes on the order of 400 µm). To overcome this limitation, a technic referred to as ultrafast Doppler (or µDoppler) has been developed. It was initially applied to perform contrast-agent-free, functional ultrasonic imaging of the vascular flow in the rat brain (Macé et al. 2011; Osmanski et al. 2014). This technique provides increased sensitivity as compared to conventional Doppler by associating ultrafast imaging (1000 fps) with compounded plane wave emissions (Macé et al. 2013). As shown in Figure 28, this innovative imaging technique coupled with tomographic scanning has demonstrated its potential to assess three-dimensional tumor microvascular network (flow rates from 2 to 20 mm/s) without any use of UCA and with an isotropic spatial resolution of 100 µm (Demene et al. 2014).

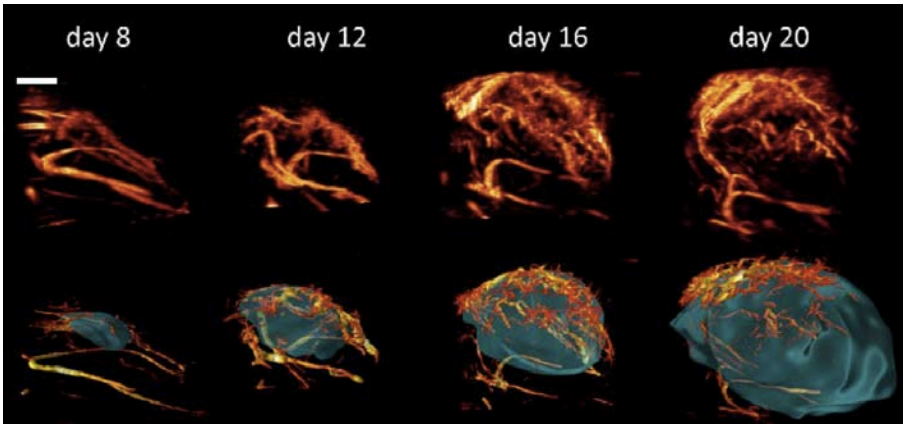

Figure 28: **Ultrafast Doppler tomography (UFD-T) used for monitoring tumor angiogenesis**. Top row: Maximum Intensity Projection (MIP) rendering of the 3D vascular volume acquired via UFD-T. Bottom row: volume rendering of the segmented tumor and of the skeletonization of the UFD-T volume. Scale bar 2 mm. *Figure from (Demene et al. 2014)*.

The current limitations of this technic reside in the duration of tomographic acquisition which is too slow for routine use but hardware improvements are anticipated to provide faster acquisition in the near future.

III.4.4. Photoacoustic imaging (PA)

PA imaging consists in exposing the tissue of interest to nanosecond laser pulses. Optical energy is absorbed by tissue chromophores[18] such as hemoglobin. This absorption of energy causes rapid heating followed by the emission of broadband acoustic waves, which are detected using ultrasound receivers. The absorption-based contrast of PA imaging makes it particularly well suited to visualizing vascular anatomy without the need for contrast agents due to the strong optical absorption of hemoglobin at visible and near infrared wavelengths. PA can provide images of vascular architecture with a spatial resolution along the z-axis ranging from tens to hundreds of microns (depending on depth) and a lateral resolution ranging from 70 to 100 µm.

It can also provide functional or physiological information. By acquiring images at multiple wavelengths, quantitative spectroscopic measurements of blood oxygen saturation and hemoglobin concentration can be assessed (Laufer et al. 2007). Figure 29-A presents part of the results reported by Laufer and colleagues (2012) using PA imaging to characterize the evolution of vascular architecture during the growth of a human colorectal tumor model (LS174T). Figure 29-B presents PA images acquired in the tumor before and after anti-angiogenic therapy in a breast cancer tumor model (MDA MB-231).

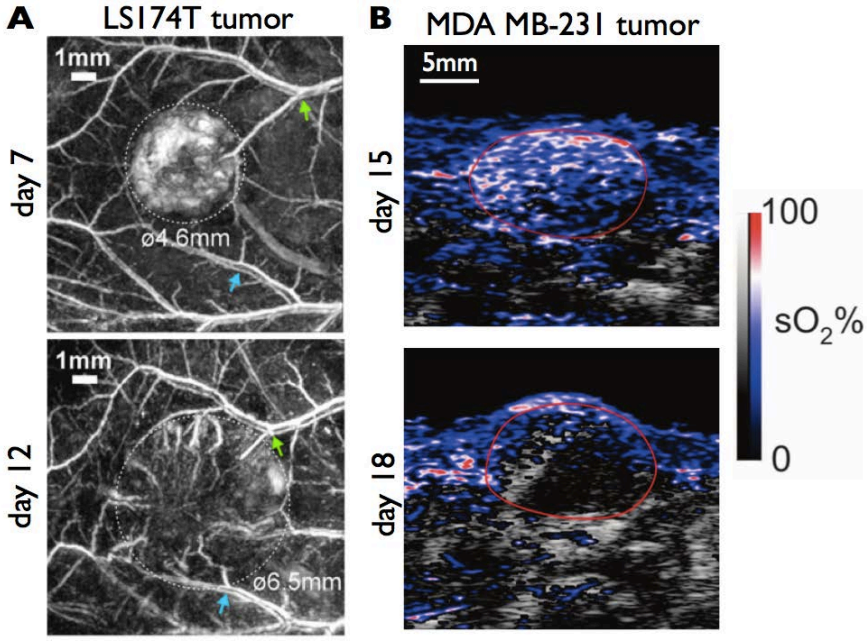

Figure 29: **Photoacoustic (PA) imaging of tumor vessels to characterize architecture and the level of sO_2. A)** Tomographic PA images showing the development of human colorectal tumor (LS174T) and the surrounding vasculature between days 7 and 12 post-inoculation. The dashed lines indicate the tumor margins. *Adapted from (Laufer et al. 2012)*. **B)** Images of a breast cancer tumor model (MDA MB-231) before and 3 days after of treatment with sunitinib (120 mg/kg daily by gavage). PA images show high abundance of well-oxygenated blood before treatment. After treatment, PA maps of sO_2 within the tumor show that blood oxygenation is reduced. *Adapted from (Needles et al. 2013)*

[18] A chromophore is the part of a molecule responsible for its color.

A significant reduction in the level of sO_2 was observed after administration of the drug (Needles et al. 2013). Similar studies have been performed in different tumor models to assess the evolution of tumor oxygenation during tumor growth and/or in response to therapy (Gerling et al. 2014; Yin et al. 2013).

Photoacoustic imaging also enables the visualization of physiology and pathology at the molecular level with deep tissue penetration and fine spatial resolution. A wide range of imaging probes such as, small-molecule dyes, metallic nanoparticles, carbon nanotubes, semiconducting polymer nanoparticles (SPNs) and porphysomes have been developed to monitor different molecular aspect of the TME (Akers et al. 2011; De La Zerda et al. 2008; Homan et al. 2012; Kim et al. 2009; Lovell et al. 2011). For example, Pu and colleagues (2014) have shown that carbon nanotubes coupled with a cyanine dye derivative (IR775S) sensitive to ROS-mediated oxidation can be used for real-time, *in vivo* evaluation of the level of the ROS present in the tumor. Moreover, based on a design comparable to the activatable probes described in the section 3.1 (Figure 19), Levi et al. (2013) demonstrated the ability of specific probe used in photoacoustic imaging to determined the presence and activity of two members of the matrix metalloproteinase family (MMP-2 and MMP-9) in tumor bearing mice.

III.4.5. Shear Wave Elastography (SWE)

Ultrasound imaging can also provide quantitative information about tissue mechanical properties. To assess stiffness of biologic tissues *in vivo*, the SWE technique applies acoustic radiation force at different depths in the tissue by focusing ultrasound waves. By thus oscillating tissues (Figure 30-A, 1), shear waves are generated that propagate cylindrically outward from the axis of longitudinal wave propagation. (Figure 30-A, 2). The shear wave propagation is monitored using ultrafast (longitudinal-wave) imaging (Tanter and Fink 2014) that is able to measure local shear wave velocity and thus assess tissue stiffness (Figure 30-B) based on the following equation :

$$E = \rho v^2$$

where E is the Young's modulus (Pa), ρ the density of medium (kg/m^3) and v is velocity of the shear wave (m/s).

In human breast cancer, SWE has demonstrated its ability to differentiate malignant and benign lesions based on their stiffness; malignant lesions are 3 to 4 times stiffer than benign ones (Al-boukai et al. 2011; Athanasiou et al. 2010; Sebag et al. 2010).The sensitivity of SWE to tumor composition has been investigated by Chamming's and colleagues (2013) in a breast cancer model. They showed that high stiffness was correlated with a high amount of fibrosis and, conversely, that soft tissue was correlated with a high amount of necrosis. These findings suggest that SWE represents an interesting imaging modality for the longitudinal monitoring of the mechanical properties of tumors during therapy.

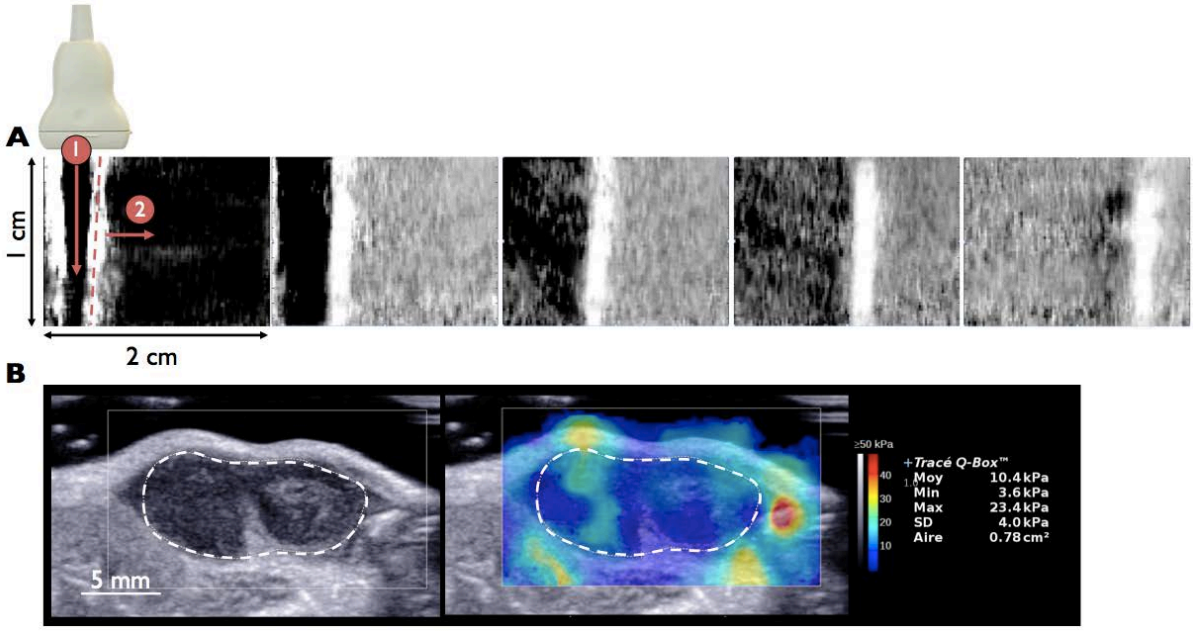

Figure 30: **Shear wave propagation. A)** A shear wave is generated by applying radiation force at different depths with focused ultrasound. The propagation of shear waves is monitored with longitudinal-wave imaging and shear-wave velocity is assessed at each point in the image to measure tissue stiffness. The red dashed line designates the shear wave front. **B)** The elastography color map of Lewis lung carcinoma (LLC) after 14 days of tumor growth, dashed line designates the tumor. Statistics of tumor stiffness (mean, max, min, SD and ROI area) are presented on the right of the imaging window.

III.4.6. Quantitative Ultrasound (QUS)

B-mode images display anatomical structure using only the information related to the envelope of the radio frequency (RF) signals backscattered from tissues. A technique known as quantitative ultrasound (QUS) uses the frequency-dependent information contained in the backscattered RF signals and provides information about tissue microstructure at spatial scales smaller than can be resolved by conventional B-mode imaging. By normalizing backscattered signals from tumor tissues with respect to echoes from a calibrated reference phantom (medium that is characterized in term of its acoustic attenuation and backscatter coefficient) two particularly interesting tissue properties can be extracted: the estimated acoustic concentration (EAC) and estimated scatterer diameter (ESD).

QUS imaging has been used to quantify EAC and ESD in two different mammary tumor models: spontaneous fibroadenoma in rat and transplanted 4T1 mammary carcinoma in mice (Oelze et al. 2004). Compared to the 4T1 mammary carcinoma, the fibroadenoma presented higher ESD (105 ± 25µm vs. 28 ± 4.6µm) and lower EAC (–15.6 ± 5 $dB*mm^{-3}$ vs. 10.6 ± 6.9 $dB*mm^{-3}$). These differences in tissue microstructure were confirmed to be consistent with the analysis of histologic slides. Carcinoma specimens presented relatively uniform morphology and minimal extracellular matrix. Fibroadenoma was associated with epithelial cells arranged in acini[19] surrounded by bands of fibrous connective tissue (Figure 31). A subsequent study using QUS showed conclusive results in the differentiation of carcinoma and sarcoma tumor models (Oelze and Zachary 2006).

[19] An acinus refers to any cluster of cells that resembles a many-lobbed berry, such as a raspberry.

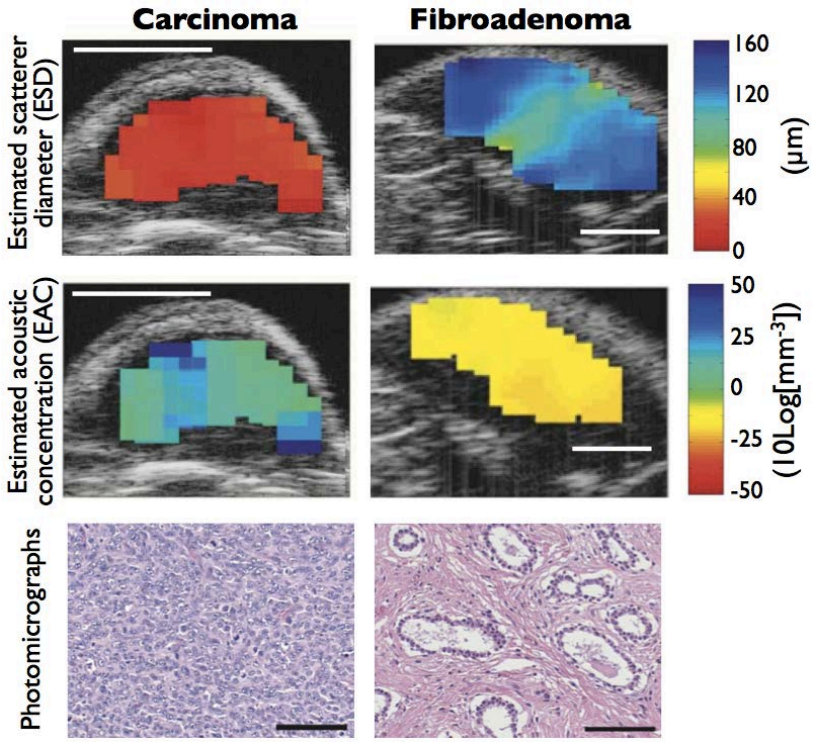

Figure 31: **Quantitative ultrasound in tumors**. QUS images of mouse carcinomas (left panel) acquired at 20 MHz and rat fibroadenomas (right panel) using the estimated scatterer diameter (ESD, upper row) and the estimated average acoustic concentration (EAC, middle row). Photomicrographs (lower row) show the tumors consisted of the carcinoma cells with relatively uniform morphology and minimal extracellular matrix (left) while fibroadenomas consisted of well-differentiated epithelial cells arranged in acini surrounded by bands of fibrous connective tissue (right). White scale bar 5 mm. black scale bar 100 µm. *Figure adapted from (Oelze et al. 2004).*

Ultrasound imaging provides a large range of complementary techniques that enable the characterization of many aspects of the tumor and its surrounding microenvironment. In comparison with the other techniques reviewed in this chapter, advantages of ultrasound imaging include the rapid data acquisition, the potential to simultaneously acquire multiple ultrasound-based parameters and the suitability of ultrasound for screening and serial follow-up studies.

III.5. Conclusions

In conclusion, Table 1 summarizes imaging modalities used in the context of tumor characterization. Values of parameters indicated in the table (resolution, depth…) are given for the purpose of preclinical research and may vary for clinical use because systems may differ. It can be appreciated from this summary, that a large range of imaging techniques can be called upon to evaluate features of the TME from the microscopic to the macroscopic scale. Development of validated imaging approaches should lead to a better understanding of mechanisms underlying tumor development and tumor response to specific treatments. Although PET/CT, SPECT/CT and PA imaging were only briefly touched upon in this chapter, multimodal-imaging represents a new paradigm for *in vivo* imaging providing significantly enhanced information for the more complete characterization of tumors. The interested reader can refer to the following references for additional details on multimodal imaging (Cai and Chen 2008; Martí-Bonmatí et al. 2010).

As described, ultrasound imaging offers unique capacities for multi-parameter assessment of tumors with rapid and repeatable data acquisition. The sensitivity of CEUS, SWE and QUS imaging to tumor changes induced by cytotoxic and antiangiogenic drug will be specifically addressed in Chapter V of this thesis. Prior to that, however, work led to determine the reproducibility of UCA injections in CEUS imaging in small animal studies will be presented in the following chapter.

	Imaging modality	Resolution	Depth	Acquisition duration	Contrast	Target
Magnetic Resonance Imaging	T1 and T2*	10-100µm	No limit	seconds to hours	endogen ^{1}H	anatomy
	BOLD	mm		seconds to minutes	inhalation of 100% oxygen	level of oxygenation
	DCE-MRI	≈ 200µm		seconds to minutes	paramagnetic chelates, magnetic particles	vasculature, IFP, pH, expression of GFR, immune cells trafficking
	MRS	mm		seconds to minutes	endogen and/or injection: ^{13}C, ^{17}O, ^{19}F, ^{31}P	pH, pO_2, cell metabolism
	Elasticity	50µm-10mm		minutes		mechanical properties
Ionizing Imaging	µCT	10µm	No limit	minutes	Iodinated molecules	anatomy, vasculature, expression of GFR
	µSPECT	1-2mm		minutes to hour	^{99m}Tc- or ^{111}In-labeled compound	hypoxia, cell metabolism, apoptosis, expression of GFR, integrins, MMPs
	µPET				^{18}F- , ^{64}Cu- or ^{11}C-labeled compound	
Ultrasound Imaging	B-mode	20 -150 µm	mm to cms	seconds	scatter properties of endogen cell	anatomy
	QUS					tissue microstructure
	CEUS	250µm	cms	seconds to minutes	Microbubbles: free and targeted (VEGFR2 /$\alpha_v\beta_3$), nanobubbles	vasculature, expression of VEGFR2 and $\alpha_v\beta_3$
	Acoustic angiography	150µm	mm	seconds to minutes	Microbubbles	vasculature
	UFD-T	100µm	cms	hour	endogen RBCs	vasculature
	SWE	mm	cms	seconds	scatter properties of endogen cell	mechanical properties (necrosis/fibrosis)
	PA	5µm-1mm	mm-cms	minutes	endogen RBCs, dyes, metallic NPs, carbon nanotubes, SPNs	vasculature, sO_2, ROS, proteases
Optical imaging	FRI	2-3mm	< cm	seconds to minutes	Photoproteins, fluorochromes	vasculature, pH, apoptosis, MMPs, GFR expression, proteins, immune cells
	FMT	1mm	cms	minutes to hours	Near-infrared fluorochromes	
	Fluorescence microscopy	1-5µm	< mm	seconds to hours	Photoproteins, fluorochromes	ECM component, tumor and immune cells trafficking, proteins, kinase activity
	OCT / OFDI	1-20µm	mm	minutes	light-scattering properties of tissue / circulating RBCs	vasculature, necrosis/ apoptosis, lymphatic system

Table 1: **Biomedical imaging for the characterization of tumors and their microenvironment**. Information given in the table refers to the context of preclinical cancer research. References used to compile this table are cited throughout this chapter.

III.6 Bibliography

Acharya S, Sahoo SK. PLGA nanoparticles containing various anticancer agents and tumour delivery by EPR effect. Adv Drug Deliv Rev Elsevier B.V., 2011;63:170–83.

Akers WJ, Kim C, Berezin M, Guo K, Fuhrhop R, Lanza GM, Fischer GM, Daltrozzo ŕE, Zumbusch ŕA, Cai ŕX, Wang L V, Achilefu S. Noninvasive Photoacoustic and Perfluorocarbon Nanoparticles. ACS Nano 2011;5:173–182.

Al-boukai A a, Al-kassimi F a, Ibrahim GF, Shaik S a. Prediction of Pulmonary Hypertension in Patients with or without Interstitial Lung Disease. Radiology 2011;260:875–883.
Al-Hallaq H, River J, Zamora M, Oikawa H, Karczmar G. Correlation of magnetic resonance and oxygen microelectrode measurements of carbogen-induced changes in tumor oxygenation. Int J Radiat Oncol Biol Phys 1998;41:151–159.
Athanasiou A, Tardivon A, Tanter M, Sigal-Zafrani B, Bercoff J, Deffieux T, Gennisson J-L, Fink M, Neuenschwander S. Breast lesions: quantitative elastography with supersonic shear imaging--preliminary results. Radiology 2010;256:297–303.
Azab AK, Runnels JM, Pitsillides C, Moreau A, Azab F, Jia X, Wright R, Ospina B, Carlson AL, Alt C, Burwick N, Roccaro AM, Ngo HT, Farag M, Melhem MR, Sacco A, Munshi NC, Rollins BJ, Anderson KC, Kung AL, Lin CP, Irene M, Leleu X, Hideshima T, Ghobrial IM. CXCR4 inhibitor AMD3100 disrupts the interaction of multiple myeloma cells with the bone marrow microenvironment and enhances their sensitivity to therapy. Blood 2011;113:4341–4351.
Barrois G, Coron A, Payen T, Dizeux A, Bridal L. A Multiplicative Model for Improving Microvascular Flow Estimation in Dynamic Theory and Experimental Validation. IEEE Trans Ultrason Ferroelectr Freq Control 2013;60:2284–2294.
Battle MR, Goggi JL, Allen L, Barnett J, Morrison MS. Monitoring tumor response to antiangiogenic sunitinib therapy with 18F-fluciclatide, an 18F-labeled αVbeta3-integrin and αV beta5-integrin imaging agent. J Nucl Med 2011;52:424–30.
Baudelet C, Gallez B. How does blood oxygen level-dependent (BOLD) contrast correlate with oxygen partial pressure (pO2) inside tumors? Magn Reson Med 2002;48:980–986.
Baudelet C, Gallez B. Current issues in the utility of blood oxygen level dependent MRI for the assessment of modulations in tumor oxygenation. Curr Med Imaging Rev 2005;229–243.
Bollineni VR, Kerner GSM a, Pruim J, Steenbakkers RJHM, Wiegman EM, Koole MJB, de Groot EH, Willemsen ATM, Luurtsema G, Widder J, Groen HJM, Langendijk J a. PET imaging of tumor hypoxia using 18F-fluoroazomycin arabinoside in stage III-IV non-small cell lung cancer patients. J Nucl Med 2013;54:1175–80.
Bremer C, Weissleder R, Tung C-H. In vivio molecular target assessment of matrix metalloproteinase inhibition. Nat Med 2001;7:743–748.
Busk M, Mortensen LS, Nordsmark M, Overgaard J, Jakobsen S, Hansen K V, Theil J, Kallehauge JF, D'Andrea FP, Steiniche T, Horsman MR. PET hypoxia imaging with FAZA: reproducibility at baseline and during fractionated radiotherapy in tumour-bearing mice. Eur J Nucl Med Mol Imaging 2013;40:186–97.
Bussink J, Kaanders JH a M, Van Der Kogel AJ. Tumor hypoxia at the micro-regional level: Clinical relevance and predictive value of exogenous and endogenous hypoxic cell markers. Radiother Oncol 2003;67:3–15.
Cai W, Chen X. Multimodality molecular imaging of tumor angiogenesis. J Nucl Med 2008;49 Suppl 2:113S–28S.
Chamming's F, Latorre-Ossa H, Le Frère-Belda M a, Fitoussi V, Quibel T, Assayag F, Marangoni E, Autret G, Balvay D, Pidial L, Gennisson JL, Tanter M, Cuenod C a, Clément O, Fournier LS. Shear wave elastography of tumour growth in a human breast cancer model with pathological correlation. Eur Radiol 2013;23:2079–86.
Chance B, Cope M, Gratton E, Ramanujam N, Tromberg B. Phase measurement of light absorption and scatter in human tissue. Rev Sci Instrum 1998;69:1998.
Charanya TT, York T, Gullicksrud K, Sudlow G, Akers WJ, Rubin D, Gruev V, Achilefu S. Polarization Imaging serves as a complimentary tool to NIR fluorescence guided colonoscopy. Biomed Opt 2014 Washington, D.C.: Osa, 2014;BW1B.3.
Chen X, Conti PS, Moats RA. In vivo Near-Infrared Fluorescence Imaging of Integrin v 3 in Brain Tumor Xenografts. Cancer Res 2004;64:8009–8014.
Cho H, Ackerstaff E, Carlin S, Lupu ME, Wang Y, Rizwan A, Donoghue JO, Ling CC, Humm JL, Zanzonico PB. Noninvasive Multimodality Imaging of the Tumor Microenvironment : Registered Dynamic Magnetic Resonance Imaging and Positron Emission Tomography Studies of a Preclinical Tumor Model of tumor hypoxia. Neoplasia 2009;11:247–259.
De La Zerda A, Zavaleta C, Keren S, Vaithilingam S, Bodapati S, Liu Z, Levi J, Smith BR, Ma T-J, Oralkan O, Cheng Z, Chen X, Dai H, Khuri-Yakub BT, Gambhir SS. Carbon nanotubes as photoacoustic molecular imaging agents in living mice. Nat Nanotechnol Nature Publishing Group, 2008;3:557–562.
Demene C, Payen T, Dizeux A, Barrois G, Gennisson JL, Bridal L, Tanter M. Comparison of tumor microvasculature assessment via Ultrafast Doppler Tomography and Dynamic Contrast Enhanced Ultrasound. 2014 IEEE Int Ultrason Symp Ieee, 2014;421–424.

Deshpande N, Ren Y, Foygel K, Rosenberg J, Willmann JK. Tumor Angiogenic Marker Expression Levels during Tumor Growth: Longitudinal Assessment with Molecularly Targeted Microbubles and US Imaging. Radiology 2011;258:804–811.
Dizeux A, Barrois G, Payen T, Baldini C, Le Guillou Buffelo D, Comperat E, Bridal SL. Differentiation of vascular distribution and flow patterns in tumors with Dynamic Contrast-Enhanced Ultrasound (DCE-US) perfusion maps. Ultrason Symp (IUS), 2013 IEEE Int 2013;1513 – 1516.
Earley S, Vinegoni C, Dunham J, Gorbatov R, Feruglio PF, Weissleder R. In vivo imaging of drug-induced mitochondrial outer membrane permeabilization at single-cell resolution. Cancer Res 2012;72:2949–56.
Elas M, Williams BB, Parasca A, Mailer C, Pelizzari C a, Lewis M a, River JN, Karczmar GS, Barth ED, Halpern HJ. Quantitative tumor oxymetric images from 4D electron paramagnetic resonance imaging (EPRI): methodology and comparison with blood oxygen level-dependent (BOLD) MRI. Magn Reson Med 2003;49:682–91.
Fischer T, Thomas A, Tardy I, Schneider M, Hünigen H, Custodis P, Beyersdorff D, Plendl J, Schnorr J, Diekmann F, Gemeinhardt O. Vascular endothelial growth factor receptor 2-specific microbubbles for molecular ultrasound detection of prostate cancer in a rat model. Invest Radiol 2010;45:675–684.
Gainkam Tchouate LO, Huang L, Caveliers V, Keyaerts M, Hernot S, Vaneycken I, Vanhove C, Revets H, De Baetselier P, Lahoutte T. Comparison of the biodistribution and tumor targeting of two 99mTc-labeled anti-EGFR nanobodies in mice, using pinhole SPECT/micro-CT. J Nucl Med 2008;49:788–95.
Gallagher F a, Kettunen MI, Day SE, Hu D-E, Ardenkjaer-Larsen JH, Zandt R in 'T, Jensen PR, Karlsson M, Golman K, Lerche MH, Brindle KM. Magnetic resonance imaging of pH in vivo using hyperpolarized 13C-labelled bicarbonate. Nature 2008;453:940–3.
Gerling M, Zhao Y, Nania S, Norberg KJ, Verbeke CS, Eng- B, Kuiper R V, Bergström Å, Hassan M, Neesse A, Löhr JM. Real-Time Assessment of Tissue Hypoxia In Vivo with Combined Photoacoustics and High-Frequency Ultrasound. Theranostics 2014;4.
Gessner RC, Frederick CB, Foster FS, Dayton P a. Acoustic angiography: a new imaging modality for assessing microvasculature architecture. Int J Biomed Imaging 2013;2013:936593.
Golman K, Zandt RI, Lerche M, Pehrson R, Ardenkjaer-Larsen JH. Metabolic imaging by hyperpolarized 13C magnetic resonance imaging for in vivo tumor diagnosis. Cancer Res 2006;66:10855–10860.
Guibal A, Taillade L, Mulé S, Comperat E, Badachi Y, Golmard J-L, Rixe O, Bridal SL, Lucidarme O. Noninvasive Contrast-enhanced US Quantitative Assessment of Tumor Microcirculation in a Murine Model: Effect of Discontinuing Anti-VEGF Therapy. Radiology 2010;254:420–429.
Gurskaya NG, Verkhusha V V, Shcheglov AS, Staroverov DB, Chepurnykh T V, Fradkov AF, Lukyanov S, Lukyanov K a. Engineering of a monomeric green-to-red photoactivatable fluorescent protein induced by blue light. Nat Biotechnol 2006;24:461–465.
Ha D-H, Choi S, Oh JY, Yoon SK, Kang MJ, Kim K-U. Application of 31P MR Spectroscopy to the Brain Tumors. Korean J Radiol 2013;14:477–486.
Hallac RR, Zhou H, Pidikiti R, Song K, Stojadinovic S, Zhao D, Solberg T, Peschke P, Mason RP. Correlations of noninvasive BOLD and TOLD MRI with pO2 and relevance to tumor radiation response. Magn Reson Med 2014 [cited 2014 Oct 17];71:1863–73.
Homan K a., Souza M, Truby R, Luke GP, Green C, Vreeland E, Emelianov S. Silver nanoplate contrast agents for in vivo molecular photoacoustic imaging. ACS Nano 2012;6:641–650.
Hompland T, Ellingsen C, Øvrebø KM, Mri C. Interstitial Fluid Pressure and Associated Lymph Node Metastasis Revealed in Tumors by Dynamic Contrast-Enhanced MRI. Cancer Res 2012;72:4899–4908.
Hu S, Kiesewetter DO, Zhu L, Guo N, Gao H, Liu G, Hida N, Lang L, Niu G, Chen X. Longitudinal PET imaging of doxorubicin-induced cell death with 18F-annexin v. Mol Imaging Biol 2012;14:762–770.
Huang T, Civelek a. C, Li J, Jiang H, Ng CK, Postel GC, Shen B, Li X-F. Tumor Microenvironment-Dependent 18F-FDG, 18F-Fluorothymidine, and 18F-Misonidazole Uptake: A Pilot Study in Mouse Models of Human Non-Small Cell Lung Cancer. J Nucl Med 2012;53:1262–1268.
Hutterer M, Nowosielski M, Putzer D, Waitz D, Tinkhauser G, Kostron H, Muigg A, Virgolini IJ, Staffen W, Trinka E, Gotwald T, Jacobs AH, Stockhammer G. O-(2-18F-fluoroethyl)-L-tyrosine PET predicts failure of antiangiogenic treatment in patients with recurrent high-grade glioma. J Nucl Med 2011;52:856–864.
Jacobson O, Weiss ID, Kiesewetter DO, Farber JM, Chen X. PET of tumor CXCR4 expression with 4-18F-T140. J Nucl Med 2010;51:1796–1804.
Jain RK. Normalization of tumor vasculature: an emerging concept in antiangiogenic therapy. Science 2005;307:58–62.

Jiang L, Weatherall PT, McColl RW, Tripathy D, Mason RP. Blood oxygenation level-dependent (BOLD) contrast magnetic resonance imaging (MRI) for prediction of breast cancer chemotherapy response: A pilot study. J Magn Reson Imaging 2013;37:1083–1092.

Jugé L, Doan B-T, Seguin J, Albuquerque M, Larrat B, Mignet N, Chabot GG, Scherman D, Paradis V, Vilgrain V, Van Beers BE, Sinkus R. Colon tumor growth and antivascular treatment in mice: complementary assessment with MR elastography and diffusion-weighted MR imaging. Radiology 2012;264:436–44.

Ke C-C, Liu R-S, Suetsugu A, Kimura H, Ho JH, Lee OK, Hoffman RM. In vivo fluorescence imaging reveals the promotion of mammary tumorigenesis by mesenchymal stromal cells. PLoS One 2013 [cited 2014 Apr 2];8:e69658.

Ke S, Wen X, Gurfinkel M, Charnsangavej C, Wallace S, Sevick-muraca EM. Near-Infrared Optical Imaging of Epidermal Growth Factor Receptor in Breast Cancer Xenografts. Cancer Res 2003;63:7870–7875.

Kedrin D, Gligorijevic B, Wyckoff J, Verkhusha V V, Condeelis J, Segall JE, Rheenen J Van. Intravital imaging of metastatic behavior through a Mammary Imaging Window. Nat Methods 2008;5:1019–1021.

Kelkar SS, Reineke TM. Theranostics: Combining imaging and therapy. Bioconjug Chem 2011;22:1879–1903.

Kim J-W, Galanzha EI, Shashkov E V, Moon H-M, Zharov VP. Golden carbon nanotubes as multimodal photoacoustic and photothermal high-contrast molecular agents. Nat Nanotechnol Nature Publishing Group, 2009;4:688–94.

Kircher MF, Willmann JK. Molecular Body Imaging : MR Imaging, CT, and US. Part I. Principles. Radiology 2012a;263:633–643.

Kircher MF, Willmann JK. Molecular Body Imaging : MR Imaging, CT, and US. Part II. Applications. Radiology 2012b;264:349–368.

Klomp DWJ, Bank BL van de, Raaijmakers A, Korteweg MA, Possanzini C, Boer VO, Van De Berg CAT, van de Bosch MAAJ, R.Luijten P. 31P MRSI and 1H MRS at 7 T: initial results in human breast cancer. NMR Biomed 2011;24:1337–1342.

Kobayashi H, Watanabe R, Choyke PL. Improving conventional enhanced permeability and retention (EPR) effects; What is the appropriate target? Theranostics 2014;4:81–89.

Kurtova A V., Tamayo AT, Ford RJ, Burger J a. Mantle cell lymphoma cells express high levels of CXCR4, CXCR5, and VLA-4 (CD49d): Importance for interactions with the stromal microenvironment and specific targeting. Blood 2009;113:4604–4613.

Lamuraglia M, Bridal SL, Santin M, Izzi G, Rixe O, Paradiso A, Lucidarme O. Clinical relevance of contrast-enhanced ultrasound in monitoring anti-angiogenic therapy of cancer: current status and perspectives. Crit Rev Oncol Hematol 2010;73:202–12.

Laufer J, Delpy D, Elwell C, Beard P. Quantitative spatially resolved measurement of tissue chromophore concentrations using photoacoustic spectroscopy: application to the measurement of blood oxygenation and haemoglobin concentration. Phys Med Biol 2007;52:141–168.

Laufer J, Johnson P, Zhang E, Treeby B, Cox B, Pedley B, Beard P. In vivo preclinical photoacoustic imaging of tumor vasculature development and therapy. J Biomed Opt 2012;17:056016.

Lee H, Akers W, Bhushan K. Near-infrared pH-activatable fluorescent probes for imaging primary and metastatic breast tumors. Bioconjugate … 2011;22:777–784.

Leff DR, Warren OJ, Enfield LC, Gibson A, Athanasiou T, Patten DK, Hebden J, Yang GZ, Darzi A. Diffuse optical imaging of the healthy and diseased breast: A systematic review. Breast Cancer Res Treat 2008;108:9–22.

Leong-Poi H, Christiansen J, Heppner P, Lewis CW, Klibanov AL, Kaul S, Lindner JR. Assessment of endogenous and therapeutic arteriogenesis by contrast ultrasound molecular imaging of integrin expression. Circulation 2005;111:3248–3254.

Levi J, Kothapalli S-R, Bohndiek S, Yoon J-K, Dragulescu-Andrasi A, Nielsen C, Tisma A, Bodapati S, Gowrishankar G, Yan X, Chan C, Starcevic D, Gambhir SS. Molecular Photoacoustic Imaging of Follicular Thyroid Carcinoma. Clin Cancer Res 2013;19:1494–1502.

Li W, Niu G, Lang L, Guo N, Ma Y, Kiesewetter DO, Backer JM, Shen B, Chen X. PET imaging of EGF receptors using [18F]FBEM-EGF in a head and neck squamous cell carcinoma model. Eur J Nucl Med Mol Imaging 2012;39:300–308.

Lovell JF, Jin CS, Huynh E, Jin H, Kim C, Rubinstein JL, Chan WCW, Cao W, Wang L V, Zheng G. Porphysome nanovesicles generated by porphyrin bilayers for use as multimodal biophotonic contrast agents. Nat Mater Nature Publishing Group, 2011;10:324–332.

Macé E, Montaldo G, Cohen I, Baulac M, Fink M, Tanter M. Functional ultrasound imaging of the brain. Nat Methods 2011;8:662–664.

Macé E, Montaldo G, Cohen I, Baulac M, Fink M, Tanter M. Functional Ultrasound Imaging of the Brain: Theory and Basic Principles. IEEE Trans Ultrason Ferroelectr Freq Control 2013;60:492–506.

Martí-Bonmatí L, Sopena R, Bartumeus P, Sopena P. Multimodality imaging techniques. Contrast Media Mol Imaging 2010;5:180–189.
Matsumoto S, Batra S, Saito K, Yasui H, Choudhuri R, Gadisetti C, Subramanian S, Devasahayam N, Munasinghe JP, Mitchell JB, Krishna MC. Antiangiogenic agent sunitinib transiently increases tumor oxygenation and suppresses cycling hypoxia. Cancer Res 2011;71:6350–9.
Matsumoto S, Saito K, Takakusagi Y, Matsuo M, Munasinghe JP, Morris HD, Lizak MJ, Merkle H, Yasukawa K, Devasahayam N, Suburamanian S, Mitchell JB, Krishna MC. In Vivo Imaging of Tumor Physiological, Metabolic, and Redox Changes in Response to the Anti-Angiogenic Agent Sunitinib: Longitudinal Assessment to Identify Transient Vascular Renormalization. Antioxid Redox Signal 2014;00:1–11.
McLarty K, Cornelissen B, Cai Z, Scollard D a, Costantini DL, Done SJ, Reilly RM. Micro-SPECT/CT with 111In-DTPA-pertuzumab sensitively detects trastuzumab-mediated HER2 downregulation and tumor response in athymic mice bearing MDA-MB-361 human breast cancer xenografts. J Nucl Med 2009;50:1340–8. A
Meier R, Golovko D, Tavri S, Henning TD, Knopp C, Piontek G, Rudelius M, Heinrich P, Wels WS, Daldrup-Link H. Depicting adoptive immunotherapy for prostate cancer in an animal model with magnetic resonance imaging. Magn Reson Med 2011;65:756–763.
Mitri Z, Constantine T, O'Regan R. The HER2 Receptor in Breast Cancer: Pathophysiology, Clinical Use, and New Advances in Therapy. Chemother Res Pract 2012;2012:743193.
Montet X, Figueiredo J-L, Alencar H, Ntziachristos V, Mahmood U, Weissleder R. Tomographic fluorescence imaging of tumor vascular volume in mice. Radiology 2007;242:751–758.
Müller A, Krämer SD, Meletta R, Beck K, Selivanova S V., Rancic Z, Kaufmann P a., Vos B, Meding J, Stellfeld T, Heinrich TK, Bauser M, Hütter J, Dinkelborg LM, Schibli R, Ametamey SM. Gene expression levels of matrix metalloproteinases in human atherosclerotic plaques and evaluation of radiolabeled inhibitors as imaging agents for plaque vulnerability. Nucl Med Biol Elsevier Inc., 2014;41:562–569.
Nedergaard MK, Kristoffersen K, Michaelsen SR, Madsen J, Poulsen HS, Stockhausen M-T, Lassen U, Kjaer A. The use of longitudinal 18F-FET MicroPET imaging to evaluate response to irinotecan in orthotopic human glioblastoma multiforme xenografts. PLoS One 2014 [cited 2014 Oct 16];9:e100009.
Needles A, Heinmiller A, Sun J, Theodoropoulos C, Bates D, Hirson D, Yin M, Foster FS. Development and initial application of a fully integrated photoacoustic micro-ultrasound system. IEEE Trans Ultrason Ferroelectr Freq Control 2013;60:888–97.
Nie F, Yu X-L, Wang X-G, Tang Y-F, Wang L-L, Ma L. Down-regulation of CacyBP is associated with poor prognosis and the effects on COX-2 expression in breast cancer. Int J Oncol 2010;37:1261–1269.
Nobis M, McGhee EJ, Morton JP, Schwarz JP, Karim S a, Quinn J, Edward M, Campbell AD, McGarry LC, Evans TRJ, Brunton VG, Frame MC, Carragher NO, Wang Y, Sansom OJ, Timpson P, Anderson KI. Intravital FLIM-FRET imaging reveals dasatinib-induced spatial control of src in pancreatic cancer. Cancer Res 2013;73:4674–86.
Ntziachristos V. Fluorescence molecular imaging. Annu Rev Biomed Eng 2006;8:1–33.
Ntziachristos V, Ripoll J, Wang L V, Weissleder R. Looking and listening to light: the evolution of whole-body photonic imaging. Nat Biotechnol 2005;23:313–320.
Ntziachristos V, Schellenberger E a, Ripoll J, Yessayan D, Graves E, Bogdanov A, Josephson L, Weissleder R. Visualization of antitumor treatment by means of fluorescence molecular tomography with an annexin V-Cy5.5 conjugate. Proc Natl Acad Sci U S A 2004;101:12294–12299.
Nwe K, Huang C-H, Tsourkas A. Gd-labeled glycol chitosan as a pH-responsive magnetic resonance imaging agent for detecting acidic tumor microenvironments. J Med Chem 2013;56:7862–9. Available from:
Oda Y, Tateishi N, Matono H, Matsuura S, Yamamaoto H, Tamiya S, Yokoyama R, Matsuda S, Iwamoto Y, Tsuneyoshi M. Chemokine receptor CXCR4 expression is correlated with VEGF expression and poor survival in soft-tissue sarcoma. Int J Cancer 2009;124:1852–1859.
Oelze ML, O'Brien WD, Blue JP, Zachary JF. Differentiation and Characterization of Rat Mammary Fibroadenomas and 4T1 Mouse Carcinomas Using Quantitative Ultrasound Imaging. IEEE Trans Med Imaging 2004;23:764–771.
Oelze ML, Zachary JF. Examination of cancer in mouse models using high-frequency quantitative ultrasound. Ultrasound Med Biol 2006;32:1639–48.
Osmanski B-F, Pezet S, Ricobaraza A, Lenkei Z, Tanter M. Functional Ultrasound Imaging of Intrinsic Connectivity in the Living Rat Brain with High Spatiotemporal Resolution. Nat Commun 2014;in press.
Padhani A, Krohn K, Lewis J, Alber M. Imaging oxygenation of human tumours. Eur Radiol 2007;17:861–872.
Payen T, Dizeux A, Baldini C, Le Guillou-Buffelo D, Lamuraglia M, Comperat E, Lucidarme O, Bridal SL. VEGFR2-targeted contrast-enhanced ultrasound to distinguish between two antiangiogenic treatments. Ultrasound Med Biol 2015;IN PRESS.

Peller M, Weissfloch L, Stehling M, Weber J, Bruening R, Senekowitsch-Schmidtke R, Molls M, Reiser M. Oxygen-induced MR signal changes in murine tumors. Magn Reson Imaging 1998;16:799–809.
Pu K, Shuhendler AJ, Jokerst J V, Mei J, Gambhir SS, Bao Z, Rao J. Semiconducting polymer nanoparticles as photoacoustic molecular imaging probes in living mice. Nat Nanotechnol Nature Publishing Group, 2014;9:233–9.
Pysz MA, Foygel K, Rosenberg J, Gambhir SS, Schneider M, Willmann JK. Antiangiogenic Cancer Therapy : Monitoring with Molecular US and a Clinically Translatable Contrast Agent (BR55). Radiology 2010;256:519–527.
Reuveni T, Motiei M, Romman Z, Popovtzer A, Popovtzer R. Targeted gold nanoparticles enable molecular CT imaging of cancer: an in vivo study. Int J Nanomedicine 2011;6:2859–1864.
Rognin N., Arditi M, Mercier L, Frinking PJA, Schneider M, Perrenoud G, Anaye A, Meuwly J, Tranquart F. Parametric imaging for characterizing focal liver lesions in contrast-enhanced ultrasound. IEEE Trans Ultrason Ferroelectr Freq Control 2010;57:2503–11.
Savai R, Langheinrich AC, Schermuly RT, Pullamsetti SS, Rau WS, Seeger W. Evaluation of Angiogenesis Using Micro – Computed Tomography in a Xenograft Mouse Model of Lung Cancer. Neoplasia 2009;11:48–56.
Schietinger A, Arina A, Liu RB, Wells S, Huang J, Engels B, Bindokas V, Bartkowiak T, Lee D, Herrmann A, Piston DW, Pittet MJ, Lin PC, Zal T, Schreiber H. Longitudinal confocal microscopy imaging of solid tumor destruction following adoptive T cell transfer. Oncoimmunology 2013;2:e26677.
Sebag F, Vaillant-Lombard J, Berbis J, Griset V, Henry JF, Petit P, Oliver C. Shear wave elastography: a new ultrasound imaging mode for the differential diagnosis of benign and malignant thyroid nodules. J Clin Endocrinol Metab 2010;95:5281–5288.
Selivanova S V., Stellfeld T, Heinrich TK, Müller A, Krämer SD, Schubiger PA, Schibli R, Ametamey SM, Vos B, Meding J, Bauser M, Hu J, Dinkelborg LM. Design, Synthesis, and Initial Evaluation of a High A ffi nity Positron Emission Tomography Probe for Imaging Matrix Metalloproteinases 2 and 9. J Med Chem 2013;56:4912–4920.
Sheu AY, Zhang Z, Omary R a, Larson AC. MRI-monitored transcatheter intra-arterial delivery of SPIO-labeled natural killer cells to hepatocellular carcinoma: preclinical studies in a rodent model. Invest Radiol 2013;48:492–9.
Smirnov P, Lavergne E, Gazeau F, Lewin M, Boissonnas A, Doan B-T, Gillet B, Combadière C, Combadière B, Clément O. In vivo cellular imaging of lymphocyte trafficking by MRI: a tumor model approach to cell-based anticancer therapy. Magn Reson Med 2006 [cited 2015 Jan 20];56:498–508.
Soundararajan A, Abraham J, Nelon LD, Prajapati SI, Zarzabal LA, Michalek JE, Mchardy SF, Hawkins DS, Malempati S, Keller C. F-FDG MicroPET Imaging Detects Early Transient Response to an IGF1R Inhibitor in Genetically Engineered Rhabdomyosarcoma Models. Pediatr Blood Cancer 2012;59:485–492.
Tanter M, Fink M. Ultrafast Imaging in Biomedical Ultrasound. EEE Trans Ultrason Ferroelectr Freq Control 2014;61:102–119.
Tardy I, Pochon S, Theraulaz M, Emmel P, Passantino L, Tranquart F, Schneider M. Ultrasound molecular imaging of VEGFR2 in a rat prostate tumor model using BR55. Invest Radiol 2010;45:573–8.
Theek B, Gremse F, Kunjachan S, Fokong S, Pola R, Pechar M, Deckers R, Storm G, Ehling J, Kiessling F, Lammers T. Characterizing EPR-mediated passive drug targeting using contrast-enhanced functional ultrasound imaging. J Control Release 2014;182:83–89.
Timpson P, McGhee EJ, Morton JP, von Kriegsheim A, Schwarz JP, Karim S a, Doyle B, Quinn J a, Carragher NO, Edward M, Olson MF, Frame MC, Brunton VG, Sansom OJ, Anderson KI. Spatial regulation of RhoA activity during pancreatic cancer cell invasion driven by mutant p53. Cancer Res 2011;71:747–57.
Tong RT, Boucher Y, Kozin S V, Winkler F, Hicklin DJ, Jain RK. Vascular Normalization by Vascular Endothelial Growth Factor Receptor 2 Blockade Induces a Pressure Gradient Across the Vasculature and Improves Drug Penetration in Tumors. Cancer Res 2004;64:3731–3736.
Tran L-B-A, Bol A, Labar D, Jordan B, Magat J, Mignion L, Grégoire V, Gallez B. Hypoxia imaging with the nitroimidazole 18F-FAZA PET tracer: a comparison with OxyLite, EPR oximetry and 19F-MRI relaxometry. Radiother Oncol Elsevier Ireland Ltd, 2012;105:29–35.
Uchugonova A, Zhao M, Weinigel M, Zhang Y, Bouvet M, Hoffman RM, König K. Multiphoton tomography visualizes collagen fibers in the tumor microenvironment that maintain cancer-cell anchorage and shape. J Cell Biochem 2013;114:99–102.
Ullrich RT, Jikeli JF, Diedenhofen M, Böhm-Sturm P, Unruh M, Vollmar S, Hoehn M. In-vivo visualization of tumor microvessel density and response to anti-angiogenic treatment by high resolution MRI in mice. PLoS One 2011;6:e19592.

Vakoc BJ, Fukumura D, Jain RK, Bouma BE. Cancer imaging by optical coherence tomography: preclinical progress and clinical potential. Nat Rev Cancer Nature Publishing Group, 2012;12:363–8. A

Vakoc BJ, Lanning RM, Tyrrell J a, Padera TP, Bartlett L a, Stylianopoulos T, Munn LL, Tearney GJ, Fukumura D, Jain RK, Bouma BE. Three-dimensional microscopy of the tumor microenvironment in vivo using optical frequency domain imaging. Nat Med 2009;15:1219–23.

Vaupel P, Mayer A. Hypoxia in cancer: Significance and impact on clinical outcome. Cancer Metastasis Rev 2007;26:225–239.

Voura EB, Jaiswal JK, Mattoussi H, Simon SM. Tracking metastatic tumor cell extravasation with quantum dot nanocrystals and fluorescence emission-scanning microscopy. Nat Med 2004;10:993–998.

Wang G, Zhang X, Liu Y, Hu Z, Mei X, Uvdal K. Magneto-Fluorescent Nanoparticles with High-Intensity NIR Emission, T1 and T2 Weighted MR for Multimodal Specific Tumor Imaging. J Mater Chem B 2015;

Williams R, Hudson JM, Lloyd BA, Sureshkumar AR, Lueck G, Milot L, Atri M, Bjarnason GA, Burns PN. Dynamic Microbubble Contrast-enhanced US to Measure Tumor Response to Targeted Therapy : A Proposed Clinical Protocol with Results from Renal Cell Carcinoma Patients Receiving Antiangiogenic Therapy. Radiology 2011;260:581–590.

Willmann JK, Kimura RH, Deshpande N, Lutz AM, Cochran JR, Gambhir SS. Targeted contrast-enhanced ultrasound imaging of tumor angiogenesis with contrast microbubbles conjugated to integrin-binding knottin peptides. J Nucl Med 2010;51:433–440.

Willmann JK, Lutz AM, Paulmurugan R, Patel MR, Chu P, Rosenberg J, Gambhir SS. Dual-targeted contrast agent for US assessment of tumor angiogenesis in vivo. Radiology 2008;248:936–944.

Yin M, Lakshman M, Stuart Foster F. Quantitative functional assessment of tumour microenvironment using contrast enhanced ultrasound and photoacoustic imaging. 2013 IEEE Int Ultrason Symp Ieee, 2013;1833–1836.

Yin T, Wang P, Zheng R, Zheng B, Cheng D, Zhang X, Shuai X. Nanobubbles for enhanced ultrasound imaging of tumors. Int J Nanomedicine 2012;7:895–904.

York T, Powell SB, Gao S, Kahan L, Charanya T, Saha D, Roberts NW, Cronin TW, Marshall J, Achilefu S, Lake SP, Raman B, Gruev V. Bioinspired Polarization Imaging Sensors: From Circuits and Optics to Signal Processing Algorithms and Biomedical Applications. Proc IEEE 2014;102:1450–1469.

Yun SH, Tearney GJ, Vakoc BJ, Shishkov M, Oh WY, Desjardins AE, Suter MJ, Chan RC, Evans J a, Jang I-K, Nishioka NS, de Boer JF, Bouma BE. Comprehensive volumetric optical microscopy in vivo. Nat Med 2006;12:1429–1433.

Zeng Z, Samudio IJ, Munsell M, An J, Huang Z, Estey E, Andreeff M, Konopleva M. Inhibition of CXCR4 with the novel RCP168 peptide overcomes stroma-mediated chemoresistance in chronic and acute leukemias. Mol Cancer Ther 2006;5:3113–3121.

Zhao D, Jiang L, Hahn EW, Mason RP. Comparison of 1H blood oxygen level-dependent (BOLD) and 19F MRI to investigate tumor oxygenation. Magn Reson Med 2009;62:357–64.

Zhao D, Jiang L, Mason RP. Measuring Changes in Tumor Oxygenation. METHODS Enzymol 2004;386:378–418.

Zhou Q, Chen Z, Wang Y, Yang F, Lin Y, Liao Y. Review Article Ultrasound-Mediated Local Drug and Gene Delivery Using Nanocarriers. 2014;2014.

IV. REPRODUCIBILITY OF CONTRAST-ENHANCED ULTRASOUND IN MICE WITH CONTROLLED INJECTION

IV.1. Introduction

Evaluation of microvascular flow and perfusion is important for the diagnosis and treatment of diseases such as cancer (Chung et al. 2010; Folkman 1995; Helminger et al. 1997) and cardiovascular disease (Blankstein et al. 2009). Non-invasive imaging techniques can provide clinical assessment and repeated follow-up of microvascular changes in tumors or organs. Among the available imaging modalities, ultrasound (US) is of particular interest because it is a safe, bed-side and well-accepted technique that can be repeated often. Contrast-Enhanced Ultrasound (CEUS) offers the possibility to obtain both qualitative and quantitative information on local microvascular flow through the assessment of contrast-agent enhancement (Dietrich et al. 2012; Gauthier et al. 2012b; Guibal et al. 2010; Lamuraglia et al. 2010; Leen et al. 2012; Quaia 2007)

The most widely-established method for CEUS relies on injection of a bolus of contrast agent microbubbles. Linearized, echo-power vs. time curves (Payen et al. 2013) are obtained within a region of interest and used to evaluate the contrast agent's first passage (wash-in) followed by the progressive echo-power decrease during the washout phase. Several models can be fit to this data to estimate parameters related to microvascular flow (Strouthos et al. 2010). For the lognormal bolus model (Rognin et al. 2010), parameters obtained from the model provide information related to the density of the microvascular network: Peak enhancement (PE, maximal echo-power value) and the area under the curve (AUC). Others provide an assessment of the microvascular function: time to peak (TTP, interval between the peak and the origin), mean transit time (MTT, the mean of the lognormal distribution), wash-in and washout rate (WIR and WOR, maximal value of the slope during wash-in and wash-out phase). As bolus injection of contrast agent often produces an initial "blooming" effect (proportional to the concentration of UCA used) current clinical guidelines recommend to use smaller amount of UCA or a continuous infusion, at a rate of 1-2mL/min for CEUS examinations (Piscaglia et al. 2012).

Because of the small blood volume, contrast agent injection can be a strong source of variability for the evaluation of microvascular flow using CEUS in mice. Stapleton et al. studied the inter-injection variability (manual injections) by imaging five Definity bolus passages in the jugular vein of mice at 30 MHz (Stapleton et al. 2009). The coefficient of variation ($CV = {Standard\ deviation}/{Mean} \times 100$) of PE and AUC were found to be 10 and 34 %, respectively. Palmowski *et al.* (2010), studied the impact of injection rate (at constant volume and quantity of contrast agent) on perfusion parameters in epidermoid carcinoma xenografts. TTP was significantly increased (+243 ± 145 % $p<0.05$), whereas, PE and WIR decreased (-55 ± 28 %, $p<0.05$, and -28 ± 16 %, $p<0.01$, respectively) when manual injection-time increased from 2 to 10 s. Furthermore, the importance of controlling hydrostatic pressure and shear stress during injection has been underlined by work demonstrating the dependence of the bubble diameter on the needle gauge and the rate used during injection (Barrack and Stride 2009; Talu et al. 2008).

Our study describes the implementation of a controlled bolus-injection system based on a system developed by Bracco Suisse SA (Hyvelin et al. 2013). Hyvelin et al. demonstrated that the PE parameter evaluated in the kidney for 3 consecutive UCA injections with the controlled injection system in mice (N=5) and rats (N=6) was just above 10% which indicates a good level of reproducibility for *in vivo* CEUS measurements. The injection system and the level of control provided for dose, rate and volume of the injection are described in our study. Its impact on the injected microbubble population is assessed. Using an *in vitro* flow phantom, the variability of echo-power curve profiles and perfusion parameters estimated from the curves are compared for

injections made with the controlled system and manually. *In vivo*, the inter-injection variability for manual and controlled injections is compared based on estimations of perfusion parameters assessed in the renal cortex and an ectopic colorectal tumor model.

IV.2. Materials and methods

IV.2.1. Experimental configuration

This study describes the validation in our lab of a controlled bolus-injection system developed by Bracco Suisse SA (Hyvelin et al., 2013) for the injection of Ultrasound Contrast Agent (UCA) (Figure 1.A-1). The injection system consists of a mixing valve with three tubes: the first tube is linked to a syringe pump (Pump11, Harvard Apparatus, Holliston, MA, USA) used for the flush of 0.9% NaCl saline at a rate of 4.5 mL/min, the second is fixed to a 100-µL Hamilton precision syringe (20 needle gauge) containing UCA and the last tube is linked to a 27 G catheter which is inserted either in the input tube of the *in vitro* flow phantom (red cross in Figure 1 B) or the tail-vein of the mouse (red cross in Figure 1 C).

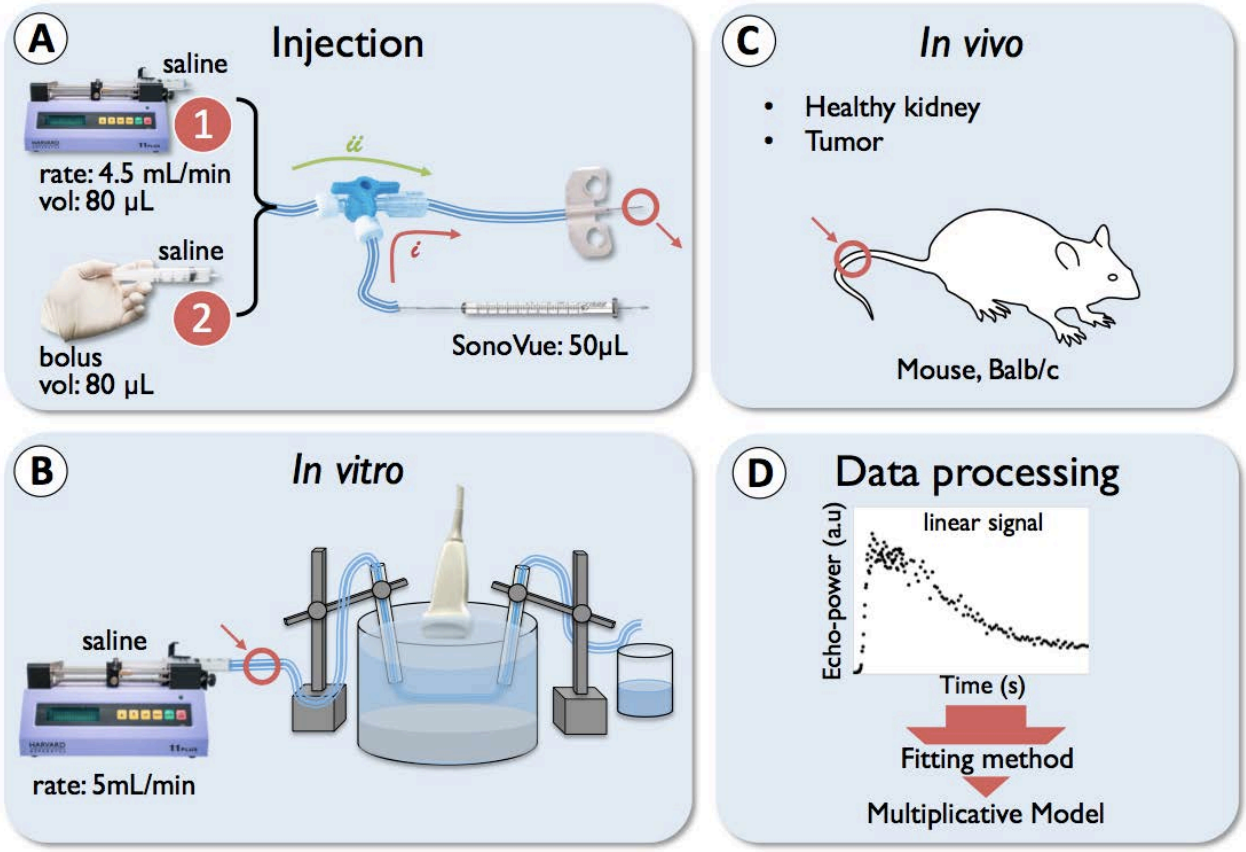

Figure 1: **Diagram of the experimental configurations**. As shown in A, the injections were made using either the controlled injection system (A-1) or by manual injection (A-2). For *in vitro* experiments (B), flow was produced with a separate syringe pump to attain a constant flow rate (5 mL/min) in the tubing and the contrast-injection catheter (A) was inserted at the position marked by a red cross. For *in vivo* injections (C), the catheter (A) was inserted within the tail vein as marked with the red cross. Linearized echo-power data acquired were processed using a fitting approach based on the multiplicative nature of the noise in CEUS sequences (D).

The injection was performed rapidly in 2 steps. First, following the passage (i) in Figure 1 A, 50 µL of UCA solution at a concentration of 0.5 mL/kg were injected manually from the Hamilton syringe into the catheter through a 3-way valve (10-µL dead volume). The valve position was then switched and saline was injected following the route denoted by (ii) in Figure 1A to flush the UCA solution into the flow channel or the mouse's tail vein. This flush was performed either with the 1-mL syringe (manual injection) or with the syringe pump (controlled injection). The internal volume of the tubing connecting the three-way valve to the catheter in the tail vein was such that no UCA was injected prior to the flush and the total 40-µl dose was administered by the 80-µL saline flush. The entire UCA injection procedure required approximately 4 seconds.

IV.2.2. Contrast agent

The UCA, SonoVue®, (Bracco Suisse SA, Geneva, Switzerland) was used in this study. The microbubbles are coated with a very thin lipid monolayer membrane shell encapsulating sulfur hexafluoride gas (SF_6). The mean diameter and concentration of SonoVue microbubbles reconstituted with 5 mL of sterile saline (0.9% NaCL) have been reported to be 2.5 µm and 1 to 5×10^8 MBs/mL, respectively (Schneider 1999a)

IV.2.3. US system and settings

Contrast imaging was performed with a Sequoia 512 clinical ultrasound system (Acuson, Siemens Healthcare, Moutain View, CA, USA) with a 15L8w transducer (7 - 14 MHz) in Contrast Pulse Sequence (CPS) mode. The frequency was set at 7.0 MHz. DICOM JPEG data were acquired with a dynamic range setting of DR80 and a gain of 0. The frame rate was fixed at 1 Hz and the MI was equal to 0.1. The focal zone was set at the center of the tube for the i*n vitro* evaluations and at the center of the renal cortex or the tumor for *in vivo* measurements. For each injection, the contrast uptake sequence was recorded and echo-power curves were assessed in a region of interest (ROI).

IV.2.4. Estimation of perfusion parameters

CEUS data curves presenting echo-power as a function of time (100 s) were fit to the lognormal distribution (Rognin et al. 2010) using a fitting algorithm based on the multiplicative nature of the noise that corrupt CEUS images (Barrois et al. 2013). This fitting approach has recently been shown to provide more accurate fitting of the initial rise of echo-power curves than the more conventionally applied least-squares fitting. The resulting fit curves were used to estimate the functional parameters of peak enhancement (PE), mean transit time (MTT), time to peak (TTP), wash in rate (WIR), wash-out rate (WOR) and area under the curve (AUC) (Rognin et al. 2010).

IV.2.5. Assessment of the injection-system impact on the microbubble population

SonoVue was recuperated after passage through the manual and controlled injection systems. Scanning ion occlusion spectroscopy (SIOS) was then used to precisely compare the microbubble populations of SonoVue after their passage through the manual and controlled injection

circuits. SIOS utilizes the well-established Coulter principle (Henriquez et al. 2004) for particle analysis. Particles are individually analyzed as they traverse an elastomeric and resizable pore under the combined action of voltage and pressure. The qNano system (Izon Science Ltd, Christchurch, New Zealand) used for measurements was equipped with the NP2000 pore (1-4 µm size range measurement) and with a variable pressure module (VPM), a manometer that applies pressures to the sample cell. Solutions of SonoVue recuperated after passage through each injection were diluted by a factor of 10 in saline solution (0.9% NaCl) before evaluation with the SIOS system. Calibration particles of 2 µm mean diameter diluted at a concentration of 5.8×10^6/ml in saline solution (CPC2000C, Izon Science Ltd) were used as a reference under the same conditions used for SonoVue measurements (46 mm pore stretch, 0.28 V applied voltage, successive measurements at pressures 9, 11 and 14 cm of H_2O (1 cm ≈ 100 Pa). The population size distribution and the concentration (number of MBs/mL) were extracted from these measurements for each injection circuit using Izon control suite software 2.1 (Astafyeva et al. 2015).

Finally the effects of the two modes of injection were assessed in a dose-ranging experiment. First, SonoVue solutions under constant stirring with dilution factor of the native agent ranging from 10^3 to 5×10^5 were imaged. For each dilution, fifty images were obtained in CPS mode at 7 MHz. After noise subtraction, the parameters were calculated to describe the linear fit of echo-power vs. agent concentration. Dose-ranging data were then acquired for matched dilutions of agent recuperated after passage through the manual and controlled injection systems, respectively.

IV.2.6. *In vitro* reproducibility experiments

For the *in vitro* experiments, the catheter was linked to a flow channel (inner diameter of 0.8 mm) maintained under a constant flow of 5 mL/min using a second syringe pump (Pump11, Harvard Apparatus, Holliston, MA, USA, Figure 1.B). This flow rate is on the order that reported in murine kidney (Milia et al. 2001). A 40-µL volume of SonoVue™ (Schneider 1999b) was injected into the flow phantom channel which was suspended in a tank of water containing a sound absorbing medium at the bottom. Injections were performed at the same site using a 27-gauge needle for both manual and controlled (syringe-pump driven) injections. Manual and controlled injections were each performed 10 times and were alternated in order to avoid any systematic difference between groups due to eventual modifications in the UCA concentration over time. After each injection, tubes and syringes were rinsed with saline so that no UCA remained in the tubes that could influence subsequent injections. For both, manual and controlled injections, the bolus passage was monitored in the longitudinal axis of the tube (Figure 2-A) with ultrasonic imaging for 15 seconds. Then perfusion parameters were extracted to characterize echo-power vs. time curves for each bolus injection of UCA. Injection reproducibility was assessed by calculating the CV for each perfusion parameter.

IV.2.7. *In vivo* reproducibility experiments

The animals were housed at the CEF (Centre d'Explorations Fonctionnelles, Cordeliers' Research Center, facility agreement no. A75-06-12). All experiments were conducted in accordance with the institutional guidelines and the recommendations for the care and use of laboratory animals established by the French Ministry of Agriculture. Mice were anaesthetized with 2% (v/v) isoflurane

in medical air at 1 L/min. The temperature of the animal was maintained at 37°C. The catheter was inserted in the tail-vein (Figure 1.C) and injections were performed on twenty two male mice from the Balb/C line (8 months old, weight = 51 ± 5 g). Ten of these mice had a subcutaneous CT26 colorectal tumor on the flank (24 days of growth, volume = 1640 ± 470 mm^3) and the other twelve were healthy. Mice were divided into groups with two different types of UCA injection: manual (M) and controlled (C). There were, thus, for each type of injection, 6 mice with no pathology and 5 tumor-bearing mice. The probe was placed to image the long axis of the studied structure (kidney or tumor). Each mouse received four, 40-µL injections with a 15-minute delay between injections for elimination of circulating microbubbles. Microbubbles were eliminated by physiological processes, without application of acoustic bursts. Typical ROIs are shown in Figure 2. For *in vivo* experiments, variability was assessed by calculating CV of perfusion parameters over the four consecutive injections.

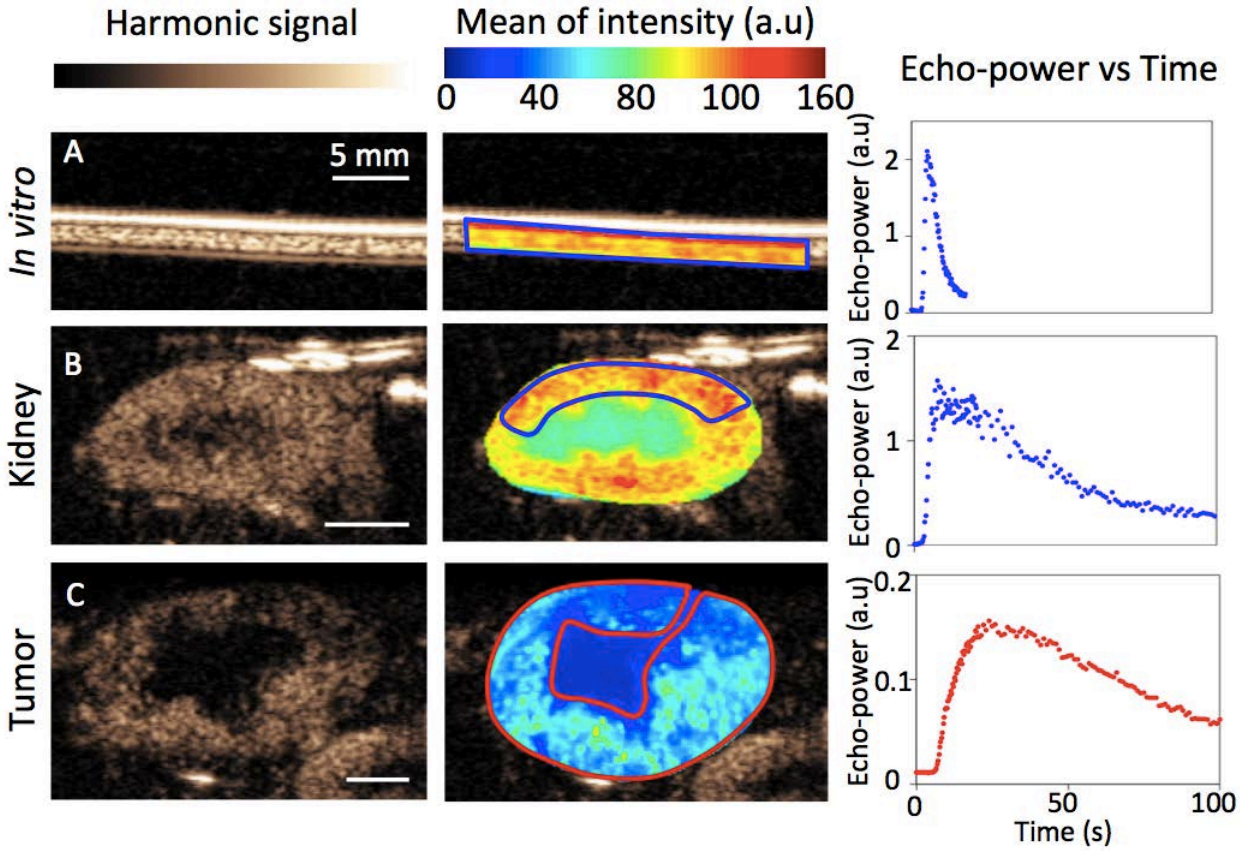

Figure 2: CEUS images for each group: *in vitro* (A), renal cortex (B) and tumor (C) with corresponding ROIs, mean of signal intensity maps and echo-power curves.

IV.3. Results

IV.3.1. Injection circuit impact on the microbubble population

The results from the SIOS measurements characterizing the effect of the injection mode on the number and size of microbubbles in the injected population are summarized in Table 1.

No significant difference was observed in terms of mean diameters and mode diameter (peak of the diameter distribution) after passage through the two different injection circuits. The polydispersity index (PDI), is equal to the ratio between d90 and d10 (d90 and d10 are the diameters superior to 90

and 10% of the distribution, respectively. The PDI was also similar for samples evaluated after passage through the two circuits. In addition, no modification of diameters and polydispersity was observed in comparison with the native solution measured under the same conditions (data not shown). It should be noted that the smaller mean diameter value (1.6 ± 0.1 µm) found with the qNano system for all measured microbubble suspensions in comparison with the reported by Schneider et al. (2.5 µm) may be attributed to measurement conditions.

SonoVue	Manual	Controlled
Mode diameter (µm)	1.30 ± 0.05	1.31 ± 0.07
Mean ± SD (µm)	1.55 ± 0.08	1.54 ± 0.06
Polydispersity index	1.6	1.6
Concentration (MB/mL)	3.6×10^8	3.0×10^8

Table 1: **Characteristics of the SonoVue microbubble** distribution for 1:10 solutions recuperated after passage through the manual and controlled injection systems. Measurements were made with the qNano device. The polydispersity index (PDI) is: $\mathrm{PDI} = \mathrm{d90/d10}$ where d90 and d10 are diameter values for which 90 and 10% of the distribution, respectively, has a diameter below these values.

The echo-power with noise subtraction measured as a function of dilution factor (dose-ranging) is plotted in Figure 3.

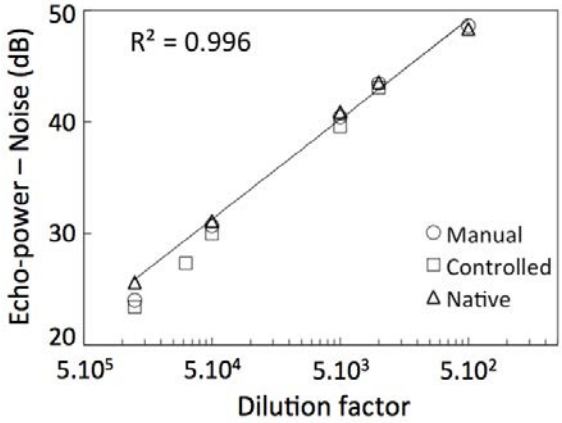

Figure 3: Echo-power estimates after noise subtraction as a function of the dilution factor for SonoVue. The line represents the linear relationship for suspensions of SonoVue directly removed from the vial (Native).

The linear relationship between echo-power and dilution found for native SonoVue is designated by the solid line (coefficient of determination $R^2 > 0.995$). The measured values of echo-power are shown for solutions recuperated after passage through the manual or controlled injection circuits. The echo-power decreased by 3.4 ± 2.1 % and 5.6 ± 2.7 % on average after manual and controlled injections, respectively, but this decrease was not significant.

IV.3.2. *In vitro* reproducibility

To evaluate the variability between injections, CV values were calculated for flow parameters estimated from echo-power curves according to the lognormal model. Results for 10 repeated manual and controlled injections are presented in Figure 4. Controlled injection significantly reduced the inter-injection variability of TTP (Fisher's test, $p<0.05$), WIR ($p<0.0005$) and WOR ($p<0.0005$)

parameters as compared to manual injections. The CV was lower than 15% for measurements of MTT, TTP and AUC with controlled injection and, for the same parameters, was greater than 15% for manual injections. Estimations of the PE demonstrated very similar CV regardless of which type of the 2 injection circuits was used.

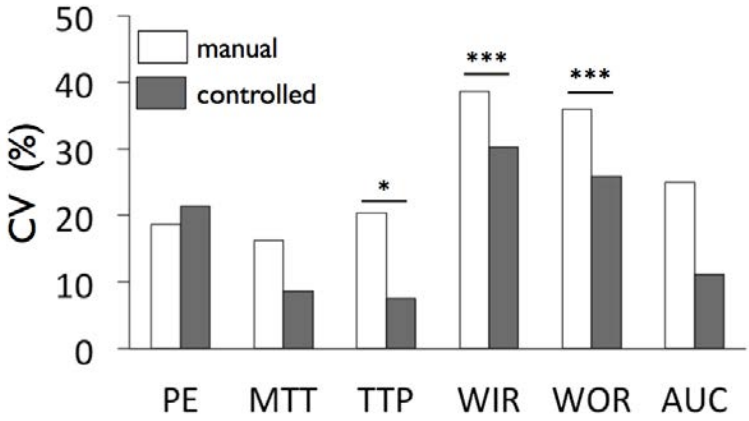

Figure 4: *In vitro* data comparing inter-injection variability, % CV of the perfusion parameters calculated for controlled (N = 10) and manual injections (N = 10). Fisher test, threshold of significance: * = p<0.05, ** = p<0.005, *** = p<0.0005.

IV.3.3. Reproducibility in the renal cortex and ectopic tumor*, in vivo*

For each set of 4 consecutive injections in the same mouse, the CV was estimated for each perfusion parameter. Results are summarized in Figure 5 (N=6 for kidney, N=5 for tumor). Two-tailed Student's t-test and Fisher's test were performed respectively to reveal significant differences between mean values and variances.

Results for measurements in the renal cortex reveal that controlled injections significantly improved reproducibility of perfusion parameter assessment for the same group of parameters as for the *in vitro* flow phantom. For these parameters (TTP, WIR, WOR), reproducibility was improved by a factor of 2 to 3 with the highest improvement for the WIR parameter (C = 18.6 ± 8.0 % vs. M = 46.7 ± 19.2 %, P_S = 0.02). For the PE and AUC parameters, the mean CV was not significantly different between manual and controlled injections but the variance of the inter-subject distribution of CV values was significantly reduced for controlled injections (PE: P_F = 0.0095, AUC: P_F = 0.0013). Low variance for a set of CV values indicates that the parameter is estimated with the same accuracy for each subject.

Except for a slight significant decrease in the CV of the MTT estimations in ectopic tumors, functional parameter assessment in the tumors did not benefit significantly from controlled injections as compared to manual ones. For both tumor and renal cortex assessments, the CV was lowest for MTT and TTP parameters with mean CV values ranging from 4.1 ± 1.1 % to 18.3 ± 6.7%.

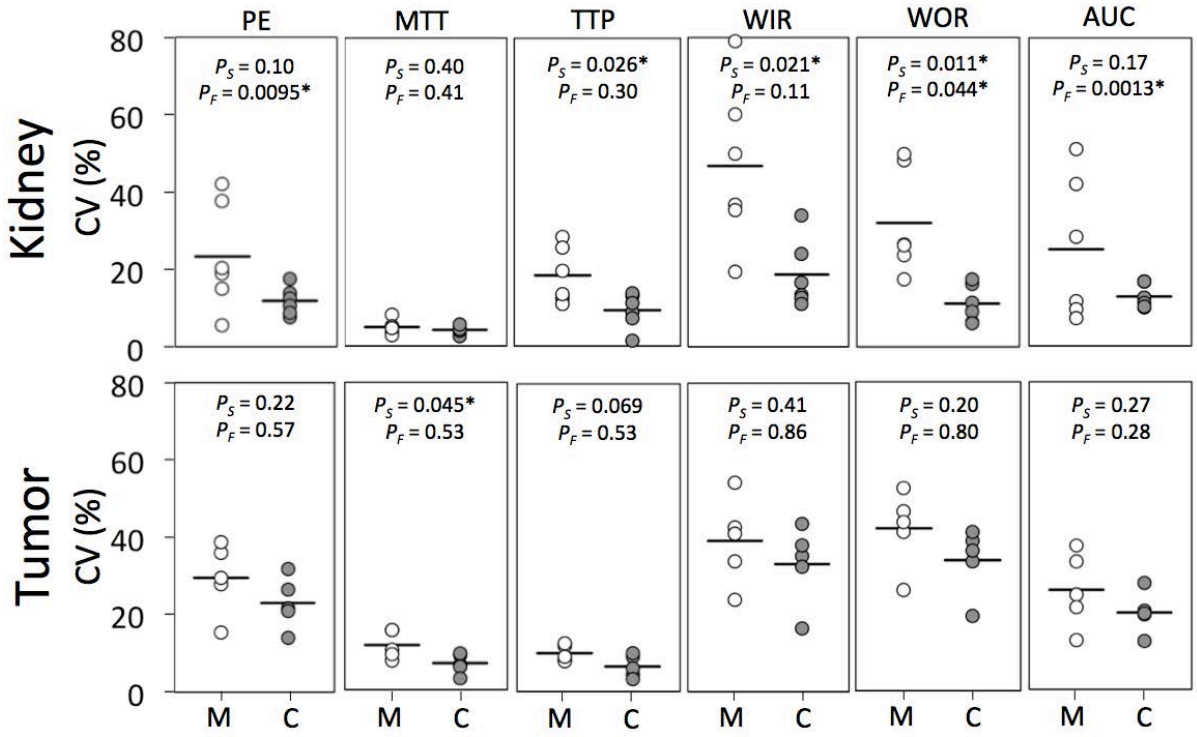

Figure 5: Inter-injection variability assessment based on the distribution of CV values for perfusion parameters estimated in the renal cortex and ectopic CT26 tumors. M (white circles) and C (grey circles) correspond, respectively, to manual and controlled injections. P_S is the p-value of the two-tailed student's test (comparison of mean values designated by horizontal lines) and P_F is the p-value of the Fisher's test (comparison of the variance between the two distribution's of CV values). The P-values, P_S and P_F, indicated on the top of each panel allow identification of differences that are significant between controlled and manual injections (marked with an asterisk). Student and Fisher's test threshold of significance: * = p<0.05, ** = p<0.005, *** = p<0.0005.

IV.4. Discussion & conclusion

An UCA's concentration and size-distribution influence its acoustic properties (de Jong et al. 2002), its susceptibility to radiation force (Dayton et al. 2002) and its echogenicity (Groce et al. 2000). Arrival rate of the microbubbles in the zone to evaluate also significantly influences apparent PE and WIR (Palmowski et al. 2010). Because contrast agent injection procedures can potentially influence size, concentration and arrival rate of microbubbles leading to variability in ultrasound contrast measurements, a system for controlled injection of UCA in mice was implemented and tested both *in vitro* and *in vivo*. The system allows control over the most relevant parameters of the injection protocol (agent dose, volume of injection, speed of injection).

Bubble filtration is the main potential limitation of the controlled injection system. Talu et al. (2008) showed that injections through a 27G-needle may cause loss of lipid-shell PFC microbubbles (0.95 µm of mean diameter) at a concentration of 5×10^8 MB/mL. They demonstrated that, for rates higher than 6 mL/min, microbubble destruction occurred and the size distribution was shifted towards the smaller diameters. However, at 1.8 mL/min, they did not see any agent loss and the population distribution was only slightly shifted (~ 2 % change in mean diameter).

Scanning Ion Occlusion spectroscopy (SIOS) was used to estimate the overall impact on the microbubble population due to the injection through the three-way valve and catheters used in the controlled injection system relative to injection with the more direct syringe-to-tail catheter route. Dose-ranging experiments were performed to assess the relative impact of these two types of

injections on echo-power relative to the echo-power assessed for solutions of native agent that had not passed through either injection system. Dose ranging and SIOS experiments (Table 1 and Figure 3) showed that controlled injection through the system used in this study at a constant flow rate of 4.5 mL/min did not significantly modify the SonoVue MBs' size or acoustic response relative to manual injection.

Injected dose must be selected to avoid signal saturation or significant acoustic shadowing effects within the evaluated tissue. In the work by Gauthier et al. (Gauthier et al. 2012c), the impact of the dose of SonoVue™ on perfusion parameter estimation was studied *in vitro* using images acquired at 3.4 MHz from a perfused dialyzer cartridge. An increase from 10 to 50 µL of the native solution resulted in an increase of 64% for the PE and 95% for the AUC calculated on a 1-minute clip acquired during injection. Stapleton et al. (Stapleton et al. 2009) studied the dose-dependency of PE, MTT and AUC in the jugular vein of mice after injection of Definity via the tail vein. PE and AUC were shown to vary linearly with the dose within a range from 10 to 60 µL/kg of Definity (4 and 9 times approximate increase across this range, respectively). The dose-dependent trend was less clear for MTT (slight increases were observed within the 10-30 µL/kg range).

A typical 1-mL syringe only has a precision of 10 µL (one graduation) which can lead to very significant variability in the injected dose of UCA when performing preclinical studies in the small animal. Indeed, while the blood volume in an adult male human is approximately 5 L for injected volumes of contrast agent ranging from 0.5 to 4.8 mL which is on the order of 0.9 % v/v (for the four approved contrast agents: SonoVue™, Optison, Sonazoid and Definity), the blood volume of a 50 g mouse is approximately 3 mL for injected contrast volumes on the order of 10 to 50 µL (≈ 1 % v/v). Small errors in the dose can thus dramatically modify the relative microbubble concentration in the blood, and if injected dose is not precisely controlled, it is very difficult to sensitively monitor therapeutic effect and validate CEUS techniques for clinical transfer. In this work, for both manual and controlled injections, the contrast agent dose was precisely controlled using a 100 µL Hamilton syringe (precision of ± 2 µL). The 40 µL dose was selected because it provided a strong signal in the tube without reaching saturation or significant acoustic shadowing effects. The dose of 500 µL/kg of SonoVue in mice was found to give optimal signal enhancement for renal cortex imaging with our settings. This dose also allowed control of the total injected volume to remain within the range that can be safely injected intravenously in an adult mouse according to veterinary recommendations ($V_{injected}$ < 10 mL/kg).

Only controlled injections, however, allowed injection at a constant rate (4.5 mL/min). This rate was selected such that the 80 µL contrast bolus was injected in 1 s which was on the order of the time taken for manual injection of the bolus. Care was also taken to use the same type of tubing (Tygon S54HL, ThermoFischer, internal diameter 0.8 mm) throughout the system to limit flow turbulence that could be caused by abrupt variations in the diameter of the flow channel. For the 0.8-mm diameter tube used in this work and the 4.5 mL/min flow speed, the Reynolds number can be calculated according to:

$$Re = \frac{Lv}{\upsilon} = \frac{D \times v_{flush}}{\upsilon_{RT}} \sim \frac{0.8 \times 10^{-3} \times 1.5 \times 10^{-1}}{0.884 \cdot 10^{-6}} \sim 140 \qquad \text{(IV.1)}$$

where L is the characteristic length which is the diameter D (in m) in the case of a circular tube, v_{flush} (in m/s) is the speed of the flow, and υ_{RT} (in m²/s) is the fluid's kinematic viscosity at room

temperature ($\upsilon_{RT} = \mu/\rho$, where μ is the dynamic viscosity and ρ the density of 0.9% NaCl). This Reynolds number is well beneath the value 2300 associated with transition toward turbulent flow. Significant improvement of the reproducibility was observed for TTP, WIR and WOR parameters estimation in the *in vitro* flow phantom and the renal cortex. The CV values were also significantly less variable between mice for PE and AUC parameters. The CVs were less than 19 and 34 % for all parameters assessed in renal cortex and in tumor, respectively.

Results for estimation of the CV *in vivo* in the renal cortex are summarized in Table 2. Controlled injections strongly reduce variability for all perfusion parameters with CV values ranging from 4.1% to 18.6%.

	Injection	PE	MTT	TTP	WIR	WOR	AUC
CV %	**Manual**	23.2 ± 12.7	4.9 ± 1.7	18.3 ± 6.7	43.1 ± 16.9	32.0 ± 12.4	25.0 ± 17.0
	Controlled	11.8 ± 3.3*	4.1 ± 1.1	9.2* ± 4.1	18.6* ± 8.0	11.2* ± 4.5*	12.8 ± 2.8*

Table 2: CV values for functional parameters assessed in the renal cortex after 4 consecutive tail-vein injections in mice (N=6). Results are indicated as mean ± SD; a sign on mean value and standard deviation indicates respectively significant differences between mean value (Student's t-test) and variance (Fisher's test).

Although the CV value for MTT and TTP remained less than 12 % when measurements were made in ectopic tumor, only the MTT demonstrated a significantly reduced CV for controlled injections relative to manual ones. To better understand this result, the average parameters found after each consecutive controlled injection in tumor and adjacent renal cortex are presented in Figure 6. To enable comparison between the different contrast enhancement parameters, for each mouse and each parameter, data were normalized with respect to the maximum value for each mouse. Then, the normalized values were averaged over the ten mice from each group of injections (controlled and manual).

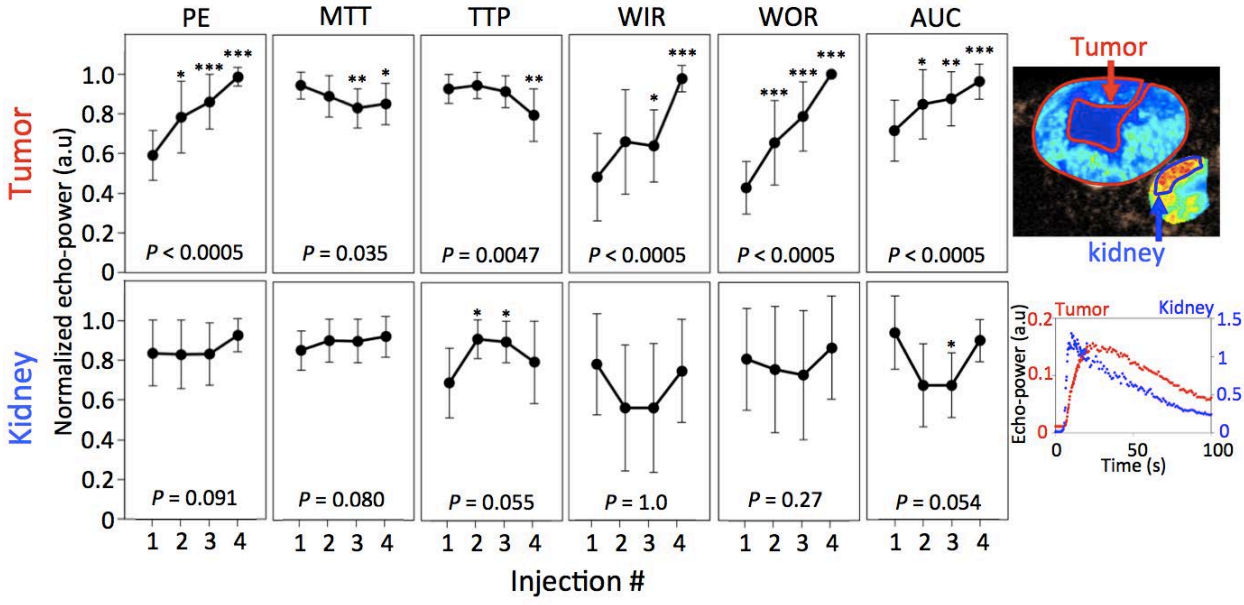

Figure 6: Effect of four consecutive, controlled injections (40 µL of SonoVue) evaluated simultaneously in tumor and renal cortex (same imaging plan). For this set of measurements only, measurements were obtained in both the tumor and the adjacent kidney cortex. A Wilcoxon signed rank test was performed between the first injection and the 3 others (threshold of significance: * = p<0.05, ** = p<0.005, *** = p<0.0005). P-values indicated at the bottom of each graph are related to the comparison between the first and the last UCA injection.

Our work has focused on improved reproducibility using controlled injections. Gauthier et al. (2012a) described the possibility to improve reproducibility in the assessment of perfusion parameters using deconvolution based on the characterization of the arterial input function (AIF). Results were compared for three, consecutive manual bolus injections of 100 µL of SonoVue^{TM} in five mice bearing B16F10 melanoma xenografts, CVs of PE, TTP, WIR and AUC_{180sec} without correction for the AIF ranged from 4-28%, 6-23%, 10-29% and 6-28%, respectively. By correcting for the AIF, the CVs of PE and AUC_{180sec} were reduced to 7-12% and 6-12% respectively. A limitation of such AIF deconvolution is described by Gauthier and co-workers (2012b). They showed that when the size of the ROI used to evaluate the AIF was varied by a factor 3 (1.17 mm^2 versus 3.65 mm^2) the estimated flow parameters were modified significantly: PE (p-ANOVA < 0.027), TTP (p-ANOVA < 0.01) and MTT (p-ANOVA < 0.001).

A significant source of variability in our measurements in the tumor was observed as a result of consecutive injections. All parameters assessed in the tumor underwent significant, systematic variation between the first and the fourth UCA injection whereas no significant variation was observed in the kidney for the same injection series. The highest variations between the first and last injection were observed for the WIR (p<0.0005) and WOR (p<0.0005) parameters with an increase of the mean value by a factor of 2 (0.48±0.23 a.u to 0.98±0.07 a.u) and 2.5 (0.43±0.14 a.u to 0.99±0.01 a.u), respectively. Values of PE and AUC parameters increased respectively by 67% and 35%, whereas, values of TTP and MTT parameters decreased slightly by 14% and 10%.

The 15-minute delay between injections is sufficient for elimination of freely circulating SonoVue microbubbles (Schneider 1999a). It is well established that tumor vasculature is poorly efficient because of its tortuosity, leakiness and high interstitial fluid pressure (Heldin et al. 2004; Weis and Cheresh 2011). Such poor efficiency was shown by the significantly higher average TTP (comparison for the 1st injection, student test, p<0.00001, N=10) in tumor (25.7 ± 5.7 seconds) as compared to the renal cortex (13.0 ± 4.3 seconds).

Furthermore, after four consecutive UCA injections WIR and WOR parameters increased significantly (Wilcoxon test, p<0.0005) which implies that UCA entered and emptied the tumors microvascularization faster for the fourth injection than for the first. Between the first and fourth injections, PE and AUC parameters also increased significantly, indicating that the tumor's microvascularization presents greater filling for subsequent injections. Reduced TTP and MTT imply that microbubbles reside for a shorter time in the tumor vasculature which is consistent with observed increases of WIR and WOR parameters. These flow parameter modifications suggest that CEUS in the tumor microvascularization may have modified the microvascular hemodynamics over a significant period (15 minutes between injections). Similar effects have been reported by Skrok et al. (2007). After performing two consecutive injections of UCA in healthy human liver with a delay of 12 min, they observed a 5 ± 1.5 dB increase in peak intensity. They hypothesized that the increase in intensity was caused by saturation of pulmonary macrophages by the first injection, leading to increased signal from the second. William et al. (2011) performed two consecutive bolus injections of UCA in 32 patients with renal cell carcinoma and observed a decreased PE in 72% of cases and an increase in the 28% others. No order of variation was indicated in their study. For the current work, the practical consequence of these systematic modifications is that any potential improvement in CEUS parameter assessment obtained by controlled injection remained undetectable due to the other, possibly physiological, modifications occurring between injections. This effect may be tumor-model dependent. For example, following multiple UCA injections (Sonovue^{TM}) in tumor-bearing

mice (melanoma B16F10) Gauthier et al. (2012a) did not observe significant variations in the perfusion parameters estimated from consecutive injections.

Reported work considering the variability of CEUS parameter estimation using the Lognormal flow model *in vivo* has largely relied on least-squares (LS) fitting to adjust the model to the experimental data (T. P. Gauthier et al. 2011; Hudson et al. 2009; Rognin et al. 2010; Strouthos et al. 2010; Wei et al. 1998). Previous work (Barrois et al. 2013) demonstrated that the LS fitting method presents a lack of accuracy during the initial filling phase and developed a maximum likelihood method accounting for the multiplicative nature of the noise to better fit the flow model to the data. To investigate the level of improvement in the CV obtained in our work through the use of this improved fitting method, we compared CEUS parameters assessed in matched ROIs with the least squares (LS) and multiplicative model (MM) fitting methods. Figure 7-A shows example data sets and curve regression with the two different techniques. As underlined previously, (Barrois et al. 2013), the LS fitting method presents a lack of accuracy during the initial filling phase. This implies that compared to the MM, the LS fitting procedure is less sensitive to variations occurring during the initial phase of contrast enhancement. Comparison of parameter estimates made in normal renal cortex of 12 mice revealed a significant improvement of both reproducibility and accuracy for the assessment of MTT (CV = 4.1 ± 1.1 %, P_S = 0.036 and P_F < 0.005) and WOR parameters (CV = 11.2 ± 4.5 %, P_S = 0.006 and P_F < 0.05) compared to LS procedure (CV = 17.9 ± 10.9% and CV = 34,7 ± 12.2 %, respectively) (Figure 7-B).

Enhanced reproducibility of CEUS is required for its widespread clinical and pre-clinical use (Hyvelin et al. 2013). In 1993, Mudra et al. (Mudra et al. 1993) performed 107 intracoronary injections of Ultravist® (iopromid) contrast agent in 18 patients. The inter-injection variability was estimated based on three parameters extracted from time-intensity curves: PE, contrast decay half time, and AUC.

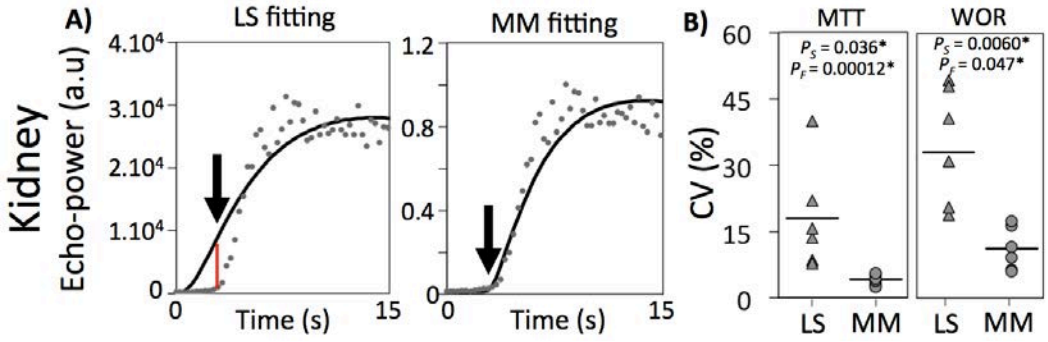

Figure 7: A) Fitting comparison demonstrating agreement during the initial rise for least squares (LS) and multiplicative fitting models (MM). B) Assessment of model fitting variability based on the distribution of CV values (white circle) for perfusion parameters estimated in the renal cortex with least squares (LS, grey triangle) and multiplicative (MM, grey circles) fitting models. Asterisks indicate significance of difference. P_S and P_F are p-value related to Student's t-test and Fisher's test, respectively. Threshold of significance: * = p<0.05, ** = p<0.005, *** = p<0.0005.

They showed that the mean percent error between injections ranged from 24 to 34 %. More recently, measurements were compared from four bolus injections (0.2 mL of Definity) per patient on 5 patients (Williams et al. 2011). The PE in the brachial artery demonstrated an average CV of 27 %. For the AUC, the mean CV was 29 %, and MTT showed an average CV of 40 %. In mice, Stapleton et al. (2009) studied the inter-injection variability (manual injections) by imaging five Definity bolus passages in the jugular vein at 30 MHz. The CVs of PE and AUC were found to be 10 and 34 %, respectively. Differences in the studied organ, the frequency of the ultrasonic probe or the contrast

agent used confound precise comparison of our results with such previous reports. Nevertheless, CVs obtained in the current work in renal cortex using the implemented controlled injection and a MM fitting procedure (11.8 ± 3.3 % and 12.8 ± 2.8 % for PE and AUC, respectively) demonstrate the potential to obtain more robust estimation of perfusion parameters.

The results of the current study demonstrate that the use of controlled injections greatly enhances the reproducibility of perfusion parameters compared to manual injection. Integration of these improvements should provide better precision and sensitivity to effects of therapy in preclinical studies using CEUS imaging.

Acknowledgments

The authors would like to acknowledge Bracco Suisse SA for their help in the implementation of the controlled injection system.

The authors also thank the CEF (Centre d'Explorations Fonctionnelles, Cordeliers' Research Center) for their technical support and help with animals care.

We gratefully acknowledge support from the French research program Plan Cancer 2009-2013 (project NABUCCO) and the Fondation Recheche Médicale (Recherche soutenue par le FRM DBS20131128436). This work was partly funded by the French program "Investissement d'Avenir" run by the 'Agence Nationale pour la Recherche'; grant 'Infrastructure d'avenir en Biologie Santé – ANR-11-INBS-0006.

IV.5. References

Astafyeva K, Somaglino L, Desgranges S, Berti R, Patinote C, Langevin D, Lazeyras F, Salomir R, Polidori a., Contino-Pépin C, Urbach W, Taulier N. Perfluorocarbon nanodroplets stabilized by fluorinated surfactants: characterization and potentiality as theranostic agents. J Mater Chem B 2015;

Barrack T, Stride E. Microbubble destruction during intravenous administration: a preliminary study. Ultrasound Med Biol 2009;35:515–22.

Barrois G, Coron A, Payen T, Dizeux A, Bridal L. A Multiplicative Model for Improving Microvascular Flow Estimation in Dynamic Theory and Experimental Validation. IEEE Trans Ultrason Ferroelectr Freq Control 2013;60:2284–2294.

Blankstein R, Shturman LD, Rogers IS, Rocha-Filho J a, Okada DR, Sarwar A, Soni A V, Bezerra H, Ghoshhajra BB, Petranovic M, Loureiro R, Feuchtner G, Gewirtz H, Hoffmann U, Mamuya WS, Brady TJ, Cury RC. Adenosine-induced stress myocardial perfusion imaging using dual-source cardiac computed tomography. J Am Coll Cardiol Elsevier Inc., 2009;54:1072–84.

Chung AS, Lee J, Ferrara N. Targeting the tumour vasculature: insights from physiological angiogenesis. Nat Rev Cancer 2010;10:505–14.

Dayton PA, Allen JS, Ferrara KW. The magnitude of radiation force on ultrasound contrast agents. J Acoust Soc Am 2002;112:2183–92.

De Jong N, Bouakaz A, Frinking P. Basic acoustic properties of microbubbles. Echocardiography 2002;19:229–40.

Dietrich C, Averkiou M, Correas J, Lassau N, Leen E, Piscaglia F. An EFSUMB Introduction into Dynamic Contrast-Enhanced Ultrasound (DCE-US) for Quantification of Tumour Perfusion. Ultraschall der Medizin 2012;33:344–351.

Folkman J. Angiogenesis in cancer, vascular, rheumatoid and other disease. Nat Methods 1995;1:27–31.

Gauthier M, Pitre-Champagnat S, Tabarout F, Leguerney I, Polrot M, Lassau N. Impact of the arterial input function on microvascularization parameter measurements using dynamic contrast-enhanced ultrasonography. World J Radiol 2012a;4:291.

Gauthier M, Tabarout F, Leguerney I, Polrot M, Pitre S, Peronneau P, Lassau N. Assessment of Quantitative Perfusion Parameters by Dynamic Contrast- Enhanced Sonography Using a. J Ultrasound Med 2012b;31:595–608.

Gauthier TP, Averkiou MA, Leen E. Perfusion quantification using dynamic contrast-enhanced ultrasound: The impact of dynamic range and gain on time-intensity curves. Ultrasonics 2011;51:102–106.

Gauthier TP, Chebil M, Peronneau P, Lassau N. In vitro evaluation of the impact of ultrasound scanner settings and contrast bolus volume on time-intensity curves. Ultrasonics Elsevier B.V., 2012c;52:12–19.

Groce J-M, Arditi M, Schneider M. Influence of Bubble Size Distribution on the Echogenicity of Ultrasound Contrast Agents: A Study of SonoVue. Invest Radiol 2000;35:661–671.

Guibal A, Taillade L, Mulé S, Comperat E, Badachi Y, Golmard J-L, Rixe O, Bridal SL, Lucidarme O. Noninvasive Contrast-enhanced US Quantitative Assessment of Tumor Microcirculation in a Murine Model: Effect of Discontinuing Anti-VEGF Therapy. Radiology 2010;254:420–429.

Heldin C-H, Rubin K, Pietras K, Ostman A. High interstitial fluid pressure - an obstacle in cancer therapy. Nat Rev Cancer 2004;4:806–13.

Helminger G, Yuan F, Dellian M, Jain RK. Interstitial pH and PO2 gradients in solid tumors in vivo: High-resolution measurments reveal a lack of correlation. Nature 1997;3:177–182.

Henriquez RR, Ito T, Sun L, Crooks RM. The resurgence of Coulter counting for analyzing nanoscale objects. Analyst 2004;129:478–82.

Hudson JM, Karshafian R, Burns PN. Quantification of flow using ultrasound and microbubbles: a disruption replenishment model based on physical principles. Ultrasound Med Biol 2009;35:2007–20.

Hyvelin J, Tardy I, Arbogast C, Costa M, Emmel P, Helbert A, Theraulaz M, Nunn A, Tranquart F. Use of Ultrasound Contrast Agent Microbubbles in Preclinical Research. Invest Radiol 2013;48:570–583.

Lamuraglia M, Bridal SL, Santin M, Izzi G, Rixe O, Paradiso A, Lucidarme O. Clinical relevance of contrast-enhanced ultrasound in monitoring anti-angiogenic therapy of cancer: current status and perspectives. Crit Rev Oncol Hematol 2010;73:202–12.

Leen E, Averkiou M, Arditi M, Burns P, Bokor D, Gauthier T, Kono Y, Lucidarme O. Dynamic contrast enhanced ultrasound assessment of the vascular effects of novel therapeutics in early stage trials. Eur Radiol 2012;22:1442–50.

Milia a. F, Gross V, Plehm R, De Silva J a., Bader M, Luft FC. Normal Blood Pressure and Renal Function in Mice Lacking the Bradykinin B2 Receptor. Hypertension 2001;37:1473–1479.

Mudra H, Klauss V, Meissner O, Metz J, Zwehl W, Theisen K. Reproducibility of myocardial contrast echocardiography in human studies. Echocardiography 1993;10:255–63.

Palmowski M, Lederle W, Gaetjens J, Socher M, Hauff P, Bzyl J, Semmler W, Günther RW, Kiessling F. Comparison of conventional time-intensity curves vs. maximum intensity over time for post-processing of dynamic contrast-enhanced ultrasound. Eur J Radiol 2010;75:149–153.

Payen T, Coron A, Lamuraglia M, Le Guillou-Buffello D, Gaud E, Arditi M, Lucidarme O, Bridal SL. Echo-power estimation from log-compressed video data in dynamic contrast-enhanced ultrasound imaging. Ultrasound Med Biol 2013;39:1826–37.

Piscaglia F, Nolsøe C, Dietrich CF, Cosgrove DO, Gilja OH, Bachmann Nielsen M, Albrecht T, Barozzi L, Bertolotto M, Catalano O, Claudon M, Clevert D a., Correas JM, Donofrio M, Drudi FM, Eyding J, Giovannini M, Hocke M, Ignee a., Jung EM, Klauser a. S, Lassau N, Leen E, Mathis G, Saftoiu a., Seidel G, Sidhu PS, Haar G Ter, Timmerman D, Weskott HP. The EFSUMB guidelines and recommendations on the clinical practice of contrast enhanced ultrasound (CEUS): Update 2011 on non-hepatic applications. Ultraschall der Medizin 2012;33:33–59.

Quaia E. Microbubble ultrasound contrast agents: an update. Eur Radiol 2007;17:1995–2008.

Rognin N., Arditi M, Mercier L, Frinking PJA, Schneider M, Perrenoud G, Anaye A, Meuwly J, Tranquart F. Parametric imaging for characterizing focal liver lesions in contrast-enhanced ultrasound. IEEE Trans Ultrason Ferroelectr Freq Control 2010;57:2503–11.

Schneider M. Characteristics of SonoVuetrade mark. Echocardiography 1999a;16:743–746.

Schneider M. SonoVue, a new ultrasound contrast agent. Eur Radiol 1999b;9:347–348.

Skrok J. Markedly increased signal enhancement after the second injection of SonoVue® compared to the first—a quantitative normal volunteer study. 12th Eur Symp Ultrasound Contrast Imaging 2007;Rotterdam.

Stapleton S, Goodman H, Zhou Y-Q, Cherin E, Henkelman RM, Burns PN, Foster FS. Acoustic and kinetic behaviour of definity in mice exposed to high frequency ultrasound. Ultrasound Med Biol 2009;35:296–307.

Strouthos C, Lampaskis M, Sboros V, McNeilly A, Averkiou M. Indicator Dilution Models for the Quantification of Microvascular Blood Flow With Bolus Administration of Ultrasound Contrast Agents. IEEE Trans Ultrason Ferroelectr Freq Control 2010;57:1296–1310.

Talu E, Powell RL, Longo ML, Dayton P a. Needle size and injection rate impact microbubble contrast agent population. Ultrasound Med Biol 2008;34:1182–5.

Wei K, Jayaweera AR, Firoozan S, Linka A, Skyba DM, Kaul S. Quantification of myocardial blood flow with ultrasound- induced destruction of microbubbles administered as a constant venous infusion. Circulation 1998;97:473–483.

Weis SM, Cheresh D a. Tumor angiogenesis: molecular pathways and therapeutic targets. Nat Med Nature Publishing Group, 2011;17:1359–70.

Williams R, Hudson JM, Lloyd BA, Sureshkumar AR, Lueck G, Milot L, Atri M, Bjarnason GA, Burns PN. Dynamic Microbubble Contrast-enhanced US to Measure Tumor Response to Targeted Therapy : A Proposed Clinical Protocol with Results from Renal Cell Carcinoma Patients Receiving Antiangiogenic Therapy. Radiology 2011;260:581–590.

V. TUMOR TISSUE CHARACTERIZATION USING ULTRASOUND BASED-IMAGING

V. Tumor tissue characterization using ultrasound based-imaging

V.1. Introduction

Several imaging modalities allow *in vivo*, longitudinal follow-up of physiopathology arising from TME modifications. For example, leakiness and tortuosity of tumor blood vessels have a direct impact on the increase of interstitial fluid pressure (IFP) which can be monitored by DCE-MRI with a Gd-DTPA blood-pool agent (Hompland et al. 2012). IFP is an interesting parameter to monitor because high pressure can lower the effective concentration of therapeutic agents arriving inside tumors (Heldin et al. 2004). High IFP has also been shown to increase the potential dissemination of metastasis (Dadiani et al. 2006). Another consequence of the defective vascular and lymphatic network accompanied by the high metabolism of tumor cells is the increase of acidity in the TME because of the accumulation of carbonic acid that dissociates into bicarbonate and free protons (H^+). The *in vivo* follow-up of acidity variation can be performed using an imaging modality such as magnetic resonance spectroscopy detection of hyperpolarized bicarbonate (Gallagher et al. 2008) or fluorescent imaging to track probes releasing fluorochromes when exposed to variations of the pH (Zhao et al. 2014).

Among the many imaging techniques available to monitor modifications of the TME, ultrasound is of particular interest because it is a safe, bedside, and repeatable technique that offers a wide range of modalities. The functionality of blood vessels that feed the tumor can be assessed with contrast enhanced ultrasound (CEUS) by injecting and detecting intravascular microbubbles (MBs) made of a gas encapsulated by a layer of lipids or phospholipids (Dietrich et al. 2012; Guibal et al. 2010; Hyvelin et al. 2013; Leen et al. 2012). Targeted contrast-agent MBs can be used to perform molecular imaging and thus to assess *in vivo* the level of expression of endothelial cell receptors such as VEGFR-2 (Pysz et al. 2010). Structural modifications of the TME can affect the elastic properties of tumor tissues which can be monitored *in vivo* by generating shear waves and monitoring their propagation with ultrafast imaging (Tanter and Fink 2014). Finally, the underlying microstructure of tumor tissues can be evaluated using quantitative ultrasound (QUS) through calibrated spectral analysis of raw, radio-frequency ultrasonic echoes scattered from the tissue (Vlad et al. 2009).

The goal of this study was to evaluate the sensitivity and complementarity of contrast-enhanced ultrasound (CEUS) shear wave elastography (SWE) and quantitative ultrasound (QUS) to characterize modifications of the TME during therapy with a cytotoxic agent (cyclophosphamide) and an angiogenesis inhibitor (sunitinib, Sutent: SU11248) in ectopic, murine Lewis Lung Carcinoma (LLC) tumors. *In vivo* and *ex vivo* follow-up *of* TME modifications should provide a better understanding of how ultrasound imaging modalities reflect changes in the tumor produced by a cytotoxic drug (cyclophosphamide) vs. changes produced by an antiangiogenic drug (sunitinib).

V.2. Materials and methods

V.2.1. Tumor cell implantation and treatment

Animal studies were approved by the Charles Darwin ethical committee (ref: Ce5/2012/081). Lewis Lung Carcinoma (LLC) fragments (20-40 mm^3) were implanted in the right flank of 7-week-old female C57Bl/6J mice (Janvier Labs, St Berthevin, France). Surgery was performed under anesthesia with 2 % isoflurane and subcutaneous injection (pre and post operative) of buprenorphine analgesic

at a concentration of 0.05 mg/kg. The temperature of the animal was maintained during anesthesia using a thermostatic, heated support (Minerve, Esternay, France).

Six days after fragment implantation, the animals were randomized into three treatment groups receiving: sunitinib (SU11248, Sutent®, Pfizer, USA), an angiogenesis inhibitor that targets VEGF and PDGF receptor signaling (40mg/kg/day *per os*, n = 21); cyclophosphamide (C7397-1G, Sigma-Aldrich, France), an alkylating cytotoxic agent (150mg/kg injected *i.p.* for 3 days, n = 24) and placebo (100µL of PBS injected *i.p*. for 3 days, n = 24). All three types of imaging (SWE, QUS and CEUS) were repeated to follow tumor development for 13 days from the initiation of cytotoxic (N = 15), antiangiogenic (N = 16), and placebo (N = 18) therapy.

V.2.2. Shear Wave Elastography (SWE)

Stiffness measurements were carried out with a clinical ultrasound system (Aixplorer, SuperSonic Imagine) using an SL15-4 probe with 256 elements, a bandwidth of 4-15 MHz and a central frequency ~8 MHz. For each tumor, SWE data were acquired from 3 independent planes along both the longitudinal and transverse directions (6 SWE measurements per tumor). Data were acquired using penetration mode with a color scale ranging from 0 to 50 kPa, mean value and standard deviation of stiffness were assessed within a ROI from each imaging plane and then the average value of each parameter from the six independent planes was calculated (Figure 2.A).

Before the SWE acquisition, the tumor dimensions were assessed on B-mode images. Tumor volume was approximated using the ellipsoid formula $V = \frac{\pi}{6}abc$, where a is the length, b is the width and c is the thickness.

V.2.3. Quantitative Ultrasound (QUS)

Radio Frequency (RF) signals were acquired in two perpendicular planes (planes 1 and 4, Figure 2.D) with the same clinical ultrasound system and SL15-4 probe as used for SWE measurement. Probe settings were set on “research mode” with the emitted frequency at 11.25 MHz. Before performing RF data processing with the QUS estimator developed by the Bioacoustics Research Laboratory (BRL, University of Illinois, USA), it was necessary to acquire RF signals from a phantom whose physical properties, backscatter coefficient and attenuation, were calibrated. A phantom was purchased from the medical physics department of Madison University of Wisconsin and the attenuation coefficient was characterized by Ernest Madsen and his team. The backscatter coefficient, was characterized by Michael Oelze in the BRL. The calibrated characteristics of the phantom are summarized in Figure 1.

QUS parameters were mapped throughout each tumor by analyzing 1 x 1 mm blocks of data with a 75% overlap in the axial and lateral directions (Figure 2.C). The average backscattered power spectrum was calculated based on the Fourier transform (512 points) of the Hanning gated segments of RF data. This data was normalized with respect to the data from the corresponding region of the reference phantom and correction for attenuation in the propagation path was applied assuming that the attenuation and sound speed in the tumor were 0.4 dB/cm/MHz and 1540m/s respectively. Two QUS parameters were estimated based on the backscatter coefficient versus frequency: the effective scatterer diameter (ESD, µm) and effective acoustic concentration (EAC, dB/cm).

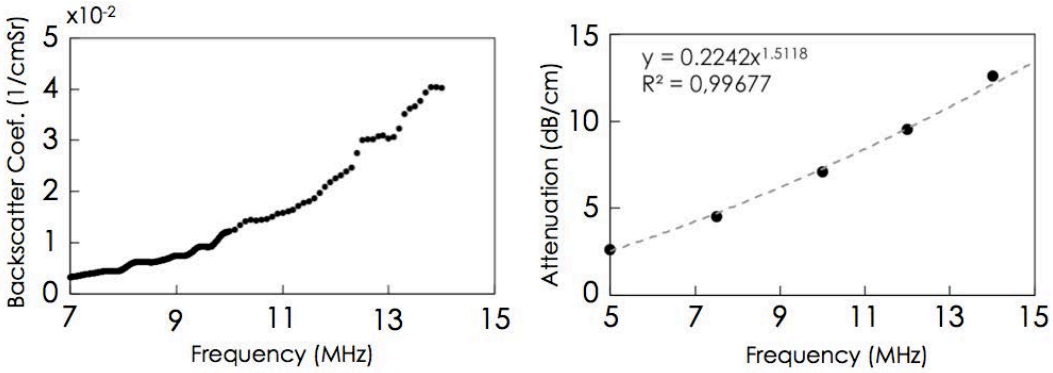

Figure 1: **Backscatter coefficient and attenuation** of the phantom used as a reference medium in this study to normalize backscattered signals acquired from tumors.

V.2.4. Contrast enhanced ultrasound (CEUS)

Contrast imaging was performed with a second clinical ultrasound system (Sequoia 512, Acuson; Siemens, Mountain view, USA) with a broadband 7-14 MHz transducer in cadence contrast pulse sequencing mode. Data were acquired with a dynamic range of 80 dB at a frame rate fixed at 1 Hz and MI equal to 0.1 to minimize destruction of microbubbles. Caudal vein injections (0.5 mL/kg in 40 µL) of the ultrasound contrast agent, SonoVue™ (Bracco Suisse SA, Geneva, Switzerland) were made using a controlled injection system. The image plane was positioned along the maximum longitudinal plane of the tumor (plane 4, Figure 2.D). Data were acquired from the instant before bolus injection up to 180 s after the injection. Average echo-power was initially measured in a region of interest including the total tumor cross-section. Regions with no contrast-enhancement () were then excluded and the echo-power from the perfused region was measured (Payen et al. 2013). A lognormal bolus model was fit to the resulting echo-power curve. Fits were made using a maximum likelihood estimator including the multiplicative nature of the noise that corrupts CEUS and Bmode images (Barrois et al. 2013). Several flow parameters were estimated (Figure 2.B): peak-enhancement (PE), mean transit time (MTT), time to peak (TTP), wash-in and washout rates (WIR, WOR) and area under the curve (AUC).

V.2.5. Immunohistochemistry

Two tumors per group were prepared for HES and Red Sirius staining to reveal necrosis and fibrosis, respectively, at Day 9 after the beginning of therapy. Remaining tumors that were not used for other analysis were prepared for histology at the end of therapeutic follow-up, on Day 13: angiogenesis inhibitor (n = 14), cytotoxic agent (n = 8) and placebo (n = 19). Blind evaluation of histological slides was made by a pathologist with 12 years of experience.

V.2.6. Statistics

All statistical tests and analysis were performed using R software (3.1.1). A Wilcoxon signed-rank non-parametric test (Mann-Witney *U* test) was used to compare the results between the different groups at each measurement date (unpaired test) and within each group between baseline

and the last day of follow-up (paired test). Differences between groups were considered significant at p-values of $p < 0.005$ (***), $0.005 < p < 0.01$ (**) and $0.01 < p < 0.05$ (*). Results for CEUS, SWE and QUS parameters are given as mean value ± standard deviation. The Spearman correlation test was carried out to assess the correlation between tumor volume and stiffness and to assess the correlation between percentage of unperfused area and the amount of necrosis and fibrosis. The data were visualized as boxplots showing the minimum, lower quartile, median, mean value (square), upper quartile and maximum values.

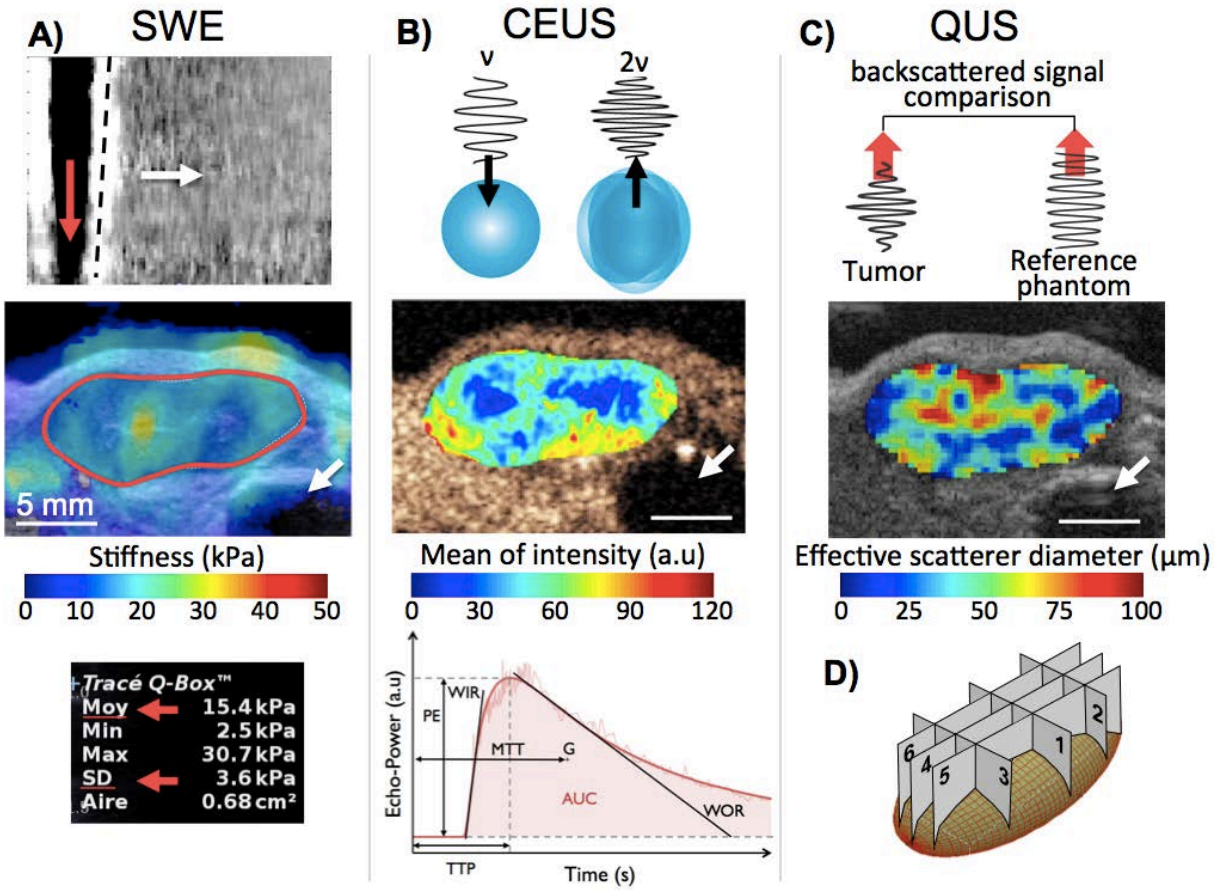

Figure 2: **Summary of the ultrasound imaging modalities**. **A)** By focusing ultrasound at different depths (push, red arrow) tissues oscillate and generate a shear wave (dash-line) that propagates transversally (white arrow) with respect to propagation direction of the imaging beam. The propagation speed of this wave, as assessed using ultrafast imaging, is directly related to stiffness of the medium in which it propagates. The mean and standard deviation of the shear wave elasticity (SWE) were quantified within ROIs selected on B-mode images to delineate the full cross section of the tumor. **B)** The echo-power from the non-linear response of the ultrasound contrast agent, SonoVue™, was analyzed as a function of time to map the functionality of the tumor microvasculature. **C)** The size of effective scatters in the tumor were estimated using quantitative ultrasound (QUS) by comparing the backscattered signal from the tumor with that from a reference phantom using estimation voxels of 1 by 1 mm. **D) Average** SWE was evaluated from the six planes, QUS was assessed and averaged from planes #1 and #4 and CEUS sequence was calculated from plane #4. White arrows indicate the position of the bladder in each image.

V.3. Results

Tumor volumes are summarized in Figure 3. From Day 3 after the beginning of therapy, tumor volume (20 ± 10mm^3) was significantly lower for the group treated with the cytotoxic agent as

compared to that receiving the angiogenesis inhibitor (42 ± 24mm^3, p=0.02) and the placebo (37 ± 16 mm^3, p=0.003). This difference was maintained throughout the follow-up to Day 13 (192 ± 253 mm^3) vs. the antiangiogenic group (635 ± 330 mm^3, p=0.0004) and the placebo group (882 ± 280 mm^3, p<0.005). The tumor volume for the group receiving placebo was not significantly higher than for that treated with the angiogenesis inhibitor (p=0.046) until Day 13.

SWE measurements are presented in Figure 4. From Day 7 after the beginning of therapy, tumor stiffness for the group receiving the angiogenesis inhibitor (14.1 ± 3.6 kPa) was significantly higher than for that receiving the cytotoxic agent (9.8 ± 2.8 kPa, p<0.005) and placebo (12.0 ± 2.4 kPa, p=0.002). Differences remained significant from Days 7 to 13 (antiangiogenic vs. cytotoxic, p=0.003; vs. placebo, p=0.002). From day 7 to day 13, tumors treated with the angiogenesis inhibitor exhibit a higher level of heterogeneity (day 13: 10.8 ± 2.4 kPa) compared to those receiving cytotoxic agent (3.6 ± 2.5 kPa, p < 0.0001) and placebo (3.6 ± 2.5 kPa, p = 0.00073).

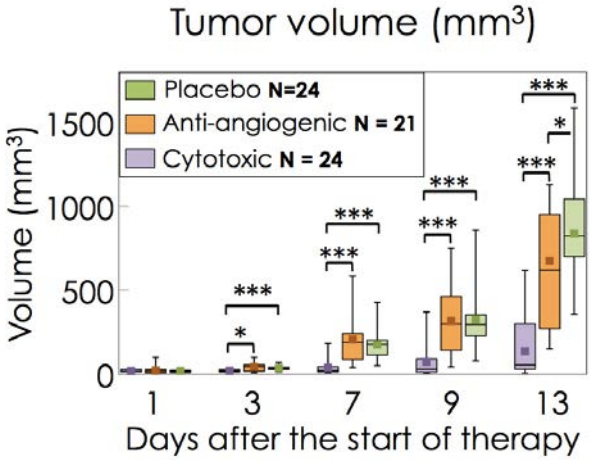

Figure 3: **Longitudinal follow-up of tumor volume** estimated for an ellipsoid with axes lengths equal to measurements made along the longitudinal, transversal and thickness of the tumor. Cytotoxic: N = 24; antiangiogenic: N = 21; Placebo: N=24.

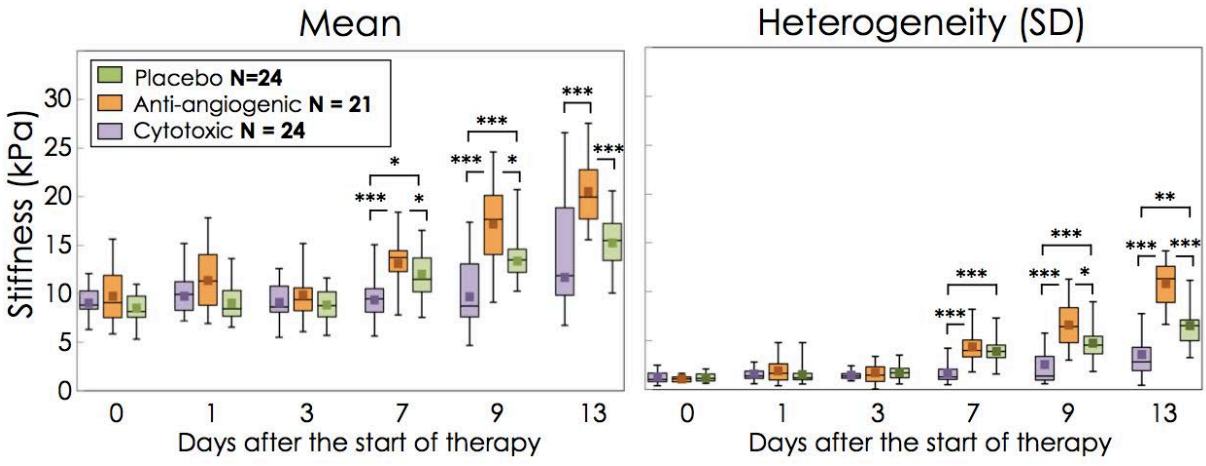

Figure 4: **Tumor stiffness assessed with SWE**. Six measurements were performed in six different planes for each tumor and averaged. Heterogeneity of the stiffness for each tumor was estimated based on the average standard deviation of the stiffness within the 6 ROIs. Cytotoxic: N = 24; antiangiogenic: N = 21; Placebo: N=24.

By plotting histograms for the ESD parameter (data not shown), it was apparent that a sub-set of the analysis blocks are thresholded at the lower limit set for the BSC estimator as selected in the calculation algorithm (0.5 µm). Parameter values corresponding to this estimator limit are

designated by white arrows in Figure 5. Because this sub-set of the pixels did not reflect tissue scattering properties, data blocks exhibiting an ESD parameter of 0.5 µm were excluded on the ESD and the corresponding EAC maps. After exclusion of these pixels, the average ESD and EAC were calculated within the ROI delineating the whole tumor.

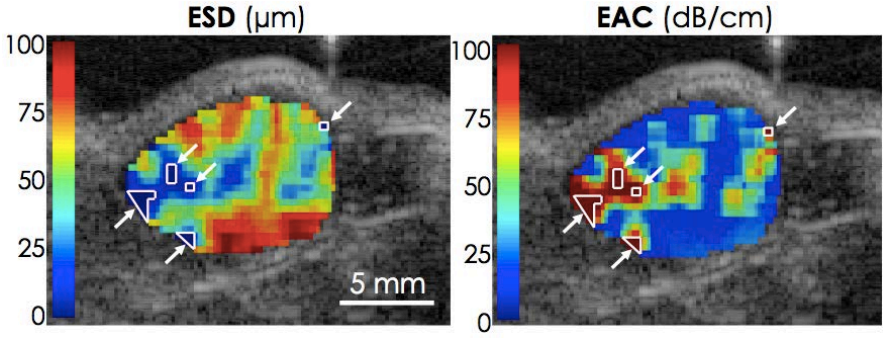

Figure 5: Diagram showing pixel clusters with a value of 0.5 µm (estimation threshold). These pixels were excluded from effective size diameter (ESD) and effective acoustic concentration (EAC) maps for the evaluation of the average parameter values. Individual data blocks: 1x1 mm.

Average QUS measurements at Day 13 are presented in Figure 6. The antiangiogenic group exhibited higher mean ESD (59 ± 6 µm) compared to the mean ESD of cytotoxic (52 ± 6 µm, p=0.015) and placebo groups (54 ± 6 µm, p=0.09). Similar mean EAC was found in all three groups. The percentage of excluded (estimation threshold) pixels for cytotoxic, antiangiogenic and placebo was, respectively, 40.5 ± 19.6 %, 29.2 ±12.4 % and 44.6 ± 12.9 % (mean ± SD).

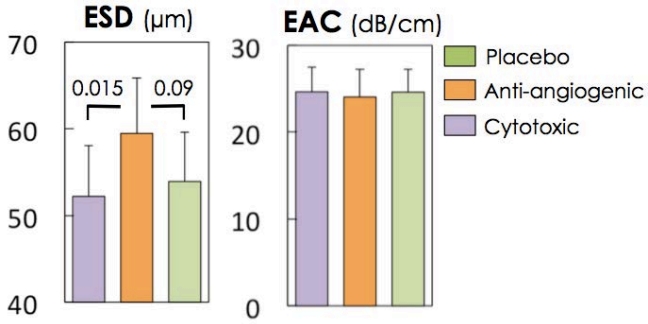

Figure 6: **ESD and EAC parameters measured by QUS at Day 13**. The antiangiogenic group has a higher mean ESD value as compared to the other groups but the threshold of significance was only reached for the comparison with cytotoxic group. The EAC was not significantly different between groups. The values indicated on the ESD graph correspond to the p-value for the Wilcoxon test.

Figure 7 summarizes the results from CEUS analysis of the tumor's microvascular function. The evolution of the percentage of unperfused area ($\mathrm{ROI}_{\mathrm{unperfused}}/\mathrm{ROI}_{\mathrm{tumor}}$) in tumor was significantly higher for the group treated with the angiogenesis inhibitor (3.1 ± 3.9 %) from Day 7 compared to those receiving the cytotoxic agent (0%, p=0.004) and the placebo (0%, p=0.004). The unperfused area in tumors treated with the angiogenesis inhibitor strongly increased at Day 13 (29 ± 21 %) and remained significantly higher compared to the cytotoxic agent (7.3 ± 15 %, p=0.004) and placebo (7.5 ± 13 %, p=0.002) groups.

Within the perfused area of the tumors, several functional parameters were significantly different between groups. The peak-enhancement, related to the blood volume, was significantly lower at day 13 for the angiogenesis inhibitor group (0.21 ± 0.12 a.u) compared to the cytotoxic agent (0.41 ± 0.22 a.u, p=0.00023) and placebo groups (0.28 ± 0.14 a.u, p=0.037).

From Days 7 to 9, the MTT parameter of the antiangiogenic group (MTT_{day7} = 32.3 ± 3.4 s; MTT_{day9} = 35.3 ± 5.8 s) was significantly higher than for the cytotoxic (MTT_{day7} = 29.1 ± 2.2 s, p=0.008; MTT_{day9} = 29.2 ± 3.1 s, p=0.002) and placebo (MTT_{day7} = 29.5 ± 3.3 s, p=0.03; MTT_{day9} = 31.6 ± 3.8 s, p=0.02) groups. For the last day of measurements the MTT in the cytotoxic group remained at a similar level (MTT_{day13} = 29.7 ± 3.9 s) compared to previous days and was significantly lower compared to that of both the antiangiogenic group (MTT_{day13} = 36.2 ± 4.9 s, p=0.0016) and the placebo groups (MTT_{day13} = 34.7 ± 5.3 s, p=0.0004).

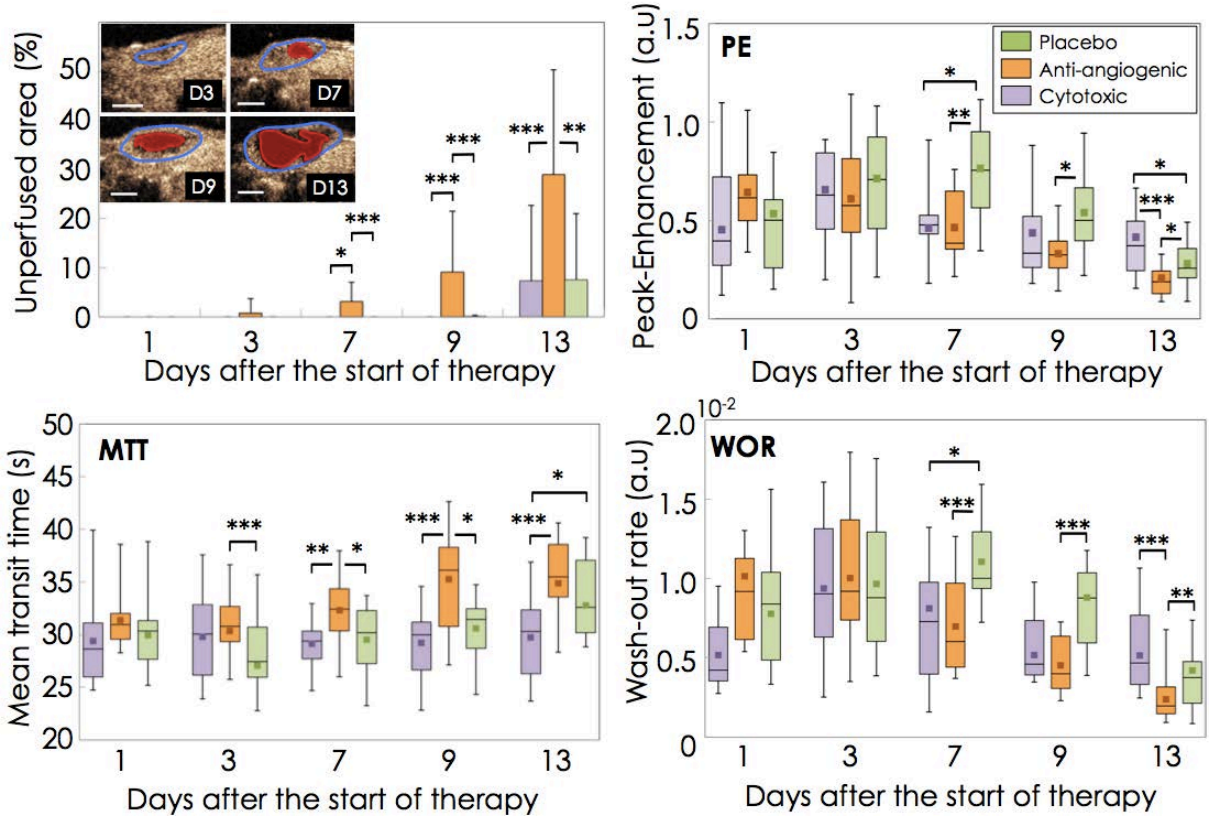

Figure 7: **Results of the follow-up performed in CEUS imaging**. Evolution of the unperfused area, peak-enhancement (PE), mean transit time (MTT) and wash out rate (WOR) are presented for cytotoxic (N=15), antiangiogenic (N=16) and placebo group (N=18).

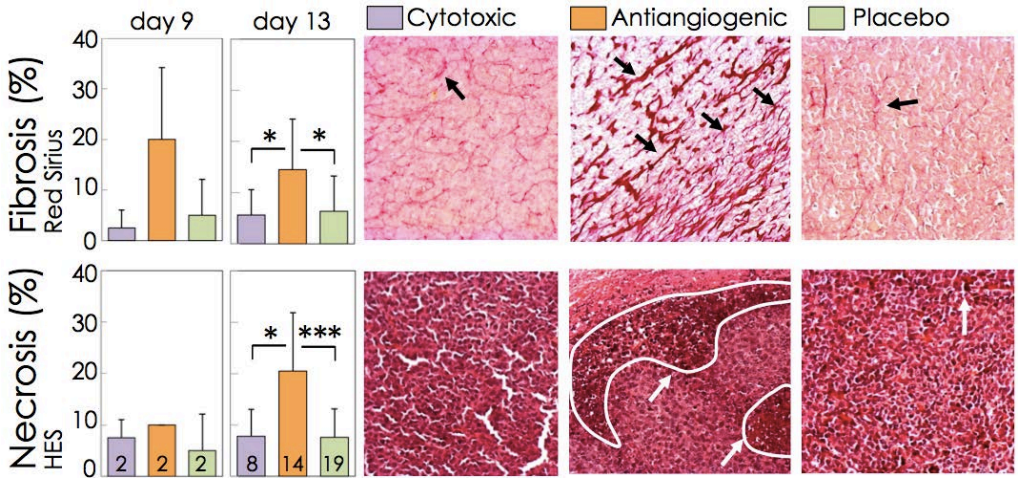

Figure 8: Fibrosis and necrosis as assessed from histology at Day 13 (cytotoxic: n=8, antiangiogenic: n=14, placebo: n=19) using, respectively, red Sirius and hematoxylin erythrosine saffron (HES) staining. White and black arrows designate necrotic and fibrotic areas respectively. Magnification x20.

Finally, the washout rate in tumors treated with the angiogenesis inhibitor decreased significantly at day 13 (0.0024 ± 0.0015 a.u) compared to cytotoxic agent (0.0052 ± 0.0023 a.u, $p<0.001$) and placebo (0.0042 ± 0.0025 a.u, $p=0.0093$).

The percentage of necrosis and fibrosis as assessed by a blinded pathologist on histological sectsions are presented in Figure 8. At Day 13, the level of necrosis and fibrosis, respectively, in the group treated with the angiogenesis inhibitor (n=14, HES = 20.5 ± 11.3 %; Sirius red = 14.5 ± 9.9 %) were significantly higher than for the cytotoxic agent (n=8, HES = 7.8 ± 5.3 %, p=0.01; Sirius red = 5.6 ± 5.0 %, p=0.04) and the placebo (n=19, HES = 7.6 ± 5.5 %, p=0.0004; Sirius red = 6.4 ± 6.9 %, p = 0.01) groups.

V.4. Discussion & Conclusion

Longitudinal follow-up of tumor modifications was performed *in vivo* using CEUS, SWE, QUS and *ex vivo* with immunohistochemistry to better understand how ultrasound imaging modalities reflect changes in the tumors produced by a cytotoxic drug (cyclophosphamide) vs. changes in the TME produced by an antiangiogenic drug (sunitinib).

V.4.1. Histology

Histological results were consistent with work of Bozkurt et al. (Bozkurt et al. 2011) who found a high level of fibrosis using sunitinib in an encapsulating peritoneal sclerosis model in rat. Findings are also supported by the study of Broutin et al. which used sunitinib on a xenograft tumor model of a medullary thyroid carcinoma and showed an increase of the level of necrosis and fibrosis by factors of 1.3 and 2.2, respectively, compared to untreated mice (Broutin et al. 2011). The development of necrotic tissues in tumor is principally due to ischemic processes that prevent oxygen from reaching tumor cells. The main macromolecules making up the ECM's three-dimensional meshwork are the fibrous proteins (collagen, elastin: structural role; fibronectin, laminin: adherence role) and polysaccharides (glycosaminoglycan, proteoglycans: retention of cytokine and growth factors). The ECM controls the physiological equilibrium of the medium by synthesizing and degrading the molecules that compose it. The development of fibrosis is linked to a rupture of this equilibrium by which the ECM increases synthesis of its constituents and at the same time decreases their degradation. The fact that sunitinib significantly increased the level of fibrosis and necrosis without strongly modifying the tumor volume is consistent with the antiangiogenic effect, not only on tumor cells but also on their microenvironment. This effect is expected to be due to the potent inhibition of angiogenesis by the tyrosine kinase inhibiting receptors such as VEGFR2, PDGFRa and PDGFRb. These results are corroborated by a study of Huang et al. in which they show that sunitinib inhibited renal cell carcinoma (RCC) xenograft growth mainly though antiangiogenic mechanisms and not through direct targeting of RCC tumor cells as no significant reduction of the tumor volume was observed (Huang et al. 2010).

V.4.2. Shear wave elastography and quantitative ultrasound

The high mean stiffness of tumors in the antiangiogenic group compared to the others found in our study (Figure 4, Days 9 and 13), seems to be associated with a higher proportion of fibrosis (Figure 8). These results can be compared with those in the study performed by Chamming's et al.

(2013) in which they used human invasive ductal carcinoma (HBCx-3) without any therapy to determine the relationship between SWE measurement in tumor and histological outcomes. They showed that there was a significant negative correlation between tumor stiffness and the percentage of necrosis (r=−0.76, p=0.0004) and a very significant positive correlation between tumor stiffness and the percentage of fibrosis (r=0.83, p<0.0001). These results suggest that necrotic and fibrotic tissues are related, respectively, to soft and stiff medium. We found the trend linking stiff tumor and fibrosis in our study with stiffest tumor for the group with the highest amount of fibrosis (antiangiogenic). The antiangiogenic group also exhibited the most heterogeneous mixture of necrosis and fibrosis. This heterogeneity was reflected *in vivo* by higher values in the SWE standard deviation (SD) across the tumor treated with sunitinib compared to others treatments (Figure 4.B at day 13).

Chamming's et al. also showed a strong correlation between the size of the tumor and its stiffness ($r = 0.94$, p<0.0001) which was explained, for their model, by higher fibrosis in the larger tumors. A similar relationship between size and stiffness was highlighted in our study in ectopic LLC tumors. SWE measurements from 280 tumors in mice (six measurements per tumor) receiving no therapy showed a significant correlation between SWE and tumor volume, $r = 0.80$ with *p-value*<0.005 (Figure 9).

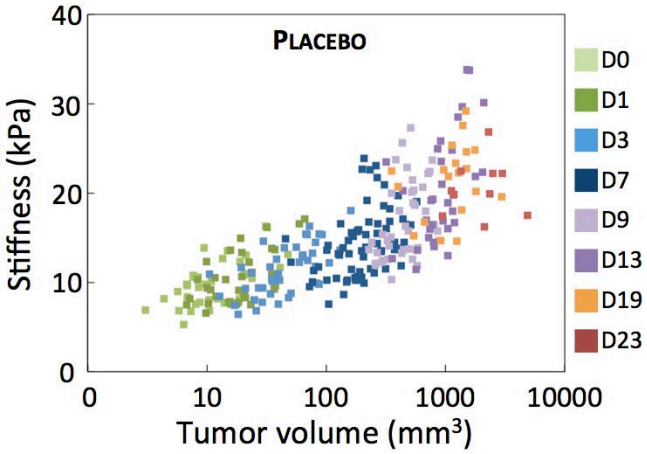

Figure 9: Correlation for placebo mice between stiffness and tumor volume (r = 0.80, p< 0.005, measurements from 280 tumors)

A similar study was performed by Jugé et al. (2012) to characterize the effect of an anti-vascular drug (combretastatin, CA4P at 100 mg/kg) on a colorectal carcinoma (CT26) using diffusion-weight (ADC) and elastography MRI. They showed a significant drop in tumor stiffness 24 h after treatment (6.6 ± 0.8 kPa to 4.8 ± 0.7 kPa, p = 0.0001). This drop in tumor stiffness was explained by authors to be the consequence of a significant reduction of the mean vessel density evaluated using CD31 staining to compare the vessel density in the viable area of the treated group to that in the control group (299 ± 37 [1/mm^2] vs 208 ± 66 [1/mm^2]; p = 0.03). A significant increase in cellularity was also observed in the treated group. Considering the work of Chamming's et al. (2013) in which they showed an inverse correlation between tissue stiffness and the level of necrosis, it could be argued that the drop in tumor stiffness observed in the work of Jugé et al. could also be attributed to the significant increase of necrosis from 7 ± 2 % to 43 ± 3 % observed 24 h after CA4P administration.

QUS imaging indicated that ESD could differentiate modifications in the antiangiogenic group as compared to changes in the two other therapy groups. The fact that the antiangiogenic group exhibited higher mean values for ESD seems consistent with histology presented in Figure 8. Indeed,

fibrosis was observed to form thicker fibrotic structures in the group treated with the antiangiogenic agent than in the other treatment groups.

V.4.3. Contrast enhanced ultrasound

CEUS imaging allowed assessment of the state of the vascular and microvascular network by measuring flow parameters after a bolus injection of contrast agent. Parameters such as PE and AUC are related to the blood volume whereas MTT, TTP, WOR and WIR parameters are directly related to the functionality of the vascular network. For each CEUS sequence, the ROI was limited to the part of the tumor cross section presenting contrast enhancement and functional parameters were estimated in this perfused ROI.

The blood volume (PE parameter) was significantly lower for tumors treated with sunitinib compared to cytotoxic and drug vehicle at Day 13 (Figure 7, PE). Several studies using different contrast imaging modalities exhibit the same trend for the decrease of blood volume in murine carcinoma treated with sunitinib (Battle et al. 2011; Matsumoto et al. 2011; Matsumoto et al. 2014; Needles et al. 2013).

Histological results at Day 13, revealed a high level of necrosis and fibrosis for tumors treated with the antiangiogenic drug compared to those treated with cytotoxic and drug vehicle (Figure 8). At the same time, during therapeutic follow-up, the percentage of unperfused area was significantly higher in the antiangiogenic group compared to the cytotoxic and placebo groups (Figure 7). The evolution of the unperfused area vs. the % necrosis was thus further evaluated based on correlations for 45 mice with *in vivo* and *ex vivo* measurements made on the same day. The unperfused area correlated much more strongly with the % necrosis (r = 0.74, $p < 0.005$) than with the fibrosis (r = 0.25, p = 0.13).

The functionality of the microvascular network that remained perfused at Day 13, was strongly affected by the antiangiogenic therapy (Figure 7). Values of MTT and WOR parameters were respectively the highest and the lowest for tumor treated with sunitinib indicating that the contrast agent stayed longer in the vasculature (high MTT) partly because vessels had difficulties to drain off (low WOR) the microbubbles. These results indicate that the microvascular network of tumor treated with sunitinib became significantly less efficient than those of tumor treated with cytotoxic and drug vehicle (placebo). Faivre *et al.* proposed a mechanism to explain the modification of tumor vasculature and the development of necrosis induced by sunitinib. In an established tumor, angiogenesis supplies cancer cells with oxygen, growth factors and nutrients. Exposure of the tumor to sunitinib alters endothelial cell shape and induces detachment of the endothelial cells from the substratum. Endothelial cell loss leads to blood-vessel congestion and reduced blood flow. As a result of the lack of oxygen, growth factors and nutrients, tumor necrosis ensues (Faivre et al. 2007). This mechanism of action is consistent with observations based on our histological results that show high levels of necrosis and fibrosis in the sunitinib group. It is also consistent with CEUS results demonstrating a strong reduction of vascularization in term of vascular distribution (unperfused area and PE, Figure 7) and functionality (MTT, WOR, WIR: Table 1, Figure 7).

V.4.4. Summary of changes in all the parameters considered

Table 1 summarizes the % variation of each measured parameter from the start to the end of therapy. During cytotoxic therapy, only the SWE was significantly modified. The increase of tumor

stiffness for the cytotoxic group was 3 to 4 times lower than that for other groups. Tumors treated with the antiangiogenic drug underwent the highest variations in parameters measured by SWE and CEUS between baseline and the end of the study. However, a similar level of SWE and CEUS modification was observed in the placebo group (Figure 3). The action of sunitinib which targets essentially the TME of tumor cells created a very heterogeneous pattern revealed by *in vivo* imaging in term of increased SD for the stiffness and vascular distribution parameters. This heterogeneity in the tumor composition was confirmed by histology outcomes.

		Cytotoxic		**Antiangiogenic**		**Placebo**	
		Var(%)	**P-value**	**Var(%)**	**P-value**	**Var(%)**	**P-value**
SWE	Mean (kPa)	20*	0.036	80*	2×10^{-5}	69*	6×10^{-6}
	SD (kPa)	130*	0.004	470*	6×10^{-4}	330*	5×10^{-4}
CEUS	PE (a.u)	-8.7	0.892	-68*	7×10^{-6}	-48*	2×10^{-3}
	WIR (a.u)	-39	0.162	-83*	8×10^{-7}	-78*	1×10^{-6}
	WOR (a.u)	-0.2	0.545	-76*	3×10^{-6}	-46*	7×10^{-4}
	MTT (s)	1.1	0.650	15*	4×10^{-3}	17*	3×10^{-3}

Table 1: **Variation between baseline and Day 13 of mean values of each parameter for each group**. $\mathrm{Var} = (\mathrm{MV_{D13}}/\mathrm{MV_{D1}} - 1) \times 100$ where $\mathrm{MV_{D13}}$ is the mean value of the parameter at Day 13 and $\mathrm{MV_{D1}}$ the mean value of the parameter at Day 1. * Indicates significant differences from Days 1 to 13, p-values were calculated using a Wilcoxon signed-rank paired test.

V.5.Conclusion

In summary, individual parameters are influenced by a relatively complex combination of underlying modifications in the tumor. Observing parameter modifications in specific tumor models allows the identification of changes in response to a relatively fixed set of changes in the tumor composition. Within the 3LL model, modifications of parameters observed with CEUS presented changes in the flow and distribution of the functional microvessels that are consistent with what is anticipated during anti-angiogenic therapy. Both tumor stiffness and QUS microstructure parameters appeared to be modified systematically as the level of fibrosis in the tumors increased. Identifying such parameter/TME relationships in specific types of tumor should ultimately enable a more physiologic, multi-parametric assessment when SWE, QUS and CEUS are applied to monitor tumor modifications during therapy.

V.6. Bibliography

Barrois G, Coron A, Payen T, Dizeux A, Bridal L. A Multiplicative Model for Improving Microvascular Flow Estimation in Dynamic Theory and Experimental Validation. IEEE Trans Ultrason Ferroelectr Freq Control 2013;60:2284–2294.

Battle MR, Goggi JL, Allen L, Barnett J, Morrison MS. Monitoring tumor response to antiangiogenic sunitinib therapy with 18F-fluciclatide, an 18F-labeled αVbeta3-integrin and αV beta5-integrin imaging agent. J Nucl Med 2011;52:424–30.

Bozkurt D, Sarsik B, Hur E, Ertilav M, Burcak K, Ozge T, Selahattin B, Fehmi A, Soner D. A novel angiogenesis inhibitor , sunitinib malate , in encapsulating peritoneal sclerosis. JNephrol 2011;24:359–365.

Broutin S, Ameur N, Lacroix L, Robert T, Petit B, Oumata N, Talbot M, Caillou B, Schlumberger M, Dupuy C, Bidart J-M. Identification of soluble candidate biomarkers of therapeutic response to sunitinib in medullary thyroid carcinoma in preclinical models. Clin Cancer Res 2011;17:2044–54.

Chamming's F, Latorre-Ossa H, Le Frère-Belda M a, Fitoussi V, Quibel T, Assayag F, Marangoni E, Autret G, Balvay D, Pidial L, Gennisson JL, Tanter M, Cuenod C a, Clément O, Fournier LS. Shear wave elastography of tumour growth in a human breast cancer model with pathological correlation. Eur Radiol 2013;23:2079–86.

Dadiani M, Kalchenko V, Yosepovich A, Margalit R, Hassid Y, Degani H, Seger D. Real-time imaging of lymphogenic metastasis in orthotopic human breast cancer. Cancer Res 2006;66:8037–41.

Dietrich C, Averkiou M, Correas J, Lassau N, Leen E, Piscaglia F. An EFSUMB Introduction into Dynamic Contrast-Enhanced Ultrasound (DCE-US) for Quantification of Tumour Perfusion. Ultraschall der Medizin 2012;33:344–351.

Faivre S, Demetri G, Sargent W, Raymond E. Molecular basis for sunitinib efficacy and future clinical development. Nat Rev Drug Discov 2007;6:734–45.

Gallagher F a, Kettunen MI, Day SE, Hu D-E, Ardenkjaer-Larsen JH, Zandt R in 'T, Jensen PR, Karlsson M, Golman K, Lerche MH, Brindle KM. Magnetic resonance imaging of pH in vivo using hyperpolarized 13C-labelled bicarbonate. Nature 2008;453:940–3.

Guibal A, Taillade L, Mulé S, Comperat E, Badachi Y, Golmard J-L, Rixe O, Bridal SL, Lucidarme O. Noninvasive Contrast-enhanced US Quantitative Assessment of Tumor Microcirculation in a Murine Model: Effect of Discontinuing Anti-VEGF Therapy. Radiology 2010;254:420–429.

Heldin C-H, Rubin K, Pietras K, Ostman A. High interstitial fluid pressure - an obstacle in cancer therapy. Nat Rev Cancer 2004;4:806–13.

Hompland T, Ellingsen C, Øvrebø KM, Mri C. Interstitial Fluid Pressure and Associated Lymph Node Metastasis Revealed in Tumors by Dynamic Contrast-Enhanced MRI. Cancer Res 2012;72:4899–4908.

Huang D, Ding Y, Li Y, Luo W-M, Zhang Z-F, Snider J, Vandenbeldt K, Qian C-N, Teh BT. Sunitinib acts primarily on tumor endothelium rather than tumor cells to inhibit the growth of renal cell carcinoma. Cancer Res 2010;70:1053–62.

Hyvelin J-M, Tardy I, Arbogast C, Costa M, Emmel P, Helbert A, Theraulaz M, Nunn AD. Use of Ultrasound Contrast Agent Microbubbles in. Invest Radiol 2013;48:571–583.

Jugé L, Doan B-T, Seguin J, Albuquerque M, Larrat B, Mignet N, Chabot GG, Scherman D, Paradis V, Vilgrain V, Van Beers BE, Sinkus R. Colon tumor growth and antivascular treatment in mice: complementary assessment with MR elastography and diffusion-weighted MR imaging. Radiology 2012;264:436–44.

Korpanty G, Carbon JG, Grayburn P a, Fleming JB, Brekken R a. Monitoring response to anticancer therapy by targeting microbubbles to tumor vasculature. Clin Cancer Res 2007;13:323–30.

Leen E, Averkiou M, Arditi M, Burns P, Bokor D, Gauthier T, Kono Y, Lucidarme O. Dynamic contrast enhanced ultrasound assessment of the vascular effects of novel therapeutics in early stage trials. Eur Radiol 2012;22:1442–50.

Matsumoto S, Batra S, Saito K, Yasui H, Choudhuri R, Gadisetti C, Subramanian S, Devasahayam N, Munasinghe JP, Mitchell JB, Krishna MC. Antiangiogenic agent sunitinib transiently increases tumor oxygenation and suppresses cycling hypoxia. Cancer Res 2011;71:6350–9.

Matsumoto S, Saito K, Takakusagi Y, Matsuo M, Munasinghe JP, Morris HD, Lizak MJ, Merkle H, Yasukawa K, Devasahayam N, Suburamanian S, Mitchell JB, Krishna MC. In Vivo Imaging of Tumor Physiological, Metabolic, and Redox Changes in Response to the Anti-Angiogenic Agent Sunitinib: Longitudinal Assessment to Identify Transient Vascular Renormalization. Antioxid Redox Signal 2014;00:1–11.

Needles A, Heinmiller A, Sun J, Theodoropoulos C, Bates D, Hirson D, Yin M, Foster FS. Development and initial application of a fully integrated photoacoustic micro-ultrasound system. IEEE Trans Ultrason Ferroelectr Freq Control 2013;60:888–97.

Payen T, Coron A, Lamuraglia M, Le Guillou-Buffello D, Gaud E, Arditi M, Lucidarme O, Bridal SL. Echo-power estimation from log-compressed video data in dynamic contrast-enhanced ultrasound imaging. Ultrasound Med Biol 2013;39:1826–37.

Pysz MA, Foygel K, Rosenberg J, Gambhir SS, Schneider M, Willmann JK. Antiangiogenic Cancer Therapy : Monitoring with Molecular US and a Clinically Translatable Contrast Agent (BR55). Radiology 2010;256:519–527.

Tanter M, Fink M. Ultrafast Imaging in Biomedical Ultrasound. 2014;61:102–119.

Vlad RM, Brand S, Giles A, Kolios MC, Czarnota GJ. Quantitative ultrasound characterization of responses to radiotherapy in cancer mouse models. Clin Cancer Res 2009;15:2067–75.

Weller GER, Wong MKK, Modzelewski RA, Lu E, Klibanov AL, Wagner WR, Villanueva FS. Ultrasonic Imaging of Tumor Angiogenesis Using Contrast Microbubbles Targeted via the Tumor-Binding Peptide. Cancer Res 2005;65:533–540.

Zhao Y, Ji T, Wang H, Li S, Zhao Y, Nie G. Self-assembled peptide nanoparticles as tumor microenvironment activatable probes for tumor targeting and imaging. J Control Release Elsevier B.V., 2014;177:11–9.

VI. SONOSENSITIZATION

VI. Sonosensitization

VI.1 Introduction

In the previous chapters, techniques using UCAs for functional imaging have been refined and applied to characterize the tumor microenvironment. Another very active field of research concerns the development of techniques to enhance drug delivery in tumors using UCA microbubbles. It has been demonstrated that sonoporation with UCA microbubbles can be used to transiently open the cell membrane (Karshafian et al. 2009). Sonoporation can be produced by inertial cavitation of MBs associated with their violent collapse. This phenomenon releases energy that can generate pores in the cell membrane (Prentice et al*.,* 2005). Sonoporation has been used to transfect genes into tumor cells *in vitro* and *in vivo* in order to modify their growth rate (Negishi et al. 2011; Sakakima et al. 2005; Suzuki et al. 2010). A similar strategy has also been used in immunotherapy to deliver antigens to immune cells and, thus, to enhance the immune response within the TME (Unga and Hashida 2014). Because sonoporation can transiently open the cell membrane, it can be applied to enhance the uptake of anticancer drugs within tumors. Iwanaga et al. (2007) applied sonoporation using a sonitron device (Sonitron 2000, Rich Mar Inc, Inola, OK) to enhance the effect of bleomycin (a cytotoxic agent) by exposing a subcutaneous squamous carcinoma (Ca9-22) to 1-MHz, 2 W/cm^2 ultrasound twice for 1 minute (50% duty cycle[20]) after the injection of Optison (GE Healthcare, connecticut, USA) MBs. Findings exhibited a significant reduction of tumor volume for mice that underwent ultrasound exposure associated with therapy compared to those that only received the drug. Goertz et al. (2013) performed a similar study, but they used a sonoporation system that was able to deliver high acoustic peak negative pressure (PNP = 1.65 MPa) with short burst duration (50 ms, 0.024% duty cycle). Stimulation of MBs was associated with the administration of docetaxel (DTX), a taxane[21] drug. Ultrasound stimulation treatments, both alone or in combination with DTX, induced an acute reduction in tumor perfusion which was accompanied, 24 hours later, with significantly enhanced necrosis and apoptosis. Moreover, tumors treated with DTX and MB stimulation presented significantly reduced tumor volume as compared to those treated only with DTX.

Several studies have investigated the impact of a technique referred to as “sonosensitization” using MB stimulation at relatively low acoustic PNP (≈500 kPa) to enhance the anti-tumor effect of radiotherapy(Al-Mahrouki et al. 2014; Briggs et al. 2013; Czarnota et al. 2012). Czarnota et al. (2012) studied the effect of sonosensitization produced by oscillating Definity MBs (Definity, Lantheus Medical Imaging, North Billerica, USA) in human PC3 prostate cancer xenografts at a pressure of 570 kPa (500 kHz, 0.25% duty cycle, 16 cycles per burst) during radiotherapy. Results revealed a significant increase in the percentage of cell death in tumors and an associated, significant reduction in tumor blood flow for the sonosensitized group as compared to the group receiving radiotherapy alone. Similar experiments were performed by Tran et al. (2012) in human bladder cancer HT-1376 xenografts using the same setup and parameters while combining radiotherapy and sonosensitization. Results exhibited significant tumor growth delay for the group of mice treated

[20] A duty cycle is the percentage of one period in which signal is active and a period is the time it takes for a signal to complete an on and off cycle. $D = \frac{T}{P} \times 100\%$ where D is duty cycle, T is the time within the signal is active, and P is the total period of the signal.

[21] Taxane is a chemotherapeutic agent. It inhibits the function of cytoskeletal microtubules and thus prevents cell duplication.

with both radiotherapy and sonosensitization (2Gy + high concentration of MBs) with an average tumor volume of 200 mm^3, 21 days after the therapy administration, whereas tumor volume of the group treated with radiotherapy alone (2Gy) reached a volume of 700 mm^3 at the same date. Based on data acquired with power Doppler, they showed a drop in tumor vascularization for the combined therapy. These results were corroborated by immunohistochemistry.

Based on specific immunohistochemical staining, Al-Mahrouki and colleagues (2014) have highlighted the implication of the ceramide molecule in the enhancement of radiotherapy. Ceramide, a central molecule in the sphingolipid[22] metabolism, is intimately involved in the regulation of cancer-cell growth, differentiation, senescence and apoptosis (Ogretmen and Hannun 2004). The ceramide pathway is well-recognized to be activated as a stress response (Chalfant and Poeta 2010) and can accumulate in tumor tissues due to mechanical stresses (Al-Mahrouki et al. (2014)). Czarnota et al. suggested that MBs and ultrasound might cause biochemical reactions when depositing energy near cell membranes, leading to lipid reactions.

Ideally, ultrasonic techniques to monitor and to enhance therapy can be combined. The following chapter applies ultrasonic monitoring to longitudinally evaluate the effects of sonosensitization during cytotoxic therapy in an ectopic model for murine Lewis lung carcinoma (LLC). The material and methods section first describes the sonosensitization apparatus and the preliminary experiments that were performed to select experimental parameters: acoustic exposure conditions and drug dose. The protocol applied to investigate the effectiveness of sonosensitization during therapy with the selected cytotoxic drug (cyclophosphamide) is then described. The effects of therapy were monitored using B-mode images, contrast-enhanced ultrasound (CEUS) and shear wave elastography (SWE) to assess, respectively, tumor volume, vasculature and stiffness. This work was developed in collaboration with the Professor Michael Oelze, Bioacoustics Research Laboratory, University Urbana Champaign Illinois. The tumor model was developed in our laboratory in collaboration with Nathalie Mignet ("Unité de Technologies Chimiques et Biologiques pour la Santé", pharmaceutical and biology sciences). The preclinical experiments described in this chapter were performed under a protocol approved by the Charles Darwin ethical committee (ref: Ce5/2012/081).

VI.2 Material and methods

VI.2.1. Sonosensitization experimental set-up

A weakly focused transducer (CTS Valpey corp., Hopkinton, USA) with a central frequency of 500 kHz and a focal length of 9.5 cm was selected to acoustically stimulate MBs (SonoVue™) throughout the tumor volume (Figure 1). A 16-cycle sinusoidal tone burst emitted from a waveform generator (Tektronix AFG 3022B, Oregon, USA) with peak-to-peak amplitude ranging from 70 to 280 mV was amplified by a ENI A150 power amplifier (Electronic Navigation Industry, Texas, USA) and used to excite the piezoelectric transducer. Tumors were positioned at the focal length of the 500 kHz transducer. As described in Figure 1, alignment was performed based on the specular echo from the tumor surface and backscattered signals observed within the tissue as observed on the radiofrequency A-line acquired with an oscilloscope (DSO3102A, Agilent technologies, California, USA) using a pulser-receiver system (Sofranel 5052PR, Sartrouville, France).

[22] The sphingolipids are a family of cell membrane lipids with important structural roles in the regulation of the fluidity and subdomain structure of the lipid bilayer.

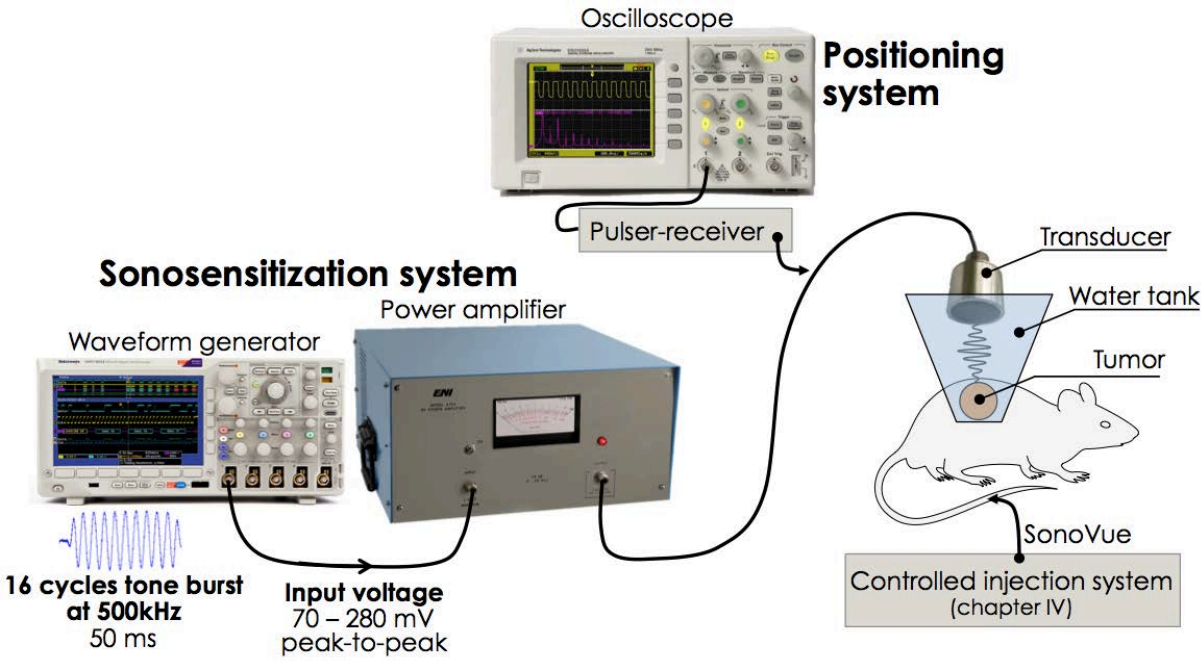

Figure 1: **Diagram of the sonosensitization experimental setup.** A 16-cycle tone burst with a frequency of 500 kHz is sent from a waveform generator to a power amplifier connected to the transducer. A water tank with a thin plastic membrane in contact with the tumor enables the stimulation of MBs injected in the tail vein of the mouse.

VI.2.1.1 Ultrasonic beam characterization

The acoustic PNP delivered by the transducer in a 2-cm^3 volume centered at the focal zone was characterized for each excitation level. This characterization was performed in a degassed water tank, at room temperature, by exposing a thin membrane to acoustic PNP and by measuring its displacement using laser (interferometry)[23].

By displacing the transducer relative to the membrane hydrophone using stepper motors with a step size of 1 mm, the acoustic PNP delivered by the 500 kHz transducer was assessed along three orthogonal axes in a volume centered on the focal position for amplifier input voltages ranging from 70 mV to 280 mV. Figure 2.A and 2.B exhibit typical acoustic PNP measured in parallel (x-y) and perpendicular (x-z) planes with respect to the face of the transducer. The theoretically calculated -6 dB beam diameter of 1 cm was confirmed with measurements in the x-y plane (Figure 2.A). Figure 2.B shows an x-z slice along the propagation axis centered on the beam's central axis and reveals that the pressure is fairly homogenous along the z-axis. The acoustic beam was weakly focused and relatively homogenous over a distance of 2 cm which is suitable for relatively uniform acoustic activation of MBs throughout the tumor volume. For an input voltage of 140 mV, an average acoustic PNP of 237 kPa was measured on the central axis of the beam at the focal distance (9.5 cm). One centimeter closer to the transducer (at 8.5 cm) the average acoustic PNP increased by 6 %. One centimeter after the focal distance (10.5 cm), the average acoustic PNP dropped by 6%.

In Figure 3, the acoustic PNP delivered by the transducer is presented as a function of the input voltage to the amplifier. Pressure is linearly related to the peak-to-peak voltage setting on the waveform generator.

[23] These measurements were done at the Institut Langevin with the kind help of Wojciech Kwiecinski.

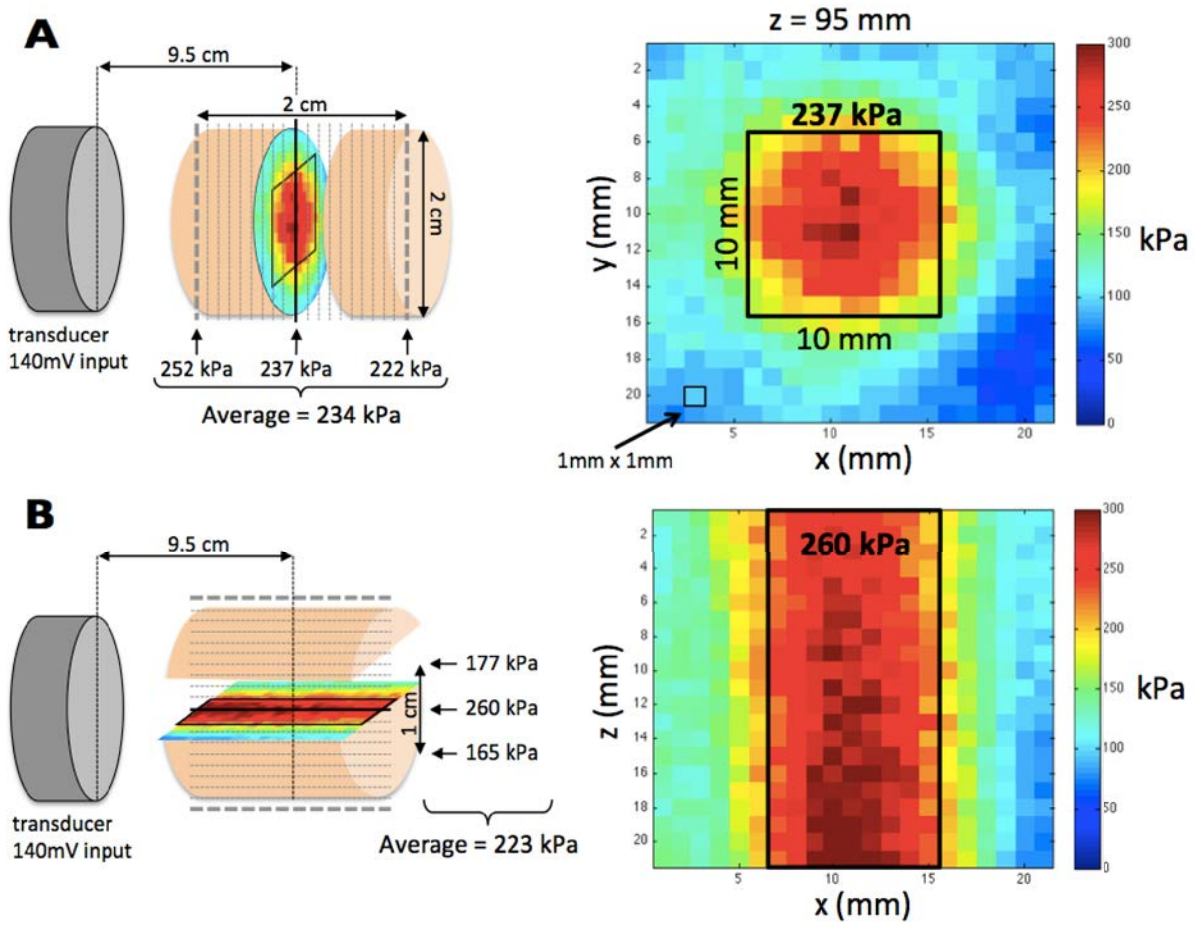

Figure 2: **Characterization of the acoustic PNP delivered by the 500 kHz transducer. B)** Acoustic PNP was assessed in a volume of 2 cm^3 with an isotropic resolution (xyz) of 1 mm. For a peak-to-peak voltage of 140 mV on the waveform generator, the acoustic PNP measured in the field is displayed in the x-z plane at the focal length (9.5 cm). **C)** For the same configuration, the acoustic PNP is displayed in the x-y plane along the central axis of the beam.

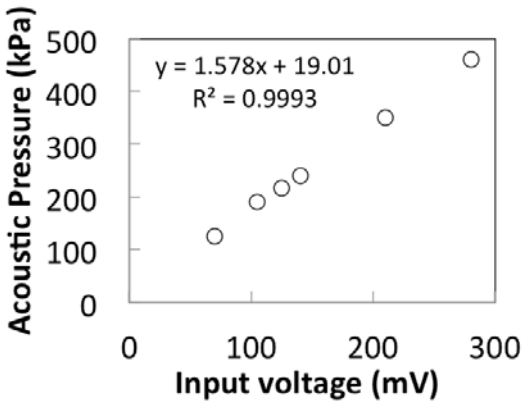

Figure 3: **Linear relationship between the peak-to-peak voltage of the sinusoidal burst generated with the waveform generator and the acoustic PNP at the focal position of the 500 kHz transducer.**

VI.2.1.2 The effects of the acoustic parameters on MB destruction in vivo

The threshold of MBs disruption was assessed *in vivo* in subcutaneous LLC tumors (V_{tumor} = 1060 ± 267 mm^3, N = 6). Anesthetized mice received a bolus injection of 80 µL of SonoVue. Contrast

enhancement was imaged with the same ultrasound system and setup described in Chapters IV and V. Images were recorded during the first 20 seconds after UCA injection, then the tumor was insonified with the sonosensitization transducer at 500 kHz during 30 seconds (100 % duty cycle) and images of the tumor were recorded again for 20 seconds. The mean echo-power in the tumor was evaluated and averaged over 4 seconds before and after MBs sonosensitization exposure. The difference in the echopower signal indicated the level of MBs destruction during sonosensitization. This procedure was reproduced twice at the six different input voltages (ranging from 70 to 280 mV) used to excite the sonosensitization transducer.

As described in Figure 4 at 125 kPa (MI = 0.17) no MB destruction was observed whereas at 190 kPa (MI = 0.27) a reduction of 80 % in the echopower signal was monitored after sonosensitization. At 350 kPa (MI = 0.49), almost all the MBs were destroyed after 30 seconds of acoustic stimulation, whereas, tumors insonified at 215 kPa and 240 kPa still presented echo-power signal. Based on these results, an acoustic PNP of 240 kPa was chosen for sonosensitization in the LLC tumor model.

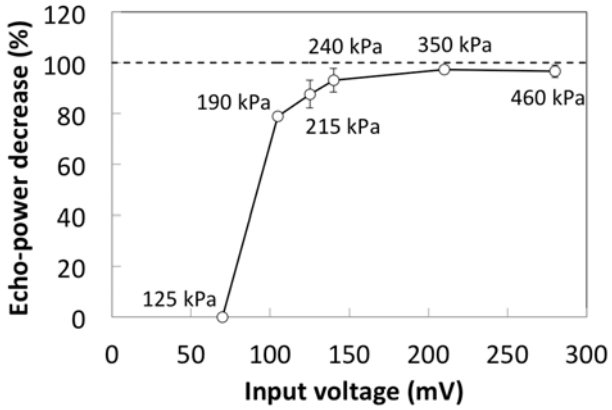

Figure 4: **Relationship between the decrease of the average echo-power signal in tumors (N = 2 per point), the peak-to-peak voltage setting on the waveform generator (mV) and the acoustic PNP at the focal position of the ultrasonic field (kPa)**. Contrast enhancement was monitored before and after 30 seconds of acoustic exposure at 500 kHz. Reduced echo-power demonstrates MB destruction by the system used for sonosensitization exposure.

VI.2.2. Drug, dose selection

Prior to sonosensitization studies, published research describing the effect of three drugs was compiled (Table I). Based on these published results, therapeutic approaches that should modify tumor growth partially (between 40 to 60% reduction in tumor growth) were selected. Lewis Lung Carcinoma (LLC) fragments (20 - 40 mm^3) were implanted in the right flank of thirty-five, 7-week-old female C57bl/6 mice. This cohort was used to evaluate the efficacy of two cytotoxic agents (cyclophosphamide and cisplatin) and one antivascular drug (combretastatin A-4). All drugs were injected via the intraperitoneal route. Cyclophosphamide was administrated on 3 consecutive days (days 15, 16 and 17 after tumor implantation) at doses of 50 mg/kg (N = 4) or 150 mg/kg (N = 5). The same schedule was followed for cisplatin using doses of 2.5 mg/kg (N = 4) and 5 mg/kg (N = 4). Combretastatin A-4 was injected once (day 9 after tumor implantation) when the tumor volume was approximately 100 mm^3 at doses of 100 mg/kg (N = 5) and 200 mg/kg (N = 5). Finally the placebo group received three injections of saline following the same schedule as applied for the cytotoxic drugs. The tumor growth was followed in all groups using ultrasonic imaging to assess the size of the tumor from day 6 to day 16 after tumor implantation. Results were used to select the therapy to combine with sonosensitization.

	Route	Dose mg/kg	Freq.	Tumor origin	Start of therapy	Effect compared to control group	References
Cyclophosphamide	i.p.	200	1	Fragment	Day 7	⇓ Number of metastasis	(Kanclerz et al. 1987)
	s.c.	30	12	Fragment	Day 4	⇓ 56% tumor volume	(Seguin 2012)
	i.p.	170	3	Cells	100 mm^3	⇓ 85% tumor volume	(Hamano et al. 2004)
	i.p.	50, 150	1	Cells	700 mm^3	⇓ 43, 77% tumor cells	(Wang et al. 2007)
	i.p.	50	5	Fragment	Day 7	⇓ 50% tumor volume	(Zhou et al. 2010)
	i.p.	150	3	Cells	Day 12	+ 50% survival	(LaVallee et al. 2008)
Cisplatin	i.p.	6	1	Cells	100 mm^3	⇓ 50% tumor volume	(Lund et al. 2005)
	i.p.	6, 2.4	1, 5	Fragment	Day 7	⇓ Number of metastasis	(Kanclerz et al. 1987)
	i.p.	1, 2.5	1	Cells	100 mm^3	⇓ 0, 45% tumor volume	(Tan et al. 2010)
	i.p.	5	4	Cells	Day 7	⇓ 62% tumor volume	(Jiang et al. 2008)
	i.p.	10	3	Cells	Day 7	⇓ 58% tumor volume	(Koh et al. 2010)
CA-4	i.v.	20	10	Cells	100 mm^3	⇓ 66% tumor volume	(Wang and Ho 2010)
	i.p.	100	1	Cells	500 mm^3	⇓ 50% tumor volume	(Schmid et al. 2011)
	i.p.	100	1	Cells	500 mm^3	+ 15% necrosis	(Shaked et al. 2009)
	i.p.	100	1	Cells	500 mm^3	+ 10% necrosis	(Horsman et al. 1998)

Table 1: Reported **effect of cytotoxic and anti-vascular drugs in the Lewis lung carcinoma**. Summary of the therapeutic effect for different doses and schedules for the administration of Cyclophasphamide, Cisplatin and CA-4 (combretastatin). Effects are presented in comparison to the control group. i.p=intraperitoneal, i.v=intravenous, s.c.=subcutaneous, Freq. = number of consecutive days for which drug is administrated.

VI.2.3. Sonosensitization protocol

Sonosensitization experiments were conducted in a cohort of 30 mice bearing ectopic LLC tumors. The sonosensitization was applied as follows. Within 10 seconds after the injection of 80 µL of SonoVue™ contrast agent (equivalent to 4.10^7 MBs) in the tail vein of mouse, MBs were stimulated at 500 kHz using a peak negative pressure (PNP) of 240 kPa (approximate mechanical index[24] of 0.34) with a sequence of 16-cycle sinusoidal 500 kHz tone bursts maintained during 2 seconds every 13 seconds for an overall time of 5 minutes which corresponded to a total ultrasound exposure of 40 seconds (13% duty cycle).

Mice were randomized into three homogenous groups in term of tumor volume at Day 15 after tumor implantation. Therapy was initiated on Day 15 after implantation when tumors had an approximate volume of 250 mm^3 and vascularization of the tumors was well established. One group received i.p. injections on Days 15, 16 and 17 of cyclophosphamide at a dose of 150 mg/kg (Drug Only, DO, N=10). A second group received cyclophosphamide according to the same therapeutic plan but was injected with microbubbles and exposed to sonosensitization during 40 seconds within 5 minutes following injection of the drug (Sonosensitization and Drug, SSD, N=10). Finally a third group was injected with MBs and exposed to sonosensitization but did not receive cyclophosphamide (Sonosensitization Only, SSO, N=10).

[24] Mechanical Index, $IM = PNP / \sqrt{F_C}$ where PNP is the derated, peak negative pressure (PNP) in MPa and F_C is the central frequency of transducer in MHz.

VI.2.4. *In vivo* imaging

Tumors were monitored using the CEUS and SWE imaging modalities described in Chapter V. Thus, only a brief description of the imaging setup is included here. B-mode images acquired with the 8-MHz transducer were acquired in orthogonal planes and used to assess tumor volume. For each tumor, SWE data were acquired from 3 independent planes along both the longitudinal and transverse directions (6 SWE imaging planes per tumor). Data were acquired using penetration mode with a color scale ranging from 0 to 50 kPa. For CEUS imaging, a 50-µL volume of SonoVue^{TM} was injected through the tail vein of each mouse using the controlled injection system described in Chapter IV and data were acquired at a frame rate of 1 Hz. Contrast injections used for imaging were performed approximately 10 minutes before sonosensitization experiments. Average echo-power was initially measured in a region of interest including the total tumor cross-section. Regions with no contrast-enhancement, defined as pixels for which the intensity does not exceed the intensity level of noise (corresponding to signal in tumor before UCA uptake), were then excluded and the echo-power from the perfused region was measured. A lognormal bolus model was fit to the resulting echo-power curves and functional parameters (PE, TTP, MTT, WIR, WOR and AUC) were extracted.

VI.2.5. Statistics

All statistical tests and analysis were performed using R software (3.1.1). A Wilcoxon signed-rank non-parametric test (Mann-Witney U test) was used to compare the results between the different groups at each study date (unpaired test). Differences between groups were considered significant at p-values of $p < 0.005$ (***), $0.005 < p < 0.01$ (**) and $0.01 < p < 0.05$ (*). Results are given as mean ± SEM (standard error of the mean). Results presented with boxplots show: the minimum, lower quartile, median, mean value (square), upper quartile and maximum values.

VI.3. Results

VI.3.1. Preliminary experiments to select drug and dose

Results presented in Figure 5 exhibit the most significant reduction of tumor growth with cyclophosphamide injected at a concentration of 150 mg/kg from Days 10 to 17 compared to the placebo group (150 ± 50 mm^3 vs. 1500 ± 220 mm^3, $p < 0.01$). Although tumors appear somewhat smaller for groups treated with cyclophosphamide at 50 mg/kg compared to Placebo, the difference was not significant (Day 17, 723 ± 245mm^3 vs. 1507 ± 220 mm^3, p=0.11). Treatment with 5 mg/kg cisplatin significantly reduced tumor growth compared to Placebo (Day 17, 590 ± 104mm^3 vs. 1507 ± 220 mm^3, $p < 0.01$) but therapy was associated with a transient weight loss approaching 10% (data not shown). Weight loss was not observed when cisplatin was administered at 2.5 mg/kg but tumor growth was not significantly reduced at this dose. Combretastatin did not reduce tumor growth at either of the tested doses. Thus, based on these results, cyclophosphamide at a concentration of 150mg/kg was selected for sonosensitization experiments due to its strong effect in the reduction of tumor growth compared to control group.

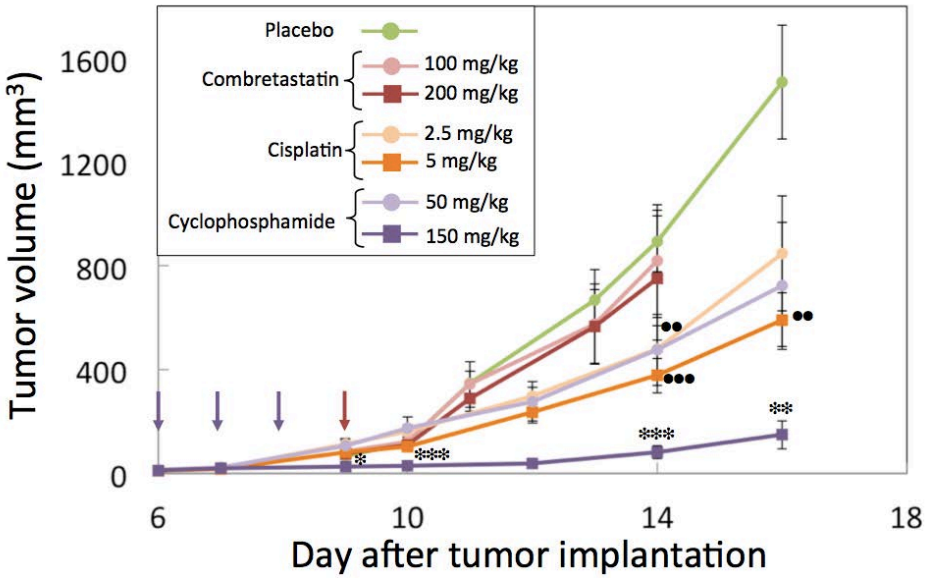

Figure 5: **Preliminary dose trial therapy**. Presentation of the effect in reduction of tumor growth for two cytotoxic therapies (cyclophosphamide and cisplatin) and an antivascular drug injected at different concentrations. Purple arrows indicate the days of injection with the cytotoxic therapies and the red arrow indicates the day for administration of combretastatin. Cyclophosphamide: N = 4 for 50 mg/kg, N = 5 for 150 mg/kg; cisplatin: N = 4 for 2.5 mg/kg, N = 4 for 5 mg/kg; combretastatin: N = 5 for 100 mg/kg, N = 5 for 200 mg/kg. Significant differences between groups treated with cisplatin and cyclophosphamide drug as compared to the group receiving placebo are designated, respectively, by ● and ❊.

VI.3.2. Sonosensitization experiment

As presented in Figure 6, eight days after the initiation of therapy (Day 23 with respect to tumor implantation) both the mice receiving only drug (DO, 1320 ± 126 mm^3, $p < 0.01$) and those exposed to sonosensitization after administration of the cytotoxic drug (SSD, 1345 ± 201 mm^3, $p < 0.03$) exhibited significantly smaller tumor volumes than for the group exposed to sonosensitized microbubbles alone (SSO, 1876 ± 220 mm^3). However, there was no significant difference between the DO and SSD groups. This indicates that sonosensitization did not modify the tumor volume.

Baseline for average tumor stiffness (SWE) and perfusion (CEUS) was performed on Day 15 just before therapy began. The follow-up of tumor stiffness presented in Figure 7 reveals a significant drop of tumor stiffness for SSD group at day 19 (13.8±1.1 kPa) compared to baseline (16.8±1.1 kPa, p=0.013) and also compared to the SSO group at day 19 (19.8±1.1 kPa p=0.003). This difference was not maintained, however, at Day 23.

Parameters related to the blood volume and the functionality of tumor vasculature as estimated from CEUS are presented in Figure 8. The percent of unperfused tumor area was similar between the three groups at baseline and was significantly higher for SSO group at Day 23 (30.4±3.5 %) as compared to SSD (14.9±6.5 %, p<0.05) and DO (11.3±4.2 %, p<0.05). Perfusion parameters were assessed only in the perfused area.

The PE parameter, related to the blood volume, was comparable at baseline between groups and reached a significantly higher mean value in the DO group at Day 23 (0.43 ± 0.05 a.u) compared to SSD (0.24 ± 0.04 a.u, p=0.03) and SSO (0.22 ± 0.04 a.u, p=0.02) groups. The same tendency was observed with the AUC parameter for which the DO group exhibited a higher value (35.6 ± 4.3 a.u) compared to SSO (22.9 ± 4.4 a.u, p<0.001) and SSD (19.8±3.4 a.u, p=0.1) group.

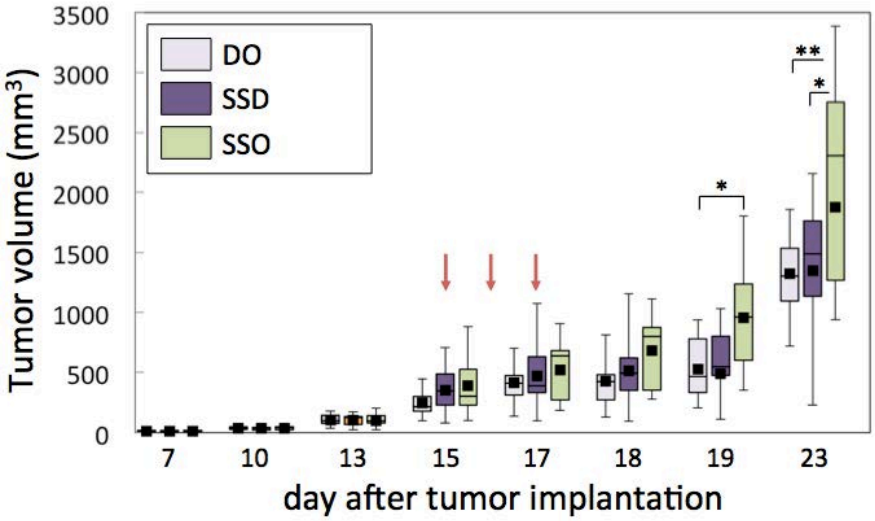

Figure 6: **Longitudinal follow-up of tumor volume.** Tumor volume was measured based on longitudinal and transversal B-mode images. Red arrows indicate the days of therapy administration. Drug only (DO) corresponds to the group that received cyclophosphamide only, sonosensitization and drug (SSD) designates the group that received both cytotoxic therapy and sonosensitization stimulation and finally SSO group indicates the group that only underwent sonosensitization without drug injection. Differences between groups were considered significant at p-values of $p < 0.005$ (***), $0.005 < p < 0.01$ (**) and $0.01 < p < 0.05$ (*).

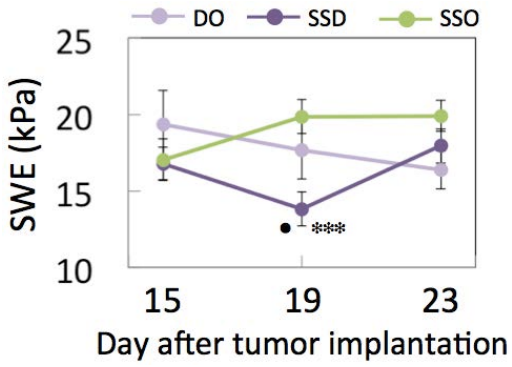

Figure 7: **Longitudinal follow-up of tumor stiffness.** Shear wave elastography (SWE) was measured for each tumor in six different planes and then averaged. A significant difference between the SSD and SSO is indicated by ❊ whereas ● designates a significant difference between SSD and DO groups.

At Day 23, WIR and WOR parameters of DO group ($1.7 \pm 0.3\ 10^{-2}$ a.u and $5.1 \pm 0.8\ 10^{-3}$ a.u, respectively) were significantly higher than those of SSO group ($0.6 \pm 0.1\ 10^{-2}$ a.u, $p=0.0012$; $5.1 \pm 0.8\ 10^{-3}$ a.u, $p<0.001$, respectively) but no significant difference was exhibited for SSD group ($1.0 \pm 0.3\ 10^{-2}$ a.u, $p=0.18$; $3.0 \pm 0.8\ 10^{-3}$ a.u, $p=0.1$, respectively) despite a trend following SSO group. In nearly every case, perfusion parameters (PE, AUC, WIR and WOR) measured in the SSD group follow a trend close to the SSO group which demonstrates a reduced microvascularization at day 23.

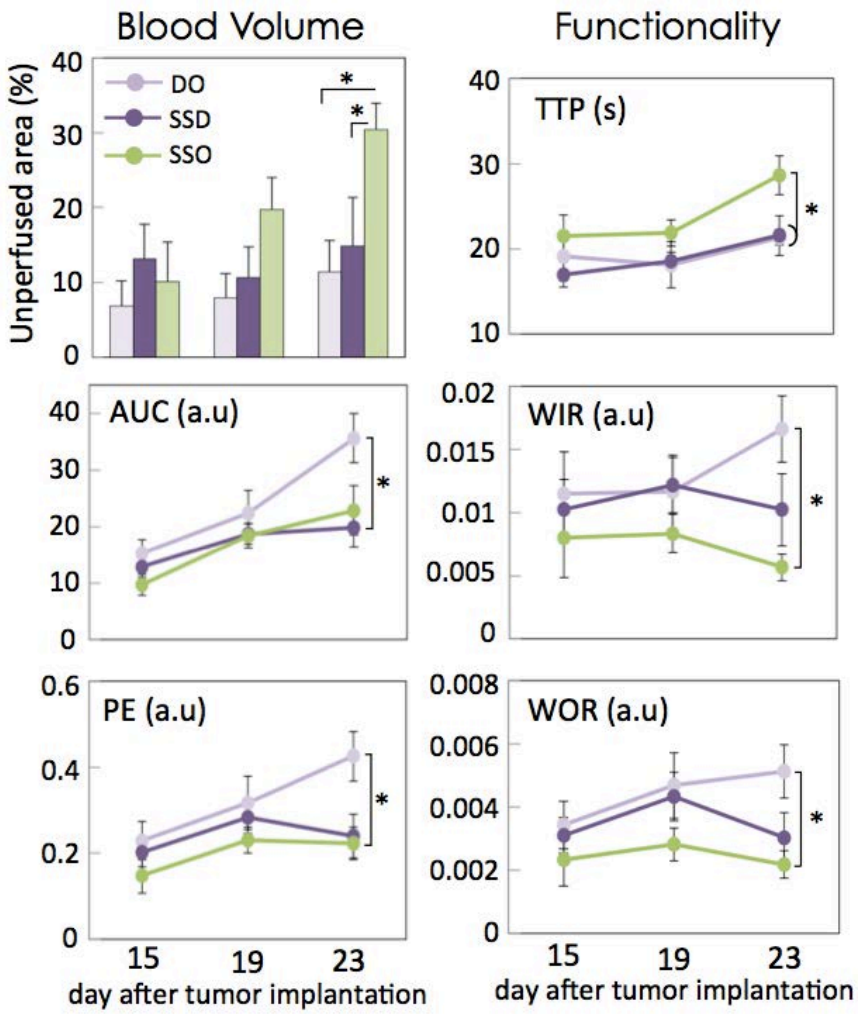

Figure 8: **Longitudinal follow-up of tumor vasculature modifications.** After defining perfused and non-perfused area, perfusion parameters were calculated only in the perfused regions. Percentage of unperfused area, peak-enhancement (PE) and area under the curve (AUC) are related to the blood volume within tumor whereas time-to-peak (TTP), wash-in rate (WIR) and washout rate (WOR) are related to the functionality of the tumor microvascular network. DO = drug only, SSD = sonosensitization and drug and SSO = sonosensitization only.

VI.4. Discussion & conclusion

The goal of this study was to non-invasively monitor the effect of the association of sonosensitization (stimulation of MBs) with a cytotoxic drug on tumor development. Tumor modifications were monitored using B-mode images to estimate tumor volume, SWE maps of tumor stiffness and CEUS characterization of the microvascular distribution and function.

The acoustic field and pressure levels used for sonosensitization were characterized to insure that the ultrasound beam was large enough (Ø 1 cm) and weakly focused enough to uniformly insonify the whole tumor. Since continuous, non-destructive MB oscillation is sought during sonosensitization, the acoustic PNP was set to 240 kPa for sonosensitization experiments because, beyond this pressure level, SonoVue MBs were very strongly destroyed by the acoustic exposure.

VI.4.1. Effect of sonosensitization

The tumor volume was significantly reduced in both the SSD and DO groups relative to the group receiving sonosensitization along but there was no significant effect on tumor volume due to sonosensitization and drug (SSD) relative to the cytotoxic drug alone (DO). In the study performed by Czarnota et al. (2012), significant effect of SSD was demonstrated based on Kaplan-Meier survival curves with ethical endpoints defined for tumor sizes greater than 2 cm in diameter. None of the mice that underwent both sonosensitization and radiotherapy (dose of 2Gy) reached this endpoint within the 28 days after therapy ended; whereas, mice that received only radiotherapy (2Gy) or exposure to MBs alone began to reach this endpoint 7 days after the end of treatment. Their results suggest that coupling sonosensitization with radiotherapy had a significant impact on tumor growth well after therapy had been applied. Due to the ethical endpoints defined for our study and the relatively rapid tumor growth, tumor volume was only followed to 6 days after the end of therapy application which may have prevented the observation of some, longer term responses to the SSD therapy.

The percentage of unperfused area evaluated with CEUS was significantly higher for the SSO group at Day 23 as compared with the groups receiving drug alone or sonosensitization with drug (Figure 7). As presented in Chapter V, unperfused areas are strongly correlated to necrotic areas in our tumor model. Thus, increased unperfused area in the SSO group may be related to the natural development of necrosis due in these more-rapidly growing tumors (no cytotoxic therapy, highest tumor volume at Day 23). Both in terms of tumor volume and the percentage of unperfused area, DO and SSD groups were very similar. The perfused microvasculature of the tumor demonstrated significantly different functionality and blood volume for the SSO group as compared to the DO group according to assessments of the AUC, PE, TTP, WIR and WOR on Day 23. Although only the TTP at Day 23 was significantly different from the DO group for the SSD group, measurements in the perfused area of the SSD group tended to lie closer to those in the SSO group than in the DO group. This may provide some indication that the SSD therapy is influencing the blood flow differently than for the DO therapy. Briggs et al. (2013) demonstrated a significant drop of perfusion and oxygen saturation for tumors that underwent sonosensitization (570 kPa) associated with radiotherapy (8Gy). Czarnota et al. (2012) also demonstrated significant reductions in blood flow 24 h after the combined sonosensitization and radiation treatments (65 ± 8% decrease in Doppler vascular index; VEVO-770, Visualsonics); whereas, moderate vascular disruption was exhibited with sonosensitization (570kPa), and with 8-Gy radiation doses alone (20 ± 21% and 20 ± 32% decrease in Doppler vascular index, respectively). If confirmed in a larger cohort or with a longer therapeutic follow-up revealing statistical significance of the effect, reduced blood volume in the SSD group would be consistent with what is expected based on the vascular effect, explained by Briggs et al. in terms of a synergic effect between the therapy and sonosensitization.

VI.4.2. Limitations of the study

The main limit of the current study resides in the lack of immunohistochemistry related to the studied tumors. Samples conserved in a -80°C freezer were lost due to an electrical problem in the conservation facility. For this reason, independent characterization of the level of cell death (necrosis, apoptosis) and the density of blood vessels was not possible.

Because the LLC tumor model presents a very high growth rate and tumors reach the ethical endpoint (V_{tumor} = 2500mm^3) within 3 weeks after tumor implantation, it was not possible to follow tumor modifications for more than 6 days after the end of therapy. Unlike conventional drugs, sonosensitization experiments appear to demonstrate greatest effect (Al-Mahrouki et al. 2014; Briggs et al. 2013; Czarnota et al. 2012; Tran et al. 2012) when tumors are well perfused at the initiation of the treatment, but if the tumor grows too rapidly from that point despite therapy, ethical endpoints are reached quickly and long term effects cannot be monitored.

Orienting future studies toward sononsensitization in tumors with slower growth rates may better reveal anti-tumor effects. Iwanaga et al. (2007) studied the combined effect of sonoporation with a cytotoxic drug (bleomycin) in a human squamous carcinoma xenograft for which the tumor volume remains inferior to 200 mm^3 after 28 days of growth. In a similar study, Goertz and co-workers (2013) used the PC3 prostate carcinoma model (same tumor model used in the following sonosensitization studies: Al-Mahrouki et al. 2014; Briggs et al. 2013; Czarnota et al. 2012) which reaches a volume on the order of only 400 mm^3 at 3 weeks after tumor implantation whereas our LLC tumor model exhibits volumes around 1500 mm^3 within the same time frame.

Thus, future experiments using multiparametric ultrasonic imaging to search for tumor modifications due to the combined effect of sonosensitization with cytotoxic drugs should use a tumor model with a slower growth rate. Preliminary experiments will also be needed to assess the optimal dose of drug in the new tumor model for the combination with sonosensitization. Moreover, histology at different time points of tumor development will be required to provide a more precise interpretation of the *in vivo* parameters measured with ultrasonography.

Bibliography

Al-Mahrouki A a, Iradji S, Tran WT, Czarnota GJ. Cellular characterization of ultrasound-stimulated microbubble radiation enhancement in a prostate cancer xenograft model. Dis Model Mech 2014;7:363–72.

Briggs K, Al Mahrouki a, Nofiele J, El-Falou a, Stanisz M, Kim HC, Kolios MC, Czarnota GJ. Non-invasive Monitoring of Ultrasound-Stimulated Microbubble Radiation Enhancement Using Photoacoustic Imaging. Technol Cancer Res Treat. 2013

Chalfant C, Poeta M Del. Sphingolipids as Signaling and Regulatory Molecules. Landes Bioscience and Springer Science and Business Media NY, ed. 2010.

Czarnota GJ, Karshafian R, Burns PN, Wong S, Al Mahrouki A, Lee JW, Caissie A, Tran W, Kim C, Furukawa M, Wong E, Giles A. Tumor radiation response enhancement by acoustical stimulation of the vasculature. Proc Natl Acad Sci USA 2012;109:E2033–41.

Goertz DE, Todorova M, Agache V, Mortazavi O, Chen B, Karshafian R, Hynynen K. Antitumor effects of combining metronomic chemotherapy with the antivascular action of ultrasound stimulated microbubbles. PLoS One 2013;132:2956–2966.

Hamano Y, Sugimoto H, Soubasakos MA, Kieran M, Olsen BR, Lawler J, Sudhakar A, Kalluri R. Thrombospondin-1 Associated with Tumor Microenvironment Contributes to Low-Dose Cyclophosphamide-Mediated Endothelial Cell Apoptosis and Tumor Growth Suppression. Cancer Res 2004;64:1570–1574.

Horsman MR, Ehrnrooth E, Ladekarl M, Overgaard J. The effect of combretastatin A-4 disodium phosphate in a C3H mouse mammary carcinoma and a variety of murine spontaneous tumors. Radiat Oncol 1998;42:895– 898.

Iwanaga K, Tominaga K, Yamamoto K, Habu M, Maeda H, Akifusa S, Tsujisawa T, Okinaga T, Fukuda J, Nishihara T. Local delivery system of cytotoxic agents to tumors by focused sonoporation. Cancer Gene Ther 2007;14:354–63.

Jiang Q, Fan L, Yang G, Guo W-H, Hou W, Chen L, Wei Y. Improved therapeutic effectiveness by combining liposomal honokiol with cisplatin in lung cancer model. BMC Cancer 2008;8:242.

Kanclerz A, Chapman JD. The effectiveness of dis-platinum, cyclophosphamide and mephalan in treating disseminated tumor cells in mice. Clin Exp Metastasis 1987;5:199–211.

Karshafian R, Bevan PD, Williams R, Samac S, Burns PN. Sonoporation by Ultrasound-Activated Microbubble Contrast Agents: Effect of Acoustic Exposure Parameters on Cell Membrane Permeability and Cell Viability. Ultrasound Med Biol 2009;35:847–860.

Koh YJ, Kim HZ, Hwang SI, Lee JE, Oh N, Jung K, Kim M, Kim KE, Kim H, Lim NK, Jeon CJ, Lee GM, Jeon BH, Nam DH, Sung HK, Nagy A, Yoo OJ, Koh GY. Double antiangiogenic protein, DAAP, targeting VEGF-A and angiopoietins in tumor angiogenesis, metastasis, and vascular leakage. Cancer Cell Elsevier Ltd, 2010;18:171–184.

LaVallee TM, Burke P a, Swartz GM, Hamel E, Agoston GE, Shah J, Suwandi L, Hanson AD, Fogler WE, Sidor CF, Treston AM. Significant antitumor activity in vivo following treatment with the microtubule agent ENMD-1198. Mol Cancer Ther 2008;7:1472–1482.

Lund EL, Hansen LT, Kristjansen PEG. Augmenting tumor sensitivity to topotecan by transient hypoxia. Cancer Chemother Pharmacol 2005;56:473–480.

Negishi Y, Tsunoda Y, Endo-Takahashi Y, Oda Y, Suzuki R, Maruyama K, Yamamoto M, Aramaki Y. Local gene delivery system by bubble liposomes and ultrasound exposure into joint synovium. J Drug Deliv 2011;2011:203986.

Ogretmen B, Hannun Y a. Biologically active sphingolipids in cancer pathogenesis and treatment. Nat Rev Cancer 2004;4:604–16.

Prentice P, Cuschieri A, Dholakia K, Prausnitz M, Campbell P. Membrane disruption by optically controlled microbubble cavitation. Nat Phys 2005;1:107–110.

Sakakima Y, Hayashi S, Yagi Y, Hayakawa A, Tachibana K, Nakao A. Gene therapy for hepatocellular carcinoma using sonoporation enhanced by contrast agents. Cancer Gene Ther 2005;12:884–889.

Schmid MC, Avraamides CJ, Foubert P, Shaked Y, Kang SW, Kerbel RS, Varner J a. Combined blockade of integrin-alpha4beta1 plus cytokines SDF-1alpha or IL-1beta potently inhibits tumor inflammation and growth. Cancer Res 2011;71:6965–6975.

Seguin J. Caractérisation de modèles de tumeurs murines et leurs applications en thérapie anti-angiogénique vectorisée. 2012.

Shaked Y, Tang T, Woloszynek J, Daenen LG, Man S, Xu P, Cai SR, Arbeit JM, Voest EE, Chaplin DJ, Smythe J, Harris A, Nathan P, Judson I, Rustin G, Bertolini F, Link DC, Kerbel RS. Contribution of granulocyte colony-stimulating factor to the acute mobilization of endothelial precursor cells by vascular disrupting agents. Cancer Res 2009;69:7524–7528.

Suzuki R, Namai E, Oda Y, Nishiie N, Otake S, Koshima R, Hirata K, Taira Y, Utoguchi N, Negishi Y, Nakagawa S, Maruyama K. Cancer gene therapy by IL-12 gene delivery using liposomal bubbles and tumoral ultrasound exposure. J Control Release Elsevier B.V., 2010;142:245–250.

Tan Q, Li J, Yin HW, Wang LH, Tang WC, Zhao F, Liu XM, Zeng HH. Augmented antitumor effects of combination therapy of cisplatin with ethaselen as a novel thioredoxin reductase inhibitor on human A549 cell in vivo. Invest New Drugs 2010;28:205–215.

Tran WT, Iradji S, Sofroni E, Giles A, Eddy D, Czarnota GJ. Microbubble and ultrasound radioenhancement of bladder cancer. Br J Cancer 2012;107:469–76.

Unga J, Hashida M. Ultrasound induced cancer immunotherapy. Adv Drug Deliv Rev Elsevier B.V., 2014;72:144–53.

Wang X, Zhang J, Xu T. Cyclophosphamide as a potent inhibitor of tumor thioredoxin reductase in vivo. Toxicol Appl Pharmacol 2007;218:88–95.

Wang Z, Ho PC. A nanocapsular combinatorial sequential drug delivery system for antiangiogenesis and anticancer activities. Biomaterials Elsevier Ltd, 2010;31:7115–7123.

Zhou HJ, Zhang JL, Li A, Wang Z, Lou XE. Dihydroartemisinin improves the efficiency of chemotherapeutics in lung carcinomas in vivo and inhibits murine Lewis lung carcinoma cell line growth in vitro. Cancer Chemother Pharmacol 2010;66:21–29.

VII. DISCUSSION AND CONCLUSIONS: PERSPECTIVES FOR DIAGNOSIS AND THERAPY

VII. Discussion and Conclusions: Perspectives for diagnosis and therapy

Two important approaches in the fight against cancer have been addressed in this thesis. The first concerns improvement of diagnosis through more sensitive detection and better characterization of the TME using emerging ultrasonic methods. The second concerns the evaluation of changes in the TME to better monitor and understand modifications of the TME produced by different types of therapeutic approaches. After the presentation of tumor biology (Chapter II), a range of techniques able to characterize the tumor at different scales (anatomic, molecular and physiologic) was reviewed in Chapter III. In principle, by combining information from biomarkers extracted from several imaging modalities, a more precise characterization of tumor tissues should be obtainable. In Chapter V, a multiparametric study based on three ultrasound modalities (CEUS, SWE, QUS) revealed their complementarity for differentiation of the tumor response during cytotoxic and antiangiogenic therapies. Finally, in Chapter VI, SWE and CEUS were used to monitor tumors during the application of novel therapy based on the acoustic stimulation of MBs at low mechanical index in conjunction with the administration of a cytotoxic drug. To conclude upon the work presented in this thesis, the future of the techniques presented in this thesis will be discussed and considered with respect to other, emerging and innovative approaches for early detection of cancer and the enhancement of therapy.

VII.1. Emerging, innovative techniques to provide earlier detection of cancer

Early detection is critical in patient outcome. For example, in the context of colorectal cancer, Table I summarizes the relation between the cancer's stage at diagnosis and the 5-year survival rate of patients. A strong increase of patient survival is revealed when cancers are detected in the early phases of development.

Cancer stage	5-year survival rate after diagnosis
Stage I, superficial lesion in the wall of intestine	94%
Stage II, deeper lesion may spread to surrounding organs	80%
Stage III, Lymph nodes near colon are invaded	47%
Stage IV, metastasis disseminated in the organism	5%

Table I: **Relation between cancer stage at detection and the 5-year survival rate for colorectal cancer.** *Data from Francim (réseau français des registres du cancer) 2007.*

The established RESIST criterion relies on the modification of tumor size but certain therapeutic approaches modify other aspects of the TME prior to size regression. For example, CEUS has been demonstrated, in several studies (Lamuraglia et al. 2010; Lassau et al. 2014; Williams et al. 2011), to provide earlier detection of anti-angiogenic effect. Such sensitivity to anti-angiogenic changes was also demonstrated by the results presented in Chapter V (Figure 5). The underlying changes in the

TME leading to modifications of the QUS (ESD) and SWE parameters further enabled the detection of different modifications in the tumor due to the antiangiogenic drug compared to a cytotoxic drug.

Cancer diagnosis is advancing towards the development of even more non-invasive tools for ever more sensitive and accurate diagnosis of tumors. These developments are associated with a dematerialization of data that will enable the centralization of data and thus will provide the possibility to study pathologies on a larger scale. Some of these emerging and highly non-invasive markers and the ways that these markers can be integrated into the clinical decision making process are described in the following paragraphs.

VII.1.1. Detection of Circulating tumor cells (CTC)

A French team has developed a technique named ISET (isolation by size of epithelial tumor cells) that enables counting, immuno-morphological analysis and molecular characterization of circulating tumor cells (CTCs) present in the patient's blood (Vona et al. 2000). Using this technique, epithelial tumor cells (carcinoma) which are larger in size as compared to peripheral blood leukocytes[25] are isolated by filtration. Vona and colleagues (2000) have shown that ISET assays can detect a single, micropipetted, tumor cell within 1 ml of blood. Since captured CTCs remain intact, subsequent cell cultures can be performed to test different chemotherapeutic agents.

The main application of CTC detection in the blood of patients with cancer resides in the prediction of clinical outcome and the dissemination of metastasis. Indeed, circulating tumor cell levels were prospectively demonstrated to be an independent prognostic factor in patients with advanced breast, prostate and colorectal cancers treated by conventional and/or hormonal therapy (Cohen et al. 2008; Cristofanilli et al. 2004; De Bono et al. 2008).

The ability to detect CTCs in the bloodstream of patients before they develop a cancer represents a new paradigm in the diagnosis of cancer that could significantly improve patient survival. Recently, ISET assay has been applied to predict cancer evolution. Chronic obstructive pulmonary disease (COPD) represents a risk factor for the development of lung cancer. A study was performed by Ilie and colleagues (2014) with 245 subjects without cancer, including 168 (68.6%) COPD patients, and 77 subjects without COPD (31.4%), including 42 control smokers and 35 non-smoking healthy individuals. Results revealed that CTCs were detected in 3% of COPD patients (5 out of 168 patients). An annual surveillance of the CTC-positive COPD patients was performed with thorax CT-scan screening potential lung nodules. The annual control enabled the detection of lung nodules from 1 to 4 years after CTC detection that allowed a prompt surgical resection and histopathological diagnosis of early-stage lung cancer.

VII.1.2. Detection of Volatile organic compounds

Exhaled breath includes small inorganic compounds, such as NO, O_2, CO_2, volatile organic compounds, VOCs (hydrocarbons, alcohols, ketones, aldehydes, esters) and nonvolatile substances such as isoprostanes, cytokines, leukotrienes and hydrogen peroxide, which can be found in breath condensate (Montuschi et al. 2002). Approximately 3000 different VOCs have been detected at least once in human breath, and most breath samples contain more than 200 VOCs (Phillips et al. 1999a; Phillips et al. 1999b; Teshima et al. 2005). The VOC profile in patients suffering from certain diseases

[25] Peripheral blood leukocytes correspond to mature leukocytes that circulate in the blood, rather than those remaining localized in specific organs.

is different from the normal VOC profile (Buszewski et al. 2007). Based on this principle, some teams have investigated the ability of dogs to detect tumors based on the scent of the breath exhaled by patients. Other groups have sought more technologically advanced techniques such as the nanoscale artificial nose to monitor VOCs in the breath.

VII.1.2.1 Dogs trained to detect the scent of cancer

The size of the olfactory area used to analyze air molecules is around 3 cm^2 for humans (≈ 6 million receptors) versus 130 cm^2 for dogs (≈ 300 million receptors) (Tyson 2012). McCulloch and colleagues (2006) have investigated the ability of dogs to detect and differentiate early- and late-stage lung and breast cancers. After a phase of training, they performed double blind experiments in which dogs had the opportunity to sniff breath samples from each subject and each control. The results of the study revealed that, among lung cancer patients (N = 55) and controls (N = 83), the overall sensitivity[26] of canine scent detection compared to biopsy-confirmed conventional diagnosis was 0.99 and the overall specificity[27] 0.99. Among breast cancer patients (N = 31) and controls, sensitivity was 0.88 and specificity 0.98. Moreover, sensitivity and specificity were similar across all 4 stages of both diseases. Using a similar protocol, Ehmann et al. (2012) showed that dogs were able to detect lung cancer with an overall sensitivity of 71 % and a specificity of 93 %. A detailed review presents findings of various studies and suggest that dogs are able to detect lung, breast, prostate, ovarian, and melanoma cancers by smelling skin lesions, urine, exhaled breath, and surgically extracted tumors (Moser and McCulloch 2010).

VII.1.2.2 The nanoscale artificial nose (NA-NOSE)

Based on the ability of dogs to smell specific molecules, several research teams have developed techniques that enable the detection of molecules exhaled from patient. Today, only a few breath tests are currently practiced in the clinic (Buszewski et al. 2007). This situation is primarily a consequence of the technological difficulties in the detection of trace amounts of disease-related VOCs within a complex exhaled breath sample. An additional reason for this situation is that the wide variety of implemented techniques has led to a major standardization problem in the field. Many methods are still in the developmental phase and, therefore, their use is confined to research. Other, established analytical approaches exist, such as mass spectrometry, but these tools suffer from high costs, complexity, and require trained personnel for their operation (Konvalina and Haick 2014).

Haick and co-workers recently designed a nanoscale artificial nose (NA-NOSE, Figure 1) that aims to reproduce the sensitivity of dog scent. The nanoscale size of sensors (organically functionalized carbon nanotubes and gold nanoparticles) provides them with several benefits such as large surface-to-volume ratio and unique chemical, optical, and electrical properties. Using this device, Xu et al. (2013) have investigated the possibility to detect and stage gastric cancer (GC) in patient. They used this nanomaterial-based sensor to analyze exhaled breath samples from 130 patients with gastric

[26] In a binary classification test four cases are possible. In the context of the detection of illness the four configurations are the following: sick people correctly diagnosed as sick (true positive, TP), healthy people incorrectly identified as sick (false positive, FP), healthy people correctly identified as healthy (True negative, TN) and sick people incorrectly identified as healthy (false negative, FN). Sensitivity measures the proportion of actual positives which are correctly identified as such. Sensitivity = TP/(TP+FN).

[27] Specificity measures the proportion of negatives which are correctly identified as such. Specificity = TN/(TN+FP)

complaints. For the study, they developed a predictive model based on discriminate factor analysis (DFA) pattern recognition which was revealed to be robust to confounding factors such as alcohol and tobacco consumption. Final results indicate an excellent discrimination between the following subpopulations: GC vs benign gastric conditions, among all the patients (89% sensitivity; 90% specificity); early stage GC (I and II) vs late stage (III and IV), among GC patients (89% sensitivity; 94% specificity); and ulcer vs less severe, among benign conditions (84% sensitivity; 87% specificity). The same NA-NOSE device has presented conclusive results in the early detection of head-and-neck, lung, colorectal, breast and prostate cancer (Hakim et al. 2011; Peng et al. 2010).

This technology can be used, not only for the diagnosis of carcinoma but it can also be applied to identify Alzheimer's disease (AD) and Parkinson's disease (PD). The results of the study performed by Tisch and co-workers (2012) revealed that the nano-sensor could clearly distinguish AD from healthy states, PD from healthy states, and AD from PD states, with a classification accuracy of 85, 78 and 84%, respectively.

Haick and co-workers raised around 35 M€ and plan to commercialize their NA-NOSE device in 2020, it will cost around 8 € and will be a connected device meaning that the analysis could be remotely transmitted to the physician. Such inexpensive biosensors could contribute to the current development of telemedicine (telehealth) and "self-monitoring".

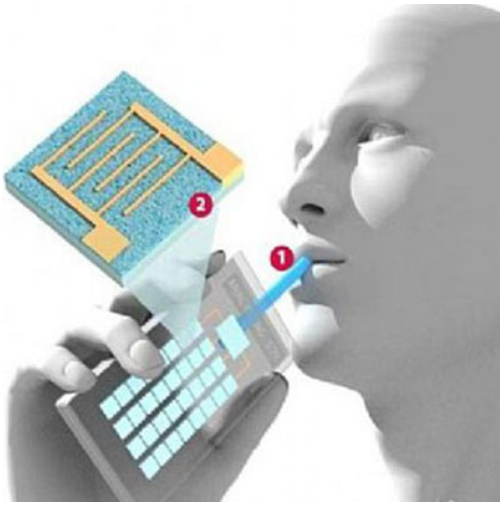

Figure 1: **Diagram of the NA-NOSE device**. Patients breath into the device and nano-wires analyze exhaled molecules.

VII.1.3. Biosensors & telemedicine

A target of telehealth is to maintain or improve the health of people outside the normal healthcare infrastructure. A modern paradigm in healthcare, and one which fits perfectly with telehealth, is "personal self-monitoring". This is associated with the concept of the "personal health record". One factor in maintaining health is to monitor physiological parameters; this is of course especially important in people with chronic disease such as diabetes or heart disease. Many physiologic parameters can be monitored including blood pressure (Tran 2009), pulse rate, temperature, weight, blood glucose (Greenwood et al. 2014), oxygen saturation, electrocardiogram (Chen et al. 2014; Leijdekkers and Gay 2006). In a paper by Simon and Seldon (2012), the

implementation of standards for data acquisition, storage and transmission is described in order to maximize the compatibility among disparate components.

Recent technological advances have provided wearable biosensors that enable the continuous monitoring of vital functions with the capability to send warning signal to health centers that can geolocalize the patient (Patel et al. 2012). Some biosensors can provide accurate monitoring of multiple biotargets including viruses (Human Immunodeficieny Virus-1), bacteria (*Escherichia coli* and *Staphylococcus aureus*), and cells ($CD41^+$ T lymphocytes) from fingerprick volumes of blood (Shafiee et al. 2015).

Diagnosis of cancer can also be integrated into self-monitoring and telehealth approaches. Sadeghi and co-workers have developed a tool based on the paradigm of self-monitoring that can help in the detection of melanoma, basal cell carcinoma (BBC) and squamous cell carcinoma (SCC). The electronic device (MoleScope®, Metaoptima, Vancouver, Canada) is made of a lens that can capture a mole image using a smartphone. Images are processed with an algorithm analyzing the appearance of detected streak lines (Sadeghi et al. 2013). Finally images of the moles and the associated classification are sent to a dermatologist. This procedure can be easily reproduced enabling a longitudinal follow-up of moles that present suspicious morphologic patterns.

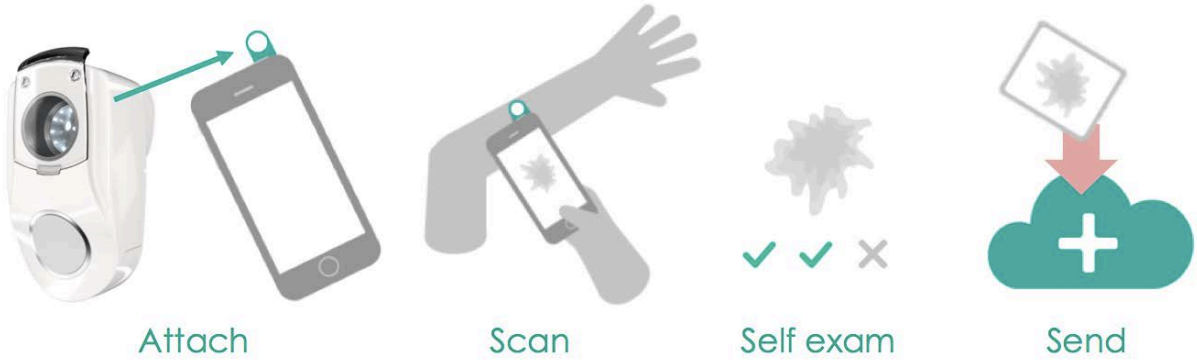

Figure 2: **MoleScope device used in the characterization of moles**. The MoleScope device has to be attached to a smartphone. The user can take images of moles. An algorithm-based application is then used to detect specific patterns related to the morphology of dangerous moles. Finally, images are sent to a dermatologist that can perform longitudinal follow-up of the morphology of the suspicious moles.

VII.1.4 Image-based evaluation of the TME

Once a cancer has been detected at an early stage, it will remain necessary to localize and follow any detectable tumors using the imaging modalities available in clinic. When a tumor is big enough, biopsy may be performed to characterize the type and the stage of cancer. Innovative *in vivo* imaging techniques need also to be in place that can provide robust, non-invasive information concerning the status of the TME, tumor physiology and immune aspects. The work presented in Chapter V provides an example of such an *in vivo* approach by which the tumor stiffness (SWE) assessment of the level of fibrosis and the functional (CEUS) assessment of the tumor microvessel distribution enabled the distinction between antiangiogenic and cytotoxic therapeutic responses. As described in Chapter III, a wide range of innovative techniques based on CT, TEP, SPECT, MRI, optical (pre-clinical) and ultrasound imaging modalities are being developed to more precisely follow tumor changes at different scales: molecular, physiologic, anatomic. In the future, information obtained via multiple

imaging modalities, will need to be analyzed together and will need to be better related to the modifications they reflect in the TME.

This is no easy task. As described in Chapter II, tumor development is a complex process resulting from a large range of molecular and physical interactions. Despite this, novel research is underway to better understand and model the process. For example, Macklin and colleagues (2009) have developed a multiscale and nonlinear model that simulates vascular tumor growth. This model requires information about necrotic, hypoxic and proliferative areas in the tumor and also considers interactions that occur within the TME. Using their model, they were able to simulate maps of tumor oxygenation, intra-tumor pressure, microvessels sprouting, the level of hematocrit and tumor growth. The main limitation of the cited work is that simulations are based on data acquired invasively and are not compared with any *in vivo* data. Ultimately, it should be possible to characterize specific characteristics of the TME (e.g. hypoxia, necrosis, blood perfusion and interstitial pressure) with *in vivo* imaging and then use these characteristics as input for a mathematical model predicting tumor development. Such a mathematical model would furthermore provide an analytical means to gather multi-scale, image-based data for the evaluation of tumor development.

VII.2. Emerging, innovative techniques to enhance the therapeutic effect

As described in Chapter II, tumor development depends strongly on the surrounding TME. The specific tumor physiology results from molecular interactions between tumor cells, endothelial cells, immune cells and others components of the ECM. The characterization of the heterogeneous TME in terms of local blood supply, oxygenation, tissue viability, acidity and IFP is crucial to better assess, predict and adapt therapeutic strategies. Imaging techniques should hold a privileged place in the future of such therapeutic guidance. In the context of cancer therapy, techniques based on ionizing radiation, ultrasound waves, photons or other particles have recently arrived in the clinic or still are in development. To reduce undesirable effects on surrounding healthy tissues and to more effectively destroy tumor cells throughout the, often heterogeneous TME many techniques applying local physical interactions with the tumor are under development. In the following sections, the state-of-the-art for several emerging therapeutic techniques that seek to more fully consider the local TME or even to modify the TME to enhance therapy are briefly considered. In particular, in Section VII.2.4, research performed during this thesis with a novel therapeutic approach, non-thermal plasma, is described.

In Section 6.3 of Chapter II different strategies to treat cancer were presented. Conventional cancer therapies consist in using chemotherapeutic agents that can be associated with radiation-therapy and/or surgical debulking. A wide range of new therapeutic molecules that target different compartments of the TME such as the ECM, vasculature or immune system are undergoing clinical trials (Junttila and de Sauvage 2013). Several therapies based on physical interactions with tumor tissues are already used in the clinic. For example, radiotherapy alters tumor cell DNA by exposing cells to photons of high energy (gamma rays, ranging from 300keV to 25MeV depending on the source and the setup). Unfortunately, energy is also delivered to the surrounding healthy tissues. Setups with specific architectures such as multi-leaf collimators (MLC) (Ge et al. 2014), intensity-modulated radiation therapy (IMRT) (Guha et al. 2012) and image guided radiotherapy (IGRT) (Zelefsky et al. 2012) can reduce the radiotherapy delivered to healthy tissues. Hadron particles such as protons and positive ions can also degrade DNA of tumor cells. These sources of radiation provide

maximum energy deposition at the end of the particle trajectory, thus significantly reducing the exposition of healthy tissues to radiation (Figure 3) (Hamada et al. 2010; Hegelich et al. 2006; Paganetti and Bortfeld 2005).

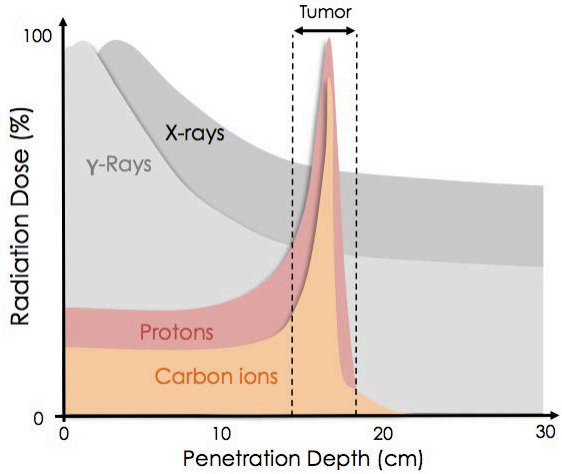

Figure 3: **Diagram of the relationship between radiation dose delivered and penetration depth in biological tissue for different sources of radiation**. The advantage of protons and positive ions in the treatment of tumor is that maximum radiation dose is delivered in tumor tissues whereas for conventional radiotherapy (gamma and X-rays) a non-negligible amount of radiation reaches healthy tissues. Nevertheless, sources of hadron particles are not easily accessible and represent high cost for therapy centers.

VII.2.1. High intensity focused ultrasound (HIFU)

High intensity focused ultrasound (HIFU) provides local deposition of acoustic energy within the body, which can cause tissue necrosis and hemostasis. In the focused ultrasound field, the acoustic intensity is sufficiently low near the transducer so that tissues are unharmed. In the focal volume, the intensity is much higher and absorption of the acoustic field is significant enough to thermally denature tissue proteins. Bailey et al. (2003) reviewed different uses of HIFU in the context of therapy including hemostasis, surgery, and stimulation of the immune response. HIFU is currently used in the clinic for various applications including the treatment of prostate cancer. Poissonnier et al. (2007) evaluated the results of HIFU treatments of localized prostate cancer in 277 patients.

Recently, it was shown that coupling HIFU treatment with MR guidance enabled transcranial ablation of tumors. Collucia and co-workers (2014) reported a successful application of noninvasive transcranial HIFU for partial brain tumor ablation in a patient suffering from a centrally located malignant glioma. They used a setup (Martin et al. 2009), made of 1024 transducers with a central frequency of 650 kHz to generate a focal spot with a submillimetric resolution. Before performing the non-invasive surgery, they acquired high-resolution CT data of the patient's head that was registered to the MR images for subsequent acoustic modeling and correction of skull-induced acoustic distortions. As shown in Figure 4, MR images acquired immediately after the intervention revealed multiple isolated lesions in the insonified tumor tissue that were clearly visible as bright zones in diffusion weighted images (DWI). The longitudinal follow-up of the patient after HIFU treatment revealed that partial tumor ablation could be achieved without provoking neurological deficits or other adverse effects in the patient.

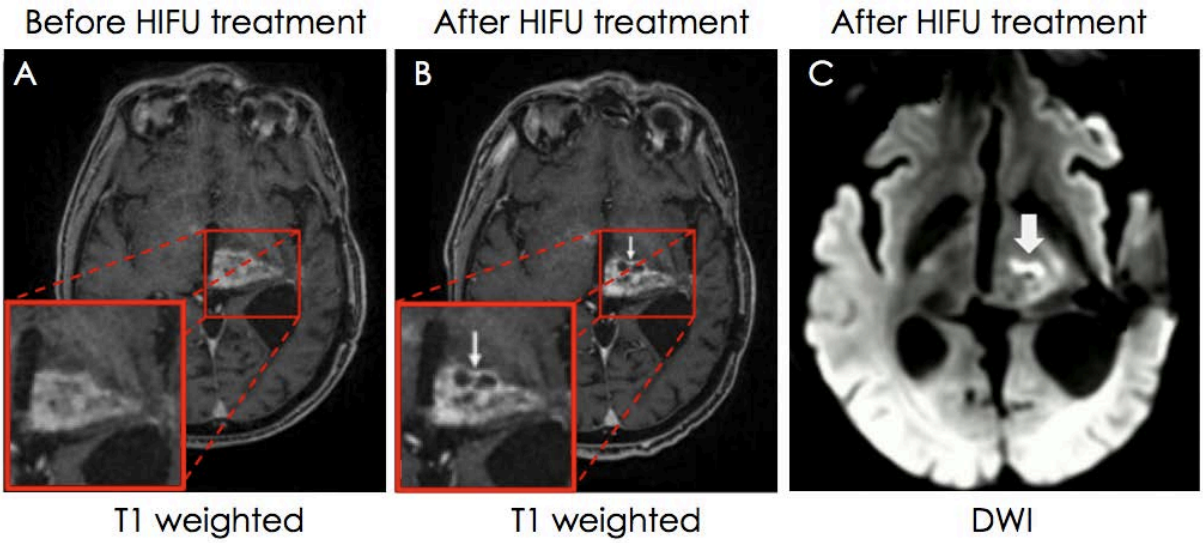

Figure 4: **Pre- and post-interventional MR findings of a brain tumor in living patient. (A, B)** T1-weighted image depicts a contrast-enhanced tumor with a progressive necrotic center in the post-interventional follow-up after 5 days. **(C)** Diffusion weight imaging (DWI) performed 30 min after intervention revealed significant damage to the sonicated tumor tissue. Over the 25 sonications, 17 sonications reached ablative temperatures >55°C with a maximum of 65°C. *Figure adapted from (Coluccia et al. 2014).*

VII.2.2. Photodynamic therapy (PDT)

PDT is a photochemistry-based therapeutic modality in which a light-activatable chemical (photosensitizer, PS) is energized by light (600–800 nm) to produce cytotoxic molecular species via electron transfer to biological tissues (type I photosensitization), and potentially indirect excitation of molecular oxygen, or direct energy transfer to molecular oxygen (type II photosensitization). The main feature of PDT is its intrinsic dual selectivity because both the PS and light must be present for photodamage which provides highly localized tissue damage and the absence of toxicity outside of the illumination field (Spring et al. 2015). PDT was first approved in 1993 in Canada, using the photosensitizer Photofrin for the preventive treatment of bladder cancer. This is the most commonly used photosensitizer in the clinic today and it is used in a wide range of cancers such as gastric, papillary bladder, cervical, oesephageal and endobroncheal (Dolmans et al. 2003). In clinical PDT protocols with Photofrin, irradiation is usually performed at doses of 50–500 J/cm^2, and many experimental studies of PDT commonly used a dose of approximately 100 J/cm^2 (Fang et al. 2015). Recent developments have enabled these PDT to diagnose and follow treatment of brain tumors (Bechet et al. 2014).

VII.2.3. Sonosensitization

In Chapter VI, research performed during this thesis to investigate the ability to use multiparametric ultrasonic imaging to monitor efficacy of sonosensitization in a Lewis lung carcinoma (chapter VI) was described and we showed the potential enhanced effect of sonosensitization coupled with cytotoxic therapy in the modification of tumor vasculature. One of the mechanisms proposed to describe the effect of sonosensitization on tumor cells is the mechanical stress that repeated oscillations of MBs induces on endothelial cells. Stressed endothelial cells increase the concentration of ceramide present in the membrane. This is known to play a role in the signaling

pathways of apoptosis (Al-Mahrouki et al. 2014). It was shown in previous studies that the association of radiotherapy with sonosensitization enhances cell death (delayed tumor growth) and reduces the tumor microvascular network (Tran et al. 2012). Because sonosensitization can enhance conventional therapy, its main interest resides in the reduction of the dose of administered drugs to reduce their toxicity effect on healthy tissues.

VII.2.4. Exposure of tumors to cold plasma

Plasmas consist of an ionized gas that is generally created under high-temperature conditions. Recent progress in cold atmospheric plasmas (CAP) has led to the creation of cold plasmas with a gas temperature close to room temperature (Fridman et al. 2008). CAP generates a variety of ions, free radicals, excited atoms and molecules, UV photons, and reactive species such as reactive oxygen species (ROS) and reactive nitrogen species (RNS) (Pozebon et al. 2010; Thiyagarajan et al. 2012). Previous studies have demonstrated the non-aggressive nature of the cold plasma: it can be applied on organic materials, also in watery environment, without causing thermal/electric damage to the surface (Stoffels et al. 2002). Very recent research demonstrated the strong potential of cold plasma for the treatment of cancer (Brullé et al. 2012; Keidar et al. 2011; Keidar et al. 2013; Vandamme et al. 2010; Vandamme et al. 2012; Walk et al. 2013).

The precise mechanism of action of plasma on living cells remains unclear and controversial. Some authors suggest that ion species play the most important role in plasma-cell interactions by triggering intracellular biochemistry (Dobrynin et al. 2009; Pei et al. 2012; Yan et al. 2012). It has also been proposed that neutral species play the primary role in some plasma-cell interaction pathways (Kalghatgi et al. 2010). It has been shown that plasma can have ambivalent effects due to the different ionized species that it can generate. Thus, CAP can either lead to deleterious or healing effects by actions promoting (Oxygen O) or acting against (Nitric oxide, NO) tumor cells (Kong et al. 2009). The roles of other species such as O_3 and OH, for example, remain unclear.

During the final year of my thesis research, a partnership between the LIB and a team from the Laboratory of Physics of Plasma (LLP) was created to investigate the potential to monitor TME modifications during therapy with CAP. The LLP has developed a cold plasma source for use in the animal imaging laboratory. The device is made of an electrode surrounded by a dielectric barrier (glass). Ambient air is ionized at the tip of the glass as shown in Figure5-B. We performed a study using this source to treat a CT26 colorectal ectopic tumor model. A group of 35 mice was divided into three homogeneous groups in terms of tumor size: a placebo group (N = 11) and two others groups that received, respectively, CAP exposure at 100 J/cm^2 (N = 12) and 300 J/cm^2 (N = 12) per day of therapy. Twelve days after tumor implantation (V_{tumor} = 70 ± 50 mm^3, mean ± SD), therapy was applied for 5 consecutive days. The area of the ionized atmospheric gas was 4 mm^2, and the tumor surface (approximation of the surface of an ellipsoid) was measured for each mouse before the initiation of plasma treatment. The number of treatment points was adapted to treat the whole tumor surface. Deposition of energy was monitored in real time using an oscilloscope to measure the transmitted energy between the two electrodes. This enabled the adaptation of the duration of therapy exposure for each point of treatment to obtain the desired level of treatment (100 J/cm2 or 300 J/cm2).

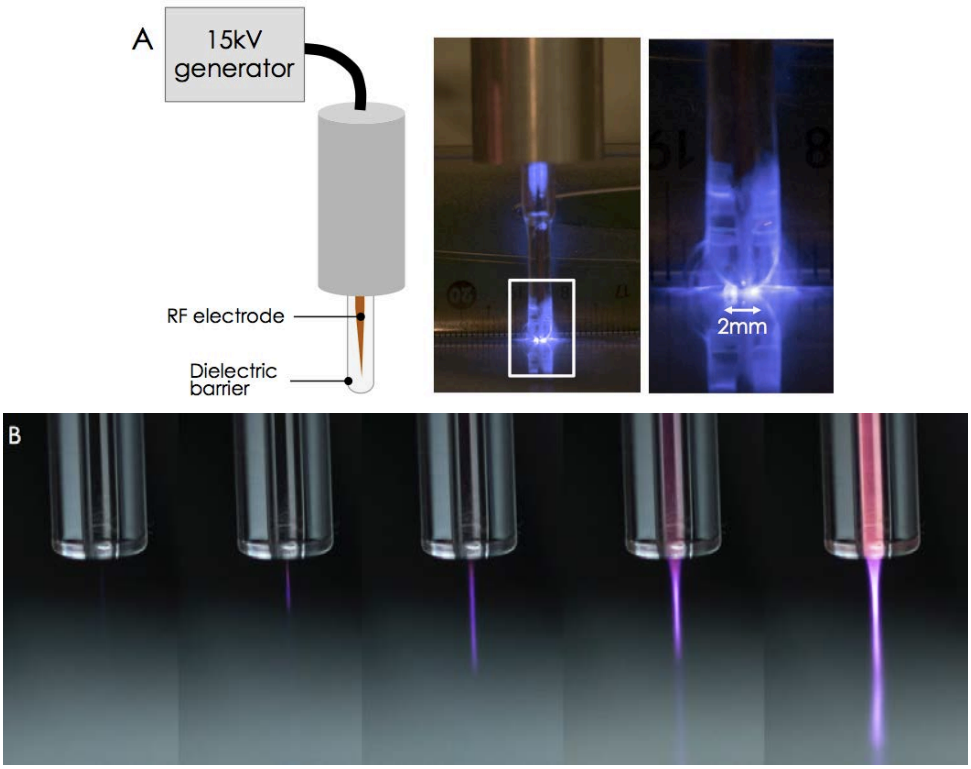

Figure 5: **Presentation of plasma jet and cold atmospheric plasma (CAP)**. A) CAP based on an electrode surrounded by a dielectric medium (glass) that provides a zone of ionization at the tip of the glass. B) For the presented plasma jet, helium gas is ionized by an electrode before being expulsed through a tube.

At baseline and at the end of the experiment (D+9), the evolution of the tumor volume (B-mode), tumor stiffness (SWE) and tumor vascularization (CEUS) were monitored. As presented in Figure 6, for matched measurement days, results from this pilot study did not reveal significant differences between size, stiffness or functional parameters of the tumors from the different treatment groups. Only results related to the control group and the 300 J/cm^2 group are presented here.

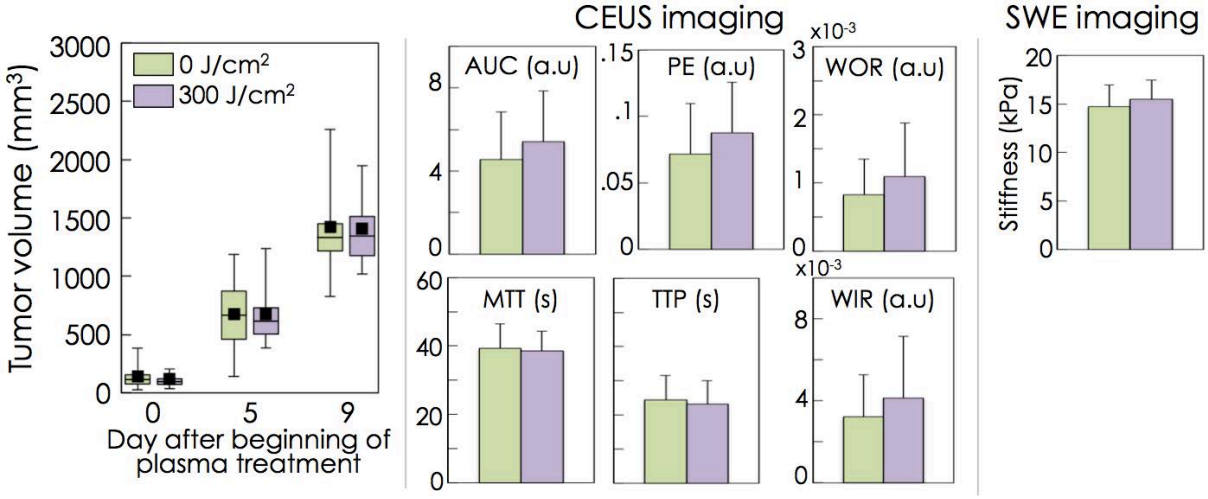

Figure 6: **Tumor volume functional parameters.** Results presented for CEUS and SWE imaging are related to the last day of experiment corresponding to 9 days after the initiation of plasma therapy. No difference was observed between the control group and the group receiving 300 J/cm^2.

Future experiments will be performed using a newly designed and improved treatment device with a higher surface-area for each treatment position which will reduce the number of points on the tumor's surface that must be treated. The LLP team has also developed a plasma jet (ionization of helium gas) which could be tested in the future on murine tumor models (Figure 5-B).

VII.3. Conclusions

As described in this chapter, current developments in the field of cancer detection and therapy are moving toward solutions that will provide earlier and more patient-adapted therapies to provide more efficient and local anti-cancer effect with reduced side effects. Multiparametric ultrasonic approaches can be expected to contribute significantly as the information on the TME provided with these noninvasive parameters becomes better understood.

Longitudinal follow-up and characterization of tumor modifications under the specific therapies described in this thesis were performed using clinical ultrasound systems. This implies that findings exhibited in the current thesis should contribute toward the interpretation of similar ultrasonic parameters measured in patients. Concerning shear wave elastography, higher values of stiffness correlate with a greater amount of fibrosis. Moreover, the standard deviation of the SWE within the tumor may be an interesting index for the characterization of tumor heterogeneity. Contrast-enhanced ultrasound imaging, provides three main types of information: the evolution of the tumor blood volume (PE, AUC), the functionality of tumor vasculature (TTP, MTT, WOR, WIR) and the distribution of perfused and unperfused areas. Moreover, during the late phase of the passage of the MB bolus, areas that remain unperfused are strongly correlated with necrotic tissues. Further experiments are still required to more precisely relate histological markers with *in vivo* ultrasonic imaging parameters. Information about the dynamic perfusion, blood volume, necrotic and fibrotic areas should provide pertinent input data for mathematical models, such as the one mentioned briefly in Section VII.I.4, in order to predict tumor evolution.

More specific and targeted therapies are under development to better preserve healthy tissues while intensifying the anti-tumoral effect. The approach based on sonosensitization that was evaluated during this thesis presents the advantage that relies on devices and agents (UCA and chemotherapy) that are already used in the clinic. Thus, once conclusive results are obtained in preclinical studies, transfer of sonosensitization to improve therapy in patients could be relatively straightforward. Eventual, clinical applications of cold plasma in tumor treatment will be less straight-forward and potential applications are limited to superficially accessible cancers such as those localized at the surface of the body (skin) or mucous membrane (mouth).

The non-invasive nature of ultrasonic techniques lends itself well to regular screening in "at-risk" patients. Ultrasound also offers significant advantages in terms of: the real-time nature, the complementary information provided by different parameters (CEUS, SWE, QUS) and the capacity to acoustically stimulate effects such as the sonosensitization. The work presented in this thesis contributes to the rich research underway to improve the detection, the characterization and the treatment of cancer.

VII.4. Bibliography

Al-Mahrouki A a, Iradji S, Tran WT, Czarnota GJ. Cellular characterization of ultrasound-stimulated microbubble radiation enhancement in a prostate cancer xenograft model. Dis Model Mech 2014;7:363–72.

Bailey MR, Khokhlova V a., Sapozhnikov O a., Kargl SG, Crum L a. Physical mechanisms of the therapeutic effect of ultrasound (a review). Acoust Phys 2003;49:369–388.

Bechet D, Mordon SR, Guillemin F, Barberi-Heyob M a. Photodynamic therapy of malignant brain tumours: A complementary approach to conventional therapies. Cancer Treat Rev Elsevier Ltd, 2014;40:229–241.

Brullé L, Vandamme M, Riès D, Martel E, Robert E, Lerondel S, Trichet V, Richard S, Pouvesle JM, Le Pape A. Effects of a Non Thermal Plasma Treatment Alone or in Combination with Gemcitabine in a MIA PaCa2-luc Orthotopic Pancreatic Carcinoma Model. PLoS One 2012;7:1–10.

Buszewski B, Martyna K, Ligor T, Amann A. Human exhaled air analytics : biomarkers of diseases. Biomed chromotography 2007;566:553–566.

Chen J, Quadri S, Pollonini L, Naribole S, Ding J, Zheng Z, Knightly EW, Dacso CC. Blue Scale : Early Detection of Impending Congestive Heart Failure Events via Wireless Daily Self-Monitoring. Heal Innov Point-of-Care Technol Conf Seattle 2014;63–66.

Cohen S, Punt C, Iannotti N, Saidman B, Sabbath K, Gabrail N, Picus J, Morse M, Mitchell E, Miller M, Doyle G, Tissing H, Terstappen L, Meropol N. Relationship of circulating tumor cells to tumor response, progression-free survival, and overall survival in patients with metastatic colorectal cancer. J Clin Oncol 2008;23:3213–3221.

Coluccia D, Fandino J, Schwyzer L, O'Gorman R, Remonda L, Anon J, Martin E, Werner B. First noninvasive thermal ablation of a brain tumor with MR-guided focused ultrasound. J Ther ultrasound 2014;2:17.

Cristofanilli M, Budd G, Ellis M, Stopeck A, Matera J, Miller M, Reuben J, Doyle G, Allard W, Terstappen L, Hayes D. Circulating tumor cells, disease progression, and survival in metastatic breast cancer. N Engl J Med 2004;351:781–791.

De Bono J, Scher H, Montgomery R, Parker C, Miller M, Tissing H, Doyle G, Terstappen L, Pienta K, Raghavan D. Circulating tumor cells predict survival benefit from treatment in metastatic castration-resistant prostate cancer. Clin Cancer Res 2008;14:6302–6309.

Dobrynin D, Fridman G, Friedman G, Fridman A. Physical and biological mechanisms of direct plasma interaction with living tissue. New J Phys 2009;11.

Dolmans D, Fukumura D, Rakesh K J. Photodynamic therapy for cancer. Nat Rev Cancer 2003;3:375–80.

Ehmann R, Boedeker E, Friedrich U, Sagert J, Dippon J, Friedel G, Walles T. Canine scent detection in the diagnosis of lung cancer: revisiting a puzzling phenomenon. Eur Respir J 2012;39:669–676.

Fang J, Liao L, Yin H, Nakamura H, Subr V, Ulbrich K, Maeda H. Photodynamic therapy and imaging based on tumor-targeted nanoprobe , polymer-conjugated zinc protoporphyrin. Futur Sci 2015;

Fridman G, Friedman G, Gutsol A, Shekhter AB, Vasilets VN, Fridman A. Applied Plasma Medicine. Plasma Process Polym 2008;5:503–533.

Ge Y, O'Brien RT, Shieh C-C, Booth JT, Keall PJ. Toward the development of intrafraction tumor deformation tracking using a dynamic multi-leaf collimator. Med Phys 2014;41.

Greenwood D a, Young HM, Quinn CC. Telehealth Remote Monitoring Systematic Review: Structured Self-monitoring of Blood Glucose and Impact on A1C. J Diabetes Sci Technol 2014;8:378–389.

Guha S, G Kelly, C, Guha R. Intensity Modulated Radiation Therapy (IMRT) in the Treatment of Squamous Carcinoma of the Oropharynx: An Overview. J Cancer Sci Ther 2012;04.

Hakim M, Billan S, Tisch U, Peng G, Dvrokind I, Marom O, Abdah-Bortnyak R, Kuten a, Haick H. Diagnosis of head-and-neck cancer from exhaled breath. Br J Cancer Nature Publishing Group, 2011;104:1649–55.

Hamada N, Imaoka T, Masunaga S, Ogata T, Okayasu R, Takahashi A, Kato T a., Kobayashi Y, Ohnishi T, Ono K, Shimada Y, Teshima T. Recent Advances in the Biology of Heavy-Ion Cancer Therapy. J Radiat Res 2010;51:365–383.

Hegelich BM, Albright BJ, Cobble J, Flippo K, Letzring S, Paffett M, Ruhl H, Schreiber J, Schulze RK, Fernández JC. Laser acceleration of quasi-monoenergetic MeV ion beams. Nature 2006;439:441–4.

Ilie M, Hofman V, Long-Mira E, Selva E, Vignaud J-M, Padovani B, Mouroux J, Marquette C-H, Hofman P. "Sentinel" circulating tumor cells allow early diagnosis of lung cancer in patients with chronic obstructive pulmonary disease. PLoS One 2014;9:e111597.

Junttila MR, de Sauvage FJ. Influence of tumour micro-environment heterogeneity on therapeutic response. Nature 2013;501:346–54.

Kalghatgi S, Friedman G, Fridman A, Clyne AM. Endothelial cell proliferation is enhanced by low dose non-thermal plasma through fibroblast growth factor-2 release. Ann Biomed Eng 2010;38:748–757.

Keidar M, Shashurin A, Volotskova O, Ann Stepp M, Srinivasan P, Sandler A, Trink B. Cold atmospheric plasma in cancer therapy. Phys Plasmas 2013;20:057101–8.

Keidar M, Walk R, Shashurin a, Srinivasan P, Sandler a, Dasgupta S, Ravi R, Guerrero-Preston R, Trink B. Cold plasma selectivity and the possibility of a paradigm shift in cancer therapy. Br J Cancer Nature Publishing Group, 2011;105:1295–301.

Kong MG, Kroesen G, Morfill G, Nosenko T, Shimizu T, van Dijk J, Zimmermann JL. Plasma medicine: an introductory review. New J Phys 2009;11:115012.

Konvalina G, Haick H. Sensors for Breath Testing : From Nanomaterials to Comprehensive Disease Detection. Acc Chem Res 2014;47:66–76.

Lamuraglia M, Bridal SL, Santin M, Izzi G, Rixe O, Paradiso A, Lucidarme O. Clinical relevance of contrast-enhanced ultrasound in monitoring anti-angiogenic therapy of cancer: current status and perspectives. Crit Rev Oncol Hematol 2010;73:202–12.

Lassau N, Bonastre J, Kind M, Vilgrain V, Lacroix J, Cuinet M, Taieb S, Aziza R, Sarran A, Labbe-Devilliers C, Gallix B, Lucidarme O, Ptak Y, Rocher L, Caquot L-M, Chagnon S, Marion D, Luciani A, Feutray S, Uzan-Augui J, Coiffier B, Benastou B, Koscielny S. Validation of Dynamic Contrast-Enhanced Ultrasound in Predicting Outcomes of Antiangiogenic Therapy for Solid Tumors: The French Multicenter Support for Innovative and Expensive Techniques Study. Invest Radiol 2014;00:1–7.

Leijdekkers P, Gay V. Personal Heart Monitoring and Rehabilitation System using Smart Phones. Proc Int Conf Mob Bus 2006;

Macklin P, McDougall S, Anderson AR a, Chaplain M a J, Cristini V, Lowengrub J. Multiscale modelling and nonlinear simulation of vascular tumour growth. J Math Biol 2009;58:765–798.

Martin E, Jeanmonod D, Morel A, Zadicario E, Werner B. High-intensity focused ultrasound for noninvasive functional neurosurgery. Ann Neurol 2009;66:858–861.

McCulloch M, Jezierski T, Broffman M, Hubbard A, Turner K, Janecki T. Diagnostic accuracy of canine scent detection in early- and late-stage lung and breast cancers. Integr Cancer Ther 2006;5:30–9.

Montuschi P, Nightingale J, Kharitonov S, Barnes P. Ozone- induced increase in exhaled 8-isoprostane in healthy subjects is resistant to inhaled budesonide. Free Radic Biol Med 2002;33:1403–1408.

Moser E, McCulloch M. Canine scent detection of human cancers: A review of methods and accuracy. J Vet Behav Clin Appl Res Elsevier Inc, 2010;5:145–152.

Paganetti H, Bortfeld T. Proton beam radiotherapy - The state of the art. New Technol. Radiat. Oncol. (Medical Radiol. Ser. 2005.

Patel S, Park H, Bonato P, Chan L, Rodgers M. A review of wearable sensors and systems with application in rehabilitation. J Neuroeng Rehabil BioMed Central Ltd, 2012;9:21.

Pei X, Lu X, Liu J, Liu D, Yang Y, Ostrikov K, Chu PK, Pan Y. Biofilm By a Room-Temperature, Battery-Operated, Handheld Air Plasma Jet. J Phys D Appl Phys 2012;45:165205.

Peng G, Hakim M, Broza YY, Billan S, Abdah-Bortnyak R, Kuten a, Tisch U, Haick H. Detection of lung, breast, colorectal, and prostate cancers from exhaled breath using a single array of nanosensors. Br J Cancer Nature Publishing Group, 2010;103:542–51.

Phillips M, Glesson K, Hughes J, Greenberg J, Cataneo R, Baker L, McVay W. Volatile organic compounds in breath as markers of lung cancer: a cross-sectional study. Lancet 1999a;353:1930–1933.

Phillips M, Herrera J, Krishnan S, Zain M, Greenberg J, Cataneo R. Variation in volatile organic compounds in the breath of normal humans. J Chromatogr 1999b;729:75–88.

Poissonnier L, Chapelon J-Y, Rouvière O, Curiel L, Bouvier R, Martin X, Dubernard JM, Gelet A. Control of prostate cancer by transrectal HIFU in 227 patients. Eur Urol 2007;51:381–387.

Pozebon D, Dressler VL, Mesko MF, Matusch A, Becker JS. Bioimaging of metals in thin mouse brain section by laser ablation inductively coupled plasma mass spectrometry: novel online quantification strategy using aqueous standards. J Anal At Spectrom 2010;25:1739.

Sadeghi M, Lee TK, Mclean D, Lui H, Atkins MS. Detection and Analysis of Irregular Streaks in Dermoscopic Images of Skin Lesions. IEEE Trans Ultrason Ferroelectr Freq Control 2013;32:849–861.

Shafiee H, Asghar W, Inci F, Yuksekkaya M, Jahangir M, Zhang MH, Durmus NG, Gurkan UA, Kuritzkes DR, Demirci U. Paper and Flexible Substrates as Materials for Biosensing Platforms to Detect Multiple Biotargets. Sci Rep 2015;5:8719.

Simon SK, Seldon HL. Personal Health Records : Mobile Biosensors and Smartphones for Developing Countries. Glob Telehealth 2012;182:125 – 132.

Spring BQ, Rizvi I, Xu N, Hasan T. The role of photodynamic therapy in overcoming cancer drug resistance. Photochem Photobiol Sci 2015;

Stoffels, Flikweert, Kroesen. Plasma needle : a non-destructive atmospheric plasma source for fine surface treatment of (bio) materials. Plasma Sources Sci Technol 2002;383.

Teshima N, Li J, Toda K, Dasgupta P. Determination of acetone in breath. Anal Chim Acta 2005;535:189–199.

Thiyagarajan M, Sarani A, Gonzalez X. Characterization of Portable Resistive Barrier Plasma Jet and Its Direct and Indirect Treatment for Antibiotic Resistant Bacteria and THP-1 Leukemia Cancer Cells. Plasma Sci IEEE Trans 2012;40:3533 – 3545.

Tisch U, Schlesinger I, Ionescu R, Nassar M, Axelrod N, Robertman D, Tessler Y, Azar F, Marmur A, Aharon-Peretz J, Haick H. Detection of Alzheimer's and Parkinson's disease from exhaled breath using nanomaterial-based sensors. Futur Med 2012;8:43–56.

Tran B. CUFFLESS BLOOD PRESSURE MONITORING APPLIANCE. USA, 2009.

Tran WT, Iradji S, Sofroni E, Giles A, Eddy D, Czarnota GJ. Microbubble and ultrasound radioenhancement of bladder cancer. Br J Cancer 2012;107:469–76.

Tyson P. Dogs' Dazzling Sense of Smell. Nov Sci 2012;1–5.

Vandamme M, Robert E, Lerondel S, Sarron V, Ries D, Dozias S, Sobilo J, Gosset D, Kieda C, Legrain B, Pouvesle JM, Pape A Le. ROS implication in a new antitumor strategy based on non-thermal plasma. Int J Cancer 2012;130:2185–2194.

Vandamme M, Robert E, Pesnel S, Barbosa E, Dozias S, Sobilo J, Lerondel S, Le Pape A, Pouvesle J-M. Antitumor Effect of Plasma Treatment on U87 Glioma Xenografts: Preliminary Results. Plasma Process Polym 2010;7:264–273.

Vona G, Sabile a, Louha M, Sitruk V, Romana S, Schütze K, Capron F, Franco D, Pazzagli M, Vekemans M, Lacour B, Bréchot C, Paterlini-Bréchot P. Isolation by size of epithelial tumor cells : a new method for the immunomorphological and molecular characterization of circulatingtumor cells. Am J Pathol 2000;156:57–63.

Walk RM, Snyder J a., Srinivasan P, Kirsch J, Diaz SO, Blanco FC, Shashurin A, Keidar M, Sandler AD. Cold atmospheric plasma for the ablative treatment of neuroblastoma. J Pediatr Surg Elsevier Inc., 2013;48:67–73.

Williams R, Hudson JM, Lloyd BA, Sureshkumar AR, Lueck G, Milot L, Atri M, Bjarnason GA, Burns PN. Dynamic Microbubble Contrast-enhanced US to Measure Tumor Response to Targeted

Therapy : A Proposed Clinical Protocol with Results from Renal Cell Carcinoma Patients Receiving Antiangiogenic Therapy. Radiology 2011;260:581–590.

Xu Z, Broza YY, Ionsecu R, Tisch U, Ding L, Liu H, Song Q, Pan Y, Xiong F, Gu K, Sun G, Chen Z, Leja M, Haick H. A nanomaterial-based breath test for distinguishing gastric cancer from benign gastric conditions. Br J Cancer 2013 [cited 2015 Apr 5];108:941–50.

Yan X, Xiong Z, Zou F, Zhao S, Lu X, Yang G, He G, Ostrikov K. Plasma-induced death of HepG2 cancer cells: Intracellular effects of reactive species. Plasma Process Polym 2012;9:59–66.

Zelefsky MJ, Kollmeier M, Cox B, Fidaleo A, Sperling D, Pei X, Carver B, Coleman J, Lovelock M, Hunt M. Improved clinical outcomes with high-dose image guided radiotherapy compared with non-IGRT for the treatment of clinically localized prostate cancer. Int J Radiat Oncol Biol Phys Elsevier Inc, 2012;84:125–129.

Publications + Communications

Dizeux, A., Payen, T., Barrois, G., Lamuraglia M., Baldini, C., Le Guillou, D., Comperat, E., Gennisson, J.L., Tanter, M., Oelze, M., Bridal, S.L. ***In vivo*** **discrimination of tumor modifications during antiangiogenic and cytotoxic therapy using ultrasonography modalities: Shear Wave Elastography (SWE), Contrast Enhanced Ultrasound (CEUS) and Quantitative Ultrasound (QUS).** *Investigative Radiology,* **2015**. en cours de soumission
+ communication to the American Association of Cancer Research annual meeting, Philadelphia April **2015**

Dizeux, A., Payen, T., Barrois, G., Baldini C., Le Guillou D., Gennisson J.L., Tanter M., S Lori Bridal. **Complementarity of shear wave elastography and dynamic contrast-enhanced ultrasound to discriminate tumor modifications during antiangiogenic and cytotoxic therapy**. *IEEE International Ultrasonics Symposium (IUS)*, 1144-1147. **2014**.

Demene, C.,Payen, T., **Dizeux, A.**, Barrois, G., Gennisson, J. L., Bridal, L., & Tanter, M., (2014). **Comparison of tumor microvasculature assessment via Ultrafast Doppler Tomography and Dynamic Contrast Enhanced Ultrasound**. *IEEE International Ultrasonics Symposium* (IUS), 421-424. **2014**.

Dizeux, A., Barrois, G., Payen, T., Baldini, C., Le Guillou Buffelo, D., Comperat, E., & Bridal, S. L. **Differentiation of vascular distribution and flow patterns in tumors with Dynamic Contrast-Enhanced Ultrasound (DCE-US) perfusion maps**. *IEEE International Ultrasonics Symposium (IUS),* 1513 – 1516. **2013**.

Barrois, G., Coron, A., Payen, T., **Dizeux, A.** & Bridal, S. L. **A multiplicative model to improve microvascular flow evaluation in the context of dynamic contrast-enhanced ultrasound (DCE-US)**. Proceedings of 2013 IEEE International Symposium in Biomedical Imaging, 724–727. **2013**.

Dizeux, A., Payen, T., Lechuga, G., & Bridal, S. L. **Implementation of a Controlled Injection System for Dynamic Contrast-Enhanced Ultrasonography**. *IEEE International Ultrasonics Symposium (IUS)*, 1339–1342. **2012**.

Publications

Payen, T., **Dizeux, A.**, Baldini, C., Le Guillou, D., Comperat, E., Lamuraglia, M., Lucidarme, O., Bridal, S.L., **VEGFR2-targeted contrast-enhanced ultrasound to distinguish between two antiangiogenic treatments.** *Ultrasound in medicine and biology,* **2015**.

Dizeux, A., Payen, T., Barrois, G., Somaglino, L., Taulier, N., Le Guillou, D., Bridal, S. L., **Reproducibility of contrast-enhanced ultrasound in mice with controlled injection**. *Ultrasound in medicine and biology*, **2015**. (en correction)

Barrois, G., Coron, A., Payen, T., **Dizeux, A.**, & Bridal, S. L. **A Multiplicative Model for Improving Microvascular Flow Estimation in Dynamic Theory and Experimental Validation**. *IEEE Transactions on Ultrasonics, Ferroelectrics and Frequency Control*, *60*, 2284–2294. **2013**

Communications

Dizeux, A., Payen, T., Barrois, G., Lamuraglia M., Baldini, C., Le Guillou, D., Comperat, E., Gennisson, J.L., Tanter, M., Oelze, M., Bridal, S.L. ***In vivo*** **characterization of tumor heterogeneity under antiangiogenic and cytotoxic therapy using ultrasonography modalities: Shear Wave Elastography, Contrast Enhanced Ultrasound and Quantitative Ultrasound.** *International congress of ultrasonics (ICU).* May **2015**, Metz.

Dizeux, A., Payen, T., Barrois, G., Baldini, C., Le Guillou, D., Comperat, E., Gennisson, J.L., Tanter, M., Bridal, S.L. **Utility of Elastography and Contrast-enhanced Ultrasound For The Differentiation of Tumor Modifications Between Antiangiogenic and Cytotoxic Therapy.** *RITS congress (Recherche en Imagerie et Technologies pour la Santé), SFGBM.* Mars **2015,** Dourdan.